An Investigation into the Synthesis and Characterisation of Metal Borohydrides for Hydrogen Storage

by

Daniel Thomas Reed

A thesis submitted to the University of Birmingham
For the degree of
Doctor of Philosophy

School of Metallurgy and Materials
College of Engineering and Physical Sciences
University of Birmingham
October 2009

SYNOPSIS

With relatively high gravimetric and volumetric hydrogen storage capacities, borohydride compounds are being investigated for their potential use as hydrogen storage media. A study has been made into the mechanical milling of metal chlorides with sodium borohydride to try to form homoleptic borohydrides. Various characterisation techniques have been used to characterise the composition and microstructure of the samples, and to monitor in-situ the thermal decomposition processes. It was found that rather than homoleptic borohydrides (such as $Zn(BH_4)_2$ or $Mg(BH_4)_2$), complex borohydrides of the form $AM_2(BH_4)_5$ and $AM(BH_4)_3$ (where A = Li or Na and M = Zn, Mg or Ca) tend to form.

Mechanical milling of zinc chloride with sodium borohydride resulted in the formation of a covalent complex $NaZn_2(BH_4)_5$. Thermal decomposition occurred at 80°C with a mass change of 12 wt.%, associated with the evolution of hydrogen and diborane. A composite mixture with magnesium hydride exhibited a large exotherm (DSC) around 90°C with a corresponding weight loss of 7.6 wt.% (TGA) corresponding to the reaction between diborane and magnesium hydride to form magnesium borohydride. The subsequent decomposition of magnesium borohydride between 260 and 360°C occurred with a weight loss of 1.5 wt.%.

Mechanical milling of calcium chloride or magnesium chloride with sodium borohydride did not produce calcium borohydride and magnesium borohydride, but rather resulted in solid solutions where chlorine ions substitute for borohydride ions within the cubic sodium borohydride lattice. Thermal decomposition of milled calcium chloride and sodium borohydride occurs at a similar temperature (325°C) to that of $Ca(BH_4)_2$ (from Sigma-Aldrich), yielding the same decomposition products of CaH_2, NaCl and CaB_6. Milled magnesium chloride and sodium borohydride thermally decomposes via several unknown phases with a weight loss of 4.4 wt.% between 290 and 400°C to yield Mg, MgB_2, B, and $[B_{12}H_{12}]^{2-}$, similar to the decomposition reaction reported for homoleptic magnesium borohydride.

Lithium borohydride has a maximum theoretical gravimetric hydrogen storage density of 18.4 wt.%, and after decomposing at 600°C, has been shown by Orimo et al [1] to reform $LiBH_4$ when heated to 600°C in 150 bar hydrogen. After heating lithium borohydride through its orthorhombic to hexagonal phase change (118°C) and melting point (280°C), shifts in Raman peak position and peak width were measured as a function of temperature, allowing the calculation of

the energy barrier to reorientation, which agreed with other studies. A sample was also heated to 600°C (under 1 bar Ar) to decompose the sample. In the literature, a number of intermediate phases and reaction products have been predicted and observed ex-situ. This work shows the in-situ formation of lithium dodecaborane ($Li_2B_{12}H_{12}$) at 340°C and amorphous boron from liquid lithium borohydride. During some measurements, an unknown phase was observed between 385 and 400°C; it is still unclear what structure the intermediate has. It is hoped that a greater understanding of the decomposition and ultimately the reformation mechanisms may lead to the development of $LiBH_4$-based materials that can absorb and desorb hydrogen under less extreme conditions.

Future work will look at the recombination of the complex borohydrides formed, with a view to reversible hydrogen storage media. This work has given a clearer understanding of the synthesis and decomposition of the complex borohydrides formed by mechanical milling.

ACKNOWLEDGEMENTS

Firstly, I am extremely grateful for the support and guidance of my supervisor Dr. David Book during my time here. He provided me with many helpful suggestions and important advice during the course of this work.

My thanks to all the members of the hydrogen materials group past and present for your friendship, support and guidance during my 5 years as part of the group. My thanks also go to Dr Paul Anderson and Phil Chater and other members of floor 5 in chemistry for their help, especially with XRD.

I also gratefully acknowledge the financial support from EPSRC to fund my project, to UKSHEC for financial support for consumables and chemicals and the opportunity to learn more about the UK hydrogen storage research program and AWM Science City for helping provide the research group with superb facilities.

Gemma Nicholson, I could never have completed this PhD without your understanding, patience and love, for this I will be eternally grateful. To Jo, Barry and Amy thanks for your support.

Finally to my parents, brother and sister for all the years of support and encouragement you have given me.

CONTENTS

LIST OF FIGURES

LIST OF TABLES

1 INTRODUCTION

This thesis will consider the use of metal borohydrides for the storage of hydrogen in mobile applications. To put the work in context, the following introduction sets out the political, financial and technical background.

Increases in energy demand, particularly in rapidly developing countries such as China and India, will place an even stronger focus on overall energy supply and its diversity. If a balance is not struck between energy supply and the amount of greenhouse gases produced during the conversion of energy, then political, ecological and economic crises will inevitably arise.

Overall, there are three broad concerns surrounding energy:

- Climate change (as a result of greenhouse gases),
- Security of supply and
- Finite source of fossil fuels.

Climate change is believed to be associated with the release of carbon dioxide and other greenhouse gases during the combustion of fossil fuels. It has been shown that there is a correlation between an increasing global release of CO_2 and climate change [2].

Security of energy supply is another key issue since some sources of energy (gas, petroleum, coal, etc.) are not evenly distributed between countries and therefore those countries which are net energy importers do not have a reliable and secure supply of energy.

Currently, significant reserves of energy are in what are described as politically unstable countries by the Western nations. An example of the energy imbalance can be seen in Figure 1.1, which shows that in 2003 the US alone consumed more petroleum than the rest of the world combined [3, 4].

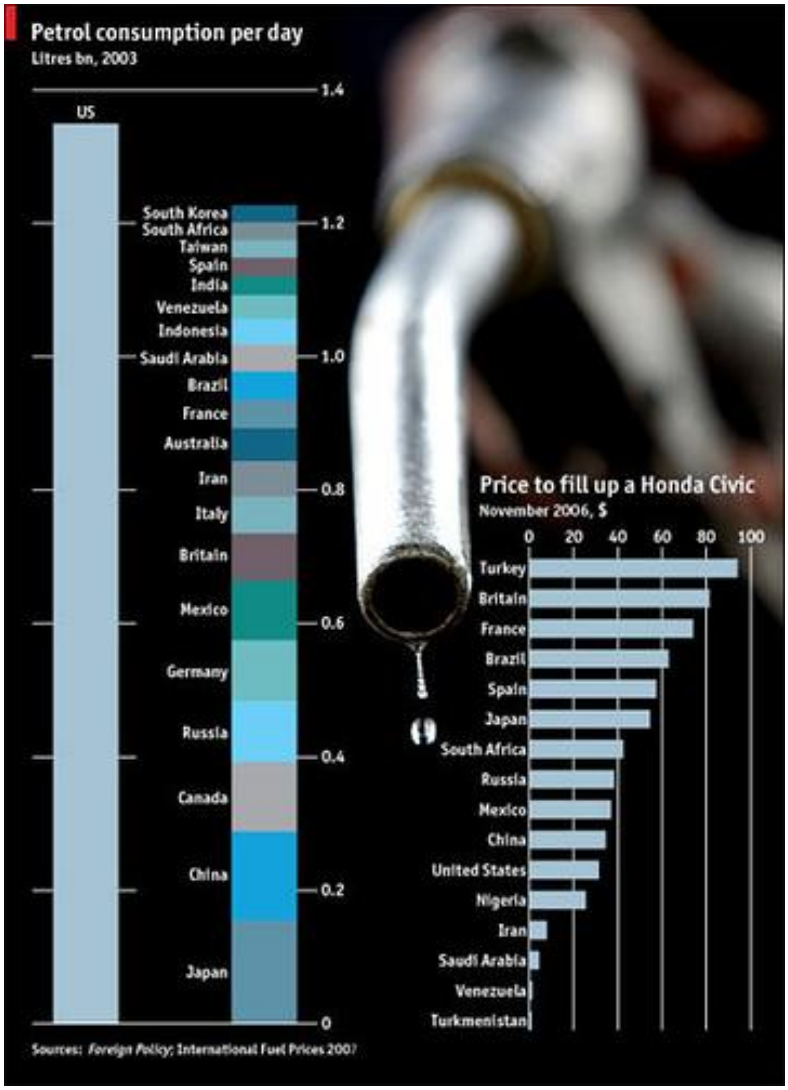

Figure 1.1 Petrol consumption per day in 2003 and the cost to fill up a Honda Civic in November 2006 [3].

There is also a **finite source of fossil fuels,** and since they are the most abundantly used source of energy [2], this limited supply will play a part in future energy scenarios. There

have been large increases in the demand for energy from non-OECD countries. As their economies have grown and the desire for technical advancement grows, demand is expected to increase [5].

The price of oil rose significantly in February 2008, exceeding the $100 a barrel mark, with a record high of $147 per barrel in July 2008. The price of oil fell to around $45 per barrel in January 2009, and then steadily rose throughout 2009 to around $70 per barrel at the end of August. With these three different concerns, a common solution is desired, and there is also a strong desire to move away from conventional fossil fuels. With energy demand increasing, it is necessary to tackle this problem in the very near future.

To consider the solutions to future energy demands, it is important to understand that the use of energy falls into two main categories:

- **Static** heating, lighting and powering equipment, used at home and industry (e.g. cooking food, steel production in a foundry and powering robots in car production etc.) and
- **Mobile** in the transport of goods and people (e.g. automobiles and aircraft).

Energy for static applications can be supplied in two ways: firstly through local generation and secondly using centrally generated electricity distributed through a grid system. Energy for use in transport can be delivered in three ways: (i) tapping into a static source (e.g. electrified railways); (ii) transportation of the energy supply (e.g. petroleum); and (iii) collection of energy during transit (e.g. solar cells on spacecraft).

This work will centre on mobile applications, specifically the challenges presented within the transport sector. Hydrogen is seen as a potential replacement for petrol, because it is not linked to a finite source; when reacted with oxygen (e.g. in a fuel cell) it only produces water; and hydrogen has the highest known energy density per unit mass (J/g). If hydrogen is to replace petroleum then it must produce fewer overall pollutants (production through transmission and storage to the final end use) and be economically and commercially viable. Some specific aspects must be addressed, such as the low energy density per unit volume of hydrogen (J/m^3), before hydrogen can become a realistic alternative to petrol and fossil fuels.

The potential benefits of moving towards hydrogen/fuel cell technologies are:

- A reduction in greenhouse and toxic gas (CO_x, NO_x and SO_x) emissions,
- A limitless supply with an improvement in energy efficiency and
- An improved security of supply, i.e. no longer dependent on imports for energy.

Hydrogen is not yet used as an energy vector in transport to any great extent, due to a number of sociological, economic, scientific and technological limitations. Public perception of hydrogen has become positive, and generally accepting of its development as a fuel when educated about benefits. There are also low levels of concern about the safety implications of using hydrogen as a fuel, as the public believe that if a large company (e.g. Honda) use hydrogen in their cars then they will have made it ‘safe’ [6]. Economically, there is currently little need to move away from using petroleum as an energy source for transport, due to the high profit margins in petrol products; the still abundant (although finite) supply; and the current infrastructure being built around the distribution of petroleum. However, the economic factors are changing through the high price of oil (linked to supply and demand) and by the structure of taxation to decrease demand for petroleum based transport.

For hydrogen to offer a realistic solution, there are a number of scientific and technological limitations that need to be addressed. It is necessary to consider every aspect of the hydrogen energy cycle, including production, storage and end use. All the individual components (production, transmission, storage, conversion and end user application) are closely integrated and interdependent. Each of these components must be individually considered in conjunction with the whole system. There are five key components:

- **Production** – Currently, the hydrogen is 'locked' in compounds and energy has to be *added* to separate the hydrogen so that it can later release the 'stored' energy. Existing techniques of methane reformation, multi-fuel gasification, and electrolysis are well understood, and the current focus is on lowering the cost, improving efficiencies, and reducing the emission of carbon. Breakthrough techniques, such as biological methods and nuclear/ solar powered thermo chemical water splitting, offer potential solutions here.
- **Transmission** – The technology is in place for transmission and distribution from the source of production to the point of delivery to the end users. There are a number of options for the transmission of hydrogen, depending upon whether the hydrogen production is onsite or centrally based. Onsite production needs little or no transmission and can therefore be achieved through a pipeline. If hydrogen is produced at a central location there are a number of technologies available to transport the hydrogen to the end user, such as hydrogen pipelines, hydrogen in natural gas pipelines, liquefied hydrogen trailers or compressed hydrogen trailers. The future will probably be a combination of all these methods depending on location and geography.

- **Storage** – The current transport infrastructure has a range of in-built requirements and constraints, such as vehicle size, road width, frequency of refuelling (linked to distance travelled), and other sources of energy built into the fabric of modern society for electronic goods (e.g. battery technology for phones). There are currently no available technologies that meet all the hydrogen storage attributes sought by manufacturers and end users. Efforts will focus on improving the performance and lowering the cost of current commercial technologies and exploring advanced material solutions.
- **Conversion** – The conversion of hydrogen into electric and thermal energy involving the use of fuel cells, reciprocating engines, turbines and process heaters. Research and development is required in fuel cells to increase durability and efficiency whilst lowering cost.

A proton exchange membrane (PEM) fuel cell is constructed using a thin layer of proton conducting polymer with inert porous layers of noble metal catalyst (few mg cm^{-2}) on either side of the membrane, or noble metal catalyst dispersed on porous carbon composite, as shown in Figure 1.2. The current collectors are typically graphite. High-power densities are possible (600 $mWcm^{-2}$), as well as low operating temperatures and short 'warm-up' times, which means that the PEM fuel cell is ideally suited for use in transport and mobile applications. The use of non-corrosive chemicals, leading to low wear and good durability, makes this fuel cell the best candidate for transport applications.

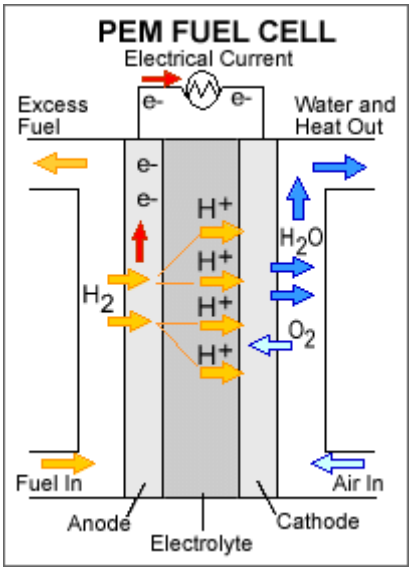

Figure 1.2 Schematic of a PEM fuel cell [7].

- **Applications** – Ultimately hydrogen energy should be used for transportation, electric generation, and portable electronic devices such as mobile phones and laptops.

For a successful transition to a hydrogen economy, breakthroughs will be needed in a number of technologies. This work will consider the technologically limiting stage of the storage of hydrogen for mobile applications. After setting out the criteria for any storage material, candidate materials will be presented as part of a detailed review of the literature. This investigation will then concentrate on the production and characterisation of borohydride materials.

1.1 Aims and Objectives of the Project

The overall aim of this work is to investigate the potential of borohydrides (zinc, magnesium, calcium and lithium) as solid state storage media for hydrogen in mobile applications.

The first objective is to attempt to synthesise zinc, magnesium and calcium borohydrides, using the metathesis reaction between metal chloride and alkali metal borohydride via mechanical milling. Characterisation of the milled products and subsequent investigation into the thermal decomposition will be performed. The thermal decomposition will be investigated both in terms of thermogravimetric and calorimetric analysis to try to understand the mechanism of decomposition.

Lithium borohydride can be commercially obtained and has been extensively studied for hydrogen storage applications. The second major aim of this project is to characterise the decomposition mechanism for the first time using in-situ Raman microscopy. Firstly, characterisation of the low temperature phase will be undertaken. Secondly the phase change from the low temperature to high temperature phase will be investigated. Finally, the decomposition products and any intermediate phases will also be characterised.

The study of the metathesis reaction using zinc, magnesium and calcium chloride and sodium borohydride will take place in parallel to compare their hydrogen storage properties (onset temperature and gravimetric hydrogen density). The decomposition mechanisms of mechanically milled products will also be investigated. The in-depth study of lithium borohydride is necessary as lithium borohydride is commonly used as a starting material in the synthesis of other metal borohydrides.

1.2 Scope of Thesis

This thesis consists of ten chapters. The next chapter will give a broad introduction to hydrogen storage, outlining the criteria for any potential storage system, and laying out some of the principal options for the storage of hydrogen in mobile applications. Chapter 3 gives an overview of current literature on the synthesis and hydrogen storage properties of borohydrides. Vibrational spectra specific to this project are introduced in Chapter 4. Chapter 5 describes the experimental procedures, techniques, basic theory and apparatus used in this work. Chapters 6, 7, 8 and 9 will present and discuss the results from zinc, magnesium, calcium and lithium borohydrides, respectively. Finally, the conclusions arising from this work and suggestions for future work are given in Chapter 10.

2 HYDROGEN STORAGE REVIEW

This chapter will review a range of hydrogen storage technologies. It will also set out the target criteria for a viable storage medium, and then identify a number of candidate hydrogen storage materials.

Hydrogen storage is one of the crucial technologies needed on the path towards commercialisation of hydrogen-powered vehicles and other mobile applications. A typical car, optimised for fuel efficiency, can cover a range of 400 km using roughly 24 kg (30 l) of petrol. For the same range it would require either 8 kg of hydrogen burnt using a combustion engine, or 4 kg of hydrogen using a fuel cell and electric motor [8]. Hydrogen is therefore a good fuel in terms of mass.

At standard temperature and pressure, 4 kg of molecular gas (H_2) would occupy a volume of 48.5 m^3, corresponding to a spherical balloon with a diameter of 4.52 m. This volume requires significant reduction to be practical for use in cars. The volume of gas relative to a typical car is shown in Figure 2.1, where it is possible to see that significant reductions in volume can be obtained by either compressing, liquefying or absorbing hydrogen.

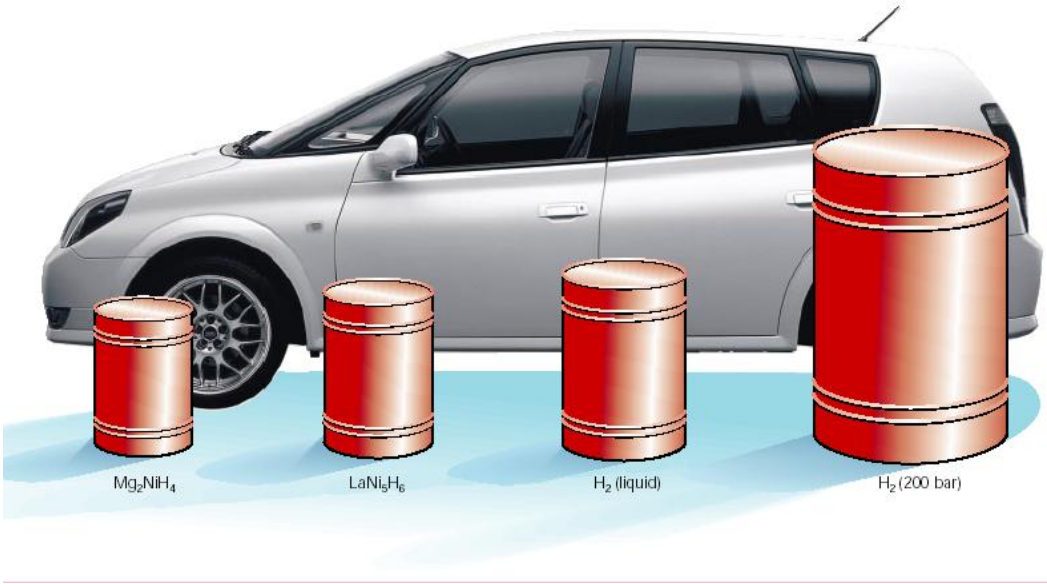

Figure 2.1 Relative volume required to store 4 kg of hydrogen using gaseous storage at 200 bar, cryogenic liquid, $LaNi_5H_6$, and Mg_2NiH_4, compared to a small family Toyota [8].

To be commercially viable the US Department of Energy (DoE) specify a hydrogen storage system must satisfy the following criteria:

- Hydrogen storage should be reversible,
- The operating pressure and temperature should be in a 'reasonable' range,
- The reaction kinetics should be fast,
- There must not be degradation after repeated cycling,
- The overall system should be cost effective,
- The possible candidate materials should have a good gravimetric and volumetric density (see examples in Figure 2.2) and
- The released hydrogen should have high purity so as not to poison the fuel cell.

No single storage system has yet been identified that meets all of these criteria. However, a number of different hydrogen storage systems (for use with hydrogen fuel cells in automobiles) have been identified, and are all currently topics of extensive research and development [9]:

- Pressurised gaseous hydrogen,
- Cryogenic liquid hydrogen,
- Irreversible reactions with water,
- Hydrogen physisorbed onto high surface area materials (porous carbon, molecular organic framework, etc.),
- Hydrogen rich chemical compounds (borohydrides, amides) and
- Hydrogen chemisorbed into metal hydrides.

Figure 2.2 is a graphical representation of a number of storage materials which are currently being evaluated. It shows gravimetric against volumetric hydrogen storage density. The most effective material will be one that has the maximum gravimetric *and* volumetric storage density. Excluding liquefied hydrogen, methane has the highest gravimetric hydrogen density of the compounds shown in Figure 2.2. However, liberation of carbon dioxide during steam methane reformation (SMR) severely limits the application of methane. Another disadvantage is that SMR requires high temperatures (700-1000°C) and requires the addition of water, adding a significant penalty to volumetric and gravimetric storage densities. Other materials such as $LaNi_5H_6$ and $BaReH_9$ have exceptional volumetric hydrogen densities, but poor gravimetric storage densities due to the presence of heavy metal atoms.

The borohydrides (XBH_4) show good gravimetric and volumetric storage densities, indicating that they are a class of compound that could potentially be used for onboard storage of hydrogen. It is this class of compound that is investigated in this thesis.

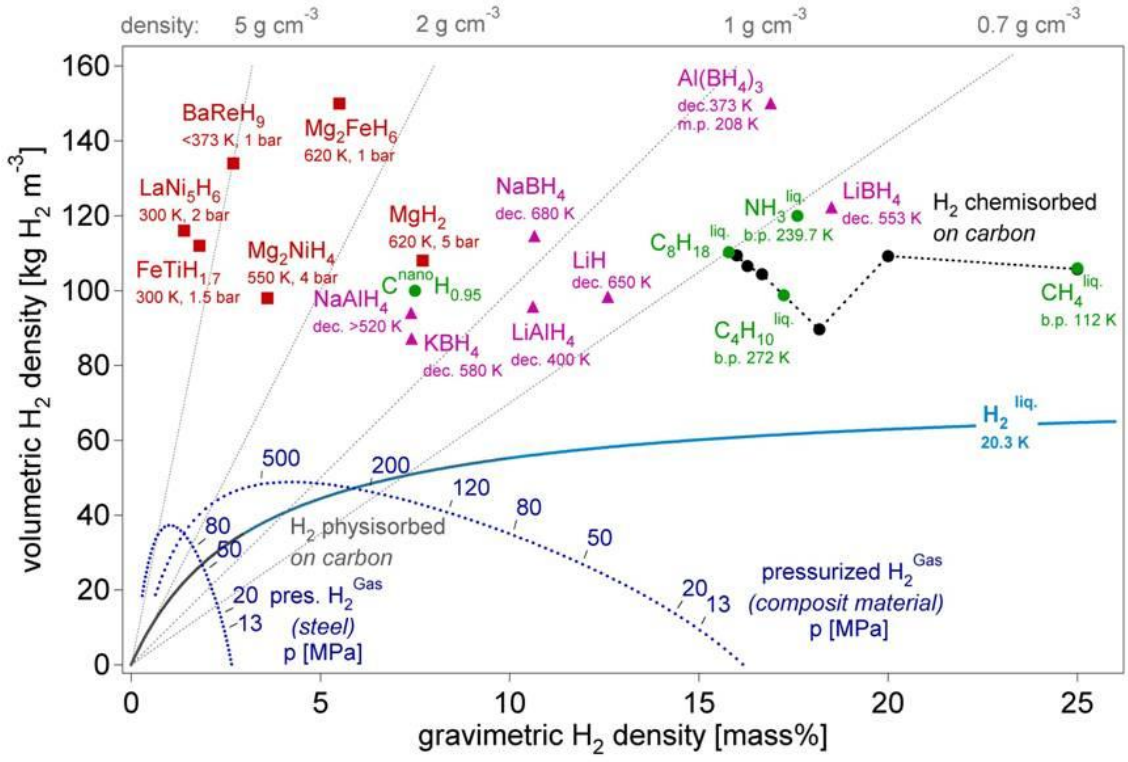

Figure 2.2 The gravimetric and volumetric densities of hydrogen for a number of possible hydrogen storage materials [9].

In addition to hydrogen density, desorption temperature must also be considered. Figure 2.3 shows the gravimetric hydrogen storage density against desorption temperature, together with the US DoE targets [10]. To be used with a fuel cell, ideally the temperature should be between 0 and 100°C, otherwise a significant amount of the stored energy is needed to release the hydrogen.

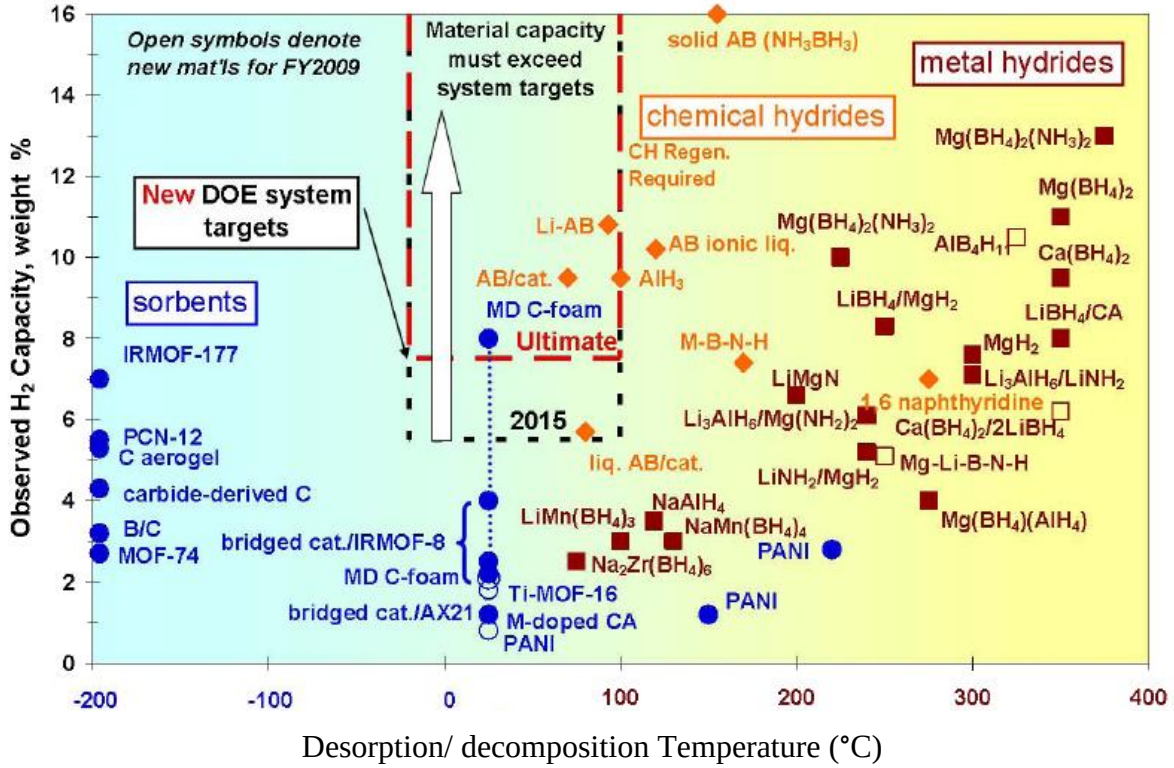

Figure 2.3 Comparison between observed hydrogen capacity and desorption/ decomposition temperature showing the 2009 US DoE targets (where AB is NH_3BH_3) [10].

2.1 Storage of Hydrogen as a Compressed Gas

Currently, compressed gas cylinders are the most common method of storing hydrogen on vehicles, due to their ease of use and because gas compression is a well-established technology.

The ideal material for a cylinder has a very high tensile strength, a low density and does not react with hydrogen or allow hydrogen to diffuse through it. The density of hydrogen increases with pressure. Gravimetric density, however, decreases with increasing pressure

with the maximum gravimetric density found for zero overpressure. Therefore, gravimetric density is sacrificed for increased volumetric density in pressurised systems.

Safety is one of the biggest concerns associated with pressurised cylinders since motor vehicles are inevitably involved in collisions, and such impacts could compromise the integrity of the pressurised cylinder. A clear solution is to deploy pressure-vessels which have impact resistance. One such approach is the use of a cylinder composed of three layers: an inner liner inert to hydrogen that acts as a permeation barrier, a middle layer overwrapped with a carbon fibre composite that acts as the stress bearing component, and an outer layer made from a corrosion-resistant material capable of withstanding mechanical impact.

Nevertheless, the relatively low volumetric hydrogen density of these high-pressure gas cylinders is the critical drawback for this technically simple and well-established storage method for hydrogen.

2.2 Storage of Liquefied Hydrogen

The conditions for cryogenic storage of liquid hydrogen are 20.3 K and atmospheric pressure. Liquid hydrogen can only be stored in an open system (i.e. a vessel with free space available) due to the low critical temperature of hydrogen (33 K) and the fact that no liquid phase is present above this critical temperature. If stored in a closed system, the pressure at standard temperature could increase dramatically due to vaporisation.

The rate at which hydrogen boils off is dependent upon the shape and size of the storage vessel. Losses through 'boil-off' are a result of heat leaks within the system, and are therefore proportional to the surface to volume ratio.

A significant amount of energy is required to liquefy hydrogen [11]. Together with the losses of hydrogen through boil-off, the net energy difference limits the range of application of liquid hydrogen due to the overall cost. In practice, the use of liquid hydrogen can only be justified when the cost of fuel is not an issue *and* the gas is consumed in a short time period, i.e. aerospace applications. Although BMW have demonstrated a 3 series saloon car powered on liquefied hydrogen running through an internal combustion engine, the overall process is not economical.

2.3 Storage of Hydrogen through a Reaction with Water

Hydrogen is generated through a chemical reaction of water or alcohols typically with chemical hydrides. These reactions are not easily reversible, and if this process was to be used sustainably in a mobile application, then the by-products would need to be removed from the vehicle and regenerated.

The classic school demonstration of a piece of sodium fizzing on water releasing hydrogen is a good demonstration of this process. Two sodium atoms react with two water molecules to produce one hydrogen molecule and two sodium hydroxide molecules (NaOH). This process has a gravimetric storage density of 3 wt.%. If the sodium is substituted with lithium, then the gravimetric hydrogen storage density increases to 6.3 wt.%, taking into account the water

required for the reaction. The main drawback of this is the lack of reversibility of the formed hydroxide product [9].

The reaction of sodium borohydrides with water [12]:

$$NaBH_4 + 2H_2O \rightarrow NaBO_2 + 4H_2 \quad (2.1)$$

This offers a high hydrogen storage capacity (10.9 wt.% for reaction (2.1)) and fast kinetics; however, regeneration cannot take place onboard for mobile applications [12]. The off-board regeneration of the hydrogen store is a possibility, though there would be a significant shift in the way vehicles are currently used and refuelled, potentially limiting the commercial viability.

Another hydrolysis reaction being considered is that of magnesium hydride (MgH_2) with water to form magnesium hydroxide ($Mg(OH)_2$) and hydrogen, shown in equation (2.2) [12]. This reaction is capable of delivering 10.6 wt.% hydrogen storage capacity for equation (2.2), but, as with the sodium borohydride, it requires external regeneration.

$$MgH_2 + 2H_2O \rightarrow Mg(OH)_2 + 2H_2 \quad (2.2)$$

2.4 Physisorption of Hydrogen on High Surface Area Materials

Physisorption of a gas molecule onto a surface of a solid is a process whereby a gas molecule interacts with several other atoms on the surface through van der Waals interactions. These are weak forces, and therefore significant physisorption is only observed at low temperatures, typically around 77 K.

Upon formation of monolayer coverage, the binding energy of subsequent layers is similar to the heat of vaporisation. Consequently, this means that only monolayer coverage can be achieved at temperatures equal to or greater than the boiling point of the adsorbate at a given pressure.

Graphitic materials such as carbon nanotubes (CNTs), activated and nanostructured carbons have large surface areas and therefore were seen as possible candidates for physorption of hydrogen [13]. Subsequently, other carbon based structures and nanoporous materials have been investigated. Zeolites of differing pore architecture and composition have been analysed. Initial work was conducted at high temperature (293-573 K). At cryogenic temperatures (77 K) physisorption occurs proportionally to the specific surface area, with a maximum gravimetric storage density of 2.1 wt.% at 16 bar, which was shown by Langmi et al. for zeolite NaY [14].

Supramolecular metal-organic frameworks (MOF) have been investigated. These involve metal centres, often Zn^{2+} or Cd^{2+} nitrate joined by ligands, topologically equivalent to terephthalic acid. MOF-5, for example, is capable of storing 4.5 wt.% at 77 K and 20 bar [15].

The principal advantage of physisorption for hydrogen storage is the low operating pressure, simple store design required, rapid sorption kinetics, high purity of hydrogen desorbed and the comparatively low cost and stability of the materials. However, the small volumetric and gravimetric hydrogen storage densities coupled with the low temperatures are a very significant drawback for this class of materials.

2.5 Hydrogen Rich Chemical Compounds

Light metals from groups 1, 2, 13 and 14 such as lithium, magnesium, boron and aluminium, along with nitrogen, all are capable of forming a number of metal hydrogen complexes. These are interesting because of their low weight and the number of hydrogen atoms per metal centre. The difference between these complex hydrides and metallic hydrides is a transition to ionic and covalent bonding of the absorbed hydrogen.

Hydrogen can be located on the corners of a tetrahedron with either a boron or aluminium centre forming a negatively charged anion, $[BH_4]^-$ or $[AlH_4]^-$, respectively, which is balanced by a corresponding cation, such as Li or Na. Borohydrides (also known as tetrahydroborates) $M[BH_4]$, and alanates (also known as tetrahydroaluminates) $M[AlH_4]$ are of interest as hydrogen storage materials [16-18]. There are many known stable borohydrides, often evolving hydrogen above their melting points.

Of this group, the compound with the highest room temperature gravimetric hydrogen storage density is $LiBH_4$ at 18 wt.%, making it ideal for use as a hydrogen storage material for

mobile applications. $LiBH_4$ desorbs three of four hydrogen atoms on heating to 600°C, forming LiH and boron, accounting for the 9 wt.% of the hydrogen released [19].

Complex hydrides have opened up a new category of hydrogen storage materials. There has been extensive work into the alanates and complex borides over the past six years and there are many new compounds to be explored.

2.6 Metal Hydride Systems

The adsorption of hydrogen into a metal was first observed by Graham in 1866 in palladium [20]. Subsequently it has been shown that it is possible to react hydrogen gas reversibly with other inter-metallic compounds (e.g. Mg_2Ni [21], $LaNi_5$ and TiFe [22]) at practical temperatures (-25 to 375°C). While many inter-metallics have been extensively investigated, and can absorb hydrogen in substantial quantities of hydrogen to metal atom ratios >1, most of these alloys are composed of high molecular weight rare-earth (f-block) or transition (d-block) metals, thus delivering a maximum storage capacity <2 wt.%. Alloys containing magnesium are the exception, giving storage capacities from 3.3 to 7.7 wt.%.

The desired reaction for the formation of an inter-metallic alloy A_yB_z with hydrogen is:

$$A_yB_z + xH_2 \leftrightarrow A_yB_zH_{2x} \quad (2.3)$$

Metal A is typically a transition metal, rare-earth metal or alkaline-earth metal and forms a stable binary hydride. Metal B (eg, Ni, Co, Cr, Fe or Al) does not form a stable hydride, but helps to catalyse the dissociation of the H_2 molecule.

Summarised below, in Table 2.1, are some of the common hydrides and their storage properties [23]:

Table 2.1 Summary of the properties of common metal hydrides [24].

Alloy Type	Hydride Phase	Maximum H capacity (wt.%)	Reversible H capacity (wt.%)	Comments
A	MgH_2	7.66	<7.0	Poor desorption kinetics at low temperatures (<300°C)
A	VH_2	3.81	1.9	Two plateaus, difficult to activate
A_2B	Mg_2NiH_4	3.59	3.3	Not metallic, very slow kinetics for T < 230°C
AB	$TiFeH_2$	1.89	1.5	Two plateaus, hard to activate
AB	$ZrNiH_3$	1.96	1.1	Two plateaus, fast kinetics
AB_2	$TiMn_{1.4}V_{0.62}H_{3.4}$	2.15	1.1	V makes it more expensive
AB_2	$ZrMn_2H_{3.6}$	1.77	0.9	Powder is highly pyrophoric
AB_5	$LaNi_5H_{6.5}$	1.49	1.28	Fast kinetics, degrades for T > 80°C
AB_5	$LaNi_{4.8}Sn_{0.2}H_{6.0}$	1.40	1.24	Slow degradation for T < 280°C

Most metal hydrides have rather low gravimetric storage capacities. Those with a higher capacity, such as Mg_2NiH_4 (3.59 wt.%) and MgH_2 (7.6 wt.%), have so far required desorption temperatures in excess of 250°C and have slow absorption and desorption kinetics[25].

Most of these materials are highly reactive and readily form oxides and hydroxides on their surfaces, which inhibit the absorption of hydrogen. Magnesium fulfils many of the criteria, except performing at a reasonable temperature, and has poor kinetics, but these can all be improved by suitable additions.

3 BOROHYDRIDES

After reviewing the options for the storage of hydrogen for mobile applications, it has become apparent that complex hydrides in the form of borohydrides present an opportunity to satisfy many of the demands, notably high gravimetric and volumetric storage densities. With such a large number of different borohydrides there are some that satisfy more criteria than others. Some borohydrides are unstable below room temperature [16], while others have decomposition temperatures above 300°C [26], which is too high to be used in mobile applications with a PEM fuel cell. The use of catalysis and/or reactive hydride composites (section 3.16) may lower the temperature to allow the potential use with fuel cells.

Borohydrides, or tetrahydroborates, as a class of compounds have been known since the 1940s [27-30]. They have been the subject of numerous studies due to their use as a common reagent in the reduction of organic compounds. The borohydride ion, BH_4^-, is the simplest known boron hydrogen anion. One property is the ability to form both ionic compounds with alkali and alkali-earth metals, and covalent complexes with transition metals. The borohydride ligand invariably bonds covalently through a three centre two electron bridging hydrogen in monodentate, bidentate and tridentate manner, as shown in Figure 3.1.

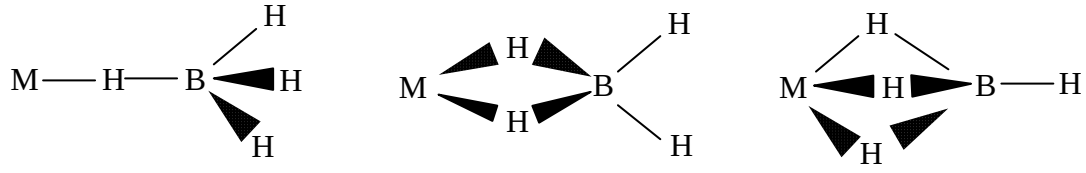

Monodentate coordination Bidentate coordination Tridentate coordination

Figure 3.1 Covalent bonding configurations.

Covalent borohydrides can often be synthesised using a metathesis reaction whereby substitution of the $[BH_4]^-$ group occurs with, in many cases, a halide ion, as per equation (3.1), where M = Metal centre and A = Alkali metal.

$$MCl_n + nABH_4 \rightarrow M(BH_4)_n + nACl \quad (3.1)$$

Many borohydrides have been successfully synthesised, as summarised in Figure 3.2. This section will detail the synthesis, and consider important physical and chemical properties of the complexes. Each group of the periodic table will be considered, with the f-block lanthanides and actinides considered together.

H																	He
Li	Be											B	C	N	O	F	Ne
Na	Mg											Al	Si	P	S	Cl	Ar
K	Ca	Sc	Ti	V	Cr	Mn	Fe	Co	Ni	Cu	Zn	Ga	Ge	As	Se	Br	Kr
Rb	Sr	Y	Zr	Nb	Mo	Tc	Ru	Rh	Pd	Ag	Cd	In	Sn	Sb	Te	I	Xe
Cs	Ba	La	Hf	Ta	W	Re	Os	Ir	Pt	Au	Hg	Tl	Pb	Bi	Po	At	Rn

Ce	Pr	Nd	Pm	Sm	Eu	Gd	Tb	Dy	Ho	Er	Tm	Yb	Lu
Th	Pa	U	Np	Pu	Am	Cm	Bk	Cf	Es	Fm	Md	No	Lr

Figure 3.2 The periodic table of elements, with known borohydride compounds shown in green [31-40].

Interest in borohydrides has intensified after Grochala and Edwards published a summary of gravimetric storage densities and desorption temperatures in 2004 [16]. Previous reviews focused on the physical and chemical properties along with synthesis of borohydrides: Marks and Kolb showed in 1977 that only 6 transition metals had not had borohydrides synthesised [31]; while James and Wallbridge summarised the spectroscopic properties and preparation of the alkali metal borohydrides and some transition metal borohydrides [41].

In 2006, Nakamori et. al. investigated the thermal decomposition of Mg, Sc, Zr, Ti and Zn borohydrides (prepared by ball-milling alkali-metal borohydrides with metal chlorides), and so correlating the thermodynamic stabilities of metal borohydrides with respect to cation electronegativity [42, 43]. The work showed a reasonably linear correlation between the ΔH (kJ/mol BH_4) and Pauling electronegativity of the cation (χ_p), using equation (3.2), to predict the heat of formation per borohydride:

$$\Delta H_{boro} = 248.7\chi_p - 390.8 \tag{3.2}$$

This work also showed a correlation between the Pauling electronegativity and desorption temperature (T_d), with the exception of zinc borohydride. Nakamori et al. assumed that thermal desorption occurs via equation (3.3).

$$M(BH_4)_n \rightarrow MH_m + nB + \frac{4n-m}{2}H_2 \tag{3.3}$$

If equation (3.2) is correct then enthalpy change for the reaction, ΔH_{des}, can be estimated using the predicted ΔH_{boro}, for $M(BH_4)_n$. The author then suggests that a $\chi_p \geq 1.6$ is too high

as it allows decomposition with the evolution of diborane, whereas when $\chi_p \leq 1.4$, only hydrogen is evolved. Cations such as Li, Na and K ($\chi_p \leq 1$) are too stable and therefore have decomposition temperatures too high for practical applications in hydrogen storage without lowering the decomposition temperature through catalysis or formation of a reactive composite. Nakamori et al. [43] suggest that potential candidates for hydrogen storage media should target a Pauling electronegativity between 1.2 and 1.5.

3.1 Group 1

Alkali metal borohydrides have historically been an interesting class of borohydrides, principally because they are subsequently used in the synthesis of many of the transition metal borohydrides. All the borohydrides in this group are ionic, with the anionic $[BH_4]^-$ group countered by an alkali metal cation in a 1:1 ratio. Recently there has been a significant amount of interest in the use of alkali metal borohydrides as hydrogen storage materials, due to their high gravimetric hydrogen content.

3.1.1 $LiBH_4$

Lithium borohydride was first prepared by Schlensinger et al. in 1940 by the reaction of diborane and ethyl-lithium [29]. Later Schlesinger reported the reaction between lithium hydride in diethyl ether with diborane to form a $LiBH_4.(C_2H_5)O$ precipitate [44], where the ether was driven off by heating to form pure lithium borohydride. Fedneva et al. reacted lithium hydride with boron trifluoride-ether in ether to form lithium borohydride [45].

Investigations to form lithium borohydride without the use of diborane have been carried out, showing that a reaction between lithium hydride and methyl borate can yield lithium borohydride, following equation (3.4) [46].

$$4LiH + B(OCH_3)_3 \rightarrow LiBH_4 + LiOCH_3 \quad (3.4)$$

In 1958 a patent was filed in Germany showing the formation of lithium borohydride from its elements ($Li + B + 2H_2 \rightarrow LiBH_4$) at 150 bar H_2 and T = 650°C [47]. In 2005 Orimo et al. showed that lithium borohydride was reversible and could be reformed from lithium hydride and boron at 350 bar H_2 at 600°C [48]. The synthesis of lithium borohydride by mechanical milling of lithium and boron in a hydrogen atmosphere was studied by Cakanyildirim et al. [49] and shown to form lithium borohydride. The mechanical milling of lithium hydride and boron in a hydrogen atmosphere shown by Agresti et al. [50] resulted in the formation of lithium borohydride.

Friedrichs et al. [51] showed in 2009 that the decomposition of a transition metal borohydride (zinc borohydride) could be used to provide diborane, to react with lithium hydride to form lithium borohydride. This can be done in a sealed system reducing the risks, toxicity and flammability associated with using diborane.

The structure and bonding of $LiBH_4$ have been extensively studied using x-ray diffraction [52, 53], NMR [54] and Raman spectroscopy [55, 56].

Structural studies of the low temperature orthorhombic (o-$LiBH_4$) phase and the high temperature hexagonal (h-$LiBH_4$) phase were investigated by Soulie et al. [52]. This showed

that the room temperature o-$LiBH_4$ phase has a P*nma* space group where the $[BH_4]^-$ tetrahedra are aligned along the two orthogonal directions, and that the $[BH_4]^-$ tetrahedrons are heavily distorted with respect to bond length (B-H 1.04-1.28 Å) and bond angle (H-B-H 85.1-120.1°). There is a first order phase transition at ~110°C to the high temperature h-$LiBH_4$ phase, that has a $P6_3mc$ space group with the $[BH_4]^-$ tetrahedra aligned along the c axis, and which become more symmetrical with bond lengths B-H 1.27-1.28 Å and bond angles H-B-H 106.4-112.4°.

The crystallography by Soulie et al. was supported by an accompanying paper by Gomes et al. [55] who investigated the Raman spectra of $LiBH_4$. This work, later continued by Racu et al. [57], identified 23 of the 36 Raman active bands present in the o-$LiBH_4$ phase, which supports the crystallographic view of a highly deformed $[BH_4]^-$ tetrahedron that becomes more symmetric in the h-$LiBH_4$ phase.

Thermal decomposition of lithium borohydride was first reported by Schlensinger et al. [44] in 1953 at 275°C with the evolution of hydrogen. Fedneva et al. [45] subsequently reported observing the phase change between 108-112°C followed by melting at 268-286°C with the loss of 2% of the hydrogen, with a vigorous decomposition at 380°C with the loss of 80% of the total hydrogen present.

In 2003, Züttel et al. began to study lithium borohydride from the point of view of hydrogen storage [19, 58]. Thermogravimetric and calorimetric analysis showed a structural phase change occurred around 118°C with a weight loss of 0.3 wt.% hydrogen (equation 3.5), with melting at around 270°C without any detectable mass loss. The first hydrogen peak with

1 wt.% mass loss was seen at 320°C (equation 3.6), with a large weight loss observed at 450°C, with a total of 9 wt.% of hydrogen being desorbed up to 600°C (equation 3.7). This work also showed that desorption has an activation energy of 156 ± 20 $kJmol^{-1}$ and is a first order reaction [19].

$$o\text{-}LiBH_4 \rightarrow h\text{-}LiBH_{4-\varepsilon} + {}^{\varepsilon}/_{2}\ H_2 \quad (3.5)$$

$$h\text{-}LiBH_{4-\varepsilon} \rightarrow \text{`}LiBH_2\text{'} + (1+{}^{\varepsilon}/_{2})\ H_2 \quad (3.6)$$

$$\text{`}LiBH_2\text{'} \rightarrow LiH + B + 1/2H_2 \quad (3.7)$$

In 2005, Orimo et al. investigated the desorption behaviour under 1 bar hydrogen, observing the phase change at 106°C, melting at 276°C with desorption occurring between 325 and 425°C with lithium hydride as the main decomposition product. Recombination was successfully performed at 600°C under a 350 bar hydrogen atmosphere after 12 hours [1].

In 2006, Ohba et al. conducted a first principle study of possible intermediates for the decomposition of $LiBH_4$ [59]. The conclusion of this work was that the thermodynamically most stable and therefore most likely possibility was $Li_2B_{12}H_{12}$, a *closo*-dodecaborane anion $[B_{12}H_{12}]^{2-}$ with two Li^+ cations. They also predicted, using density function theory (DFT), the vibrational spectrum for $Li_2B_{12}H_{12}$. In the same year, Orimo et al. showed the presence of $Li_2B_{12}H_{12}$ experimentally using ex-situ Raman [60], predicting a reaction path above 430°C of:

$$LiBH_4 \rightarrow {}^{1}/_{12}\ Li_2B_{12}H_{12} + {}^{5}/_{6}\ LiH_2 + {}^{13}/_{12}\ H_2 \quad (3.8)$$

$$\rightarrow LiH + B + {}^{3}/_{2}\ H_2 \quad (3.9)$$

The presence of the $[B_{12}H_{12}]^{2-}$ intermediate was also confirmed by magic angle spinning nuclear magnetic resonance (MAS NMR) spectroscopy by Hwang et al. [61]. This work also speculated that it is a probable decomposition product for many borohydrides, including magnesium borohydride.

Züttel et al. [58] showed that mixing lithium borohydride with silica (SiO_2), led to the desorption of 9 wt.% hydrogen below 400°C, with a further rapid desorption at 450°C. It was suggested that SiO_2 catalysed the reaction.

In 2003 Züttel et al. were unable to reform lithium borohydride from the elements at elevated temperature and pressure, up to 650°C and 150 bar [19]. In 2006 Au et al. showed that the addition of additives Mg, Al, MgH_2, CaH_2, $TiCl_3$ and $MgCl_2$ reduce the decomposition temperature of lithium borohydride, while the addition of Ni, C, In, Ca and NaH were shown to have a negative effect. The lowest decomposition temperature was observed at 60°C for $LiBH_4 + 0.2MgCl_2 + 0.1TiCl_3$. It desorbed 5 wt.% at 400°C, and absorbed 4.5 wt.% of hydrogen at 325°C and 70 bar on several cycles [62].

Further work by Au et al. [63] showed the addition of metal halides such as $TiCl_3$, TiF_3 and ZnF_2 reduce the decomposition temperature through a cation exchange. Increasing the concentration of halides such as $TiCl_3$, TiF_3 and $ZnCl_2$ from 0.1-0.5 mol.% makes lithium borohydride less stable, where 0.5 mol.% releases hydrogen at room temperature, but reversibility is not possible due to the uncontrolled release of diborane. The addition of 0.1 mol.% TiF_3 to lithium borohydride desorbs 3.5 and 8.5 wt.% hydrogen at 150 and 450°C, respectively, with recombination of 6 wt.% hydrogen at 500°C and 70 bar.

3.1.2 $NaBH_4$

Sodium borohydride was first synthesised in 1953 by Schlesinger et al. through the reaction between diborane and sodium methoxide [64]. Studies to synthesise sodium borohydride without the use of diborane, were achieved using the reaction of sodium hydride and methyl borate at 225-275°C according to the following reaction (3.10) [64, 65].

$$4NaH + NaBH(OCH_3)_3 \rightarrow NaBH_4 + 3NaOCH_3 \quad (3.10)$$

Li et al. have investigated the synthesis of sodium borohydride by mechanical milling of magnesium hydride with dehydrated borax and sodium compounds, with the greatest yield using Na_2CO_3 progressing by reaction (3.11) [66].

$$8MgH_2 + Na_2B_4O_7 + Na_2CO_3 \rightarrow 4NaBH_4 + 8MgO + CO_2 \quad (3.11)$$

The thermal decomposition was first reported by Schlesinger [67], and showed no appreciable weight loss up to 400°C, with hydrogen liberated slowly at 400°C. In 1962, Sterlyadkina et al. found that sodium borohydride has a melting point of 505°C followed by decomposition with the rapid evolution of hydrogen occurring at 565°C [68].

3.1.3 KBH_4

Potassium borohydride was first synthesised in 1953 by Schlesinger et al. via the reaction of potassium tetramethyloxyborohydride with diborane via reaction 3.12 [64].

$$3KB(OCH_3)_4 + 2B_2H_6 \rightarrow 3KBH_4 + 4B(OCH_3)_3 \quad (3.12)$$

Work by Li et al. showed that potassium borohydride can be synthesised without the use of diborane, by mechanically milling potassium borate and magnesium hydride via reaction (3.13) [69].

$$2MgH_2 + KBO_2 \rightarrow KBH_4 + 2MgO \quad (3.13)$$

The thermal decomposition properties of potassium borohydride were investigated by Mikheeva et al. [70]: showing a melting point at 590°C; weight loss starting at 640°C due to the evolution of hydrogen; and all the hydrogen liberated by 700°C, following equation (3.14). Isothermal decomposition was also observed at 500°C, with only part of the hydrogen being slowly liberated.

$$2KBH_4 \rightarrow 2KH + 2B + 3H_2 \quad (3.14)$$

3.1.4 $RbBH_4$ and $CsBH_4$

Rubidium and caesium borohydrides were synthesised by Mikheeva et al. by reacting metal hydroxide and sodium borohydride in alcohol solution [71].

$$AOH + NaBH_4 \rightarrow ABH_4 + NaOH \quad (3.15)$$

where A = Rb or Cs

Both thermally decompose with the vigorous evolution of hydrogen with an onset temperature in an inert atmosphere of 600°C and 660°C for rubidium and caesium borohydride, respectively. The liberation of hydrogen is accompanied by simultaneous fusion of the borohydride and the sublimation of the alkali metal.

The onset of thermal decomposition is lowered under vacuum, to 560°C and 570°C for rubidium and caesium borohydride, respectively. A condensation product was observed on the walls of the reactor, containing alkali metal, amorphous boron and a small amount of metal borate, indicating a path similar to equation (3.16).

$$ABH_4 \rightarrow xA + xB + (1-x)AB + 2H_2 \quad (3.16)$$

3.2 Group 2

3.2.1 $Mg(BH_4)_2$

Wiburg and Bauer [72] synthesised magnesium borohydride by allowing an ethereal solution of organo-magnesium in excess diborane (MgR_2: $(BH_3)_2$ = 1:1.5) react at room temperature according to reaction (3.17).

$$3MgR_2 + 4(BH_3)_2 \rightarrow 3Mg(BH_4)_2 + 2BR \quad (3.17)$$

R = OMe

In 1952, further work by Wiburg and Bauer predicted a structure where the borohydride group resonated between a bidentate covalent and ionic structures [73]:

$BH_4^-\ Mg^{2+}\ BH_4^- \leftrightarrow$ 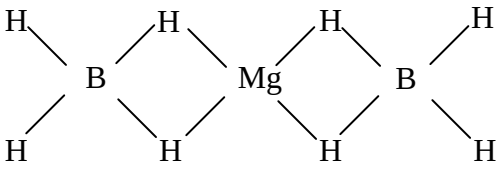 (3.18)

Chlopek et al. attempted formation using the alkyl borohydride and magnesium chloride [74]. Three metathesis approaches were attempted, following equation 3.19: (i) using a THF solvent but this gave poor results so; (ii) a diethylether solvent was used, giving a 50% yield, after 24 hour reflux, the product was filtered and the remaining liquid was removed under vacuum 180°C; (iii) they also used mechanical milling under argon.

$$MgCl_2 + 2\ MBH_4 \rightarrow Mg(BH_4)_2 + 2\ MCl \quad (3.19)$$

M= Li, Na

Vajeeston et. al. determined that the crystal structure of the low temperature phase of magnesium borohydride has an orthorhombic P*mc*2_1 where a = 4.3086, b = 6.0878, c = 8.3888 [75]. However, there is consensus between Dai et al. [76] and Filinchuk et al. [77] that the low temperature structure of magnesium borohydride is hexagonal P$6_1$22; in addition, several low temperature phases have been predicted using computer simulation, but these have not been observed experimentally [78, 79]. The structure of the high temperature phase is orthorhombic F*ddd* and both Filinchuk et al. [77] and Her et al. [80] agree with this symmetry group.

Konoplev and Bakulina [81] found IR peaks (within the region 400-2800 cm^{-1}) showing two B-H stretch at 2300 and 2660 cm^{-1} and 2 B-H deformation vibrations 1130 and 1265 cm^{-1}.[81]. Filinchuk et al. [77] present both IR and Raman vibrational spectra of the low temperature phase, showing the B-H stretching modes around 230 cm^{-1} and the BH_4 bending modes between 1000 and 1400 cm^{-1}. Filinchuck et al. [77] assign these vibrations to the BH_4^- molecule bridging in a bidentate manner to the Mg^{2+} ion.

A number of studies have been carried out into thermal decomposition in an inert atmosphere, these indicate four or five endotherms [73, 81].

180-185°C polymorphic phase transition (3.19)

304-314°C melting + $Mg(BH_4)_2 \rightarrow MgH_2 + 2B + 4H_2$ (3.20)

375°C this was an unknown process observed by Konoplev (3.21)

402-410°C $MgH_2 \rightarrow Mg + H_2$ (3.22)

The phase transformation was observed by Konoplev and Bakulina [81] and Wiberg [73]. Wiberg reported decomposition at 280°C [73]. Konoplev and Bakulina showed melting and magnesium borohydride decomposition to form magnesium hydride, and the decomposition of magnesium hydride [81].

The heats of formation for magnesium borohydride from a number of starting materials were calculated by Vajeeston et al. [75] and shown in Figure 3.3.

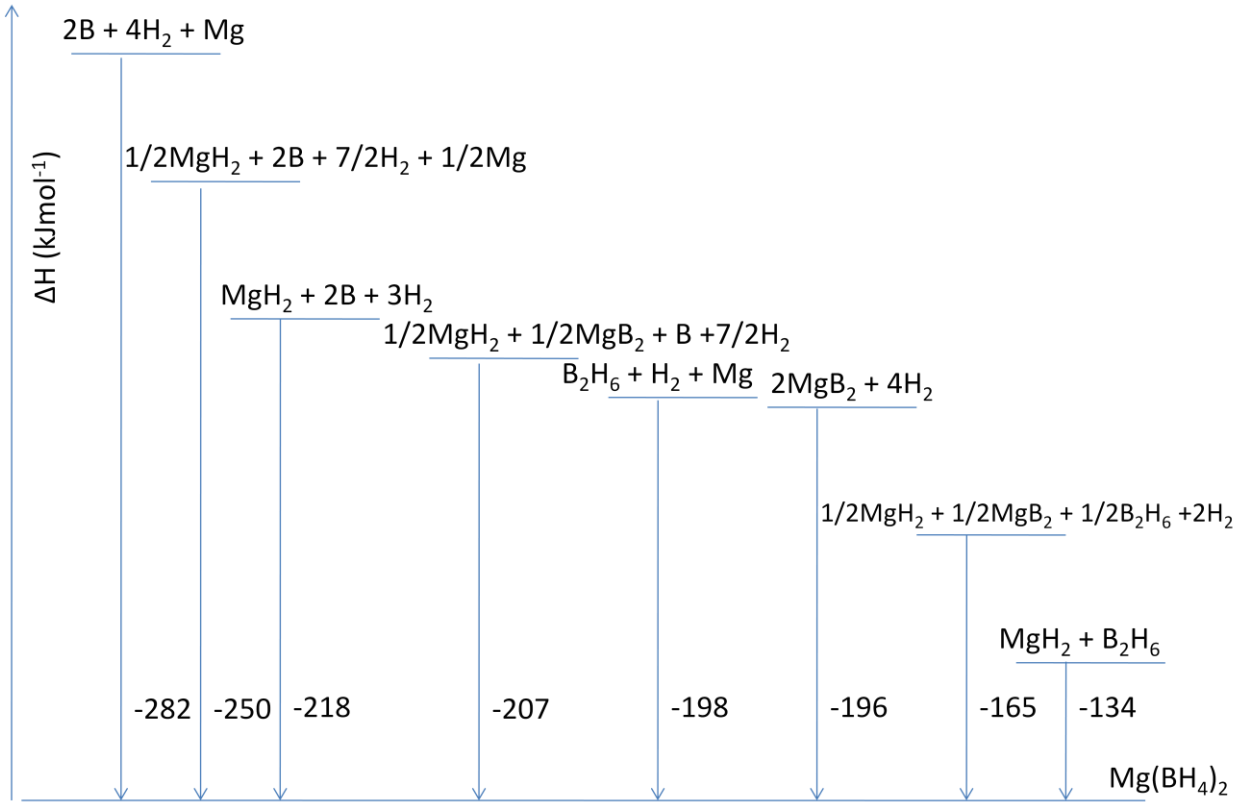

Figure 3.3 Heats of formation of different magnesium borohydride precursors [75]

In 2007, Li et al. investigated magnesium borohydride as a candidate for hydrogen storage [82]. In this work magnesium borohydride was synthesised by the metathesis reaction of magnesium chloride and sodium borohydride in ether solution. It was reported that decomposition occurred via two reactions, with the evolution of hydrogen. This corresponds to equations (3.20) and (3.22), where the intermediate magnesium hydride is formed and then subsequently desorbs. Further studies have investigated magnesium borohydride as a potential hydrogen storage medium [80, 83, 84]; they have concluded that, with a high gravimetric hydrogen storage density, it remains a promising candidate.

Zanella et al. approached the challenge of the synthesis of adduct- or solvent-free magnesium borohydride [85]. Using a metathesis reaction of an organo-magnesium compound with aluminium borohydride followed by filtration or sublimation reaction of organo-magnesium with $BH_3S(CH_3)_2$ followed by vacuum treatment to give pure hexagonal phase.

Varin et al. used mechanical milling to synthesise disordered magnesium borohydride, using the metathesis reaction of magnesium chloride and sodium borohydride [84]. Their work postulated the formation of a solid solution where unreacted sodium borohydride was able to substitute for the magnesium to form a (Na, Mg)BH_4 compound. They observed thermal decomposition in four steps:

T ~ 100-240°C	~0.4-1.3 wt.%	Decomposition of $MgCl_2.xH_2O$
T ~ 275-335°C	~1.0-1.5 wt.%	Melting and simultaneous decomposition of d-$Mg(BH_4)_2$ → β-$Mg(BH_4)_2$ + B+ H_2
T ~ 335-420°C		Unknown exothermic reaction
T ~ 410-420	~1.0-1.8 wt.%	Decomposition of β-$Mg(BH_4)_2$

Varin et al. investigated the synthesis and thermal decomposition of magnesium borohydride, through ball milling sodium borohydride and magnesium chloride [84]. On milling it was believed that disordered d-$Mg(BH_4)_2$, sodium chloride and a solid solution of (Na, Mg)BH_4 was formed by the unreacted sodium borohydride by Mg substitution. Between 100 and 240°C a weight loss of between 0.4 and 1.3 wt.% was observed, due to the decomposition of magnesium chloride hydrate ($MgCl_2.xH_2O$). Between 275 and 335°C a weight loss between

1.0 and 1.5 wt.%, due to the melting and simultaneous decomposition of $Mg(BH_4)_2$ into MgH_2, B and H_2 with an endotherm with a maximum at around 298°C on the DSC. An unexplained heat flow was observed between 350 and 360 °C. MgH_2 decomposes between 335 and 420°C with a weight loss between 1.0 and 1.8 wt.%. The noisy TGA with a 'zig-zag' decomposition observed by Varin et al. indicates that there is some volatility and that decomposition is violent [84].

Li et al. continued investigations into the dehydriding and rehydriding process of magnesium borohydride and came to the conclusion there are some intermediate phases in the decomposition reaction between β-$Mg(BH_4)_2$ and the formation of MgH_2 [86]. This intermediate is believed to be $MgB_{12}H_{12}$; similar to that observed during the decomposition of lithium borohydride.

$$Mg(BH_4)_2 \leftrightarrow {}^{1}/_{6}\, MgB_{12}H_{12} + {}^{5}/_{6}\, MgH_2 + {}^{13}/_{6}\, H_2 \quad (3.24)$$

$$\leftrightarrow MgH_2 + 2B + 3H_2 \quad (3.25)$$

$$\leftrightarrow Mg + 2B + 4H_2 \quad (3.26)$$

Li et al. found that around 6.1 wt.% of hydrogen, including the 3.7 wt.% from the formation of MgH_2 from magnesium, could be stored reversibly [86].

Soloveichik et al. investigated the thermal decomposition of magnesium borohydride in a static vacuum [87]. They observed four decomposition steps (D1-4) with corresponding endothermic peaks on the DSC, there was also one endothermic (E1) and one exothermic (X1) reactions that did not result in the release of hydrogen. Soloveichik et al. therefore proposed the following reaction mechanism considering only the solid phases:

E1 $\alpha\text{-}Mg(BH_4)_2 \rightarrow \beta\text{-}Mg(BH_4)_2$ (3.27)

D1 $\rightarrow MgB_2H_{5.5}$ (3.28)

D2 $\rightarrow MgBH_{2.5} + MgB_4$ (3.29)

X1 $\rightarrow {}^{1}/_{12}MgB_{12}H_{12} + MgH_2 + MgB_4$ (3.30)

D3 $\rightarrow {}^{1}/_{12}MgB_{12}H_{12} + Mg + MgB_4$ (3.31)

D4 $\rightarrow MgB_2$ (3.32)

Where the E1 is the first stage of the reaction (3.27), followed by D1 and D2 reactions (3.28) and (3.29) respectively, the two decomposition steps release 4.7 and 4.9 wt.%, respectively. The rearrangement to form $MgB_{12}H_{12}$ and MgH_2 in reaction (3.30) is the exothermic reaction, X1. The subsequent D3 reaction is the decomposition of magnesium hydride (3.31) releasing 3.3-3.7 wt.%, with the final D4 reaction being the decomposition of $MgB_{12}H_{12}$ (3.32) releasing 0.8-1 wt.% hydrogen, resulting in the formation of magnesium diboride rather than magnesium and boron. This mechanism yields a maximum weight loss of 14.3 wt.% all of which is hydrogen.

There is still a great deal of uncertainty about the decomposition mechanism of magnesium borohydride, especially the amorphous intermediates which cannot be characterised by conventional in-situ XRD, instead relying on ex-situ techniques at room temperature. The disagreement in the final reaction products, between magnesium, boron, magnesium diboride and magnesium dodecaborane, could be dependent on the decomposition atmosphere and other factors. With this in mind magnesium borohydride is still a candidate for use as a hydrogen storage material due to the 14.3 wt.% hydrogen release [88].

3.2.2 $Ca(BH_4)_2$

In 1964, Titov showed that calcium borohydride could be synthesised through the reaction of calcium chloride and sodium borohydride at room temperature in a tetrahydrofuran (C_4H_8O, THF) solution as per equation (3.33) [89]:

$$CaCl_2 + 2NaBH_4 \rightarrow Ca(BH_4)_2.2THF + 2NaCl \quad (3.33)$$

The calcium borohydride product was then purified by vacuum distillation at 190°C. Titov reported a thermal decomposition temperature in the range of 245-358°C [89].

Further investigations into the structure of calcium borohydride were carried out in 1975 by Tomkinson and Waddington [90]. Inelastic neutron scattering was carried out, this showed the presence of the $[BH_4]^-$ anion. However, without a crystal structure it was not possible to determine any further information.

In 2006, Miwa et al. measured and predicted Raman spectra and XRD patterns, showing an orthorhombic structure with a space group F*ddd* [91]. They also showed the thermal desorption via the equation (3.34), with a weight loss of 9.2 wt.% up to 525°C.

$$3Ca(BH_4)_2 \rightarrow 2CaH_2 + CaB_6 + 10H_2 \quad (3.34)$$

Barkhordarian et al. also showed that calcium hydride and magnesium diboride reacted under hydrogen to form calcium borohydride and magnesium hydride as per equation (3.35) [92]. Heating at 300°C under 200 bar hydrogen for 48 hours resulted in a 4.7 wt.% uptake, and

400°C under 350 bar hydrogen for 24 hours gave 7 wt.%. Ronnebro et al. presented work showing similar results for the reaction of borides with binary hydrides to form a borohydride, showing calcium hydride and magnesium boride as an example to form calcium borohydride [93]. This work also showed that the low temperature phase has a F*ddd* space group and forms a high temperature phase above 150°C, decomposes at 400°C to give CaB_6 and CaH_2 with a loss of 9.6 wt.% with reversibility of 1% at 100 bar and 390°C and 80% at 700 bar and 400°C.

$$CaH_2 + MgB_2 + 4H_2 \rightarrow Ca(BH_4)_2 + MgH_2 \quad (3.35)$$

In 2007, Barkhordarian et al. confirmed the reaction between calcium hydride and magnesium diboride forming calcium borohydride at 350°C and 140 bar of hydrogen pressure for 24 hours, and subsequently desorbing 7 wt.% [94]. The decomposition of this composite occurred via equations (3.36)-(3.38).

$$\alpha\text{-}Ca(BH_4)_2 + MgH_2 \rightarrow \beta\text{-}Ca(BH_4)_2 + MgH_2 \ (130°C) \quad (3.36)$$

$$\rightarrow xMg + CaH_2 + yCa_4Mg_3H_{14} + 2B + zH_2 \quad (3.37)$$

$$\rightarrow Mg + CaH_2 + 2B + kH_2 \quad (3.38)$$

Kim et al. performed a number of investigations into calcium borohydride [95-97]. Again observing the polymorphic phase transition at 170°C with a two stage decomposition occurring at 350°C and 400°C, with the first decomposition yielding CaH_2 and an unknown intermediate, that subsequently decomposed leaving CaH_2 and boron and/or calcium boride. The addition of 0.05 mol.% $TiCl_3$ to calcium borohydride resulted in recombination at 350°C

(and 90 bar for 24 hours), desorbing 7.1 wt.% after recombination compared to 8.7 wt.% on the first desorption. In addition, the $TiCl_3$ reduced the decomposition temperature by 50°C.

Ronnebro and Majzoub [98] showed that milling CaB_6 and CaH_2 with 4-8 wt.% additives $TiCl_3$, Pd, $TiCl_3$ + Pd and $RuCl_3$. The milled mixture was then pressed into a 10 mm pellet and reacted with hydrogen in a steel reactor, between 400-440°C with 700 bar being the optimum pressure. The $TiCl_3$ + Pd additive was shown to have a 60% yield on hydrogenation, and the $RuCl_3$ yielding slightly more.

Riktor et al performed in-situ synchrotron diffraction studies of calcium borohydride [35], identifying a continuous phase transition from low temperature α-phase to the high temperature β-phase and thereafter to an unknown phase, possibly δ-$Ca(BH_4)_2$. The release of hydrogen occurred in two steps, firstly the decomposition of β-$Ca(BH_4)_2$ and secondly the decomposition of δ-$Ca(BH_4)_2$. With the only products observed at 500°C being CaH_2, CaO and one unidentified phase.

In 2008, Aoki et al. continued to investigate the different phases of calcium borohydride [99], showing that pure α-$Ca(BH_4)_2$ can be synthesised from Sigma-Aldrich $Ca(BH_4)_2$ by heating to 160°C for 10 hours under dynamic vacuum, and pure β-$Ca(BH_4)_2$ by heating to 250°C for 80 hours.

Fichtner et al. also looked at the vibrational spectra, synthesising pure α-$Ca(BH_4)_2$ by heating Sigma-Aldrich $Ca(BH_4)_2$.2THF for 1 hour at 160°C, and pure β-$Ca(BH_4)_2$ by heating to 250°C for 90 minutes and quenching [100].

Buchter et al. conducted neutron and synchrotron x-ray powder diffraction studies [101] and showed the α- $Ca(BH_4)_2$ phase to be the same as that earlier reported by Miwa [91]; they also published an indexed pattern for the γ-$Ca(BH_4)_2$ phase. Synthesis through a gas-solid reaction with MgB_2 predominantly gave the α-phase, which when heated to 130°C formed the β-phase. A wet chemical preparation yielded γ-phase with a space group of P*bca*.

Filinchuk et al. also investigated the phase transformations of calcium borohydride [102]. They obtained: an F*2dd* structure for the α-$Ca(BH_4)_2$ phase; a P-*4* structure for the high temperature β- $Ca(BH_4)_2$ phase, formed by the removal of solvent from $Ca(BH_4)_2$.2THF; and an I-*42d* structure for an α'-phase formed by a second order transformation of the α-phase at 225°C. Majzoub and Ronnebro have also conducted a study into the different phases using theoretical energy calculations [103].

3.3 Group 3

3.3.1 $Sc(BH_4)_3$

Makhaev et al. first found that scandium borohydride could be synthesised via a two stage process [104]. The stirring of $ScCl_3$ and $NaBH_4$ in diethylether for 10 hours yielded $NaSc(BH_4)_4$.4DME, then heating the sample to 100˚C for 5 hours resulted in the formation of $Sc(BH_4)_2$

$$ScCl_3 + NaBH_4 \rightarrow NaSc(BH_4)_4.DME \quad (3.39)$$

$$NaSc(BH_4)_4.DME \rightarrow NaBH_4 + Sc(BH_4)_3.DME + 3DME \quad (3.40)$$

Melting of the compound was observed at 97-107°C with the loss of solvent, and decomposition of the borohydride occurred at 162°C.

Marks and Kolb [31] note the reaction of anhydrous $ScCl_3$ with a slight excess of lithium borohydride at room temperature in a solution of THF, forming $Sc(BH_4)_3$, a volatile white solid that sublimes at 80˚C.

3.3.2 $Y(BH_4)$

Marks and Kolb [31] showed that the borohydride complex of yittrium can be formed by the reaction of lithium borohydride with YCl_3 in THF, yielding $YCl(BH_4)_2$. At 100-200˚C decomposition and disproportionation occurs:

$$YCl(BH_4)_2 \rightarrow Y(BH_4)_3 + YCl_2(BH_4) \quad (3.41)$$

Therefore it is possible to form three different borohydride complexes from one reaction.

3.4 Group 4

Homoleptic borohydrides exist for all three $M(BH_4)_n$ compounds where n = 3 for Ti and n = 4 for Zr and Hf.

3.4.1 $Ti(BH_4)_3$

Hoekstra and Katz reported that titanium (III) borohydride can be formed by the reaction of $TiCl_4$ and $LiBH_4$, as shown in reaction (3.42) [105].

$$2TiCl_4 + 8LiBH_4 \rightarrow 2Ti(BH_4)_3 + 8LiCl + B_2H_6 + H_2 \quad (3.42)$$

Titanium (III) borohydride has been found to be unstable at room temperature, with complete decomposition occurring over several days into hydrogen and a non-volatile solid.

In 1987 Volkov and Myakishev [106] mechanically milled lithium borohydride with titanium (III) chloride to form titanium (III) borohydride:

$$TiCl_3 + 3LiBH_4 \rightarrow Ti(BH_4)_3 + 3LiCl \quad (3.43)$$

Elemental analysis and IR spectroscopy was performed on the resultant products in THF, showing 13.0% H, 34.8% B, 51.79% Ti, which corresponds to reaction (3.43) [107].

3.4.2 $Zr(BH_4)_4$

Hoekstra and Katz first investigated zirconium borohydride in 1949 [105], showing the reaction between zirconium fluoride and aluminium borohydride to form zirconium borohydride, this reaction was assisted by pre-reacting zirconium fluoride with sodium fluoride to allow reaction (3.44).

$$NaZnF_5 + 2Al(BH_4)_3 \rightarrow Zr(BH_4)_4 + 2AlF_2BH_4 + NaF \quad (3.44)$$

Reid et al. [108] showed the preparation of zirconium borohydride from the reaction of zirconium chloride and aluminium borohydride as per Hoekstra and Kratz [105]. Reid et al. also demonstrated the reaction of zirconium ether and diborane in an ether solution as in equation (3.45), and the dry reaction between zirconium chloride and lithium borohydride as in equation (3.46).

$$Zr(OR)_4 + B_2H_6 \rightarrow Zr(BH_4)_4 \quad (3.45)$$

$$ZrCl_4 + 4LiBH_4 \rightarrow Zr(BH_4)_4 + 4LiBH_4 \quad (3.46)$$

James et al. and Jensen et al. [109-111] indicated that zirconium borohydride was composed of four $[BH_4]$ groups bound to the zirconium metal centre by hydrogen bridges, as seen by the presence of strong absorption in the IR spectra around 2000-2200 cm^{-1} indicating that the structure was somewhere between the ionic bonding of sodium borohydride and the covalent bonding of aluminium borohydride.

In 1975, Tomkinson [112] reproduced Reid's 1957 work [108] showing the structure at 113 K has T_d symmetry with a space group of P43*m*. Many have characterised the vibrations with both Raman and IR, with the work by Jensen being the most comprehensive; showing a zirconium centre with four borohydride groups bound in a tridentate manner [113].

3.4.3 $Hf(BH_4)_4$

Hoekstra and Katz first synthesised hafnium borohydride [105]. Other workers have measured the IR and Raman spectra [109, 114, 115] showing hafnium to have a similar structure to zirconium borohydride.

3.5 Group 5

There are relatively few borohydride complexes of group 5 transition metals, with none reported for tantalum.

3.5.1 $V(BH_4)_3$

Vanadium borohydride can be formed via reactions between vanadium alkoxides and diborane to produce $V(BH_4)_3$ [41]. Vanadium borohydride has been used as a polymerization catalysts for olefins.

Jensen and Girolami [116-118] showed the reaction between $VOCl_3$ with $LiBH_4$ in Et_2O or $NaBH_4$ in DME to form $[V(BH_4)_4]^-$. This intermediate was then reacted to form various structures of $V(BH_4)_3(PMe_3)_2$ where the borohydride ligand is bidentate.

3.5.2 Nb(BH_4)

There are two known covalent niobium borohydride compounds. The first being a cyclopentadiene complex, $(\eta^5\text{-}C_5H_5)NbCl(BH_4)$, synthesised via the reaction between niobium pentachloride, sodium cyclopentadiene and lithium borohydride under a pressure of hydrogen. The resulting red-violet solid is soluble in both methyl chloride and benzene [31].

The other reported compound is similar; produced when $(\eta^5\text{-}C_5H_5)NbCl_2$ reacts with an excess of sodium or lithium borohydride in a THF or diethyl ether at 0°C to form $(\eta^5\text{-}C_5H_5)NbBH_4$. The structures of both these products have the borohydride ligand bonding in a bidentate fashion through two bridging hydrogen atoms [31].

3.6 Group 6

3.6.1 Cr(BH_4)

Parry et al. reported in 1958 [119] the synthesis of hexamine chromium (III) tri-borohydride, $[Cr(NH_3)_6](BH_4)_3.0.5NH_3$, where the borohydride ion is a counter anion for the complex cation. This complex was prepared through the reaction of hexamine chromium fluoride and sodium borohydride in liquid ammonium. This complex decomposes at 60°C with the

release of hydrogen, ammonia and $(H_3N.BH_3)_n$ leaving a black solid consisting of CrB and NBH compounds.

In 1967, Hein and Schmiede [120] isolated a bis(biphenyl)chromium borohydride in aqueous solution, $(C_{12}H_{10})_2CrBH_4$. This is an ionic species with two biphenyl ligands bound to the chromium (I) ion, with the borohydride group acting as an anion for the organometallic complex.

Noth and Seitz [121] evaluated a number of methods to synthesize chromium (II) borohydride, such as the reaction between $Cr(OMe)_3$ and diborane in THF which was described by Mirviss et al. [122], and which gave inconsistent results. The Mirviss et al. found that the reduction of $Cr(OBu^t)_4$ by diborane in a THF solution formed $Cr(BH_4)_2$. The reduction of Cr (IV) to Cr (II) starts at around -40°C and is complete at -20°C. $Cr(BH_4)_2$ is stable at -20°C but readily decomposes at room temperature. IR shows bands that are attributed to bridging and terminal hydrogen atoms, indicating covalently bound BH_4 groups, giving the coordination number for the chromium atom of 6 indicating tridentate borohydride bonding to the chromium.

3.7 Group 7

There are no known covalent or ionic complexes for technetium or rhenium.

3.7.1 $Mn(BH_4)_2$

Noth reports that manganese (II) chloride reacts with lithium borohydride in an ether solution to form compounds of the type $Li[Mn(BH_4)_2Cl_2].n(C_2H_5)_2O$ [46].

Subsequently Monnier [123] reports that manganese (II) borohydride $Mn(BH_4)_2$ can be formed by the reaction between manganese (II) chloride and lithium borohydride as per reaction (3.47). Monnier also shows that the reaction of Li_2MnBr_4 and lithium borohydride in anhydrous ether at -80°C yields manganese (II) borohydride. There is little data on the chemical and physical properties of the product.

$$MnCl_2 + 2LiBH_4 \rightarrow Mn(BH_4)_2 + 2LiCl \quad (3.47)$$

A tris-borohydride $Mn(BH_4)_3$ has been claimed to have been formed by the reaction of manganese (III) alkoxide and diborane in THF, but reports are sparse and uncertain.

The reaction between manganese pentacarbonylbormide and aluminium borohydride forms a volatile and unstable covalent manganese borohydride as per equation (3.48). This compound decomposes at 25°C. Interestingly, the bulky CO ligands force the $[BH_4]$ group to bond via a single bridging hydrogen.

$$3Mn(CO)_5Br + Al(BH_4)_3 \rightarrow 3Mn(CO)_4(BH_4) + AlBr_3 \quad (3.48)$$

Choudhury et al. [124] investigated manganese (II) borohydride as a potential solid state hydrogen storage material. Choudhury et al. predicted a thermodynamically stable I-4m2 structure at room temperature for $Mn(BH_4)_2$. The I-4*m*2 was predicted to have a ΔH_f of -58.89 kJ/mol BH_4, with the most feasible decomposition mechanism being the evolution of hydrogen and the formation of metallic manganese and boron [124].

The solvent free homoleptic manganese (II) borohydride, $Mn(BH_4)_2$, was formed by the mechanical milling of alkali metal borohydride with manganese chloride as shown in reaction (3.47) by Cerny et al. [125]. The refined structure was a $P3_112$ phase very similar to α-$Mg(BH_4)_2$. This phase was shown to be stable until 180°C where the compound melts.

3.8 Group 8

There are few borohydrides of this group with the majority being iron-based, and only a few ruthenium compounds known. Iron (II) borohydride, or ferrous tetrahydroborate, $Fe(BH_4)_2$ was prepared by Schaeffer et al. in 1956 [126], by reacting iron (III) chloride with lithium borohydride in ether at -45°C. The compound formed is very temperature sensitive, completely decomposing at -10°C to form a number of pyrophoric products.

3.9 Group 9

Stewart and Schaeffer [127] reported that a reaction between cobalt (II) bromide and lithium borohydride in diethyl ether yielded $Co(BH_4)_2$, although the gray solid product was not fully characterised. The compound was unstable when heated above -80°C, decomposing to form cobalt metal and hydrogen.

3.10 Group 10

Nickel has the only known covalent borohydride complex known for the group, and several ionic species of nickel borohydride are known, here the borohydride group is considered to be a counter ion for the nickel complex, e.g. $Ni(NH_3)_6(BH_4)_2$ [128].

Nickel bis-borohydride has been postulated by Maltseva et al. as an intermediate in the preparation of nickel borides [129].

3.11 Group 11

3.11.1 $Cu(BH_4)$

There is a reaction between copper (I) [130] and copper (II) [130, 131] chloride and lithium borohydride in ether at -45°C, to produce copper (I) borohydride. $CuBH_4$ is stable at -45°C but rapidly decomposes at -12°C to form metallic copper with the evolution of diborane and hydrogen.

$$2CuCl_2 + 4LiBH_4 \rightarrow 2CuBH_4 + 4LiCl + B_2H_2 + 3H_2 \quad (3.49)$$

$$2CuBH_4 \rightarrow 2Cu + B_2H_6 + H_2 \quad (3.50)$$

3.11.2 $Ag(BH_4)$

Silver (II) borohydride has been shown to be stable at -30°C, prepared by the reaction of silver chloride and lithium borohydride, in both ether and aqueous ammonia solutions [132].

3.11.3 $Au(BH_4)_3$

Gold (III) chloride has been reacted with lithium borohydride in an ether solution to yielding gold (III) borohydride at -120°C [133].

$$AuCl_3 + 3LiBH_4 \rightarrow Au(BH_4)_3 + 3LiCl \quad (3.51)$$

Decomposition occurs upon heating above -120°C yielding metallic gold, hydrogen and diborane.

3.12 Group 12

3.12.1 $Zn(BH_4)_2$

Zinc borohydride $Zn(BH_4)_2$ initially appears to be an attractive candidate for hydrogen storage with a high gravimetric hydrogen capacity (8.4 wt.%), and low decomposition temperature (85°C) [16]. It was first reportedly synthesised in 1952 by Wiberg and Henle [134], by a metathesis reaction of zinc chloride and lithium borohydride in a diethyl ether, at room temperature (3.52). In 1989, Malteseva et al. [135] were the first to report that zinc borohydride could be formed by mechanochemical synthesis; mechanically milling sodium borohydride with zinc chloride under an inert atmosphere. This route was then investigated in more details by Matthews [136] and by Jeon and Cho [137]

$$ZnCl_2 + 2NaBH_4 \rightarrow Zn(BH_4)_2 + 2NaCl \quad (3.52)$$

Two different routes for thermal decomposition have been proposed:

$$Zn(BH_4)_2 \rightarrow Zn + 2B + 4H_2 \quad (3.53)$$

$$Zn(BH_4)_2 \rightarrow Zn + B_2H_6 + H_2 \quad (3.54)$$

Equation (3.53), as proposed by Wiberg and Henle [134], has an expected weight loss of 8.49 wt.% that is only due to the evolution of hydrogen, (or 3.74 wt.% if the by-product NaCl is present in the reaction products). However, equation (3.54), proposed by Jeon and Cho [137], forms gaseous diborane, and will therefore have an associated weight loss of 31.22 wt.% (or 13.77 wt.% if the by-product NaCl is present).

Noth further investigated the solvent synthesis of zinc borohydride in 1961 [133] suggesting that remaining alkali borohydride could further react with zinc borohydride to form a different complex to the one subsequently proposed. Changing the alkali borohydride also has an effect on the final borohydride.

$$Zn(BH_4)_2 + LiCl \rightarrow Li[ClZn(BH_4)_2] \quad (3.55)$$

$$3LiBH_4 + ZnCl_2 \rightarrow 2LiCl + Li[Zn(BH_4)_3] \quad (3.56)$$

$$3NaBH_4 + ZnCl_2 \rightarrow 2NaCl + Na[Zn(BH_4)_3] \quad (3.57)$$

$$NaBH_4 + Zn(BH_4)_2 \rightarrow Na[Zn(BH_4)_3] \quad (3.58)$$

$$3KBH_4 + ZnBr_2 \rightarrow Zn(BH_4)_2.2THF + 2KBr \quad (3.59)$$

Ravnsbaek et al. [138] synthesised zinc borohydride based compounds, $LiZn_2(BH_4)_5$, $NaZn_2(BH_4)_5$ and $NaZn(BH_4)_3$ through ball milling $ZnCl_2$ and ABH_4, where A is Li or Na.

The optimum ratio between ABH_4 and $ZnCl_2$ is 2.5:1 which allows the formation of $AZn_2(BH_4)_5$ as per equation (3.60).

$$5ABH_4 + 2ZnCl_2 \rightarrow AZn_2(BH_4)_5 + 4ACl \quad (3.60)$$

In addition, Ravnsbaek et al. [138] showed that when sodium borohydride is used as a reagent there is a competing reaction with an optimum $NaBH_4$ to $ZnCl_2$ ratio of 3:1 forming the compound $NaZn(BH_4)_3$ via reaction (3.61)

$$3NaBH_4 + ZnCl_2 \rightarrow NaZn(BH_4)_3 + 2NaCl \quad (3.61)$$

The crystal structure and thermal decomposition temperatures differ significantly between the three compounds, and are summarised in Table 3.1. Previous work by Malteseva et al. [139], Matthews [136] and Jeon and Cho [137] assumed that the formation of sodium chloride indicated that the reaction had occurred via (3.51), with unassigned XRD peaks being attributed to $Zn(BH_4)_2$ by Jeon and Cho [137]. Ravnsbaek et al. [138] were able to use synchrotron radiation powder x-ray diffraction and NMR to determine the structure of the zinc borohydride complex formed by mechanical milling. It is unclear what products are formed by other synthetic approaches such as the metathesis reaction using a solvent [134].

Ravnsbaek et al. [138] believe the main $AZn_2(BH_4)_5$ phases decompose to form metallic zinc and ABH_4. There is then a simultaneous reaction between the ABH_4 and A_2ZnCl_4 to form metallic zinc and ACl. The overall reaction scheme can be written as shown in equation (3.62).

Table 3.1 Crystal structure, hydrogen content and decomposition temperature of the three Ravnsbaek alkali-metal zinc borohydrides [138].

	$LiZn_2(BH_4)_5$	$NaZn_2(BH_4)_5$	$NaZn(BH_4)_3$
Space group	C*mca*	$P2_1/c$	$P2_1/c$
a (Å)	8.6244(3)	9.397(2)	8.2714(16)
b (Å)	17.8970(8)	16.635(3)	4.5240(7)
c (Å)	15.4114(8)	9.1359(16)	18.757(3)
β (°)	90	112.658 (19)	101.689(11)
Theoretical gravimetric density (wt.%)	9.51	8.84	9.10
T_d (°C)	127	95	103

$$2AZn_2(BH_4)_5 + A_2ZnCl_4 \rightarrow 5Zn + 4ACl + 5B_2H_6 + 5H_2 \quad (3.62)$$

3.12.1 $Cd(BH_4)_2$

Cadmium borohydride, $Cd(BH_4)_2$, may be synthesised at 0°C in an ether solvent [140], as per equation (3.63):

$$CdCl_2 + 2LiBH_4 \rightarrow Cd(BH_4)_2 + 2LiCl \quad (3.63)$$

$Cd(BH_4)_2$ is an air-sensitive and thermally unstable compound decomposing at around 25°C into its three constituent elements. The toxicity of cadmium and its salts make it a poor choice for a hydrogen storage material.

3.13 Group 13

The borohydrides of group 13 typically form covalent compounds. The stability of the +3 oxidation state of the group 13 borohydride decreases dramatically as one goes down the group Al >> Ga > In. There are no reported thallium (III) borohydrides, and attempts to prepare this have resulted in the formation of thallium (I) borohydride which is ionic in character [141, 142]. Aluminium (III) borohydride, $Al(BH_4)_3$, is a low boiling point liquid at room temperature, which is stable for long periods at 25°C with predominantly covalent bonding whose general properties resemble that of diborane [27, 30, 36].

3.13.1 $Al(BH_4)_3$

The preparation of aluminium borohydride was first shown by Schlesinger et al. in 1940 from the reaction of trimethyl aluminium with diborane [27].

$$Al_2(CH_3)_6 + 4B_2H_6 \rightarrow 2Al(BH_4)_3 + 2B(CH_3)_3 \quad (3.64)$$

The preparation can be carried out via a metathesis reaction between an alkali metal borohydride and aluminium (III) halide, preferably the chloride, in the absence of solvent at 100-150°C [27].

$$6MBH_4 + Al_2X_6 \rightarrow 2Al(BH_4)_3 + 3MX \quad (3.65)$$

(where M = Li, Na and X = Cl, Br.)

Aluminium borohydride may be conveniently regarded as an aluminium atom surrounded trigonally by three borohydride groups. The borohydride atoms bind in a bidentate fashion, in which the aluminium and boron atoms are connected by a double hydrogen bridge (Al-H_2-B) that is similar to that observed in diborane B-H_2-B.[30, 143, 144]

Decomposition of the vapour up to 60°C proceeds slowly. At a higher temperature (~150°C) decomposition occurs with the evolution of hydrogen and the production of an unknown solid [27]. The rate of the reaction is increased by the addition of aluminium chloride or copper, however, the rate of the reaction is not altered by particle size [44]. Brokaw and Pease have studied the kinetics of decomposition and found it to be a first order reaction between 159 and 189°C, whilst the actual mechanism for decomposition was not determined [145].

3.13.2 $Ga(BH_4)_3$

The preparation of gallium borohydride, through the reaction of gallium (III) chloride and lithium borohydride, was reported by Wiberg et al. in 1957 [146]. Initially a $Li[Cl_3GaBH_4]$ complex is formed, which reacts with excess lithium borohydride to form gallium (III) borohydride at 15°C.

$$GaCl_3 + LiBH_4 \rightarrow Li[Cl_3GaBH_4] \rightarrow Ga(BH_4)_3 + 3LiCl \quad (3.66)$$

Schlesinger et al. found that the reaction between trimethyl gallium and diborane at -45°C formed a dimethyl gallium borohydride, Me_2GaBH_4. This compound is stable at -80°C but decomposes at room temperature, yielding boranes, gallium and hydrogen [39].

3.13.3 $In(BH_4)_3$ and $Th(BH_4)_3$

Wiberg and Noth reported that the reaction of trimethyl indium with diborane in a THF solvent at -40°C yielded an indium borohydride complex [146].

$$Me_3In + 2B_2H_6 \rightarrow In(BH_4)_3.THF + B(C_2H_5)_3 \quad (3.67)$$

Warming to -10°C caused decomposition into indium metal, diborane and hydrogen and THF [146].

Wiberg et al. [146] also attempted synthesis via a metathesis reaction between indium chloride and lithium borohydride. This resulted in the formation of the complex $Li[Cl_3InBH_4]$, however, further substitution of the chlorine ions with borohydride was not possible without decomposition to metallic indium.

The reaction between thallium (III) chloride and lithium borohydride does not result in the substitution of chloride ions by borohydride ions, but reduces the thallium oxidation state from +3 to +1 [34].

$$TlCl_3 + 2LiBH_4 \rightarrow TlCl + 2LiCl + B_2H_6 + H_2 \quad (3.68)$$

Thallium (I) borohydride, $TlBH_4$, has been synthesised by the reaction of lithium borohydride with thallium (I) ethoxide in ether, and by the reaction between potassium borohydride and thallium (I) nitride in aqueous solution. Thallium (I) borohydride slowly hydrolyses at room temperature, and thermally decomposes at 40°C evolving diborane and leaving a TlH residue [141, 142].

Waddington showed that unlike aluminium and gallium borohydrides, thallium is ionic in character, forming a face-centred cubic lattice (lattice parameter of 6.88 Å) that is similar to that of the alkali metal borohydrides [142].

3.14 Group 14

Tin (II) borohydride has been obtained via the reaction (3.69) between diborane and tin (II) methoxide at -78°C in ether [147].

$$Sn(OMe)_2 + B_2H_6 \rightarrow Sn(BH_4)_2 + HB(OMe)_2 \quad (3.69)$$

This compound decomposes at -65°C, forming tin with the evolution of hydrogen and diborane gas.

The reaction between potassium borohydride and trimethyl lead (IV) chloride in liquid ammonia has been shown to form an ammoniate complex with trimethyl lead (IV)

borohydride. This compound readily decomposes at -5°C to leave a trimethyl lead (IV) hydride residue.

$$Me_3PbCl + KBH_4 \rightarrow Me_3PbBH_4.NH_3 + KCl \quad (3.70)$$

Siddiqi et al. [148] showed that the reaction between germanium and tin tetrachlorides and excess potassium borohydride in THF yielded $M(BH_4)_4$ as per equation (3.71). All compounds were stable in air and soluble in dimethylformamide (DMF, C_3H_7NO) and dimethyl sulfoxide (DMSO, C_2H_6OS). The IR spectrum showed a single absorption at 2560 cm^{-1}, indicating a single terminal hydrogen environment that is characteristic of a tridentate borohydride group [113, 115].

$$MCl_4 + KBH_4 \rightarrow M(BH_4)_4 + 4KCl \quad (3.71)$$

3.15 F-block

Borohydride complexes of the lanthanides and actinides are relatively rare. Zange synthesised a number of lanthanide borohydrides via the reaction of anhydrous lanthanide trichloride with diborane in THF as per equation (3.72) [149]. These compounds were insoluble in the solvents tested and little analysis was performed.

$$MCl_3 + B_2H_6 \rightarrow M(BH_4)_3.nTHF \quad (3.72)$$

M = Sm, Eu, Gd, Tb, Dy, Ho, Er, Tm, Yb and Lu, n is not an integer

Mirsaidov et al. investigated the borohydrides of lanthanum and neodymium [150]. These compounds were synthesised through the reaction between lanthanide trichloride and sodium borohydride in a THF solution, as per equation (3.73).

$$MCl_3 + 3NaBH_4 \rightarrow M(BH_4)_3 + 3NaCl \quad (3.73)$$

M = La or Nd

Lanthanum and neodymium borohydrides thermally decompose at 157°C and 147°C, respectively, via equation (3.74) [150]

$$2M(BH_4)_3 \rightarrow MB_6 + MH_2 + 11H_2 \quad (3.74)$$

M = La or Nd

Thorium borohydride was investigated by Hoekstra and Katz [105]. Preparation was achieved by the reaction of aluminium borohydride with thorium fluoride.

$$ThF_4 + 2Al(BH_4)_3 \rightarrow Th(BH_4)_4 + 2AlF_2BH_4 \quad (3.75)$$

Thorium borohydride was shown to be stable up to 150°C. On passing the vapour through a tube heated to 300°C, decomposition was observed resulting in an amorphous solid $ThB_{3.83}$.

The first prepared actinide borohydrides were uranium (IV) [65] and thorium (IV) borohydrides [105], prepared by the reaction of a metal fluoride with aluminium borohydride. Ehemann and Noth [151] reported, however, that the most convenient method of synthesising

the thorium compound was by reacting thorium tetrachloride with lithium borohydride in an ether solution, and then subliming the product under vacuum.

Schlesinger and Brown [65] synthesised uranium (IV) borohydride, by reacting uranium (IV) chloride with aluminium borohydride at room temperature to form uranium (IV) borohydride. On heating to 100°C, rapid decomposition occurs to form uranium (III) borohydride with the evolution of hydrogen and diborane [65].

$$2U(BH_4)_4 \rightarrow 2U(BH_4)_3 + B_2H_6 + H_2 \quad (3.76)$$

On continued heating above 150°C, further decomposition occurred but the authors were unable to ascertain the decomposition products [65].

$$U(BH_4)_3 \rightarrow UB_4 \text{ (or U + 4B)} + 8H_2 \quad (3.77)$$

Banks et al. investigated protactinium, neptunium and plutonium borohydrides: $Pa(BH_4)_4$, $Np(BH_4)_4$ and $Pu(BH_4)_4$, respectively [152]. These compounds were synthesised by reacting the metal tetraflouride with aluminium borohydride. $Pa(BH_4)_4$ was found to sublime at 55°C, $Np(BH_4)_4$ and $Pu(BH_4)_4$ decomposed at room temperature evolving hydrogen and diborane.

3.16 Reactive Mixtures

In 1967 Reilly and Wiswall showed the intermetallic compound Mg_2Cu reacted with hydrogen at ~300°C to form MgH_2 and $MgCu_2$ with excess Mg also forming MgH_2 [153]. When a pressure-composition isotherm was measured, two plateaus were recorded, firstly for the reaction of hydrogen with Mg_2Cu and secondly the reaction of hydrogen with Mg. When the thermodynamic of the system were compared it showed that alloy (Mg_2Cu) had a lower enthalpy of formation.

In 2005 Vajo and co-workers attempted to modify the thermodynamics and kinetics of the sorption reaction of lithium borohydride by adding magnesium [154-156]. They proposed forming a stabilised alloy as a decomposition product, to make recombination possible. Generally a binary hydride AH_2 decomposes to form $A + H_2$, and if the enthalpy is large the equilibrium hydrogen pressure will be relatively low or the temperature required for an equilibrium pressure of 1 bar (T(1 bar)) will be high. However, if the binary hydride AH_2 is combined with species B, then upon decomposition the product is AB_x. Because the formation of AB_x from $A + xB$ is exothermic, the energy of the decomposition products are lower in energy compared to A. This has the effect of increasing the equilibrium hydrogen pressure and lowering the temperature (at 1 bar), and therefore thermodynamically destabilising the binary hydride AH_2. Figure 3.4 shows a generalised energy diagram for the binary hydride AH_2 and a single non-hydriding additive B.

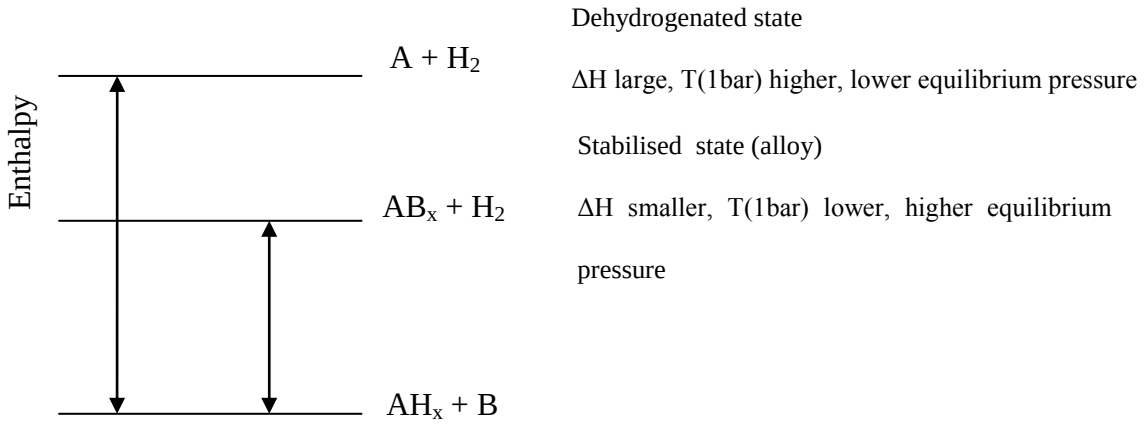

Figure 3.4 Generalised enthalpy diagram showing the destabilisation through formation of the alloy AB_x[156].

Figure 3.4 shows the additive B does not form a hydride, and therefore destabilisation comes with a gravimetric penalty that is dependent on the atomic mass of A and B and the stoichiometry of the resulting AB_x alloy. However, if the additive used can form a hydride, the gravimetric penalty can be minimised. Vajo et al. used the example of lithium borohydride being destabilised by magnesium hydride [156]. In Figure 3.5, destabilisation is achieved through the formation of MgB_2; the theoretical enthalpies and equilibrium pressure at 1 bar are shown, and equation (3.78) shows the reaction that Vajo predicted.

$$2LiBH_4 + MgH_2 \rightarrow 2LiH + MgB_2 + 4H_2 \quad (3.78)$$

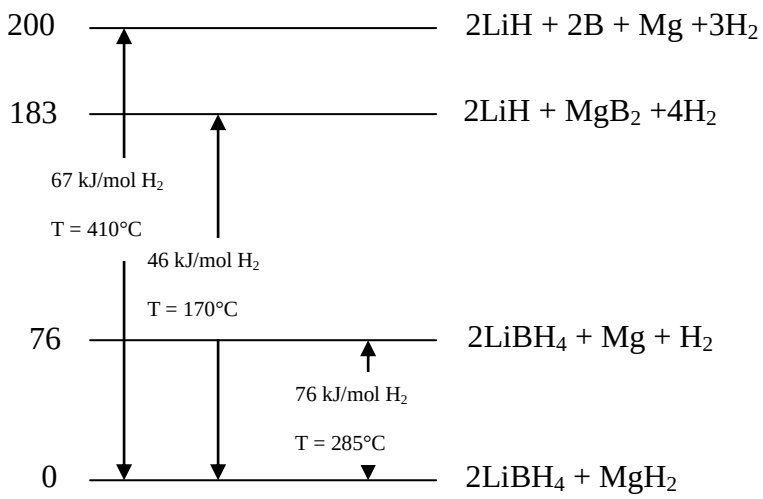

Figure 3.5 Enthalpy diagram for the destabilisation of $LiBH_4$ by MgH_2. The intermediate step of the dehydrogenation of magnesium is shown as a possible intermediate to the reaction [156].

Recently, Nakagawa et. al. [157] investigated the effect of Mg/MgH_2 additions to $Zn(BH_4)_2$, speculating that a solid state reaction between the desorbed B_2H_6 and Mg/MgH_2 should result in the formation of magnesium diboride, as per equation (3.79). Previously, it was shown that it was possible to form alkali metal borohydrides by reacting the metal hydride with diborane in a solvent such as diethyl ether, as described in equation (3.80), where M = Li, Na and K [64].

$$MgH_2 + B_2H_6 \rightarrow MgB_2 + 4H_2 \quad (3.79)$$

$$MH_x.(solvent) + x/2B_2H_6 \rightarrow M(BH_4)_x.solvent \quad (3.80)$$

3.17 Summary

Complex hydrides, and borohydrides in particular, have potential for use as hydrogen storage media for onboard mobile applications. With such a wide and varied series of compounds it is necessary to select only a few candidate materials for consideration. Materials that use chemicals that are extremely poisonous, for example diborane or cadmium, are not going to be considered here due to limitations in synthesis equipment. Also, materials that decompose below room temperature are not going to be considered in this study. However, in the longer term, the use of such materials may be investigated, as increasing the compound stability is still an option.

For this work the magnesium, calcium and zinc borohydrides will be considered. Zinc borohydride offers an excellent opportunity for a high gravimetric storage of hydrogen with a low decomposition temperature. Magnesium and calcium borohydrides have higher decomposition temperatures but have a greater prospect for reversibility, as well as having a number of intermediate phases that raise the possibility of finding alternative reaction paths.

In addition, reactive composites with magnesium hydride will be investigated, with a view to enhancing reversibility and decreasing the decomposition temperature. To improve the hydrogen sorption kinetics, the use of catalytic additives will also be studied.

4 VIBRATIONAL SPECTROSCOPY

There is a range of standard techniques that are potentially available to analyse the formation of borohydrides and subsequently the thermal decomposition and reaction products. Vibrational spectroscopy is the major technique that is widely used. Although x-ray diffraction (XRD) has many strengths for probing the structure of materials, limitations such as the inability to determine the position of hydrogen atoms relative to heavy metal nuclei, and the lack of structural data for liquid or amorphous phases rule out this technique for this particular application. Neutron diffraction allows the determination of hydrogen (deuterium) position using crystallography, but access to facilities is limited and it is a time consuming and expensive technique. Nuclear magnetic resonance (NMR) gives information on the short-range structure of borohydrides, and about the environment of the nuclei. NMR has been used to investigate the decomposition products, although, because it is normally performed ex-situ, only analysis of phases that are stable at room temperature is usually possible [61].

Vibrational spectroscopy does not suffer from the shortfalls described above; infrared absorption and Raman scattering provide the required data on metal-ligand coordination, symmetry and bonding. Furthermore, these techniques can also be used to study the thermal decomposition products and, significantly, any intermediate products that are formed.

In this chapter, vibrational spectroscopy will be discussed in detail. To allow the discussion to concentrate on the present application, some background on metal borohydrides needs to be presented.

4.1 Background Theory

The main spectroscopies employed for the characterisation of the molecular vibrations are Raman scattering and infrared absorption spectroscopy. Inelastic neutron scattering (INS) can also give information on molecular vibrations, however, sample preparation is expensive and results concentrate on low energy lattice vibrations and therefore will not be considered here.

Both Raman and infrared provide information on chemical structures and physical form; 'fingerprinting' the identification of substances through characteristic patterns is the most common use of both Raman and infrared. Samples can be measured in a whole range of states, including crystalline solid, amorphous solid, liquid and gas at a variety of temperatures, allowing the possibility of in-situ monitoring of reactions.

Raman and infrared techniques involve an interaction of photons with matter where they can either be absorbed or scattered (some radiation will not interact with the material and pass straight through which is not considered here). If the energy of the incident photon is equal to that of the energy gap between the ground and an excited state within a molecule, the photon may be absorbed and the molecule promoted to this higher energy excited state. In absorption spectroscopy the reduction in intensity of the absorbed wavelengths compared to the incident light is measured. It is also possible, however, for the photon to interact with the molecule and be scattered. In this instance the energy of the incident photon does not need to be of an energy exactly matching the difference in energy levels within the molecule of the sample. The scattered photon can be observed by collecting light at an angle different to that of the incident radiation.

Radiation is typically expressed by its wavelength (λ). In spectroscopy, however, it is the interaction of radiation with a molecule that is examined and therefore it is useful to express the radiation by frequency (v) or wavenumber ($\tilde{\omega}$) which are linearly related to the energy (ΔE), as shown in equations (4.1) and (4.2):

$$1/\lambda = \tilde{\omega} = v/c \tag{4.1}$$

$$v = \Delta E/h \tag{4.2}$$

In equations (4.1) and (4.2) c is the speed of light and h is Plank's constant.

Infrared and Raman spectroscopy use radiation in different ways, with infrared spectroscopy directing photons covering a range of frequencies from the infrared part of the electromagnetic spectrum at a sample. If the incident photon has energy equal to that of the energy difference between the ground and excited vibrational states of the sample then it will be absorbed. The difference in observed frequencies between the incident beam before and after interaction with the sample is recorded. Raman spectroscopy, however, uses a single frequency incident radiation, and it is the scattered radiation that is detected. Thus unlike infrared absorption, Raman scattering does not require exactly matching energy from the incident radiation and the energy difference between vibrational states of the sample.

In Raman scattering the incident radiation interacts with the molecule and polarises the electron cloud to form a short-lived virtual state. This state is not stable and a photon is rapidly released. The energy changes that are detected within vibrational spectroscopy are those required to move nuclei. If the photons are scattered by distortion of the electron cloud

the change in frequency will be very small, as electrons are comparatively light. This scattering process is regarded as elastic scattering. This is the dominant process in Raman scattering and is called Rayleigh scattering. If during the scattering process nuclear motion is induced, energy will be transferred from either the incident photon to the nuclei or from the nuclei to the scattered photon. This process is inelastic and the energy of the scattered photon will have a different frequency to that of the incident radiation. This is called Raman scattering; it is an inherently weak process with only one in every 10^6-10^8 photons undergoing an inelastic interaction.

Figure 4.1 shows the basic process that occurs for one vibration. At room temperature most molecules exist in their vibrational ground state (m), with a few existing at a higher level (n). The incident photons cause the molecule to exist in a virtual excited state.

Rayleigh scattering is the most dominant process, with most photons interacting this way. In this type of scattering, the molecule returns to the state that it was in before excitation accompanied by the emission of a photon of frequency equal to that of the incident radiation.

There are two possible types of Raman interaction. When a molecule relaxes from the virtual state it absorbs energy from the photon and is promoted to the excited vibrational state, n. The emitted photon has less energy than the incident radiation; this is called Stokes scattering. There will be some molecules that, due to thermal energy, are in the excited vibrational state, n. On relaxation from the virtual state these will give energy to the photon and return to the ground state, m, with the resultant photon having more energy compared to that of the incident radiation; this is called anti-Stokes scattering. The relative intensities of

the two processes depend on the population of the various states in the molecule. These populations can be worked out using the Boltzmann equation (4.3).

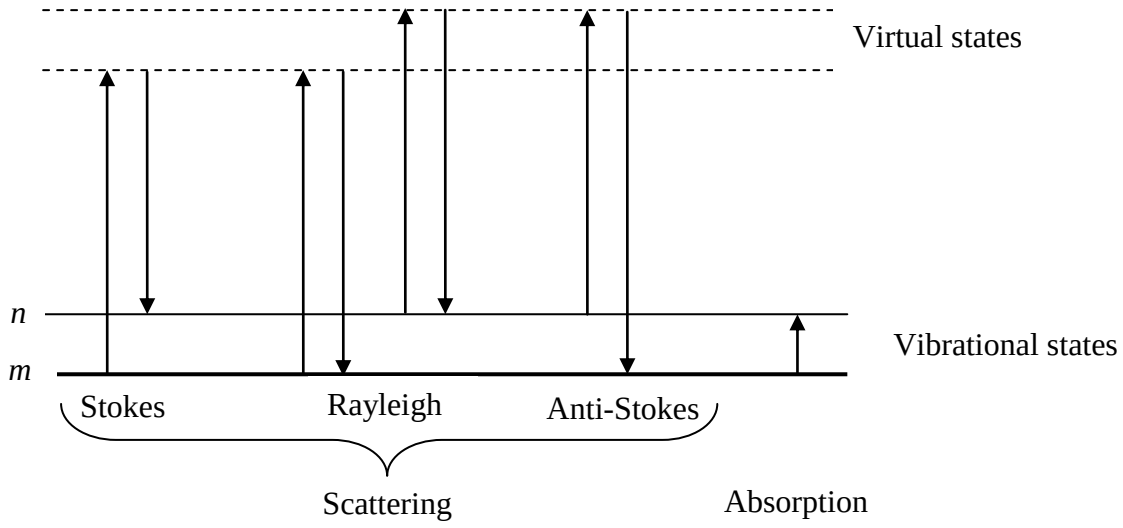

Figure 4.1 Diagram of the Rayleigh and Raman scattering processes. The ground vibrational state, m, is the lowest energy with all subsequent vibrational energies increasing above this level. Both the excitation energy (up arrow) and scattered energies (down arrow) have a larger energy than the energy of the vibration.

$$\frac{n_n}{n_m} = \frac{g_n}{g_m} e^{\frac{-(E_n - E_m)}{k_B.T}} \tag{4.3}$$

The fundamental difference between Raman scattering and infrared absorption is also illustrated in Figure 4.1. As previously described, infrared absorption involves the direct excitation from the ground state, m, to the excited state, n, by a photon of energy exactly equal to the difference in energy between the levels. Raman scattering, however, uses much

higher energy photons to excite the molecule to a virtual state and measures the difference in energy between m and n by observing energy losses in the emitted photons.

4.2 Borohydrides

Understanding the simplest boron hydrogen compound, BH_3, is instructive for consideration of the vibrational spectra of metal borohydride complexes. In BH_3 the 2s and two 2p orbitals hybridise to form three sp^2 hybrid orbitals of equal energy arranged in a trigonal planar configuration. The remaining p_z orbital remains vacant perpendicular to the plain of the hybrid orbitals. Three hydrogen atoms can bond easily to the three bonding orbitals, however, boron wants to complete the octet to fill the empty p_z orbital. Dimerisation satisfies this desire, forming diborane, when a pair of electrons from a B-H bond is shared with the other boron to form a H-B-H three centre two electron bond [158, 159]. The weakened B-H bond of the bridging component is longer than the unbridged two centre two electron bonds of the terminal B-H bonds.

Price [160] first determined the structure of diborane through the use of infrared spectroscopy, as shown in Figure 4.2. This was different to the preconception that it had a structure similar to ethane. Bell and Longuet Higgins [161] showed that there are 18 fundamental vibrational modes, eight of which are infrared active, summarised in Table 4.1a and seven are Raman active, summarised in Table 4.1b.

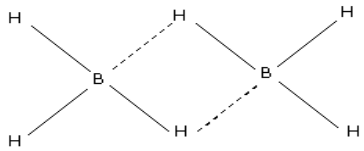

Figure 4.2 Structure of diborane.

Table 4.1 (a) Infrared and (b) Raman peak positions of diborane with the fundamental vibrations assigned [161].

(a)

ν (obs.) cm^{-1}	**Intensity**	**Assignment**
393 412 431	Strong	ν_{10}
679	Weak	
831	Weak	
981	Strong	ν_{14}
1154 1178 1197	Very Strong	ν_{18}
1292	Medium	
1377	Medium	
1405	Medium	ν_9
1587 1608 1626	Very strong	ν_{17}
1722	Weak	?
1863	Strong	ν_{13}
1993	Medium	
2134	Very weak	
2217	Very weak	
2353	Strong	
2558	Strong	ν_{16}
2625	Strong	ν_8

(b)

ν (obs.) cm^{-1}	**Intensity**	**Assignment**
793	5	ν_4 (B^{11}-B^{11})
806	4	ν_4 (B^{11}-B^{10})
821	3 (broad)	ν_4 (B^{10}-B^{10}) ν_{12}
1008	Diffuse	ν_7
1180	2	ν_3
2102	10	ν_2
2489	3	ν_{11}
2523	10	ν_1

The next step from diborane is the consideration of an isolated MBH_4 unit. It is well established that a borohydride group can bind to a metal centre in one of four ways (shown in Figure 4.3) [31]:

- ionic,
- monodentate,
- bidentate and
- tridentate.

Specifically, the vibrational spectra of these four different modes of bonding are different and allow ready distinction between the four modes.

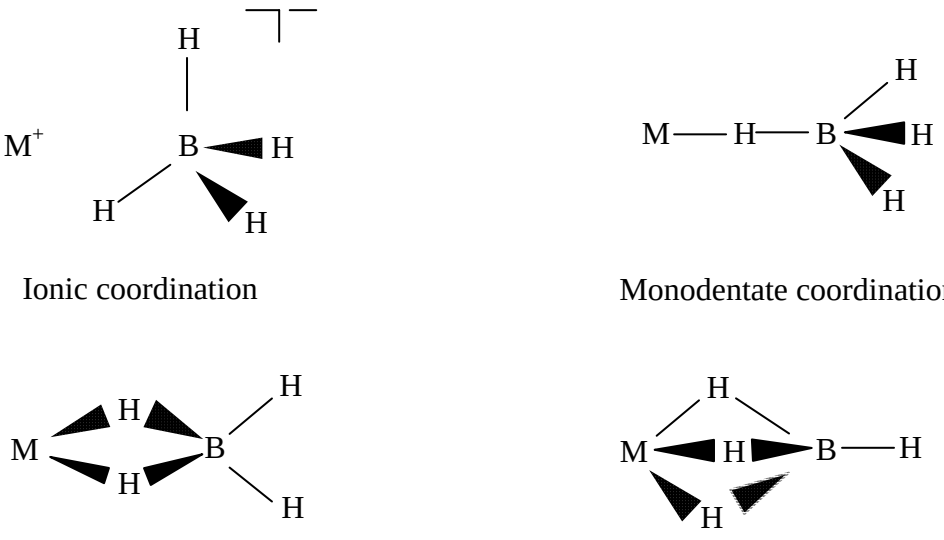

Figure 4.3 Bonding configurations of the BH_4 ligand [31].

Tables 4.2 and 4.3 show some of the normal modes of vibration for different bonding modes described earlier: monodentate, bidentate, tridentate and ionic. The region between 1000 and 2500 cm^{-1} contains the bands involved in the deformation of the B-H

bond and some M-H bonding, allowing structural determination. Marks and Kolb [31] used the analysis of model compounds of known structure in the literature, to populate Table 4.2 and

Table 4.3.

Table 4.2 Infrared active fundamental vibrational frequencies typically observed for mononuclear $M(BH_4)_x$ configurations [27]

Bonding Mode	Approx. Freq. (cm^{-1})	Type of internal change	Symmetry Type	Comments
Monodentate	2300-2440	B-H_t stretch	A_1, E	Strong, probably a doublet
	~2000	B-H_b stretch	A_1	Strong
	~1700 – 2000	M-H_b stretch	A_1	May be broad
	1000-1150	BH_3 deformation	A_1, E	Strong band, possible weaker one at higher frequency
Bidentate	2400-2600	B-H_t stretch	A_1, B_1	Strong doublet, 50-80 cm^{-1} splitting
	1650-2150	B-H_b stretch	A_1, B_2	Medium-strong band
	1300-1500	bridge stretch	A_1	Strong band
	1100-1200	BH_2 deformation	B_2	Medium-strong, possible doublet
Tridentate	2450-2600	B-H_t stretch	A_1	Strong singlet
	2100-2200	B-H_b stretch	A_1, E	Doublet, 50-80 cm^{-1} splitting
	1150-1250	bridge stretch	E	Strong
Ionic	2200-2300	B-H stretch	T_2	Strong, broad
	1050-1150	BH_2 deformation	T_2	Strong, broad

Table 4.3 Raman active fundamental vibrational frequencies typically observed for mononuclear $M(BH_4)_x$ configurations [31].

Bonding Mode	Approx. Freq. (cm^{-1})	Type of internal change	Symmetry Type	Comments
Monodentate	2300-2440	B-H_t stretch	A_1	Strong
	~2000	B-H_b stretch	A_1	Strong
	~1700 - 2000	M-H_b stretch	A_1	May be broad
	1000-1150	BH_3 deformation	A_1	Strong
Bidentate	2400-2600	B-H_t stretch	A_1	Strong singlet, possible shoulder
	1650-2150	B-H_b stretch	A_1	Medium-strong band
	1300-1500	bridge stretch	A_1	Strong broad
	1100-1200	BH_2 deformation	A_1, B_2	Medium-strong, possible doublet
Tridentate	2450-2600	B-H_t stretch	A_1	Strong singlet
	2100-2200	B-H_b stretch	A_1	Strong singlet, possible shoulder
	1150-1250	bridge stretch	A_1	Strong
Ionic	2200-2300	B-H stretch	A_1	Strong, broad
	1050-1150	BH_2 deformation	E	Weak

The two most important vibrations for diagnosis of the bonding configuration are those that involve the terminal hydrogen-boron stretch (vB-H_t) and the bridging hydrogen-boron stretch (vB-H_b). These vibrations are believed to be relatively 'pure' vibrations, in that they are unmasked by other low frequency modes. Infrared has been the most commonly used form of vibrational spectroscopy, with Table 4.2 setting out criteria for the assignment of vibrations depending on the structure of the BH_4 ligand. Raman

spectroscopy has developed significantly over the past few decades, with the development of types of Raman microscopy that allow samples to be measured without degradation or significant fluorescence. It has been shown that the most intense vibrations are found for the totally symmetric modes: the Raman criteria are set out in

Table 4.3.

4.2.1 Monodentate

The structure should exhibit A_1 and E B-H_t transitions around 2300-2450 cm^{-1}, and a single B-H_b transition around 2000 cm^{-1} [31]. Prediction of the metal hydrogen bond is difficult. It has been suggested that the vibration would occur in the region of 1600 cm^{-1} [31], however, this would be a broad peak, and at room temperature this vibration may be so broad that it is not observed. Monodentate borohydrides should also exhibit a two A_1 and one E transition due to the deformation modes of BH_3, with the E transitions being weak. These would occur with a frequency between 1000 and 1150 cm^{-1} [31].

4.2.2 Bidentate

Bidentate configuration is the most common configuration of covalent bonding between the borohydride ligand and the metal centre. The two strong B-H_t stretches, symmetric A_1 and asymmetric B_1 are observed in the region 2400-2600 cm^{-1}. Also, analogous A_1 and B_2 B-H_b stretches are predicted around 1650-2150 cm^{-1}. A broad band associated with the bridge expansion and M-H_b stretch is typically observed around 1300-1500 cm^{-1}, and a band due the

deformation of the BH_2 is observed at 1050-1150 cm^{-1}. The principal difference between mono- and bidentate spectra occurs in the B-H_b region and the B-H deformation region [31].

4.2.3 Tridentate

Tridentate infrared spectra are unique in most regions. The B-H_t stretch region has a single A_1 band at 2450-2600 cm^{-1}. The B-H_b modes A_1 and E typically appear as a doublet at 2100-2200 cm^{-1}. The only other band of significant intensity is the bridge deformation at 1100-1200 cm^{-1}. Jensen experimentally measured and assigned the spectra for the tridentate compounds $Zr(BH_4)_4$ and $Hf(BH_4)_4$ [113, 115].

4.2.4 Ionic

Ionic borohydrides should only exhibit two bands in the infrared spectrum, a T_2 B-H stretch between 2260 and 2300 cm^{-1} and a T_2 BH_2 deformation between 1050 and 1150 cm^{-1}. When the BH_4 group has symmetry lower than T_d, broadening or splitting of these bands may occur. When considering ionic borohydrides, $LiBH_4$ is a good example, with Raman spectra expected to contain 36 single modes in the orthorhombic *Pnma* structure [52, 55]:

$$\Gamma = 11A_g + 7B_{1g} + 11B_{2g} + 7B_{3g} \tag{4.4}$$

Eighteen of these are external vibrations where the $[BH_4]^-$ tetrahedrons move relative to the Li^+ species, and 18 are internal vibrations due to bending and stretching of the BH_4 tetrahedrons [55, 57]. In 1971 Harvey and McQuaker observed 6 lines, 5 internal and 1 external [162]. Further work by Gomes et al. [55] showed 13 of the single modes and 4

combined modes. The first principal density functional theory (DFT) calculations were performed by Miwa et al. [163] in 2004 indicating the theoretical positions of the bands. In 2008 Racu et al. [57] reported the position of 27 single modes through the use of high resolution Raman at 4 K, observing 22 in $LiBH_4$ and 25 in $LiBD_4$.

4.3 Decomposition Products

Many borohydrides go through a liquid phase where the hydrogen is evolved and the decomposition products are precipitated, giving rise to large volume changes in the sample. Due to the nature of the decomposition, the products are often amorphous and unable to be determined by diffraction studies. In-situ NMR is being used more extensively for investigating potential hydrogen storage materials since specialised reactors may be used that can control both temperature and pressure to evaluate complex hydrides and their decomposition mechanism [88, 164, 165]. Using Raman microscopy coupled to a variable temperature cell, it is possible to perform in-situ measurements rapidly enough to observe short-lived intermediates, and the decomposition route.

There have been many decomposition paths suggested for metal borohydrides, often put forward on the basis of XRD studies of the decomposed products. Many involve the evolution of hydrogen to leave boron, (4.5) and (4.7), or a metal boride (4.6)

$$M(BH_4)_x \rightarrow M + xB + 2xH_2 \text{ (or } (2x\text{-}z)\ H_2 + zB_2H_6) \quad (4.5)$$

$$M(BH_4)_x \rightarrow MB_x + 2xH_2 \text{ (or } (2x\text{-}z)\ H_2 + zB_2H_6) \quad (4.6)$$

$$M(BH_4)_x \rightarrow MH_x + xB + 3x/2H_2 \text{ (or } (2x\text{-}z)\ H_2 + zB_2H_6) \quad (4.7)$$

Ravnsbaek et al. showed the formation of $NaZn_2(BH_4)_5$ and $NaZn(BH_4)_3$ through ball milling zinc chloride with alkali metal borohydride [166]. The predicted decomposition is shown in reaction (4.8) where A = Alkali metal, M = metal and E = halogen. It is also conceivable that the decomposition of an $AM_w(BH_4)_x$ compound can yield similar products to those shown in reactions (4.5) to (4.7).

$$2AM_w(BH_4)_x + A_yZnE_z \rightarrow aM + bME + cB_2H_6 + dH_2 \quad (4.8)$$

Many of these products are classed as 'Raman active', especially the boron-containing compounds and hence are ideally suited for investigation using Raman microscopy.

The work presented here focuses on zinc, magnesium, calcium and lithium borohydrides and combinations with magnesium hydride. It is therefore logical to concentrate on the vibrational spectra of likely intermediates or decomposition products for these borohydrides.

Calcium hexaboride, CaB_6, was shown to be a decomposition product of calcium borohydride by Kim et al [167]. Like with many other metal hexaborides, CaB_6 has a cubic P*m3m* structure where the Ca and the B_6 form a lattice analogous to that of CsCl as shown in Figure 4.4 [168-170].

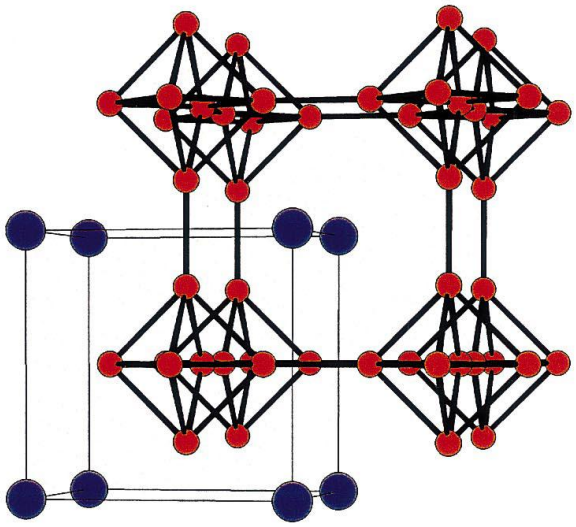

Figure 4.4 Section of the crystal structure of calcium hexaboride [168].

The P*m3m* symmetry gives 7 vibrational modes and one acoustic phonon T_{1u} [170],

$$\Gamma = A_{1g} + E_g + T_{1g} + T_{2g} + 2T_{1u} + T_{2u} \quad (4.6)$$

where the A_g, E_g and the T_{2g} modes are Raman active, the two T_{1u} modes are IR active and the T_{1g} and T_{2u} are silent modes. Shang, Wang and Liu summarised the energies of these vibrational modes [171].

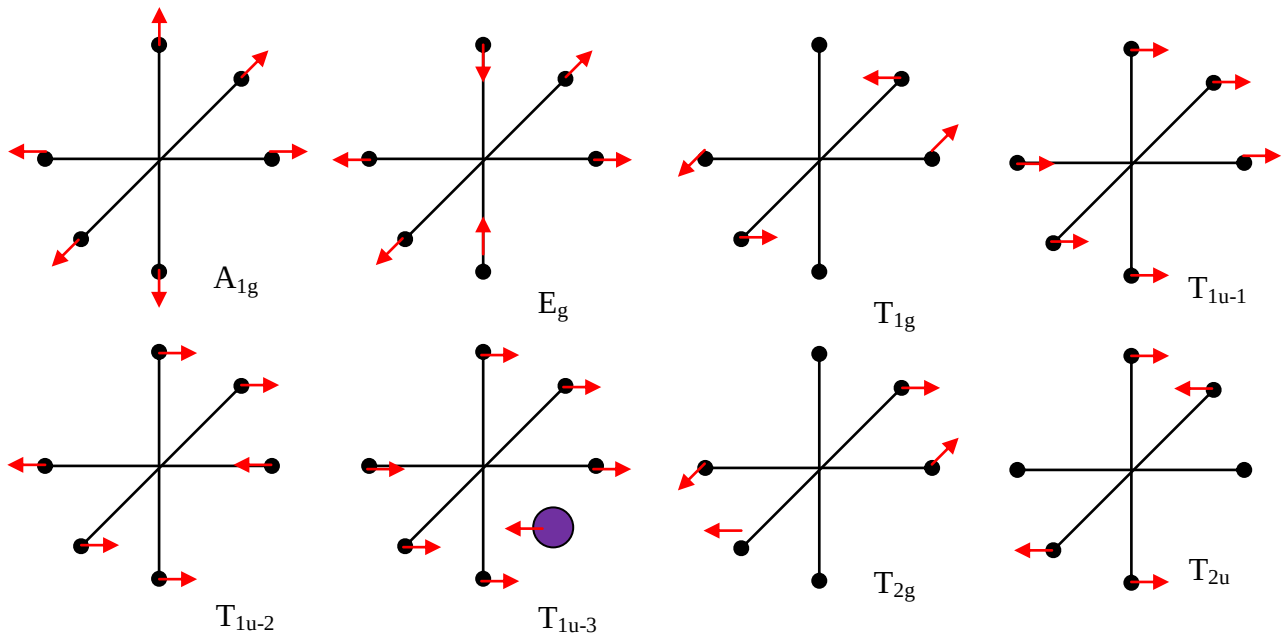

Figure 4.5 Atomic displacement of the phonon modes of CaB_6 [170].

Table 4.4 Vibrational frequencies for CaB_6 (cm^{-1}).

	A_{1g}	**E_g**	**T_{1u}**	**T_{2g}**	**T_{1g}**	**T_{2u}**	**T_{1u}**
	Raman	Raman	IR	Raman			IR
Shang et. al.[171]	1268.9	1136.1	876.9	778.2	591.4	463.7	118.7
Ogita et al.[172]	1287.2	1153.5		782.4			

Magnesium diboride, MgB_2, is a decomposition product of both magnesium borohydride and 'destabilised' mixtures using magnesium hydride. Magnesium diboride has a P6/mmm crystal structure where the boron atoms form graphene-like sheets with magnesium atoms between the layers, as shown in Figure 4.6.

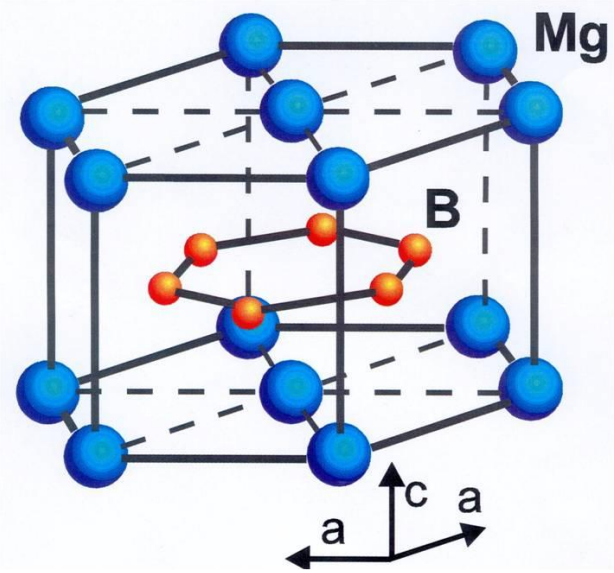

Figure 4.6 Unit cell of MgB_2 [173].

There are 6 phonon vibrational modes:

$$\Gamma = B_{1g} + E_{2g} + 2A_{2u} + 2E_{1u} \tag{4.7}$$

The E_{2g} mode is the only Raman active mode, where the boron atoms are displaced in the plane occurring with a Raman shift around 600 cm^{-1}. The IR active A_{2u} and E_{1u} modes are due to movement of the planes of boron atoms and magnesium atoms, with the A_{2g} mode due to the planes moving against each other, and the E_{1u} mode due to the planes sliding along the xy plane. Bohnen et al. [174] predicted the frequencies of the phonon modes, shown in Table 4.5.

Table 4.5 Calculated Γ-point phonon frequencies for I – experimental geometry, II – optimised geometry [174].

	I	II
$\mathbf{E_{1u}}$	322	327
$\mathbf{A_{2u}}$	394	405
$\mathbf{E_{2g}}$	536	571
$\mathbf{B_{1g}}$	696	702

4.3.1 Boranes

Boranes are a class of chemicals based on boron hydrogen (BH) units. As the BH units are electron deficient, they form clusters and cages. Diborane is the simplest borane. As more BH units are added, clusters are formed, which are polyhedral with BH units at their vertices.

The dodecaborane ion, $[B_{12}H_{12}]^{-2}$, with the metal acting as the counter ion has recently been observed as an intermediate in the thermal decomposition of alkali metal borohydrides, principally lithium borohydride, and is believed to be present in many other metal borohydrides [60].

A large number of borane species may be being formed. The most important is the $[B_{12}H_{12}]^{2-}$ as it is thermodynamically more stable than other closo-boranes. The Raman and IR spectra of isolated $[B_{12}H_{12}]^{2-}$ have been recorded and interpreted previously by Muetterties et al. [175], showing that there are B-H stretches associated with the equatorial breathing mode at 2470 cm^{-1} with a shoulder due to the apical mode. There are also cage deformation modes

between 1015 and 1070 cm^{-1}. There are 3 IR active modes of $[B_{12}H_{12}]^{2-}$ at 2488, 1070 and 720 cm^{-1}, and 6 Raman modes of A_g at 2518, 743 cm^{-1} and of H_g at 2470, 949, 770 and 584 cm^{-1}.

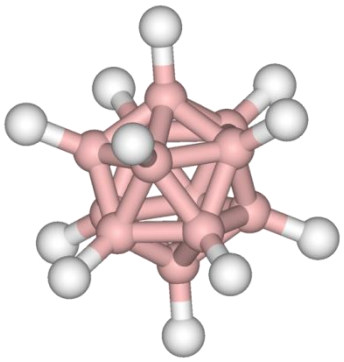

Figure 4.7 An illustration of the $[B_{12}H_{12}]^{2-}$ anion, pink – B and white - H [176].

The phonon densities of state (PDOS) of $Li_2B_{12}H_{12}$ were predicted using DFT by Ohba et. al. [59] and have been subsequently confirmed by Orimo et al. [60] experimentally. The spectra predicted show good correlation with the Raman spectra reported by Muetterties [175].

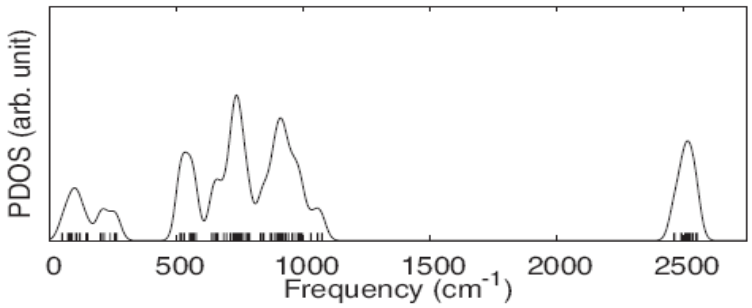

Figure 4.8 Predicted peak position using DFT for $Li_2B_{12}H_{12}$ by Li et al. [59].

Li et al. also predicted the PDOS for free $[B_{12}H_{12}]^{2-}$ as shown in Figure 4.9, which shows the predicted vibrational modes for $Li_2B_{12}H_{12}$. The $B_{12}H_{12}$ cage itself is largely unaffected by the cation.

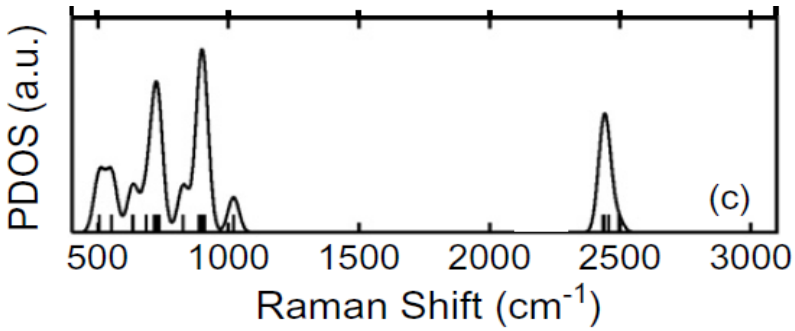

Figure 4.9 Theoretically calculated PDOS for $B_{12}H_{12}$ as calculated by Li et al [177].

Li et al. predicted that $MgB_{12}H_{12}$ would be present in the decomposition of magnesium borohydride, and using DFT they predicted the phonon density of states for monoclinic $MgB_{12}H_{12}$ as shown in Figure 4.10 [178]. The most obvious difference between the predicted vibrations for $Li_2B_{12}H_{12}$ and $MgB_{12}H_{12}$ is the splitting of the B-H stretch at around 2500 cm^{-1}. The $MgB_{12}H_{12}$ peak has been split into two peaks symmetrically spaced around 2600 cm^{-1}. Other work by Li et. al. predicted PDOS for $MgB_{12}H_{12}$ where the $B_{12}H_{12}$ units were not affected by the magnesium cations, as shown in Figure 4.9 [177]. The difference between the predicted spectra is due to the different crystal structures predicted for $MgB_{12}H_{12}$. Literature on $[B_{12}H_{12}]^{2-}$ suggests that transition metal dodecaborane compounds do not affect the hydrogen breathing modes, though the cage deformation modes of silver, cuprous and mercuric salts are weakened [159]. It is therefore more likely that the Raman spectra of $MgB_{12}H_{12}$ will look like Figure 4.9 rather than Figure 4.10. The main difference between $[B_{12}H_{12}]^{2-}$ compounds is likely to be within the lattice vibration region below 400 cm^{-1}.

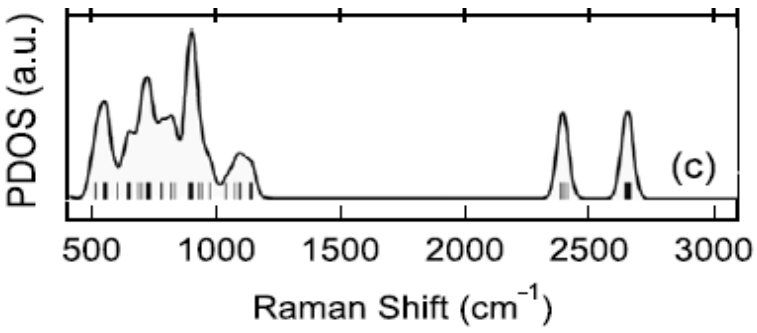

Figure 4.10 Theoretically calculated PDOS for $MgB_{12}H_{12}$ as calculated by Li et al [178].

Raman shifts are available for closo-boranes where n = 6, 9, 10 and 12. There are vibrational modes split into two areas: around 2400-2550 cm^{-1} for the B-H stretches, and 1000-1100 cm^{-1} for the cage deformation. This should make it possible to distinguish between the different closo-boranes.

5 EXPERIMENTAL

The experimental programme was split in-to five areas:

- Synthesis of the borohydride through mechanical milling,
- Structural and compositional characterisation of the milled borohydride,
- Study of the thermal decomposition of the borohydride,
- Study of the reaction products from decomposition and recombination and in-situ monitoring throughout the reaction and
- Recombination and cycling of the decomposed borohydride.

The flow diagram in Figure 5.1 illustrates the five main experimental areas and the characterisation techniques employed in each.

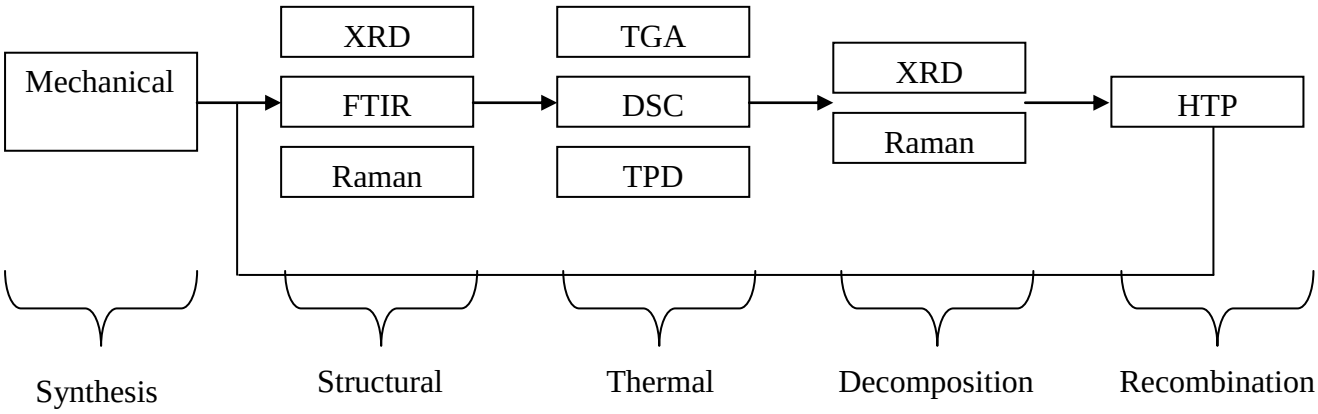

Figure 5.1 Flow diagram of experimental techniques used.

The following section examines each of the above aspects and describes the equipment and techniques used.

Metal borohydrides were synthesised using the metathesis reaction whereby an alkali borohydride was reacted with a metal chloride by mechanical milling as described in section 5.1 and by equation (5.1).

$$xABH_4 + MCl_x \rightarrow M(BH_4)_x + xACl \quad (5.1)$$

This project used mechanical milling to achieve this reaction due to its ability to form a small particle size and the potential to change the stoichiometry. As well as synthesis of the borohydride, reactive additives were added to the milling vessel prior to milling in an attempt to alter the decomposition characteristics of the synthesised material. All milled material contains the by-product NaCl. This was not removed as solvent extraction is a difficult process due to the solvent molecules binding to the metal centre, which could affect the characteristics of the material.

The milled material was then characterised by XRD, Raman and IR to establish whether any reaction had taken place, which (if any) products were formed and their structures. The reagent and alkali metal chloride, typically NaCl, have very clearly defined XRD patterns. The variations in the $[BH_4]^-$ vibrations were observed by Raman and IR spectroscopy to determine changes in bonding from the ionic alkali metal borohydrides to covalent transition metal borohydriedes or ionic alkaline metal borohydrides.

The hydrogen storage properties of the milled products were analysed: the main parameters determined were the decomposition temperature and the amount of hydrogen (and other gases) released during thermal decomposition. The quantity of gases released was determined using thermogravimetric analysis (TGA). This was also connected to a mass spectrometer (MS) to identify any gas species evolved during decomposition.

To better understand the mechanisms of decomposition, calorimetric measurements were used to identify phase changes, the number of steps involved in decomposition and the corresponding change in enthalpy. To understand the mechanism of decomposition further, in-situ XRD and Raman measurements were used to identify intermediate phases and decomposition products.

Finally the reversibility of the system was evaluated following thermal decomposition. Rehydriding was attempted using a volumetric Sieverts system, measuring uptake of hydrogen as a function of pressure. This type of measurement allows hydrogen uptake to be determined for materials that have slow kinetics during recombination and/ or only absorb a small amount of gas.

5.1 Material Synthesis

Optimised conditions for the synthesis of metal borohydrides by mechanical milling was previously investigated by Matthews [136]. These conditions were used for this work. Sodium or lithium borohydride was milled with the metal chloride using a Retzch PM400 planetary mill rotating at 175 rpm. 6.1 g of powder was loaded into a 250 ml stainless steel

milling pot with 12 mm stainless steel balls (ball to powder ratio 67:1) under an argon atmosphere.

The starting materials consisting of sodium borohydride ($NaBH_4$, 99.995%), sodium boroduteride ($NaBD_4$, >95%), calcium chloride ($CaCl_2$, anhydrous 99.999%) and magnesium chloride ($MgCl_2$, anhydrous 99.999%) were all purchased from Sigma-Aldrich. Anhydrous zinc chloride ($ZnCl_2$) (98%) was purchased from Alfa Aesar. All materials were stored and handled in an argon-filled glovebox (>100 ppm O_2).

Additions were added in an attempt to alter the decomposition path, with the aim of reducing or suppressing the release of diborane and reducing the decomposition temperature and aiding reversibility. The additives included nano-sized nickel (activated powder, 99.9+% stored in hexanes from Sigma-Aldrich), titanium (activated powder 99.9+% stored in mineral oil from Sigma-Aldrich), titanium (III) chloride ($TiCl_3$) (99.9%) and magnesium hydride (MgH_2) (95% from, Goldschmidt). They were added prior to milling, maintaining a total charge mass of 6.1 g.

5.2 Material Characterisation

Characterisation of the as-milled, thermally decomposed and the ex-situ and in-situ intermediates was performed using a combination of x-ray diffraction (XRD), vibrational spectroscopy (infrared and Raman) and scanning electron microscopy (SEM).

XRD has the advantage of a large database of patterns that have been indexed for cross-reference and that it is a good technique for examining crystalline solids. However, amorphous solids and liquids are unable to be characterised using XRD. In addition, if there

is any variation in height of the sample during an in-situ measurement this will also affect the accuracy of the results.

Infrared spectroscopy is very good at room temperature measurements, giving information on the bulk material whereas Raman microscopy is good for variable temperature measurements.

SEM can be used to give information about particle size and morphology. However, as borohydrides are very good reducing reagents, reactions with mounting materials tend to occur making studies difficult on the as-milled material.

5.2.1 X-ray Diffraction

X-ray diffraction occurs when parallel monochromatic beams of x-rays interact with an ordered solid. Figure 5.2 shows a series of lattice points arranged in three planes with an inter-planar distance, d.

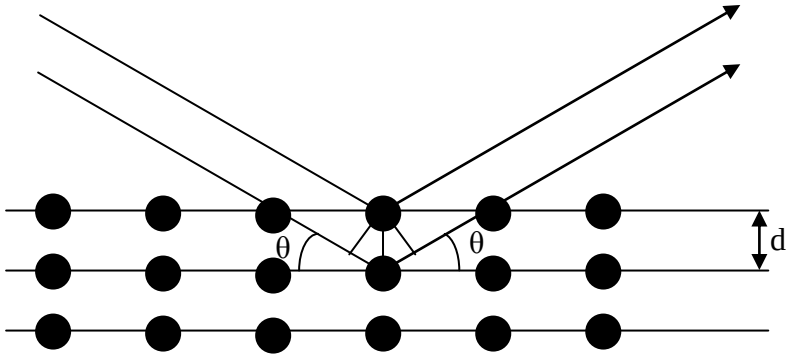

Figure 5.2 Diffraction of x-rays by a crystal.

For diffraction to occur, two parallel beams need to exhibit a difference in path length equal to a multiple of the wavelength for constructive interference to occur. For diffraction to occur the following conditions set out by the Bragg equation (5.2) must be satisfied:

$$n\lambda = 2d\ sin\theta \tag{5.2}$$

where *n* is an integer, λ is the wavelength of the incident radiation, θ is the angle between the incident radiation and the planes of the lattice and d is the planar spacing.

All samples analysed by XRD were in powdered form. In this work it is assumed that samples are composed of an infinite number of particles/ crystallites orientated in an infinite number of orientations. This arrangement means that all the crystal planes are orientated so that diffraction occurs across all available crystallographic planes. Diffraction is measured by moving the source and detector through a range of angles to detect the pattern by varying x-ray intensity on a detector. The diffractometer produces a pattern where the intensity of the diffracted radiation is related to the angle 2θ.

The resultant diffraction pattern generated is characteristic of the material; this then allows analysis of the phases and materials present in a qualitative manner. Refinement of the XRD patterns to allow quantitative phase analysis was performed using Topas 3.0 (Academic) supplied by Bruker AXS, using jEdit to create the input (.inp) files. A Pawley refinement was used for this thesis relating the diffraction intensities to determine the relative contribution of different phases in the sample.

Macros for use in jEdit were obtained through a Durham University website managed by Prof. John Evans [179], and by Mr P. Chater. Crystallographic information files (.cif) files were obtained through the chemical crystal database (http://cds.dl.ac.uk/) operated by STFC Daresbury.

A Bruker D8 advance spectrometer using either CuK_{α} radiation with a Geöbel mirror or $CuK_{\alpha 1}$ radiation with a two bounce germanium monochromator was used during the course of this work. Detection of the diffracted x-rays was performed using a Vantec position sensitive detector (PSD) allowing the simultaneous collection of 6° 2θ data. Inert sample loading was performed in an argon glovebox using a Kapton dome-shaped, vacuum-tight sample holder preventing contact with air during the XRD measurement.

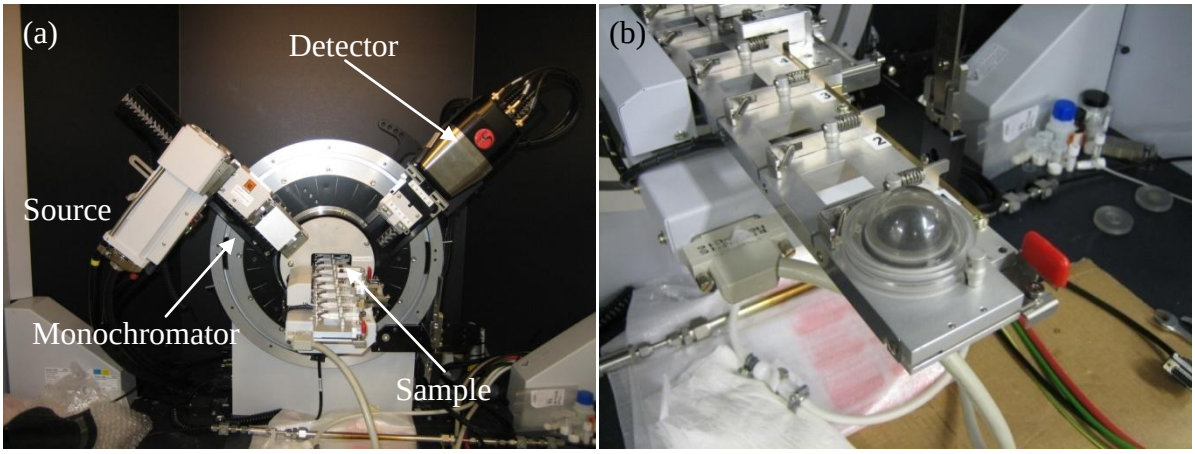

Figure 5.3 a) Bruker D8 advanced XRD with 9 position multi-changer and monochromator and b) the inert sampler holder.

In-situ XRD characterisation was performed using an Anton Paar XRK900 cell under flowing helium. The cell was loaded in the glove-box to prevent contact with air. In-situ measurements were performed by heating the sample at 0.2 K/s to the set temperature where

a diffraction pattern was collected isothermally before heating to the next temperature set point. Flowing helium was used at a flow rate of 100 ml/min and at a pressure of 1.5 barg.

5.2.2 Vibrational Spectroscopy

5.2.2.1 Infrared spectroscopy

Attenuated total reflectance (ATR) was used during this work. ATR works on the principle that if the angle of incidence of a beam of radiation is greater than that of the critical angle at the interface of two materials then total internal reflectance occurs. The use of ATR in infrared spectroscopy is based on the fact that although total internal reflectance occurs at the interface, there is some penetration into the material, setting up an evanescent wave which is partially absorbed by the material according to the chemical bonding. Figure 5.4 shows a schematic of the single bounce ATR as used in this work.

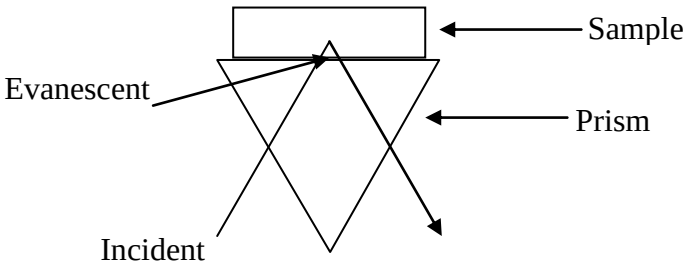

Figure 5.4 Schematic of single bounce ATR.

Infra-red spectroscopy was carried out using a Thermo Nicolet 8600 Fourier transform Infra-Red (FTIR) spectrometer fitted with a Specac 'Golden Gate' ATR attachment allowing the inert loading of samples within a glove-box. Prior to the measurement the system was purged with dry oxygen free nitrogen to reduce the background signals from water and carbon dioxide. Each spectrum was a result of 100 scans at a resolution of 4 cm^{-1}.

5.2.2.2 Raman spectroscopy

Raman spectroscopy has a number of advantages over other techniques for following reactions, as it is possible to observe and measure small samples, and be able to detect discrete phases within a sample. In addition, fluorescence from the sample can be minimised as only the portion of the sample that is in focus is irradiated with a high power laser. High quality visible lasers and optics help boost the quality of the spectrometer. Figure 5.5 shows the configuration used in this work, which is typical of spectrometers of this type. The laser is focused onto the sample and the emitted light is then channelled back through the objective where a holographic notch filter removes all photons with a shift of $\pm 100 cm^{-1}$ along the laser line, removing the Rayleigh scattering. The remaining photons are then focused through a series of lenses and slits prior to being separated using a grating before detection using a charge coupled device (CCD).

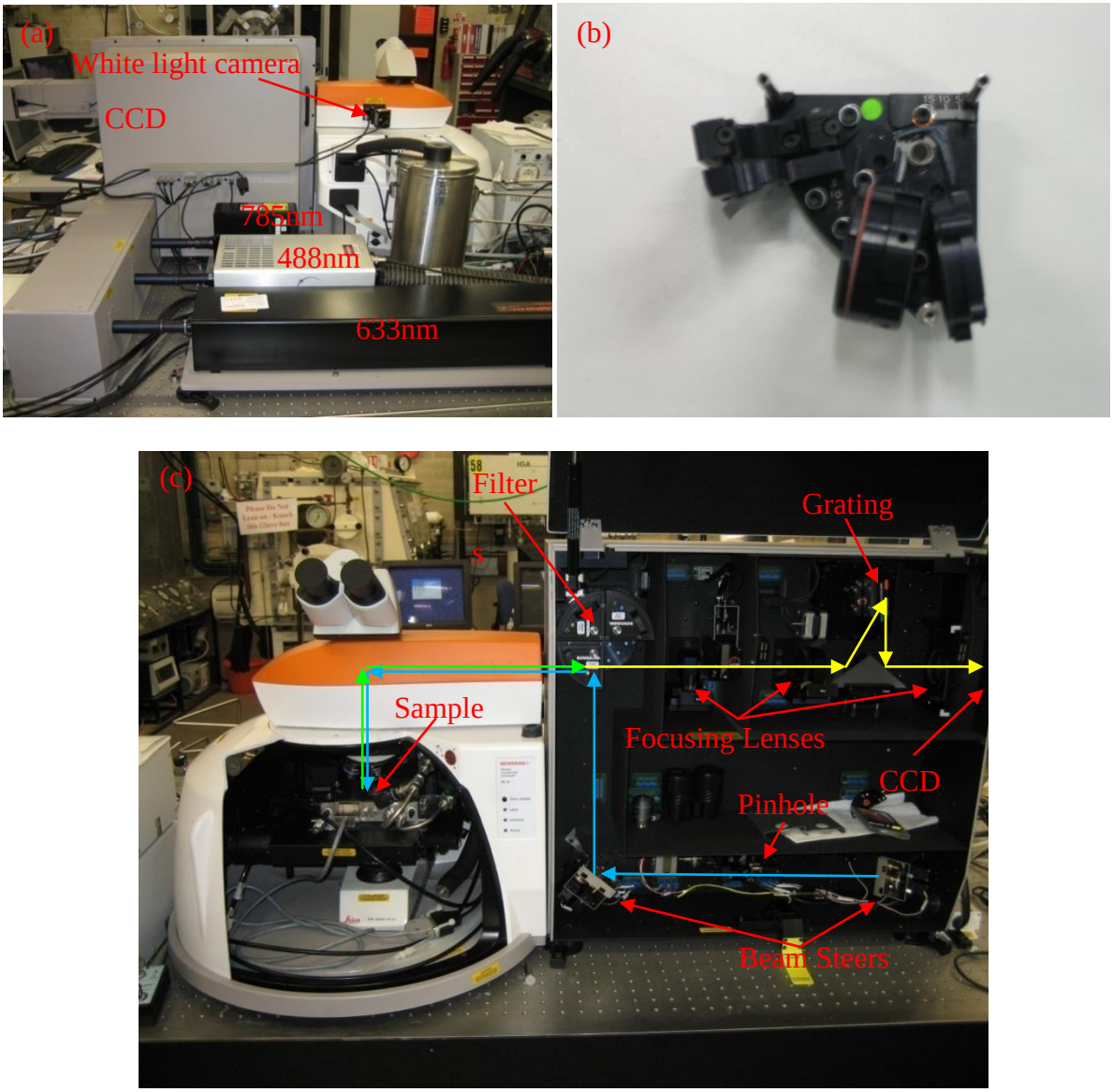

Figure 5.5 (a) The location of the three excitation lasers, 633 nm, 488 nm and the 785 nm also shown is CCD and the white light camera. b) The Rayleigh rejection notch filter. c) The path of the incident laser (blue) the scattered photons Stokes, anti-Stokes and Rayleigh (green) and the filtered Stokes and anti-Stokes photons (yellow).

Raman microscopy was performed using a Renishaw InVia reflex, using both 488nm and 633nm excitation coupled to a grating consisting of 2400 and 1800 lines/mm, respectively,

with a power of ~2 mW on the sample. The system was initially aligned using an internal neon light source and calibrated on a daily basis using an internal silicon reference. The laser was directed concentrically through the objective and the silicon reference was used to calibrate the slit position on the CCD using a 520 cm^{-1} vibration.

Inert sample transfer and in-situ measurements were performed using an Instec HCS621V sample cell with a flow of 100 ml/min argon. Samples were heated using a ramp rate of 2°C/min to a set temperature where the spectra were taken. Constant heating and sampling was also performed whereby a heating rate was set at either 1 or 2°C/min and spectra were collected continually back to back and the focus on the sample was checked automatically by the software every 10 spectra. The spectra were collected by either keeping the grating static and measuring ±300 cm^{-1}, allowing rapid collection of the small regions of the spectra, or by moving the grating allowing the collection of the whole spectra.

5.2.2.3 Baseline correction

Some samples may exhibit Raman spectra with varying degrees of fluorescence when phases within the sample relax from the excited state via a different mechanism to Raman scattering. Providing that there is sufficient Raman signal 'on top' of the sloping background, the baseline may be subtracted to yield a spectrum with a flat baseline. Ideally, the measurement would be re-performed with an alternative excitation wavelength to minimise or remove the effects of fluorescence.

There are a number of baseline options available within the Renishaw Wire 3.1 software: linear, polynomial and cubic spline. The linear baseline is fitted using a $y = mx + c$ formula between the two end points of the spectrum, and is then subtracted from the obtained spectra as shown in Figure 5.6. However, as the response of the CCD is not linear with wavelength, and the fluorescence is not constant across the whole spectrum the linear baseline is a poor fit. Non-linear baselines based on a polynomial fit (e.g. $y = ax^2 + bx + c$) can be subtracted using a series of data points placed along the obtained spectra, as shown for when x^2 is used in Figure 5.7 and when x^6 is used in Figure 5.8. The best results, however, are obtained when a cubic spline interpolation method is used. Here a number of cubic equations are combined to give the best fit to the data points added along the collected spectrum as shown in Figure 5.9.

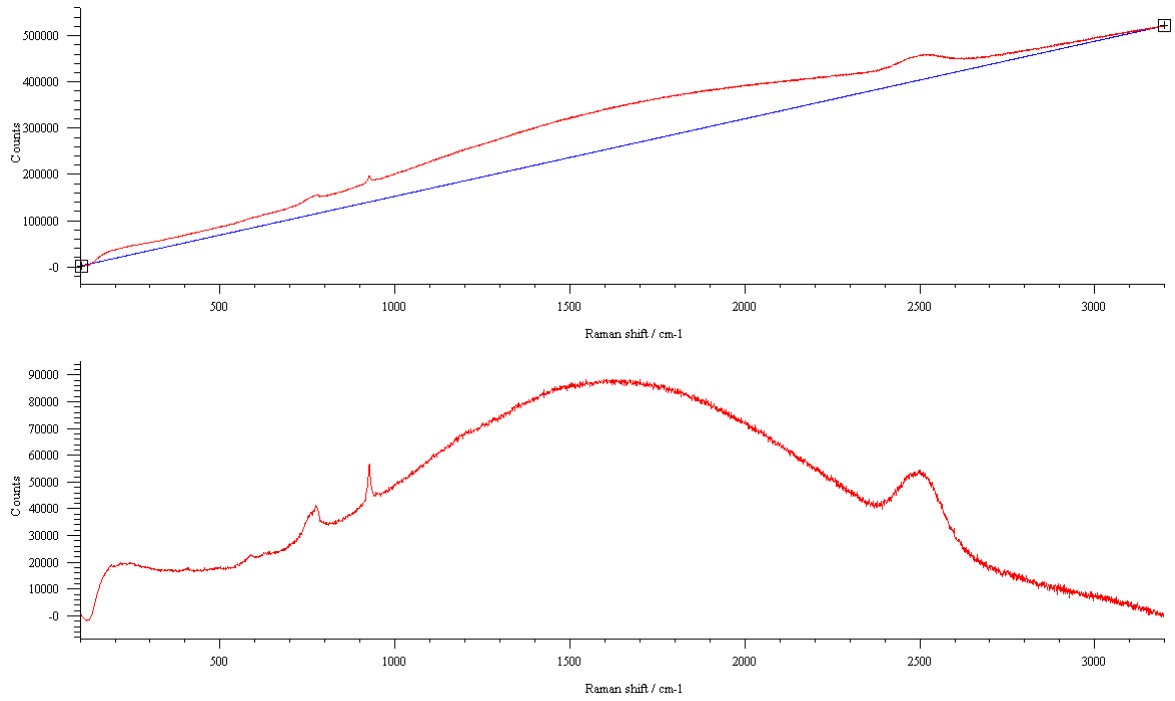

Figure 5.6 Subtraction of a linear baseline from a decomposed $LiBH_4$ sample cooled to room temperature.

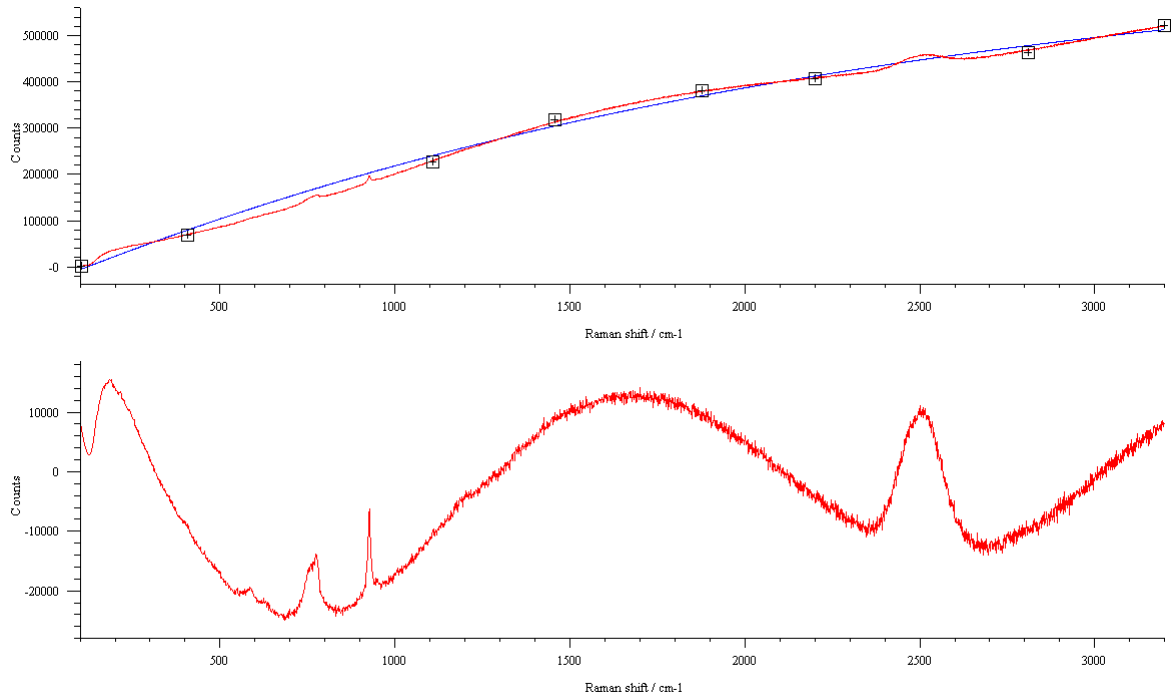

Figure 5.7 Subtraction of a polynomial (x^2) baseline from a decomposed $LiBH_4$ sample cooled to room temperature.

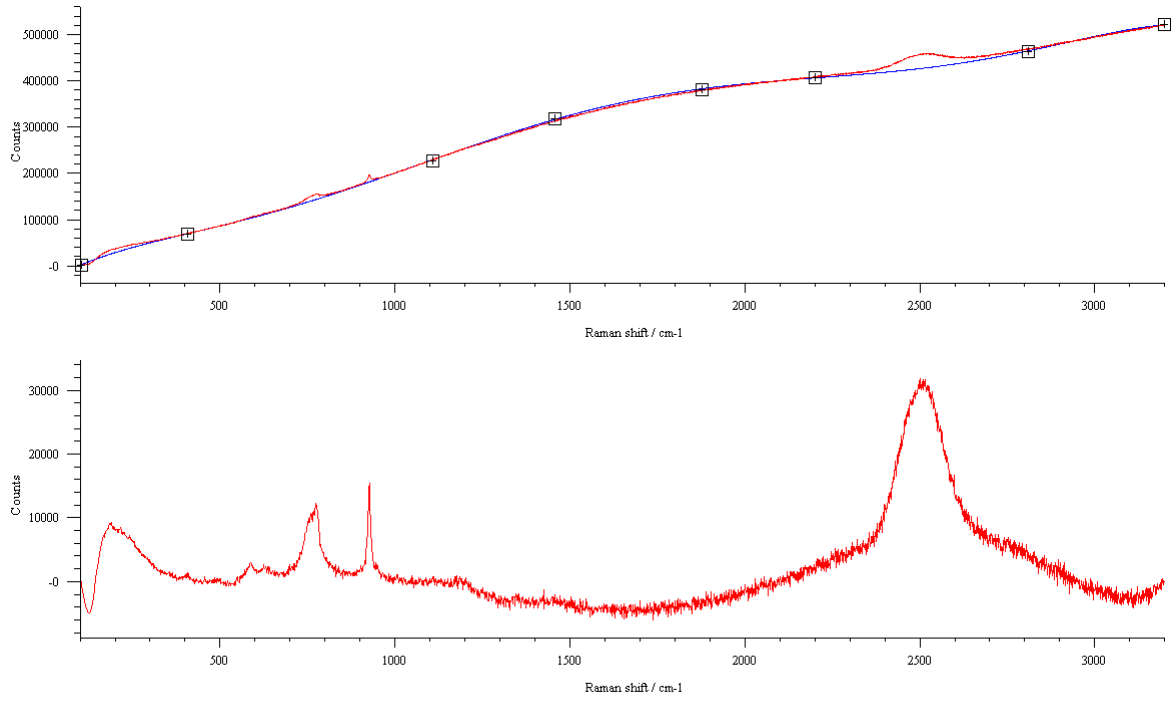

Figure 5.8 Subtraction of a polynomial (x^6) baseline from a decomposed $LiBH_4$ sample cooled to room temperature.

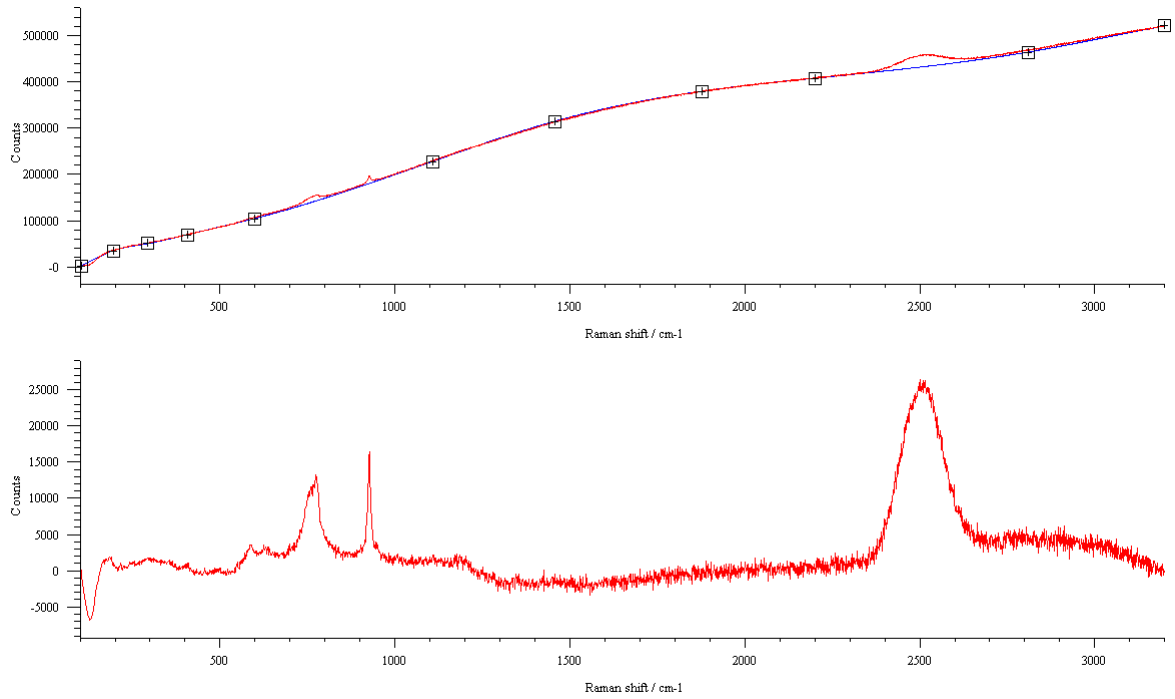

Figure 5.9 Subtraction of a cubic spline interpolation baseline from a decomposed $LiBH_4$ sample cooled to room temperature.

The judicious use of baseline subtraction of the Raman spectrum can allow easier determination and characterisation of the vibrational modes of a material whose spectrum contains a significant amount of background.

5.2.2.4 Curve Fitting

Parameters of bands can be determined from the raw data. Values of the band centre, the full width at half maximum (FWHM), intensity and area can be obtained through the use of the curve fit function within the Renishaw Wire 3.1 software. Curve fitting is possible for both single bands and overlapping bands where there may be two or more bands that overlap.

To begin curve fitting, a baseline is added to the spectrum to provide a datum for the curves. The appropriate number of curves are selected and located near to the peaks, as shown in Figure 5.10 where the four added curves are in green and the spectrum is shown in red. The combination of the baseline and curves is shown in blue.

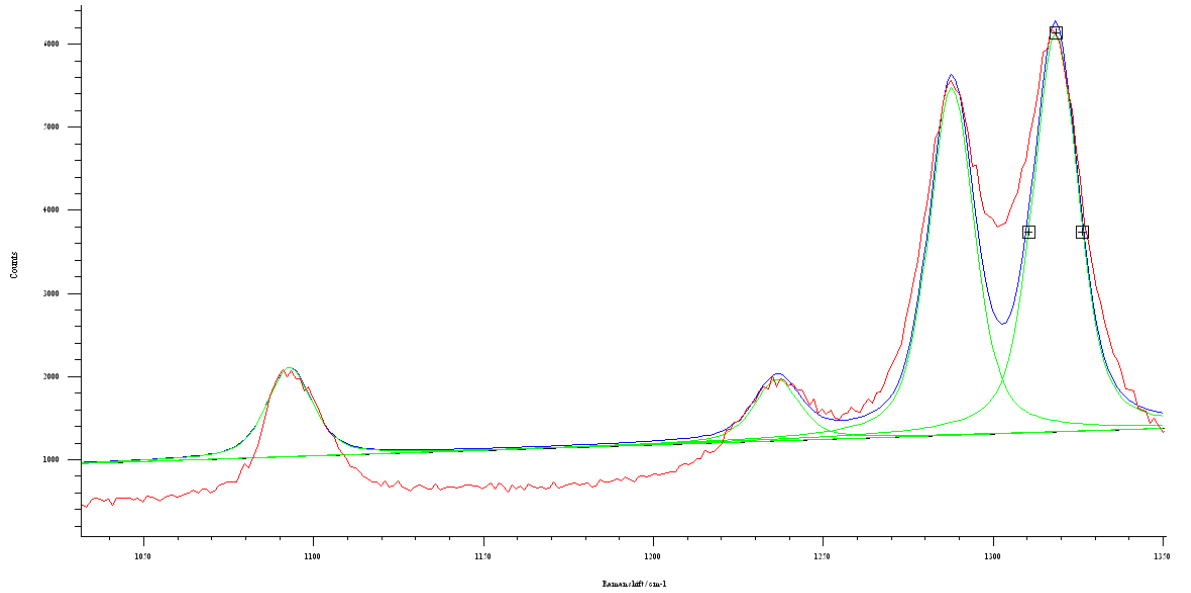

Curve Name	Centre	Width	Height	Area
Curve 1	1092.7	15.9666	1076.08	22638.8
Curve 2	1236.44	15.9666	743.223	15636
Curve 3	1287.93	15.9666	4195.97	88275.4
Curve 4	1318.58	15.9666	4816.93	101339

Figure 5.10 Unfitted curves on the Raman spectrum of $LiBH_4$ between 1030 and 1350 cm^{-1}. Red represents raw data, green individual curves, and blue is the combination of the curves and baseline.

Wire 3.1 then runs an algorithm to fit the curves using a combination of Gaussian and Lorentzian peak shapes until the change in chi squared is lower than 0.001, deemed to be a good fit. The data is then reviewed by comparing the (red) raw data and the (blue) fitted data.

For subsequent calculations using the peak width the FWHM is converted to a half width half maximum (HWHM) by dividing the FWHM by 2. This then allows the calculation of physical properties of the sample.

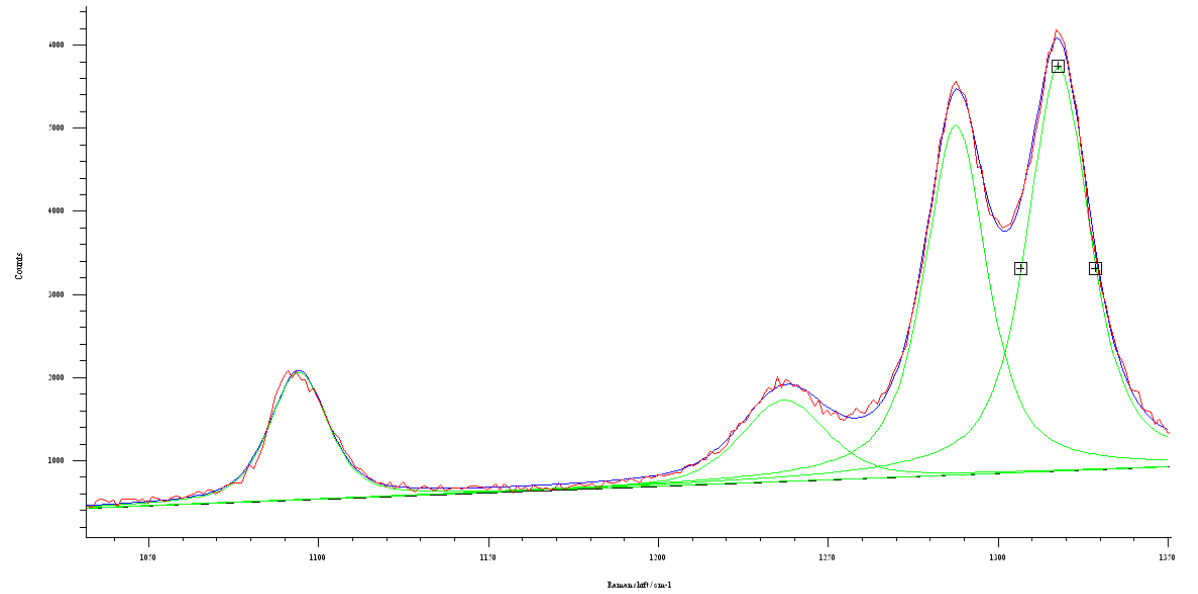

Curve Name	Centre	Width	Height	Area
Curve 1	1093.89	20.4237	1547.04	41785.3
Curve 2	1237	29.845	981.788	36770.7
Curve 3	1287.67	21.7731	4225.12	128931
Curve 4	1317.97	22.0329	4881.31	151639

Figure 5.11 Fitted spectra of $LiBH_4$ between 1030 and 1350 cm^{-1}. Red represents raw data, green individual curves, and blue is the combination of the curves and baseline.

5.2.3 Microscopy

Scanning electron microscopy was used to identify the morphology and topography of the decomposed samples, coupled to x-ray detection to provide an elemental composition of the different phases present. It was not possible in this work to investigate the milled material, as the borohydride reacted too vigorously with any mounting material (required for the SEM), and without inert loading the samples rapidly oxidised on contact with air.

During the SEM measurement the inner shell electrons are knocked out by incoming high-energy electrons. An outer electron then falls back into the vacancy left in the inner shell. In dropping to the lower energy the electron releases a photon with wavelength in the x-ray part of the electromagnetic spectrum. The energy of this photon is characteristic of the electronic structure of the atom. Figure 5.12 illustrates the different emissions.

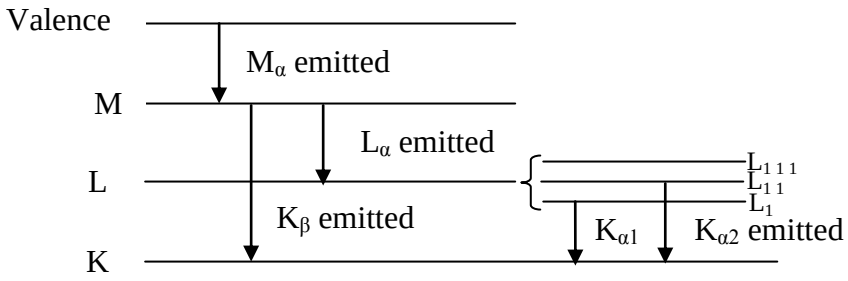

Figure 5.12 The energy levels and x-ray emission from atoms.

This phenomenon can be used in several ways. Firstly, the characteristic x-rays can be produced from one element such as copper and used for XRD. Secondly, it can be utilised to identify which elements are present in a sample, such as in energy dispersive x-ray (EDX) and wavelength dispersive x-ray (WDX) analysis. EDX uses a Si(Li) detector which produces an electric pulse proportional to the energy of the x-ray bombarding the detector. However, due to the need to protect the detector a beryllium window is present between the detector and sample. This means that light elements (lighter than sodium) cannot be detected using conventional EDX. The resultant spectrum gives peaks corresponding to the energy of the x-rays emitted; these peaks can then be used to identify which element is present, with the intensity giving a guide to the quantity present. WDX uses specific crystals of a known d-spacing to diffract the x-ray beam to provide a diffraction position, as per the Bragg equation

(5.2). Since mechanical movement of the crystals and detector are required, only one element can be analysed at once so knowledge of the elements present in the sample is required. As no windows are used, light elements can also be measured.

This work was performed using a JOEL 7000 SEM fitted with a field electron gun (FEG) allowing high-resolution imaging, coupled with INCA software providing analysis of EDX and WDX. The samples were mounted using an Epovac resin in an argon-filled glove-box, before grinding and polishing with diamond paste using dry alcohol as a lubricating fluid to prevent oxidation of the sample, and coated with carbon to allow conduction.

5.2.4 Thermal Decomposition

Thermal decomposition of milled products was monitored by two methods: differential scanning calorimetry (DSC) using a Netzsch DSC204HP with an argon flow rate of 100 ml/min at a pressure of 4 bar, and TGA using a Netzsch TG209 connected to a Hiden Analytical HAL IV quadropole mass spectrometer (MS), with an argon flow rate of 40 ml/min. A heating rate of 2°C/min was used for both TGA/MS and DSC. TGA used approximately 20 mg of sample loaded in an alumina (Al_2O_3) crucible, and approximately 5 mg of sample was used for DSC measurements, where both sample and reference crucibles were made of aluminium.

5.2.4.1 Differential Scanning Calorimetry

DSC is a technique that can measure the energy corresponding to a temperature difference between a substance and an inert reference material, as the two specimens are subjected to identical pressure and temperature regimes, where heating or cooling is at a controlled rate.

The Netzsch DSC204HP used for this work is known as a heat-flux DSC. In a heat-flux DSC the sample and reference are connected by a low-resistance heat flow path, such as a metal disc contained within a single furnace. Changes in enthalpy or heat capacity cause a temperature difference between the sample and reference. The difference between this and differential thermal analysis (DTA) is that the resulting heat flow is small due to the good thermal contact between sample and reference.

The measured temperature difference is related to enthalpy change within the sample through calibration. Calibration was performed using five metal standards (In, Bi, Sn, Pb and Zn) whose melting points are accurately defined, and spread within the temperature range of the equipment. This allows a calibration curve of the expected vs. measured onset temperature and work done (ΔQ), to calibrate the temperature and the response, respectively. A baseline was also performed using the exact conditions to be used during the measurement, to account for any background between empty sample and reference crucibles.

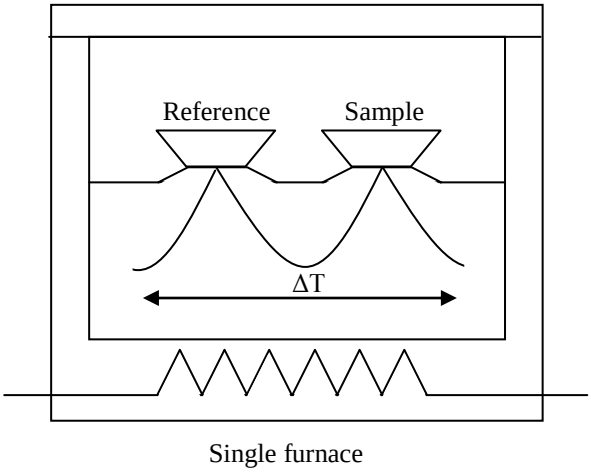

Figure 5.13 Schematic of a heat-flux DSC.

5.2.4.2 Thermogravimetric Analysis

TGA involves the measurement of the mass of a sample with changing temperature. Figure 5.14 shows a cross section schematic of the TGA used in this work. The sample is mounted onto a thermocouple within the furnace. Argon gas flows in through the sample gas port below the sample and exhausts above the sample are present to ensure any desorbed gases are carried to the mass spectrometer. The thermocouple is attached to a microbalance which records the weight of the sample.

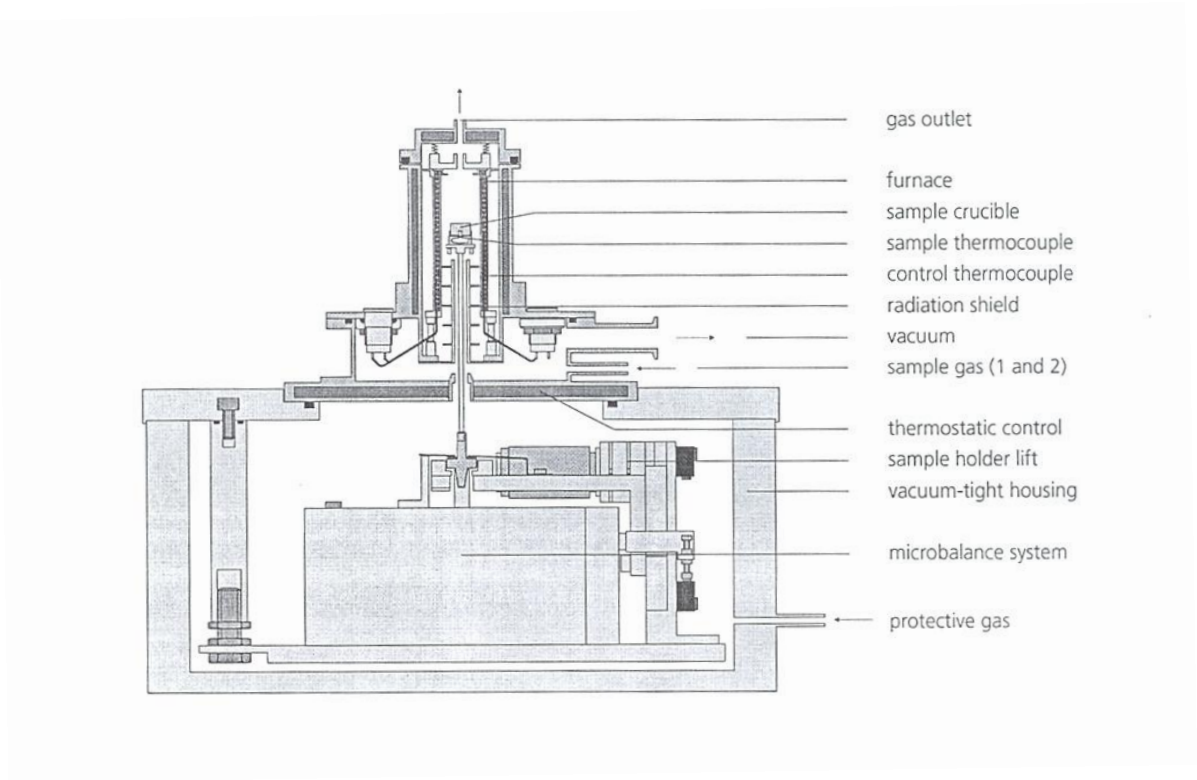

Figure 5.14 Schematic cross-section of Netzsch TG 209.

Calibration is performed using six metal standards (In, Bi, Sn, Zn, Al and Ag) whose melting points are accurately defined and spread within the temperature range of the equipment. A baseline is also performed using the exact conditions to be used during the measurement, using an empty crucible to account for any buoyancy effects upon heating. Calcium oxalate was also measured to check the temperature calibration and mass loss.

5.2.4.3 Mass Spectrometry

In its simplest form, the mass spectrometer (MS) is designed to perform five basic functions:

- Vaporise compounds,
- Ionise from the gas-phase molecules,

- Accelerate the ions to known speed,
- Separate the ions according to their mass-to-charge ratios (*m/z*) and
- Detect and record the number of ions for a given *m/z.*

In this work vaporisation was not necessary as the input is desorbed gas from the TGA. The gas is ionised using electron impact, where a heated filament is used to accelerate electrons to an anode causing ionisation of the gas molecules, and also fragmentation of larger molecules. The positively charged ions are then accelerated through a slit system to the ion analyser. Separation is performed using a quadrupole, where the arrangement of the electrodes in a quadrupole mass filter is shown in Figure 5.15. A constant voltage, U, and a radio-frequency potential, V, are applied between opposite pairs of four parallel rods. Ions are injected along the x direction. A mass spectrum is scanned by varying either the amplitude of U or V, whilst keeping the ratio U/V constant.

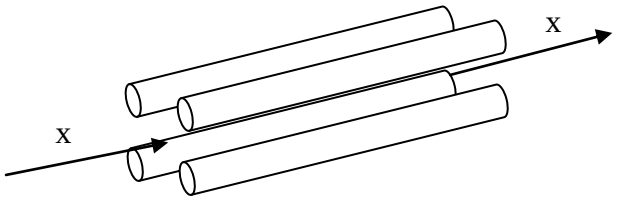

Figure 5.15 Arrangement of electrodes in a quadropole mass filter.

Detection is performed using either a Faraday cup (high concentrations) or a secondary electron multiplier (low concentrations).

By monitoring the concentration of specific ions, hydrogen (*m/z* =2), deuterium (*m/z* = 4) and diborane (*m/z* = 26) with time (and therefore temperature) it is possible to record the desorption temperature of different gases.

5.2.5 Recombination

Recombination was attempted using a Hiden Isochima HTPS-2 volumetric system. Figure 5.16 shows a schematic of the layout of the valves, pipe-work and mass flow controllers. For Sieverts-type measurement, two chambers of similar known volume are connected by a fast opening valve. A dosing volume of ~6 ml corresponding to the volume of the pipes between PCV1, 2, 3, 4 and 5 is used. The sample reactor has a volume of ~5 ml corresponding to the reactor and pipe work between PCV 4, 6 and 7. To allow accurate measurements of pressure and pressure drop, a number of considerations were taken into account. Firstly, the temperature of only a small amount of piping is not temperature-controlled, and secondly the emergency burst-disc chosen does not significantly deform with pressure.

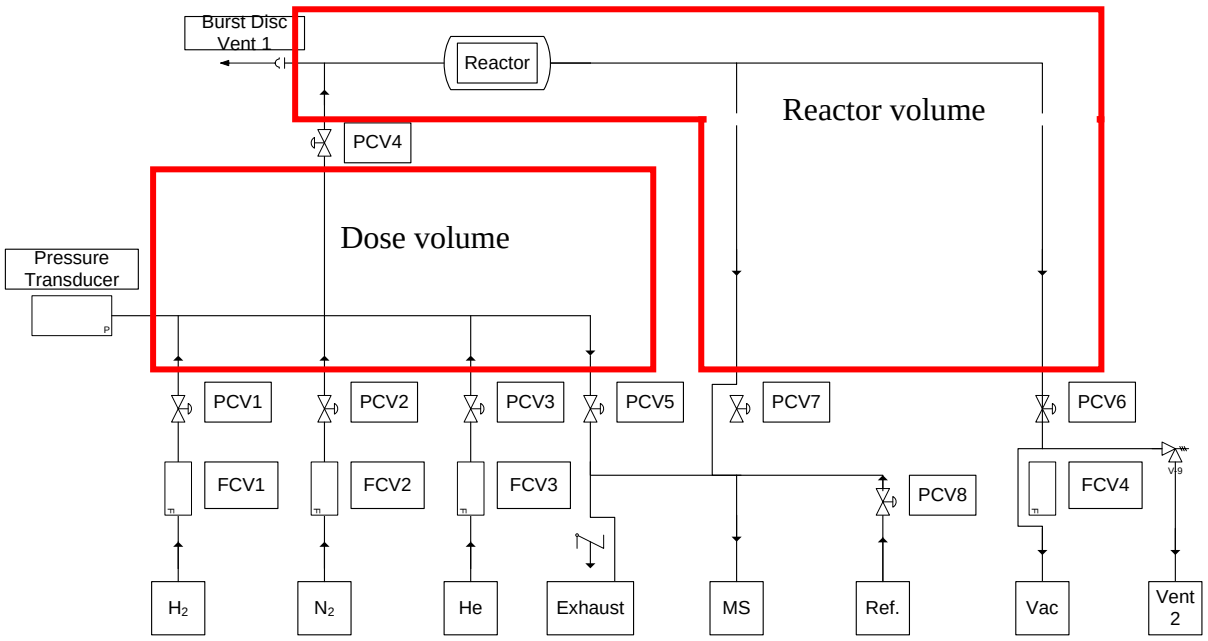

Figure 5.16 Schematic of the valves and pipe work on the Hiden Isochema HTPS-2.

The sample volume must be determined before any pressure composition temperature (PCT) measurements can be performed; this is done through helium densitometry. The system is evacuated to a pressure of $5x10^{-6}$ mbar. 5000 mbar of helium is then introduced into the dosing chamber, and an accurate pressure is measured. Gas is then allowed to flow into the sample chamber, the pressure is allowed to equilibrate for 2 minutes, and then another pressure measurement is taken of only the dose volume to calculate the pressure drop. This process is then repeated four more times and the average pressure drop is then taken, which, when compared to the same procedure without sample, allows the calculation of the sample volume.

Absorption measurements can be conducted by either PCT isotherms, or by setting a single pressure point and monitoring any pressure drop. PCT isotherms are performed by measuring the uptake of gas at several pressure steps, at a single temperature. Gas is

introduced through the dosing volume and once the desired pressure is reached it is recorded and the gas is allowed to flow into the sample chamber. Once equilibrium (or the time out) is reached, the pressure is measured, and any pressure change monitored and converted into uptake, before the next pressure is measured.

Decomposition can be measured in two ways; firstly as a PCT isotherm and secondly through temperature programmed desorption (TPD) into a mass spectrometer. The PCT isotherm is the opposite of the adsorption isotherm, where the pressure is reduced in the dosing volume. In TPD mode the sample will be heated from room temperature to above the decomposition temperature at a heating rate of 5 K/min. Helium flows at a flow rate of 100 ml/min over the sample allowing any desorbed gas to be carried through to the MS. The hydrogen response from the MS is then calibrated using the mass flow controllers to produce a series of compositional mixtures of hydrogen in helium.

Volumetric systems like this require a leak-free system, as any pressure drop is attributed to sorption by the sample.

6 RESULTS AND DISCUSSION: ZINC BOROHYDRIDE

With a theoretical maximum hydrogen capacity of 8.48 wt.% and a reported decomposition temperature below 100°C, zinc borohydride is seen as a potential hydrogen storage material [16]. There are, however, concerns about the decomposition products and lack of reversibility that would seriously limit the use of zinc borohydride as a storage material. This chapter discusses the possible synthesis of zinc borohydride through the metathesis reaction via mechanical milling, and the structure and bonding of the milled products. Thermal decomposition is characterised to try to gain an understanding of the decomposition mechanism, and recombination is attempted to ascertain whether zinc borohydride can be reformed.

The metathesis reaction between zinc chloride and sodium borohydride with a 1:2 molar ratio to form zinc borohydride and alkali metal chloride has been previously discussed (section 3.12.1) and is shown below in equation (6.1)

$$ZnCl_2 + 2ABH_4 \rightarrow Zn(BH_4)_2 + 2ACl \quad (6.1)$$

A = Li or Na

However, recent work by Ravnsbaek et al. shows that the metathesis reaction (6.1) is not achieved using ball milling [138]. Instead of forming the homoleptic zinc borohydride, an alkali metal zinc borohydride complex is formed, depending on the ratio of alkali metal borohydride to zinc chloride used. An ABH_4:$ZnCl_2$ ratio of 2.5:1 was shown to form $AZn_2(BH_4)_5$ as shown in equation (6.2). If sodium borohydride is the starting material there

is also the competing reaction (6.3) which forms $NaZn(BH_4)_3$. Na_2ZnCl_4 was also formed during the reactions, especially in the $ZnCl_2$ rich compositions.

$$5\ ABH_4 + 2\ ZnCl_2 \rightarrow AZn_2(BH_4)_5 + 4\ ACl \quad (6.2)$$

$$3\ NaBH_4 + 2\ ZnCl_2 \rightarrow NaZn_2(BH_4)_3 + 2\ NaCl \quad (6.3)$$

If the standard enthalpies of formation are compared as shown in Figure 6.1, it can be seen that there is a change in enthalpy ($\Delta H_f^{\ominus}$) of -38.71 $kJmol^{-1}$ for reaction (6.1). The driving force of the reaction is the formation of sodium chloride.

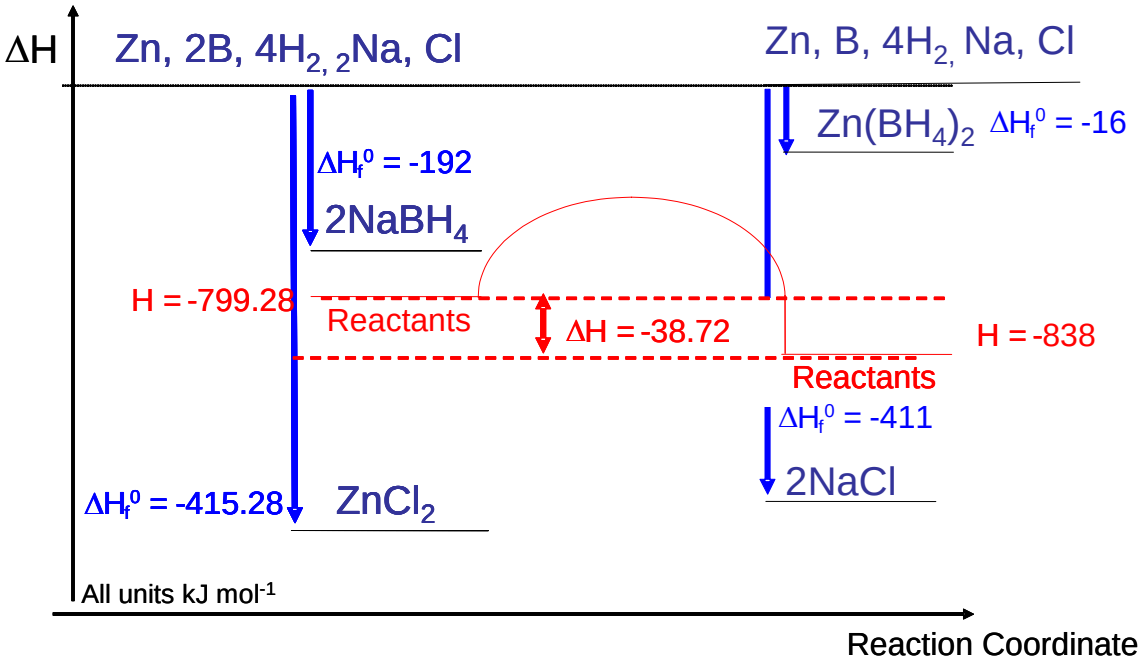

Figure 6.1 Change in enthalpy for the reaction of zinc chloride and sodium borohydride [134, 180].

Decomposition of homoleptic zinc borohydride can theoretically occur by a number of different mechanisms. The reactions (6.4) and (6.5) are at either end of the possible mass loss scale during thermal decomposition.

$$Zn(BH_4)_2 \rightarrow Zn + B + 4H_2 \quad (6.4)$$

$$Zn(BH_4)_2 \rightarrow Zn + B_2H_6 + H_2 \quad (6.5)$$

The expected mass losses for evolved gases for reactions (6.4) and (6.5) are 8.48 and 31.22 wt.%, respectively. A sample prepared using the metathesis reaction contains sodium chloride and therefore 44.86 wt.% of the total sample is zinc borohydride. This would give a mass loss due to evolved gases of 3.8 and 14.01 wt.% for reactions (6.4) and (6.5), respectively.

Upon examination of the standard enthalpies of formation for the two different routes of decomposition, the energies expected for reactions (6.4) and (6.5) are +16 and +51.6 $kJmol^{-1}$, as shown in Figure 6.2.

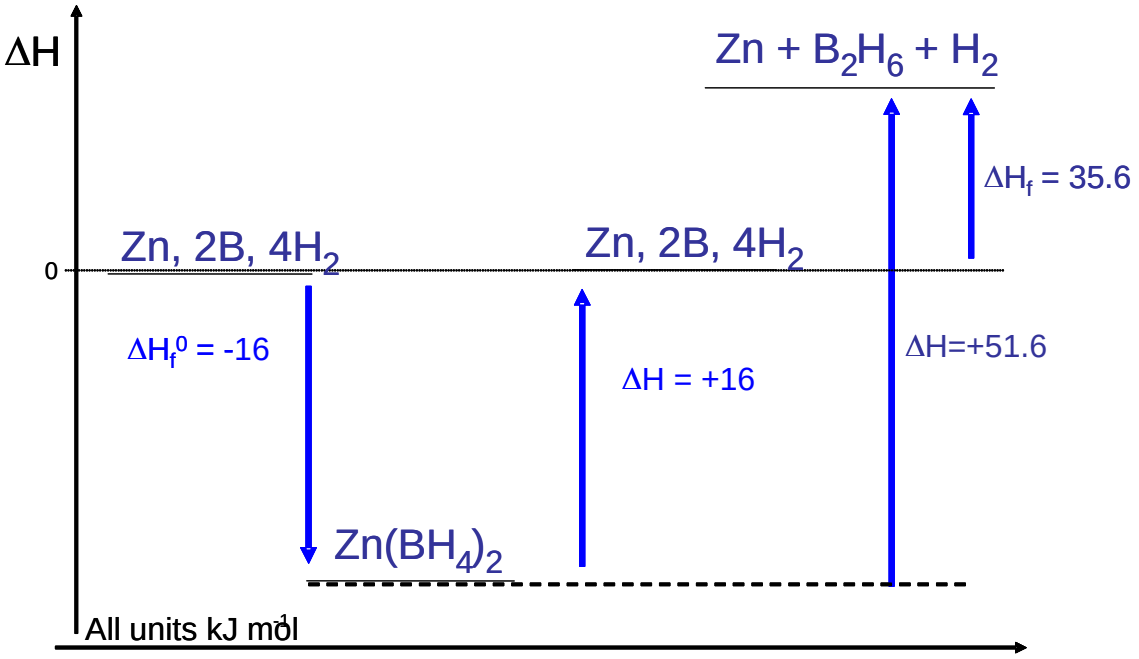

Figure 6.2 Change in enthalpy for decomposition of zinc borohydride [134, 180].

The decomposition mechanism proposed by Ravnsbaek et al. involves formation of metallic zinc and alkali metal borohydride (ABH_4). Simultaneously, the alkali ABH_4 reacts with A_2ZnCl_4 to form metallic zinc, ACl, with the evolution of hydrogen and diborane, to give an overall reaction scheme shown by equation (6.6). Decomposition via reaction (6.6) has a weight change of 23.0 and 20.9 wt.% for lithium and sodium, respectively. Ravnsbaek et al. observed mass losses of 16.5 and 14.6 wt.% for lithium and sodium, respectively, from the milled mixture. It has not been possible as yet to determine the enthalpy of formation of the Ravnsbaek et al. compound [138], and the subsequent changes in energy for the decomposition reactions.

$$2\ AZn_2(BH_4)_5 + M_2ZnCl_4 \rightarrow\ 5\ Zn + 4\ ACl + 5\ B_2H_6 + 5\ H_2 \qquad (6.6)$$

Work by Matthews investigated the milling conditions needed to synthesise zinc borohydride [136]. This work relied heavily upon XRD to monitor milling progress using the patterns of zinc chloride and sodium chloride. The presence of sodium chloride indicated that the reaction had started after five minutes and that no zinc chloride was present after twenty minutes. The formation of metallic zinc after eight hours indicated that the borohydride was beginning to decompose and that shorter milling times were required. Therefore, this work will focus on milling times of two hours and below. Matthews also investigated the vibrational spectra using infrared absorption spectroscopy, which also confirmed the start of the reaction after five minutes and that there was no sodium borohydride present after twenty minutes.

This work continues that of Matthews by concentrating on samples milled for 20, 40, 60 and 120 minutes to ascertain reaction progress and any changes in mechanism or kinetics associated with milling time. Work will also be performed to establish whether there are any effects on the decomposition mechanism caused by the addition of Ni, Ti, $TiCl_3$ and MgH_2.

The investigation will be separated into six sections. Firstly, the as-milled products for both the $LiBH_4$ and the $NaBH_4$ starting materials will be characterised through XRD, Raman and FTIR. Secondly, thermal decomposition will be evaluated using TGA/MS and DSC to determine the onset temperature, and to evaluate whether the reaction proceeds via equation (6.2) or (6.3). Thirdly, to further understand the decomposition mechanism, the decomposition products will be analysed by Raman spectroscopy and XRD studies. Next, recombination will be attempted at 100 bar in a Sieverts PCT system (Hiden HTP), to ascertain whether zinc borohydride is reversible (under these conditions). The effect of adding 2 mol% Ni, Ti, $TiCl_3$ and MgH_2 will then be examined using TGA/MS and DSC.

Finally, the addition of large amounts of magnesium hydride to form a 'reactive composite' will be investigated to understand any changes in the decomposition mechanism of zinc borohydride and magnesium hydride using TGA/MS, DSC and FTIR.

6.1 Characterisation of Milled Material

XRD was performed on the samples synthesised using both $LiBH_4$ and $NaBH_4$ as the starting materials. Figure 6.3 shows the patterns of the samples synthesised by $2LiBH_4 + ZnCl_2$. There are peaks due to the formation of LiCl. The disappearance of peaks due to $ZnCl_2$ and the lack of peaks due to $LiBH_4$ indicate that a reaction has occurred. There is a broad hump due to the Kapton dome around 20° 2θ, which should be ignored.

Pawley refinement of the sample milled for 120 minutes (Figure 6.4) shows that lithium chloride is formed and that there is no residual lithium borohydride or zinc chloride. It also shows a good fit with the structure determined by Ravnsbaek et al. [138] for $LiZn_2(BH_4)_5$ discussed previously (in section 3.12.1). The tetragonal $LiZn_2(BH_4)_5$ phase has lattice parameters of a = 8.638 (5), b = 17.953 (11) and c = 15.427 (9).

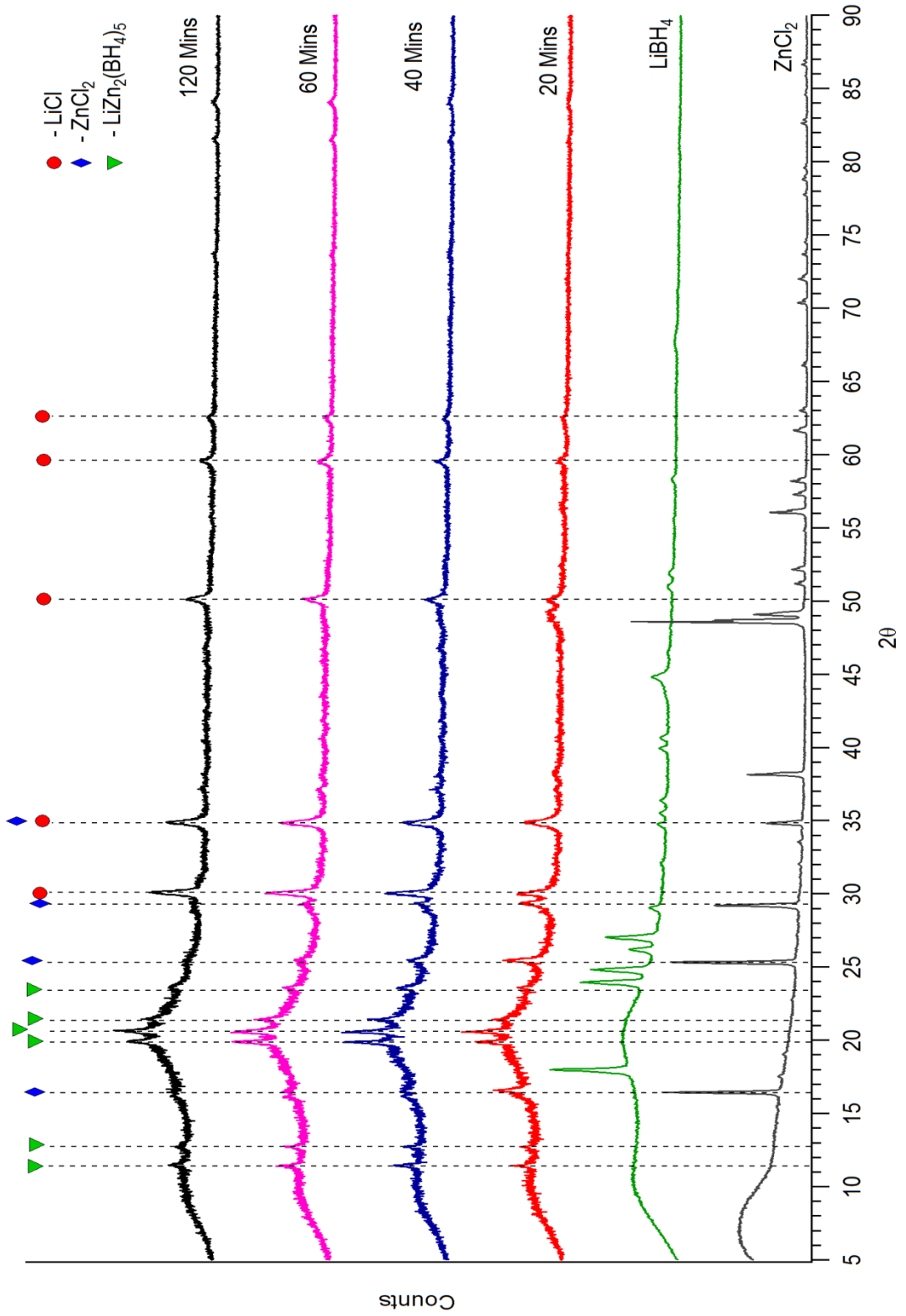

Figure 6.3 XRD patterns of milled $2LiBH_4 + ZnCl_2$.

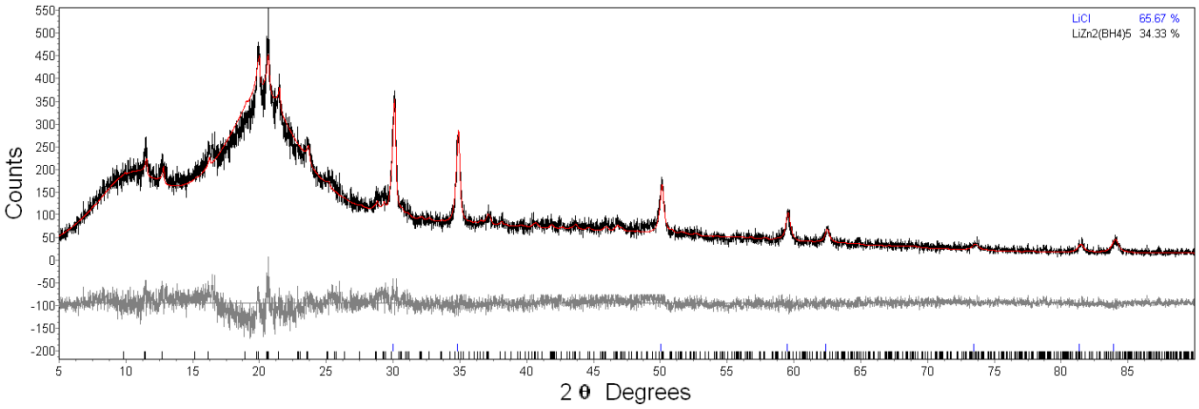

Figure 6.4 Pawley refined XRD pattern of $ZnCl_2$ + $2LiBH_4$ milled for 120 minutes.

The samples prepared by milling $2NaBH_4$ + $ZnCl_2$ are shown in Figure 6.5. The presence of sodium chloride and the disappearance of reagents indicate that a reaction has occurred as seen by Jeon and Cho [137]. Figure 6.6 shows the Pawley refined XRD pattern of the sample milled for 120 minutes. The refinement shows that there is sodium chloride and a $NaZn_2(BH_4)_5$ phase determined by Ravnsbaek et al [138]. The monoclinic cell has parameters a = 9.433 (7), b = 16.612 (10), c = 9.137 (5) and β = 112.764 (69).

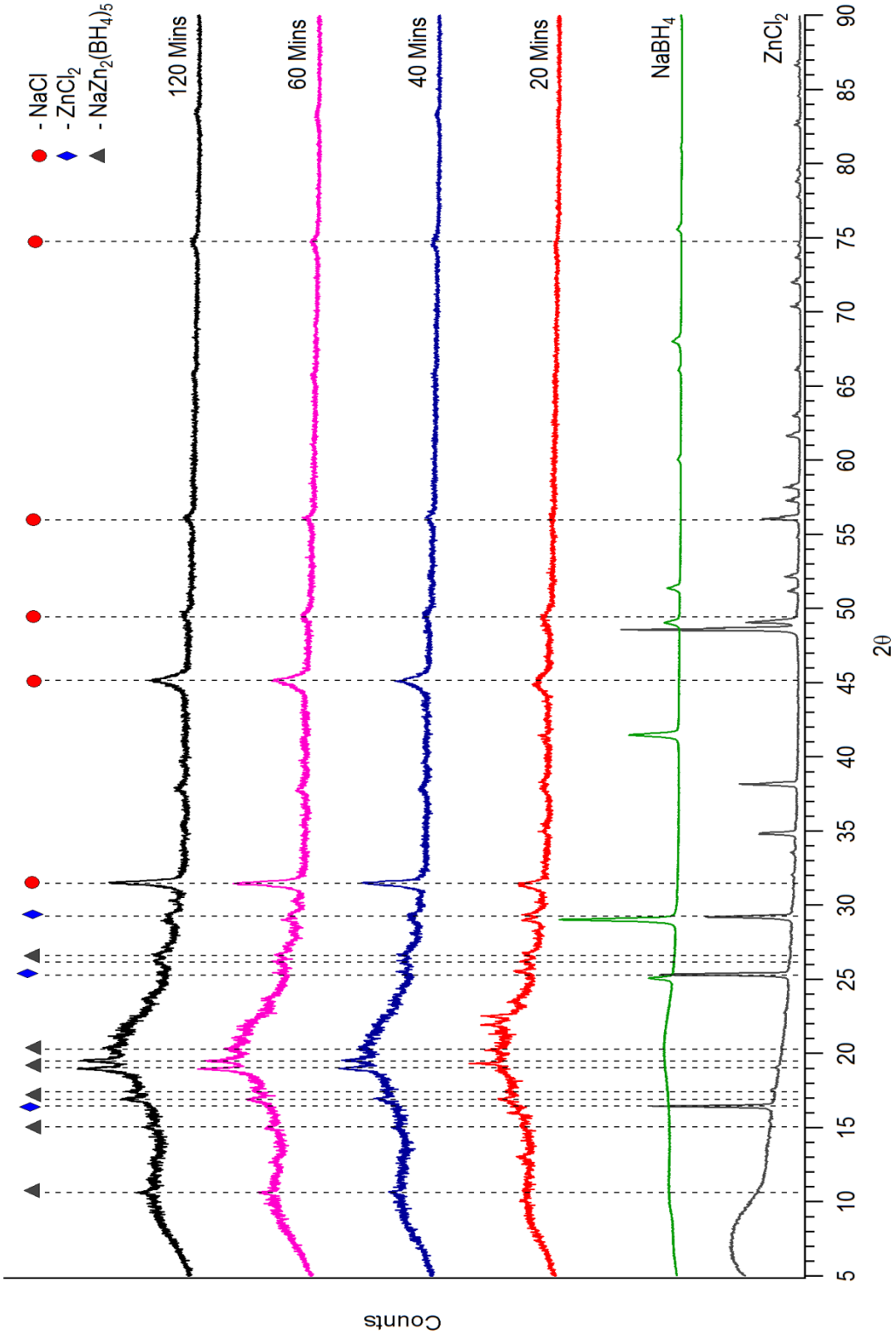

Figure 6.5 XRD patterns of milled $2NaBH_4 + ZnCl_2$.

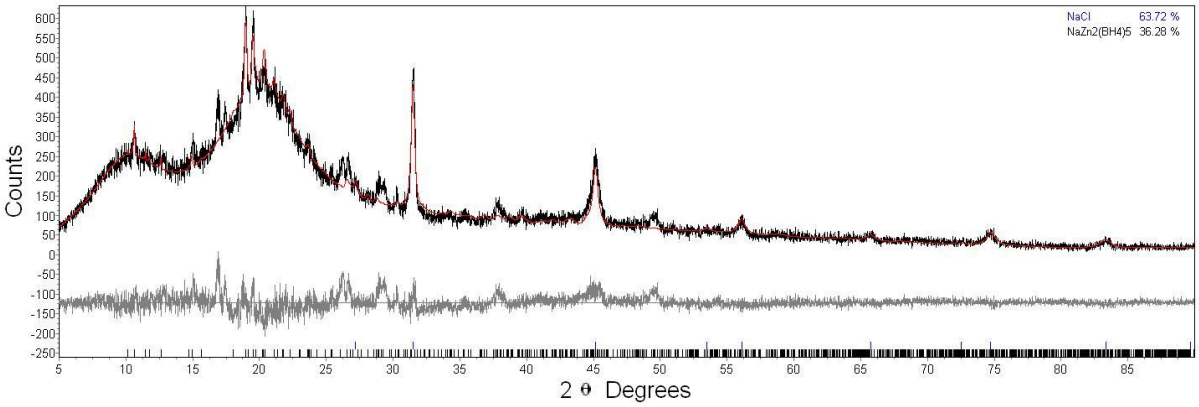

Figure 6.6 Pawley refined XRD pattern of $ZnCl_2$ + $2NaBH_4$ milled for 120 minutes.

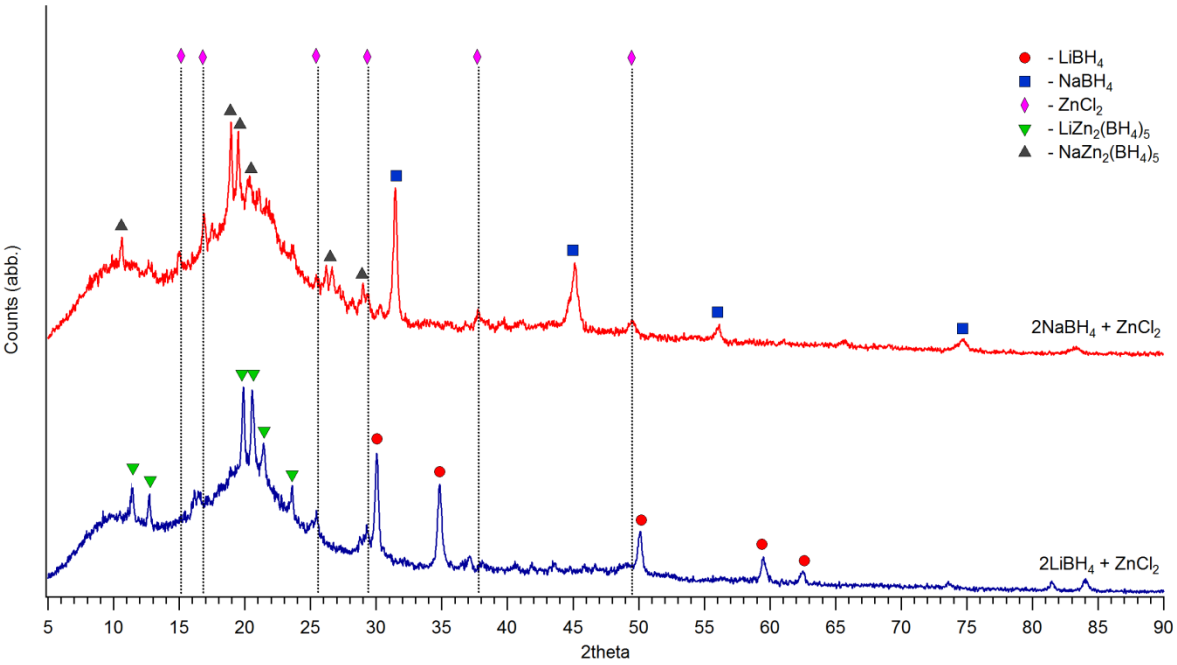

Figure 6.7 Comparison of samples milled for 60 minutes using $LiBH_4$ and $NaBH_4$ as starting material.

The refinement of the XRD patterns shows that reaction (6.1) is not followed and that zinc borohydride, $Zn(BH_4)_2$, is not formed as expected. Rather, an $AZn_2(BH_4)_5$ compound is formed, along with ACl, where A = Li or Na as per reaction (6.2). While this compound is not what was expected to form (based on the literature discussed in section 3.12.1), it is a zinc borohydride and thus requires further investigation.

The XRD patterns of the reaction products of sodium and lithium borohydride show similar stoichiometry, but very different unit cells were formed, with lithium forming a cubic C*mca* and sodium a monoclinic $P2_1/c$. On studying the Raman spectra of the samples milled for 60 minutes, Figure 6.8 shows that the structure is not that of the bidentate configuration previously reported [135]. The differences between the two samples are as follows. There are ionic borohydrides present in the lithium-based material which are not present in the sodium sample. There is also a shift in the vibrations attributed to the bidentate borohydride group, with an increase in the Raman shift of the B-H_t vibration and a corresponding decrease in the B-H_b vibration, and an increase in the Zn-H vibration. This indicates an increase in bonding strength between the borohydride and zinc centre. The vibrations are summarised in Table 6.1 showing the shift in position. The ionic B-H stretch could be due to remaining alkali metal borohydride.

Table 6.1 Summary of the peak positions of the $ABH_4 + ZnCl_2$ (A = Li and Na) milled for 60 minutes.

			$LiBH_4$	**$NaBH_4$**	**Change**
			Raman shift (cm^{-1})		
Monodentate	A_1	BH_3 deformation	988.593	984.149	-4.444
Bidentate	A_1, B_2	BH_2 deformation	1154.64	1181.61	26.97
Bidentate	A_1	Bridge stretch	1420.96	1418.41	-2.55
Bidentate	A_1	B-H_b stretch	2100.24	2117.55	17.31
Ionic	A_1	B-H stretch	2245.5	2229.17	-16.33
Monodentate	A_1	B-H_t stretch	2353.15	2328.24	-24.91
Bidentate	A_1	B-H_t stretch	2454.57	2420.11	-34.46

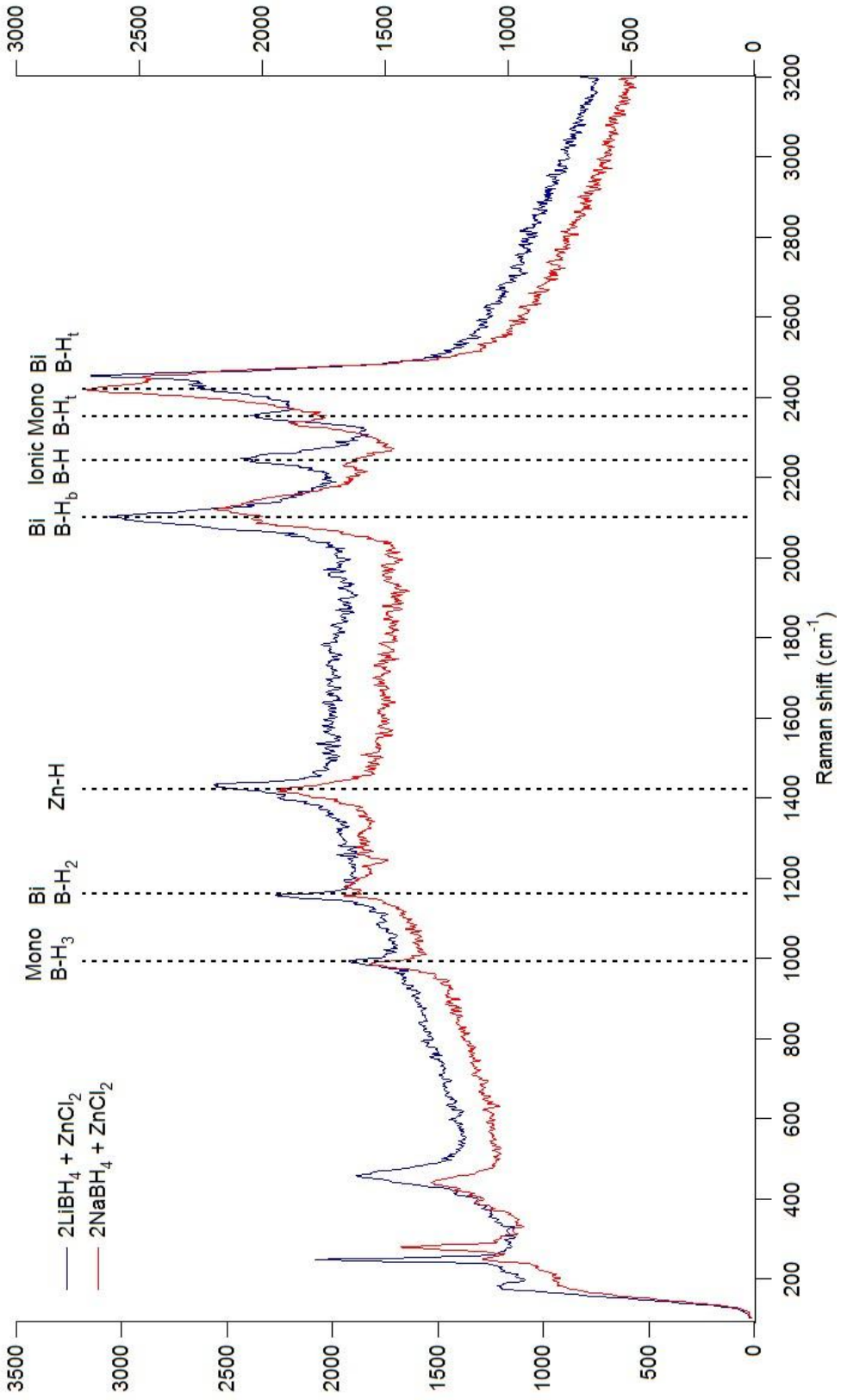

Figure 6.8 Raman spectra of $2ABH_4 + ZnCl_2$ (A = Li or Na) samples milled for 60 minutes.

Figure 6.9 shows the comparison between the Raman spectra of samples prepared using $LiBH_4$ and $LiBD_4$. The comparison between the peak positions is summarised in Table 6.2. The ratio of the Raman shifts for the hydrogen to deuterium prepared samples is around 1.4 [57, 181], indicating that all the vibrations involve the displacement of either hydrogen or deuterium. Vibrational modes are assigned using

Table 4.3.

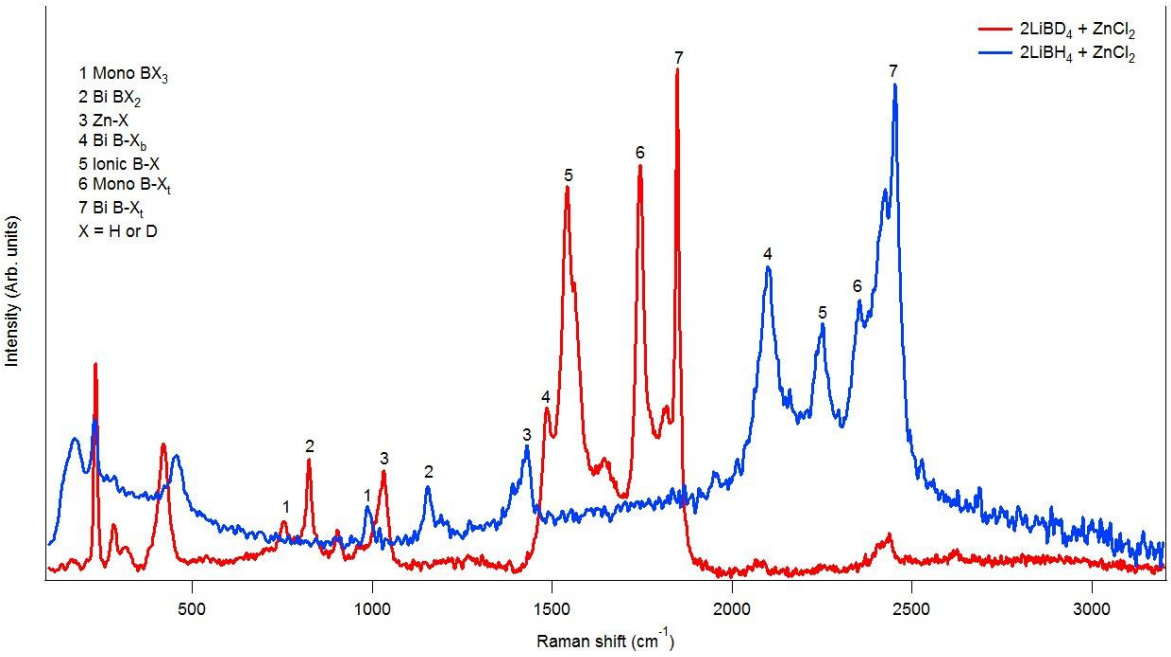

Figure 6.9 Raman spectra of $2LiBX_4 + ZnCl_2$ (X = H or D) samples milled for 60 minutes.

Table 6.2 Summary of the peak positions of the $2LiBX_4 + ZnCl_2$ (X = H or D) samples milled for 60 minutes**.**

			$LiZn_2(BH_4)_5$	$LiZn_2(BD_4)_5$	ν_H/ν_D
			Raman shift (cm^{-1})		
Monodentate	A_1	BX_3 deformation	988.593	754.859	1.31
Bidentate	A_1, B_2	BX_2 deformation	1154.64	824.843	1.40
Bidentate	A_1	Bridge stretch	1420.96	1028.04	1.38

Bidentate	A_1	B-X_b stretch	2100.24	1485.48	1.41
Ionic	A_1	B-X stretch	2245.5	1542.04	1.46
Monodentate	A_1	B-X_t stretch	2353.15	1745.25	1.35
Bidentate	A_1	B-X_t stretch	2454.57	1848.52	1.33

The vibrational spectra of a sample milled for 60 minutes were collected using both Raman scattering and infrared absorption as shown in Figure 6.10 with the peaks summarised in Table 6.3. Comparison of the positions of the peaks with those in

Table 4.3 shows that zinc borohydride does not have a bidentate configuration as predicted in the literature [135, 137], but has a combination of monodentate, bidentate and ionic configurations. The latter is possibly due to unreacted sodium borohydride. The terminal hydrogen peaks are in the range for both mono- and bidetate borohydrides. The bridging hydrogen could be either mono- or bidentate, but the Zn-H bridging hydrogen is in the correct position for a bidentate configuration. The BH_2 deformations are present as well as the wag and twist of the BH_4 group in the Raman spectra.

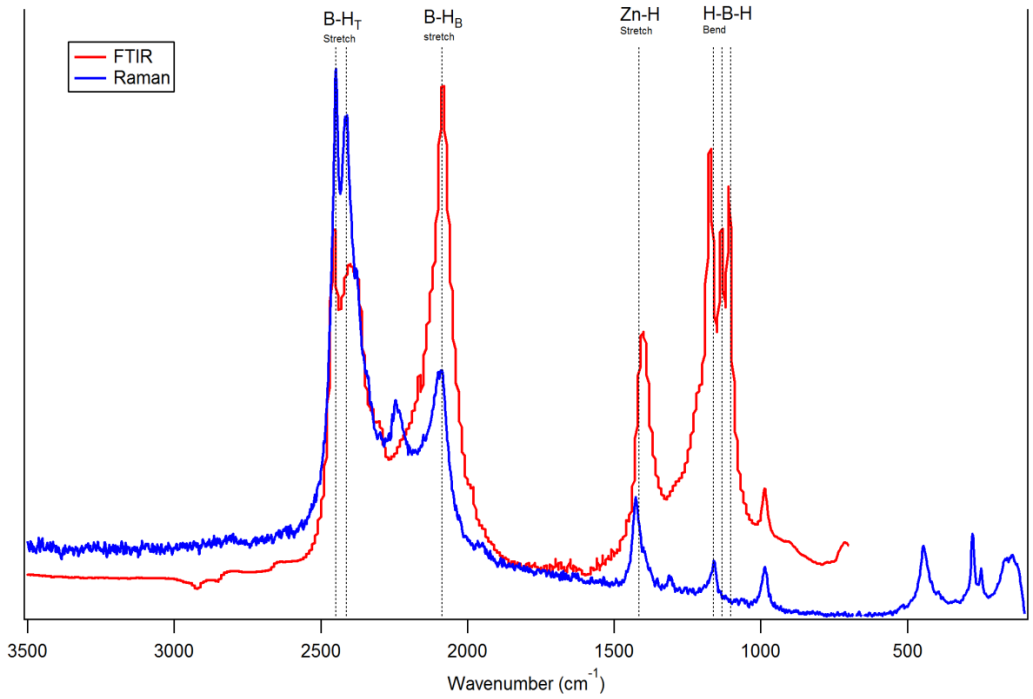

Figure 6.10 FTIR and Raman spectra of $ZnCl_2$ + $2NaBH_4$ milled for 60 minutes.

Table 6.3 Peaks in the vibrational spectra of $ZnCl_2 + 2NaBH_4$ milled for 60 minutes.

Raman		**FTIR**	
Raman shift (cm^{-1})		**Wavenumber (cm^{-1})**	
2450	B-H_t Bidentate	**2450**	B-H_t
2417	B-H_t Monodentate	**2390**	B-H_t
2248	B-H stretch Ionic		
2100	B-H_b Bidentate	**2080**	B-H_b
1429	Zn-H Bidentate	**1400**	Zn-H
1160	BH_2 deformation	**1170**	BH_2 deformation
		1130	BH_2 deformation
		1110	BH_2 deformation
987	B-H_3 monodentate	**985**	
448	External mode		
280	External mode		

6.2 Thermal Decomposition

Having now established that $Zn(BH_4)_2$ was not formed, it is important to determine the thermal decomposition characteristics of the $AZn_2(BH_4)_5$ and $NaZn(BH_4)_3$ compounds.

TGA was performed to determine the mass loss and, when coupled with MS, which gases were evolved. Figure 6.11 compares the mass loss of samples milled for durations from 5 to 120 minutes, with weight losses summarised in Table 6.4.

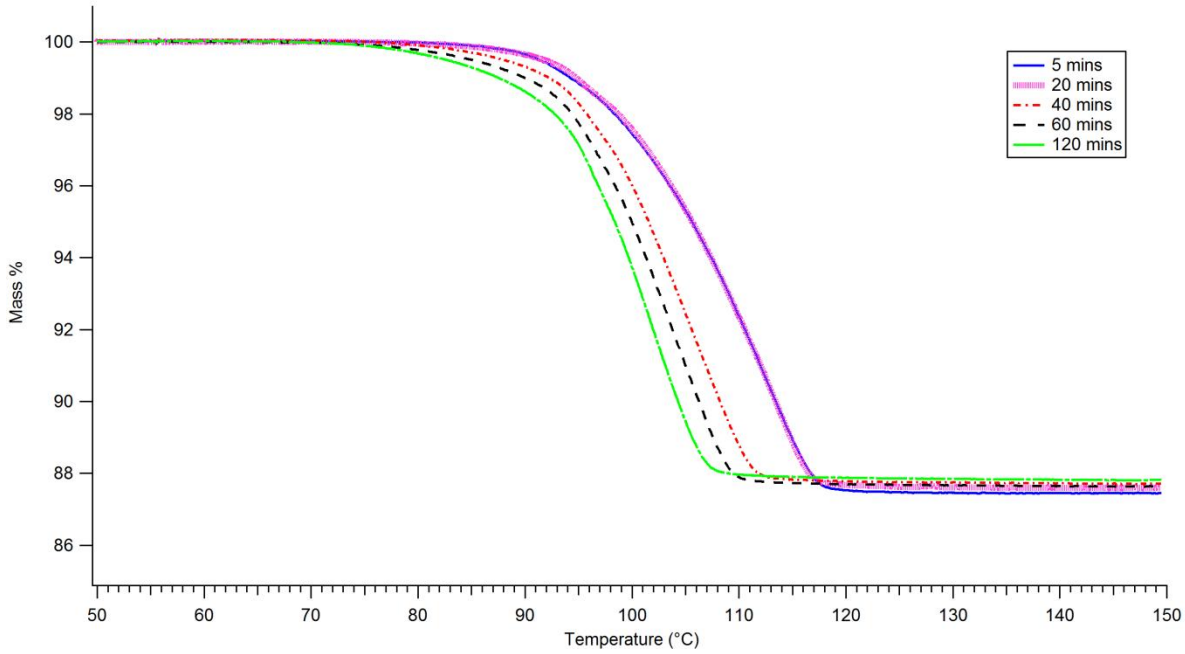

Figure 6.11 TGA of $ZnCl_2$ + $2NaBH_4$ samples mechanically milled for 5, 20, 40, 60 and 120 minutes, heated 2°C/min under flowing 1.5 bar argon at 40 ml/min.

Table 6.4 Summary of weight loss and T_d of ball milled $ZnCl_2$ + $2NaBH_4$**.**

Milling duration (minutes)	Weight loss (%)	Initial weight loss temperature (°C)	Onset temperature (°C)	Mid point temperature (°C)	End temperature (°C)	Time (min)
5	12.55 ± 0.22	79.8	98.6	107.9	117.2	9.3
20	12.40 ± 0.24	79.6	98.9	107.9	116.9	9.0
40	12.28 ± 0.24	76.6	95.2	103.1	111.0	7.9
60	12.22 ± 0.24	69.1	94.0	101.5	109.1	7.6
120	12.19 ± 0.23	69.6	92.9	99.8	106.7	6.9

Increased milling time reduces the onset of decomposition. Initial weight loss is observed from around 80°C for 5 minutes milling to around 70°C after 120 minutes, with an onset of 98.6°C for 5 minutes milling reducing to 92.9°C for 120 minutes milling. The reaction time also decreases from 9.3 minutes after 5 minutes milling to 6.9 minutes after 120 minutes

milling at 2°C/min. These values are comparable to those measured by Jeon and Cho [137]. If these results are considered in isolation, then the weight loss is highly favourable when considering zinc borohydride as a potential hydrogen storage material. However, the weight loss of between 12.2 and 12.6 wt.% indicates that the decomposition does not progress via either reaction (6.4) or (6.5). This observed weight loss is also lower that that observed by Ravnsbaek et al. of 14.6 wt. % [138].

Using MS to analyse the gases evolved, is it possible to see (Figure 6.12) that both hydrogen and diborane are released during decomposition. It was not possible to accurately derive the amounts of hydrogen and diborane due to problems with calibration of the MS. It also cannot be guaranteed that all diborane evolved is transmitted to the MS because diborane has a tendency to deposit onto the inner surface of the pipes forming a variety of borate compounds. An attempt was made to measure the concentration of any other borane compounds, however, none were detected.

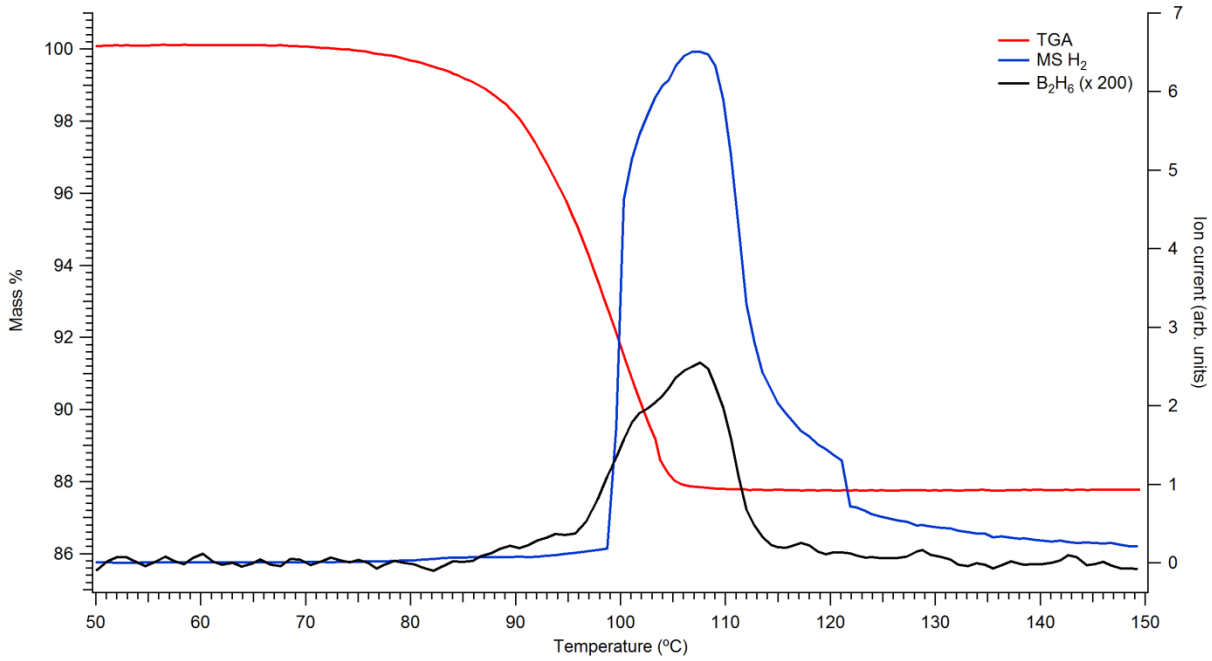

Figure 6.12 TGA/MS of $NaZn_2(BH_4)_5$ milled for 60 minutes heated at 2°C/min in flowing 1.5 bar argon.

TGA of samples prepared by milling $ZnCl_2$ with either $2LiBH_4$, $2NaBH_4$ or $3NaBH_4$ for 60 minutes are shown in Figure 6.13. The sample prepared with $3NaBH_4$ has a weight loss of 10.9 wt.% with a T_d of 79°C compared to the 12.2 wt.% weight loss of the sample prepared with $2NaBH_4$, and 14.5 wt.% weight loss and a T_d of 74°C for the sample prepared with $2LiBH_4$.

It is difficult to compare the absolute weight loss due to the difference in mass between lithium and sodium and the different relative amounts of sodium. Considering that BH_4 is the sole group that changes in mass during decomposition, only the mass of BH_4 will further be considered for this comparison. Figure 6.14 shows the change in mass of the BH_4 groups. Samples prepared with $2NaBH_4$ and $2LiBH_4$ have similar weight changes of 87.3 and 86.0 wt.%, respectively. The sample prepared with $3NaBH_4$ has a weight change of 61.3 wt.%.

This weight loss is greater than that expected for a sample prepared with $2NaBH_4$ with excess $NaBH_4$ present (where approximately a 54 wt.% change is expected). Samples prepared with $2ABH_4 + ZnCl_2$ decompose via similar mechanisms, evolving a similar amount of gas. The sample prepared by milling $3NaBH_4 + ZnCl_2$ decomposed via a different mechanism. All reactions proceed with the evolution of both hydrogen and diborane. Therefore this also confirms that zinc borohydride, $Zn(BH_4)_2$ is not formed through the metathesis reaction (6.1), using the conditions used in this study.

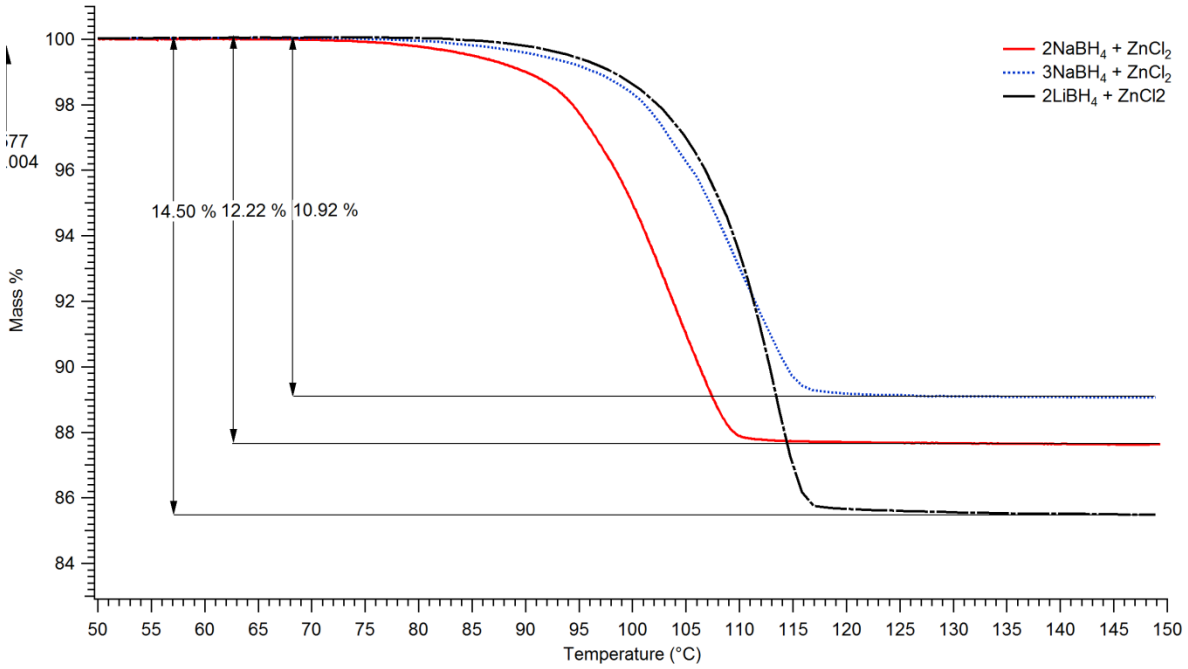

Figure 6.13 TGA of $xABH_4 + ZnCl_2$ samples milled for 60 minutes, where A = Li or Na and x = 2 or 3 heated at 2°C/min under flowing 1.5 bar argon at 40 ml/min.

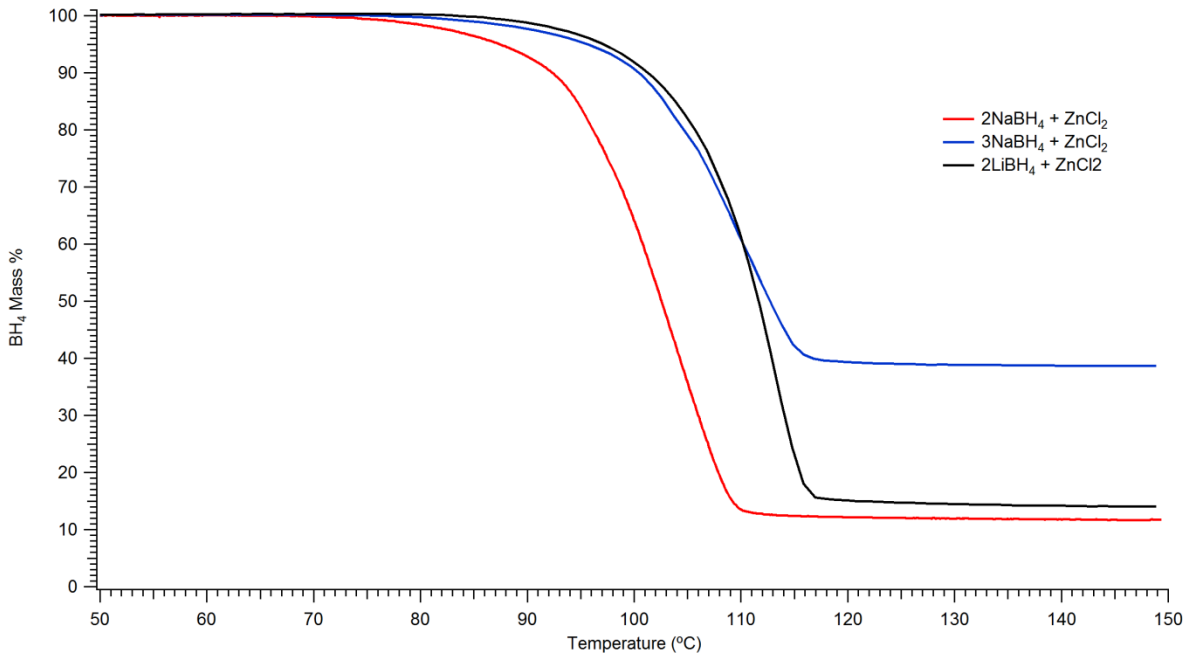

Figure 6.14 TGA normalised to the mass of BH_4 of $xABH_4 + ZnCl_2$ samples milled for 60 minutes, where A = Li or Na and x = 2 or 3 heated at 2°C/min under flowing 1.5 bar argon at 40 ml/min.

The rate of hydrogen and diborane evolution measured on the MS is very similar for the samples prepared using sodium borohydride as seen in Figure 6.12 and Figure 6.15. There is a very smooth and rounded peak at 108°C for $2NaBH_4 + ZnCl_2$ and 116°C for $3NaBH_4 + ZnCl_2$. The sample prepared by milling $2LiBH_4 + ZnCl_2$, shown in Figure 6.16, has a sharper peak with a maximum at 117°C with the evolution of diborane occurring at a higher temperature compared to the samples prepared with sodium borohydride. While the absolute temperatures of the gas evolution cannot be determined using MS due to the pipe-work between the TGA and MS, an accurate comparison is still possible.

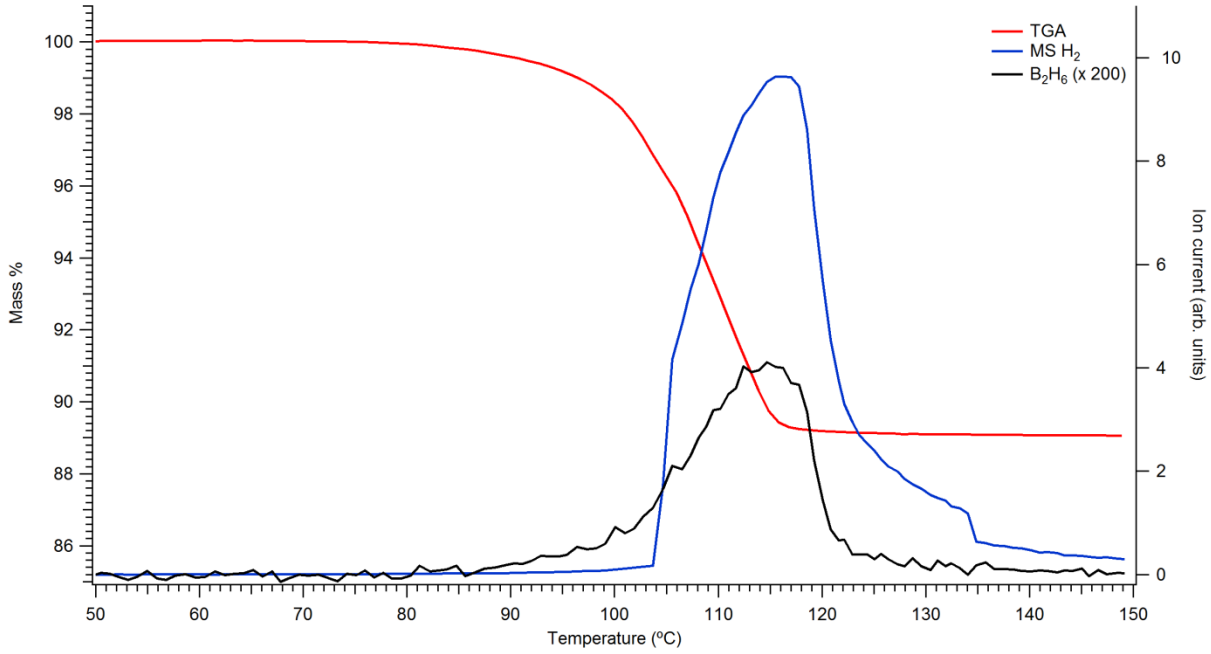

Figure 6.15 TGA/MS of $3NaBH_4 + ZnCl_2$ milled for 60 minutes heated at 2°C/min in flowing 1.5 bar argon at 40 ml/min.

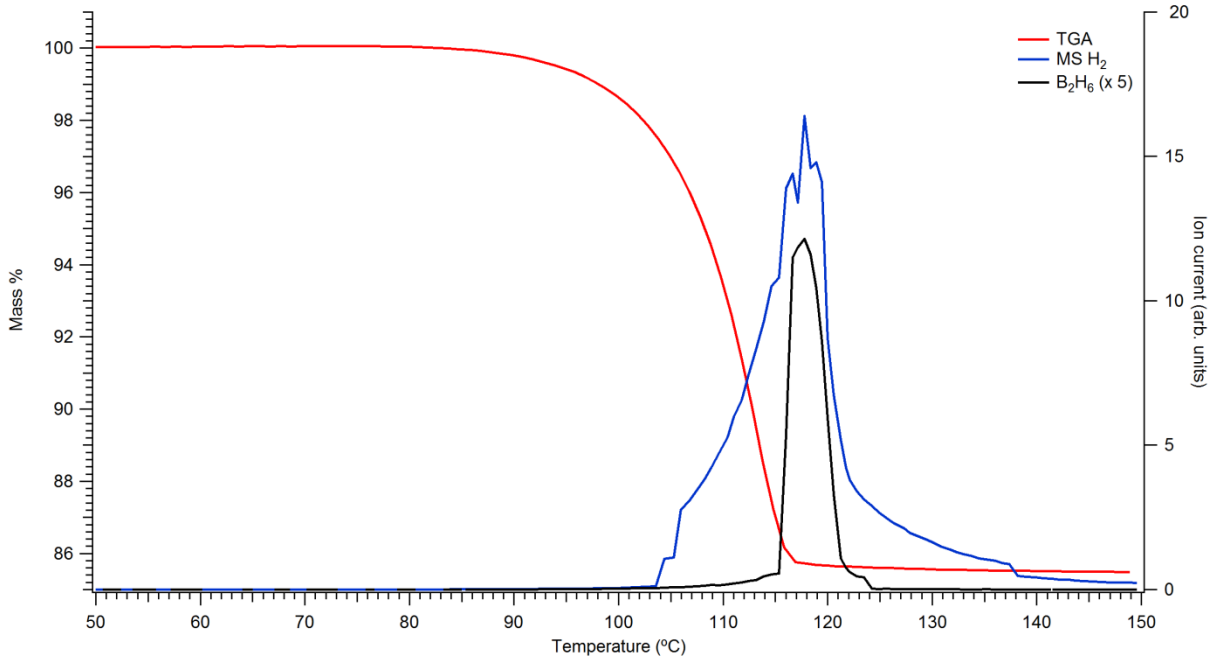

Figure 6.16 TGA/MS of $2LiBH_4 + ZnCl_2$ milled for 60 minutes heated at 2°C/min in flowing 1.5 bar argon at 40 ml/min.

The stability of zinc borohydride at room temperature was also studied using TGA. Samples were stored in an airtight container within an argon-filled glovebox. Figure 6.17 shows that within 14 days there is a significant change in the weight loss of the sample coupled with a colour change from white for the as-milled sample through grey and then to a black powder. Any sample left to stand for between 7-10 days has significantly different properties to a fresh sample.

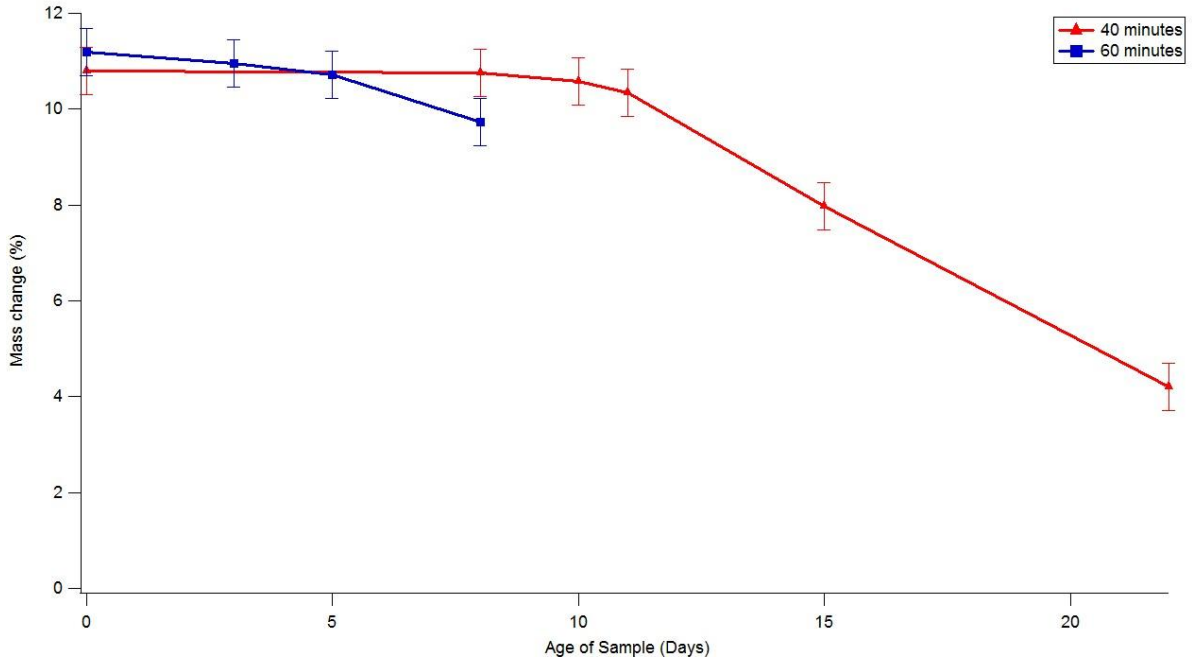

Figure 6.17 TGA mass loss of $2NaBH_4 + ZnCl_2$ samples milled for 40 or 60 minutes, that had been stored for different periods within an Ar glovebox.

DSC was undertaken to understand how many steps are involved in thermal decomposition and the energies involved in these steps. Figure 6.18 shows the change in DSC with milling duration. Upon heating the sample there is a sharp endothermic peak at 85-105°C which is attributed to the melting of zinc borohydride. There is another broad endothermic peak

between 95 and 115°C which is attributed to the decomposition of zinc borohydride. The peak position and shapes are comparable to those presented by Jeon and Cho [137].

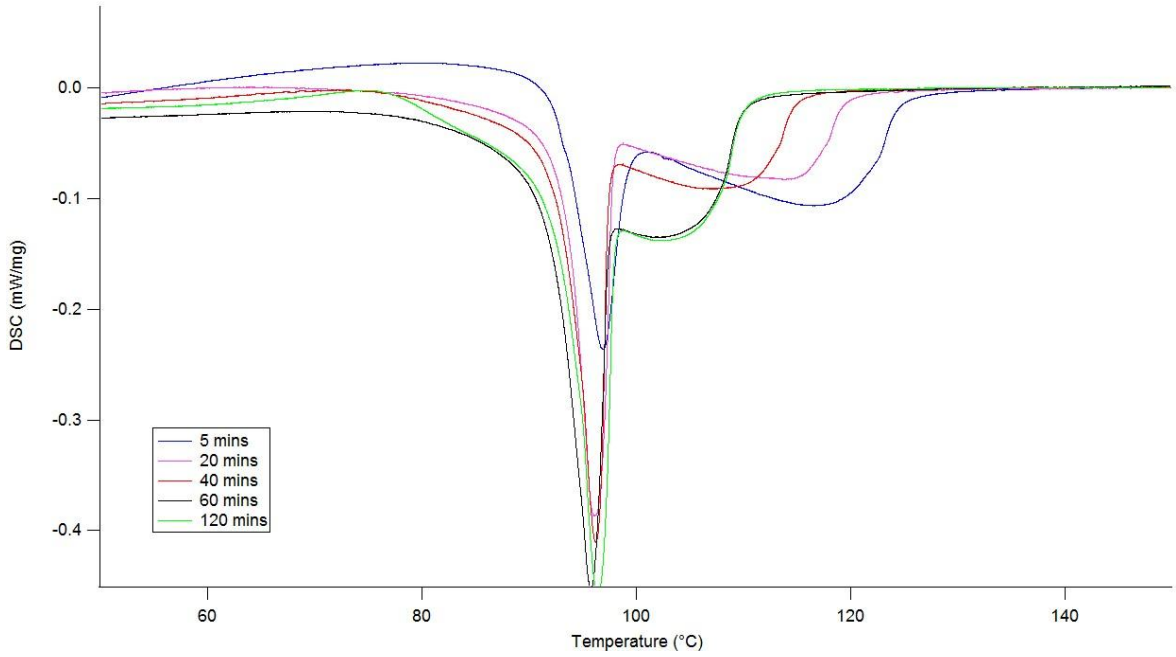

Figure 6.18 DSC of $ZnCl_2$ + $2NaBH_4$ samples milled for 5, 20, 40, 60 and 120 minutes, heated at 2°C/min under flowing 4 bar argon at 100 ml/min.

If we consider the sample milled for 60 minutes, the measured total exothermic energy is $\Delta Q = 28.07$ kJmol^{-1}. This measured energy is between the two predicted different decomposition routes of $\Delta H = 16$ and 61.6 kJmol^{-1}, for reactions (6.4) and (6.5) respectively. This again indicates that the experimentally observed decomposition path is not through either reaction (6.4) and (6.5). This would indicate that the decomposition proceeds through a mixture of reactions (6.4) and (6.5) or that $NaZn_2(BH_4)_2$ decomposes through another mechanism.

6.3 Analysis of Decomposition Products

The thermal decomposition products were analysed using FTIR, Raman, XRD and SEM with EDX and WDX. The Raman spectrum in Figure 6.19 shows that borohydride vibrations are no longer present at 150°C indicating the decomposition of all B-H bonding. The two peaks that are formed are attributed to a boron containing compound, the Raman shift is significantly higher than that of amorphous boron, and is believed to be due to the formation of a boron oxide (B_xO_y). The absence of vibrational modes around 2500 cm^{-1} indicates that a borane, such as $[B_{12}H_{12}]^{2-}$ has not been formed.

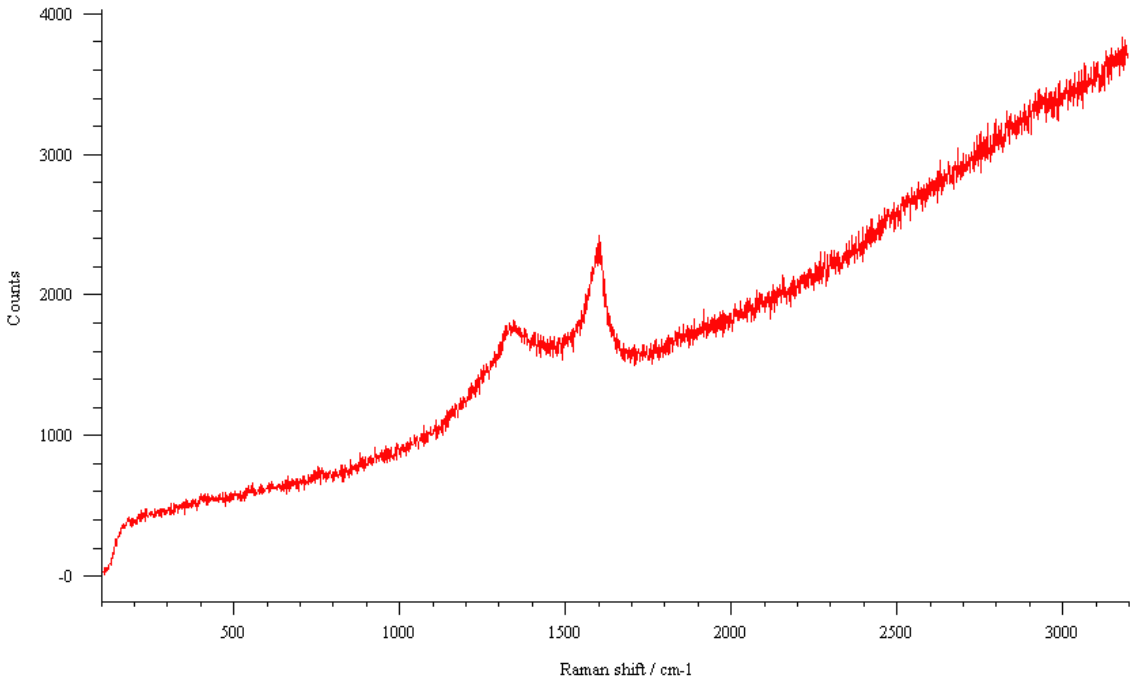

Figure 6.19 In-situ Raman at 150°C of $NaZn_2(BH_4)_5$ ($ZnCl_2$ + $2NaBH_4$ milled for 60 minutes) and heated to 150°C at 2°C/min using the 488 nm excitation laser.

The XRD patterns in Figure 6.20 show that the as-milled material contains reflections attributed to sodium chloride. Upon heating, the peaks due to sodium chloride become sharper. This is attributed to the formation of larger crystals or the formation of sodium chloride from the decomposition of the $NaZn_2(BH_4)_5$ system. The formation of metallic zinc was expected for decomposition paths of reactions (6.4), (6.5) and (6.6). The lack of any boron compound peaks indicates that no crystalline boron compounds are present in the desorbed mixture. However, the presence of a boron containing compound would indicate the decomposition mechanisms (6.4) and (6.6) cannot be sole decomposition mechanisms.

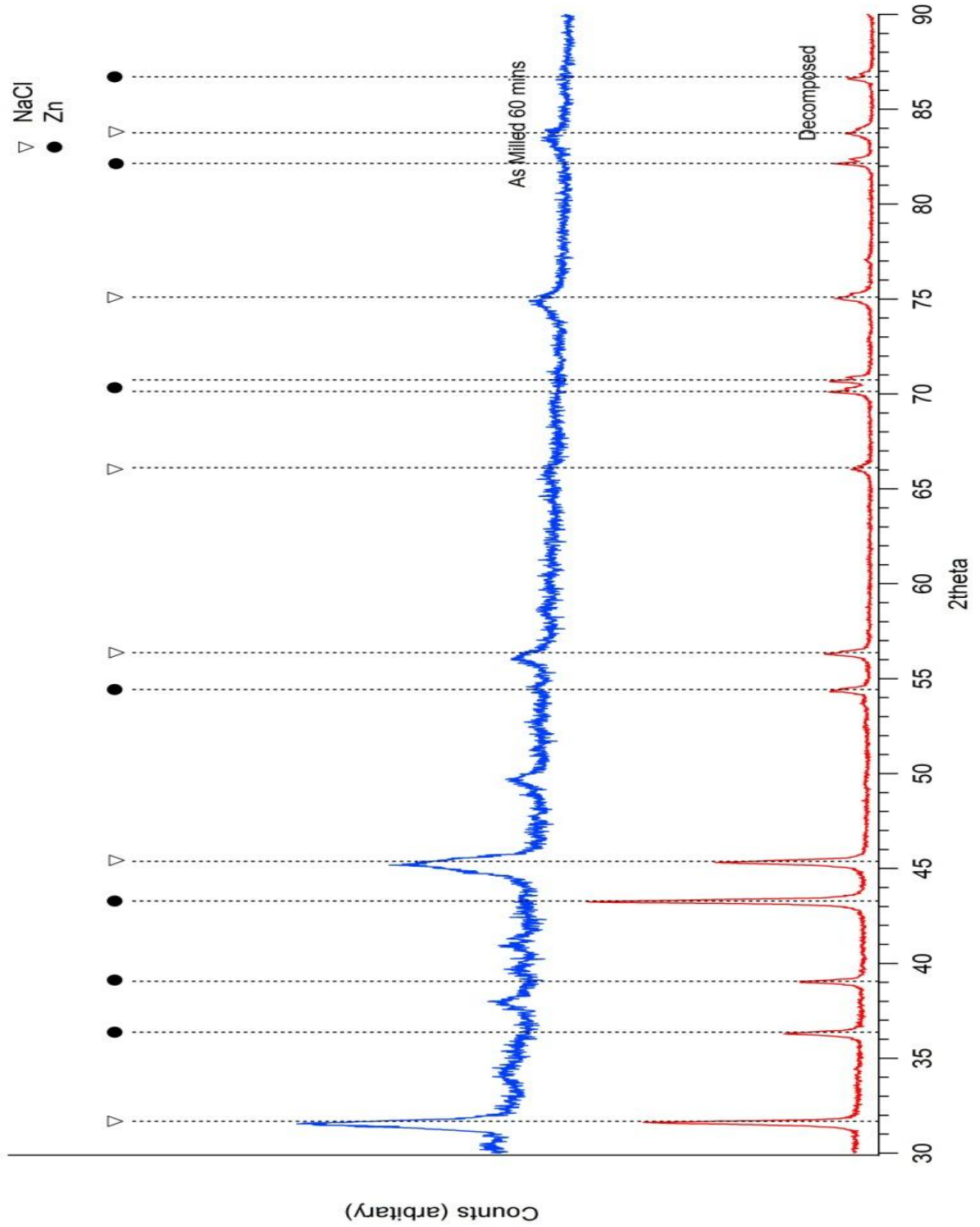

Figure 6.20 Room temperature XRD patterns of $NaZn_2(BH_4)_5$ samples ($ZnCl_2$ + $2NaBH_4$ milled for 60 minutes) before and after heating at 2°C/min to 150°C in 1 bar argon.

The SEM micrographs in Figure 6.21 show different phases, consisting of regions of zinc and sodium chloride of a $2NaBH_4 + ZnCl_2$ sample milled for 60 minutes and decomposed at 150°C. The particles in the top micrograph of Figure 6.21 are around 2 μm in length, and have a lenticular morphology. Table 6.5 shows the average atomic percentage for boron sodium chlorine and zinc. This indicates that on average there is 4.8 wt.% boron, confirming the presence of boron after decomposition. This again indicates that the decomposition of milled zinc borohydride occurs by a combination of reactions (6.4) and (6.5).

Table 6.5 Summary of SEM EDX and WDX analysis of decomposition products in the sample shown in Figure 6.21**.**

	Boron	**Sodium**	**Chlorine**	**Zinc**
	WDX	EDX	EDX	EDX
Mean	4.8	32.5	28.9	33.8
Standard deviation	5.2	12.6	11.9	25.5
Maximum	26.7	50.8	44.2	85.3
Minimum	0.0	7.0	4.5	8.4

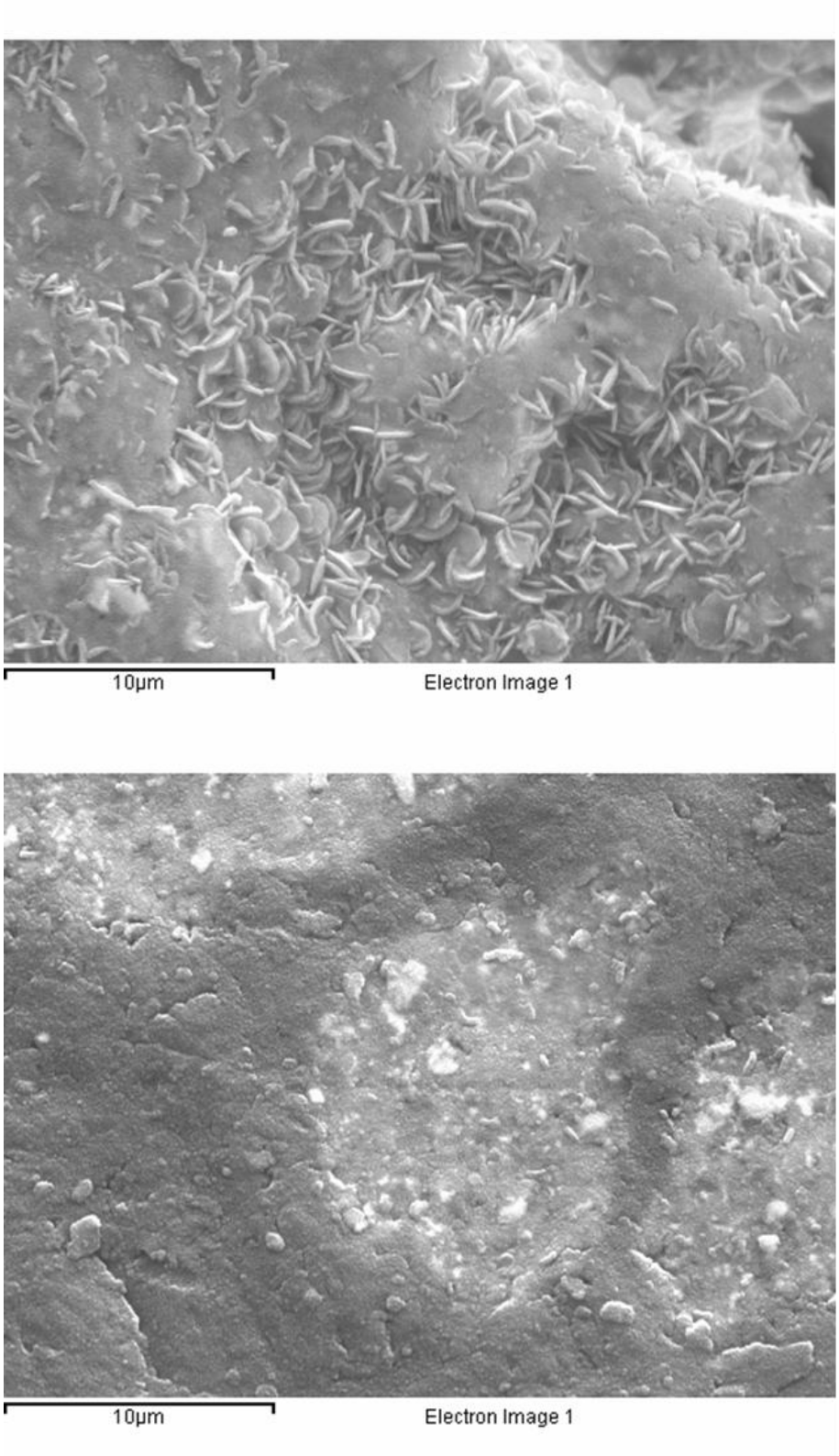

Figure 6.21 SEM micrographs of samples of $ZnCl_2$ + $2NaBH_4$ milled for 60 minutes after heating at 2°C/min to 150°C in 1.5 bar argon at 40 ml/min.

6.4 Recombination

Recombination was attempted under 100 bar hydrogen, on a $2NaBH_4 + ZnCl_2$ sample that has been milled for 60 minutes and then heated to 100°C under Ar. Figure 6.22 shows the pressure change upon heating to 100°C for the first and second decomposition. Under these conditions it was not possible to reform zinc borohydride, as there is no pressure change in the volumetric measurement. Figure 6.23 shows the FTIR spectra of the sample heated to 100°C at 100 bar in an attempt to recombine zinc borohydride. There is no appreciable change in the spectra between the decomposed and the sample for which recombination was attempted.

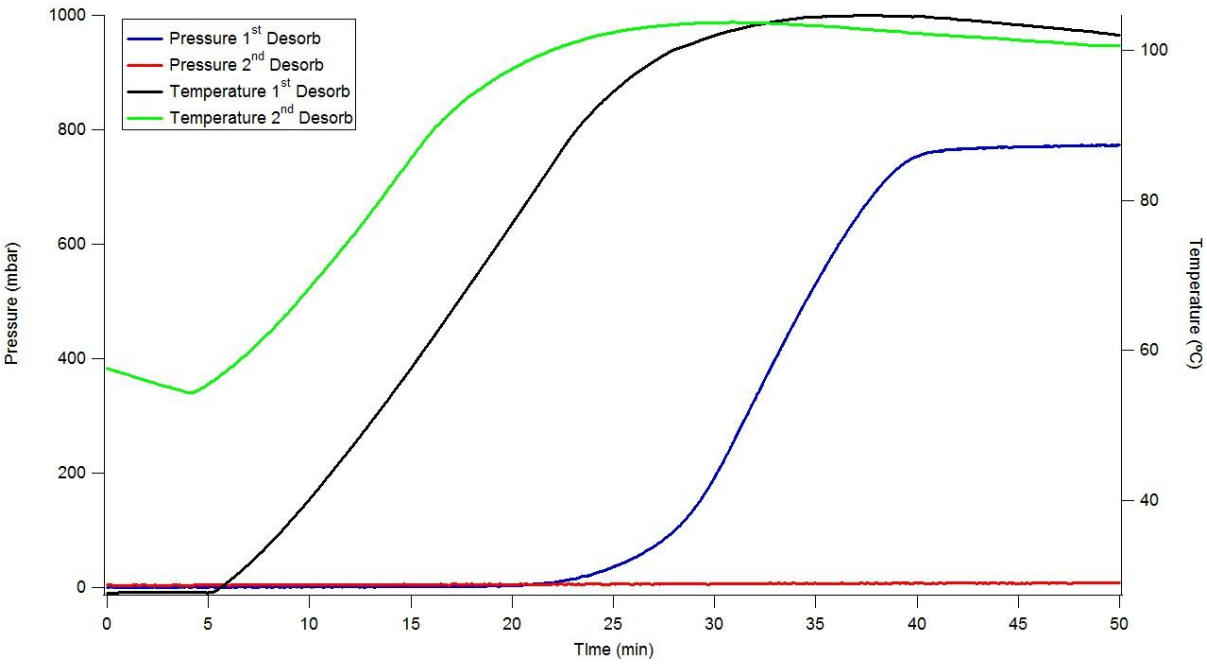

Figure 6.22 Comparison of the pressure change for the first and second decomposition of a $2NaBH_4 + ZnCl_2$ sample milled for 60 minutes, heated in a static vacuum using a Sieverts PCT system (Hiden HTP).

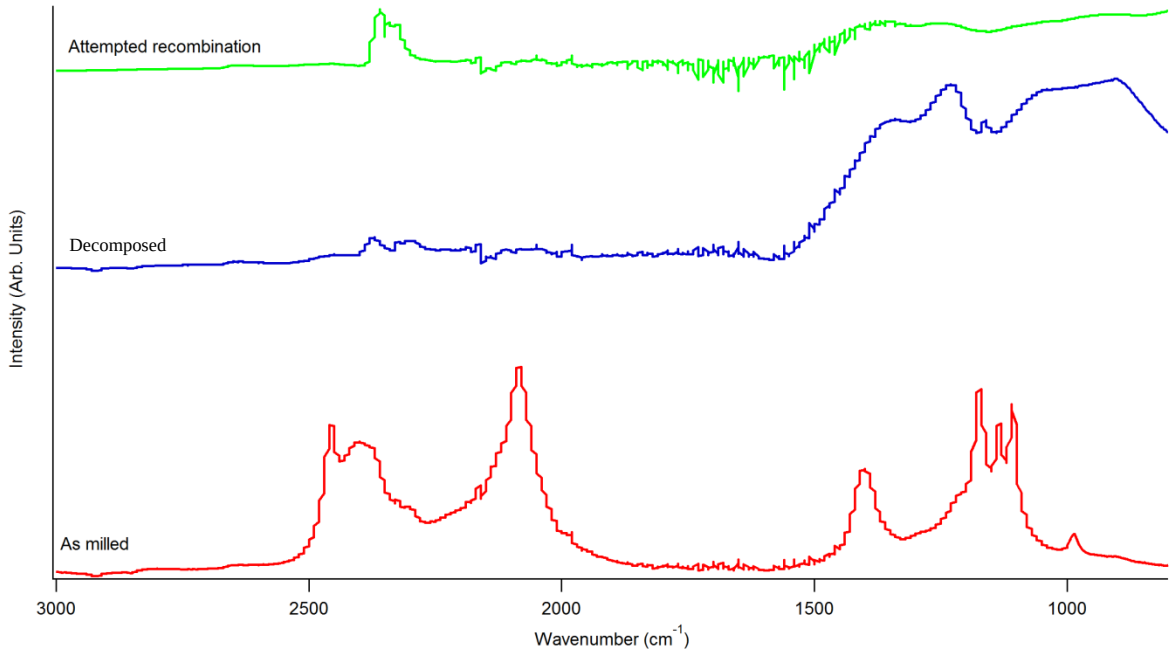

Figure 6.23 FTIR spectra of $ZnCl_2$ + $2NaBH_4$ milled for 60 minutes, decomposed (100°C, 1 bar argon), and attempted recombination (100°C, 100 bar hydrogen).

6.5 Decomposition Under Hydrogen Atmosphere

Thermal decomposition was investigated using DSC under different hydrogen pressures. Figure 6.24 shows that there is a significant change in the position of the melting peak, initially being evident as a shoulder at 25 bar developing in to a broad peak at 50 bar and at 75 bar a single peak, with the peak shifting from 94°C at 3 bar to 93°C at 100 bar. There is no large change in the decomposition peak between 3 and 75 bar. When the pressure is at 100 bar the onset of decomposition occurs at the same temperature but decomposition occurs at a slower rate with the end to decomposition occurring 8°C higher in temperature, with a similar enthalpy value.

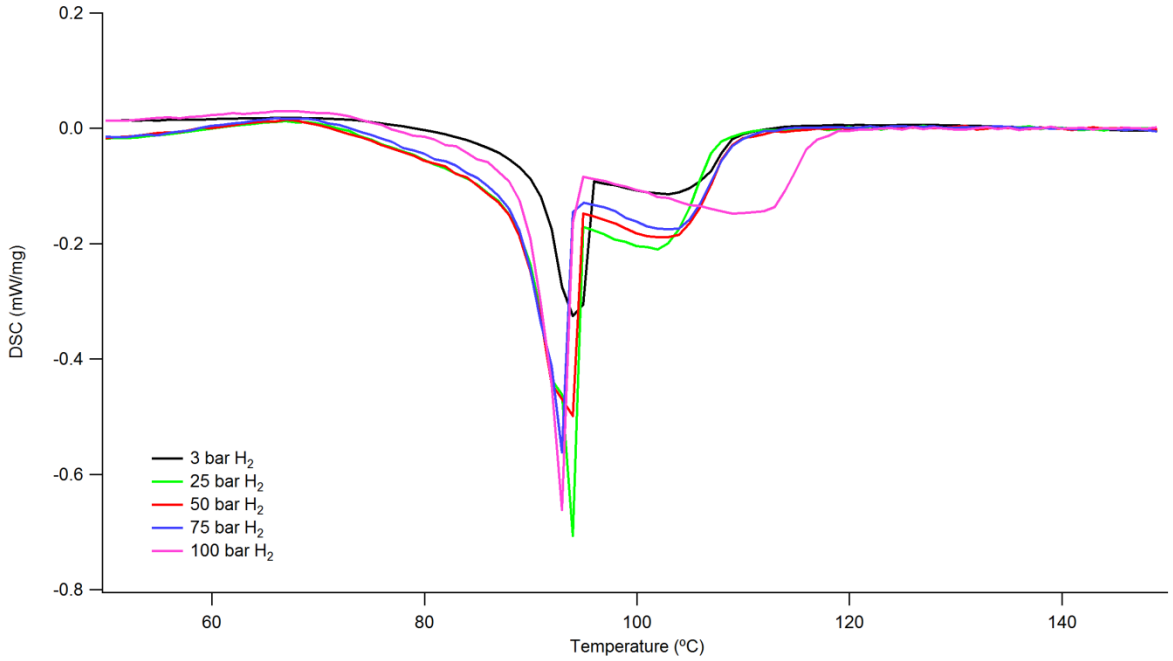

Figure 6.24 DSC of $ZnCl_2$ + $2NaBH_4$ samples milled for 60 minutes, heated at 2°C/min under different hydrogen pressures (3 to 100 bar gauge) at 100 ml/min.

6.6 $NaZn_2(BH_4)_5$ with the Addition of 2mol% of Additive

As shown in the previous section, $NaZn_2(BH_4)_5$ desorbs at 80°C with the release of both hydrogen and diborane. The addition of titanium, nickel, titanium (III) chloride ($TiCl_3$) and magnesium hydride (MgH_2) were used to try to modify the reaction path by changing the mechanism of decomposition.

The TGA in Figure 6.25 shows that all the additions alter the kinetics of the system with the most noticeable being the addition of $TiCl_3$, where the onset temperature was reduced by 15°C to 70°C, compared to the sample without additive. In addition, the weight loss is reduced by 0.6 to 11.66 wt.%. There is less of an improvement in the kinetics with the other

additives, but all speed-up the decomposition process with no change to the release of diborane.

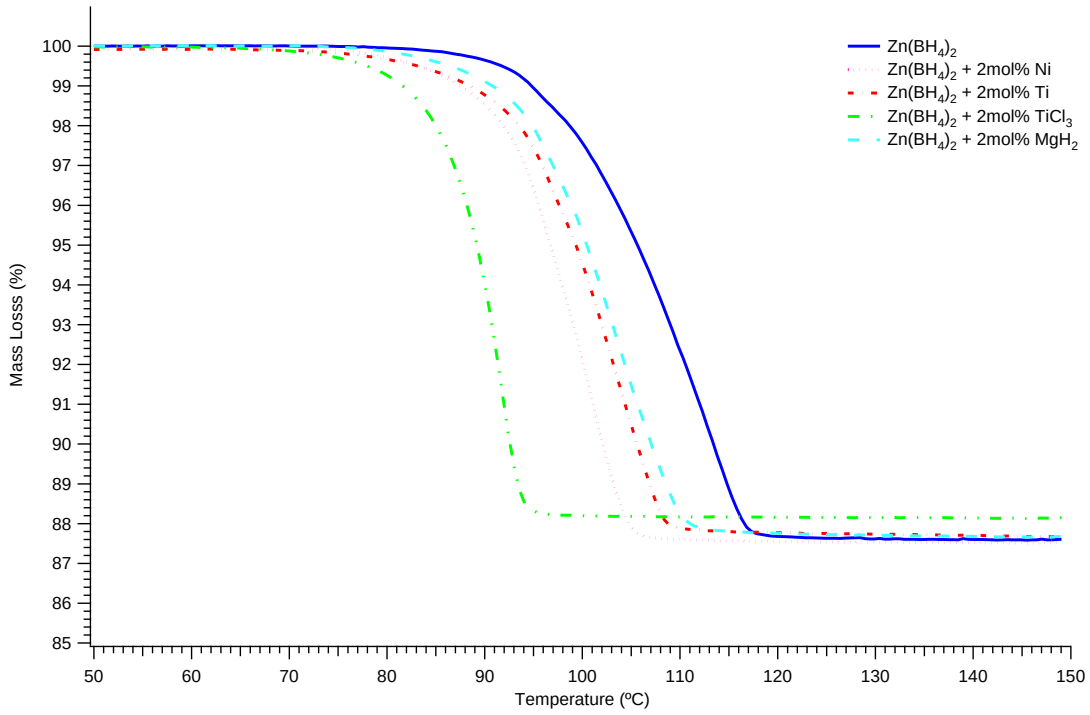

Figure 6.25 TGA decomposition of $ZnCl_2$ + $2NaBH_4$ + 2mol% X (X= Ti, Ni, $TiCl_3$ and MgH_2) milled for 20 minutes, heated at 2°C/min in flowing 1 bar argon at 40 ml/min.

With increasing milling times the relative ordering of the improvement in kinetics is the same. However, the difference between the additives becomes less, as seen in Figure 6.25, Figure 6.26, Figure 6.27 and Figure 6.28.

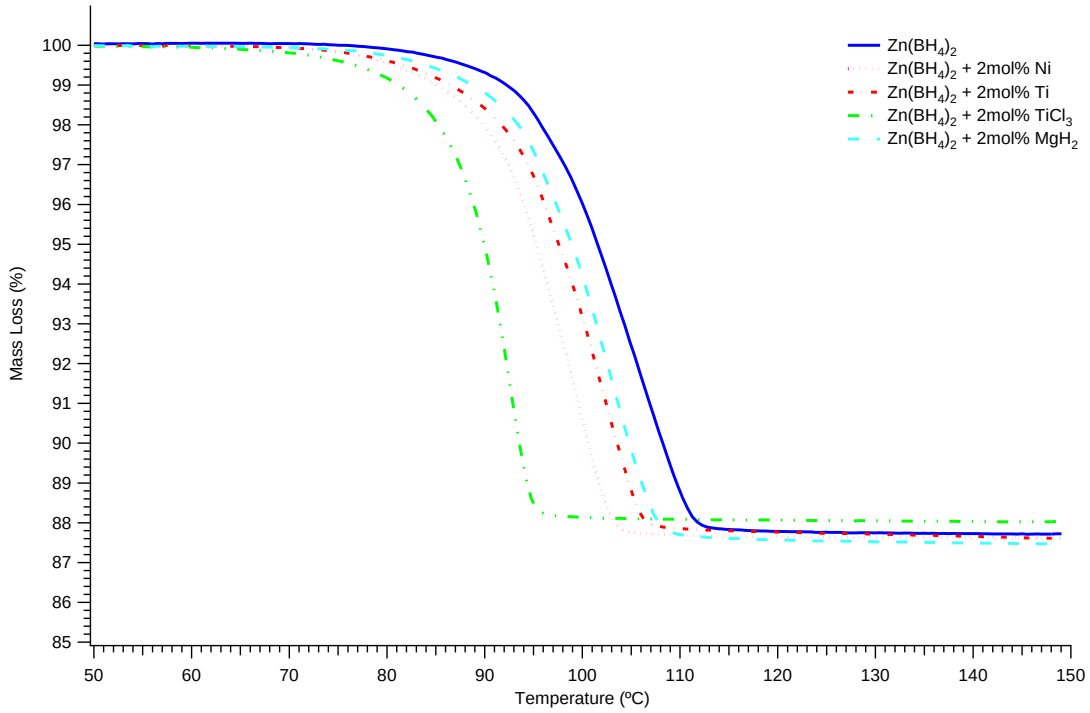

Figure 6.26 TGA decomposition of $ZnCl_2$ + $2NaBH_4$ +2mol% X (X= Ti, Ni, $TiCl_3$ and MgH_2) milled for 40 minutes, heated at 2°C/min in flowing 1 bar argon at 40 ml/min.

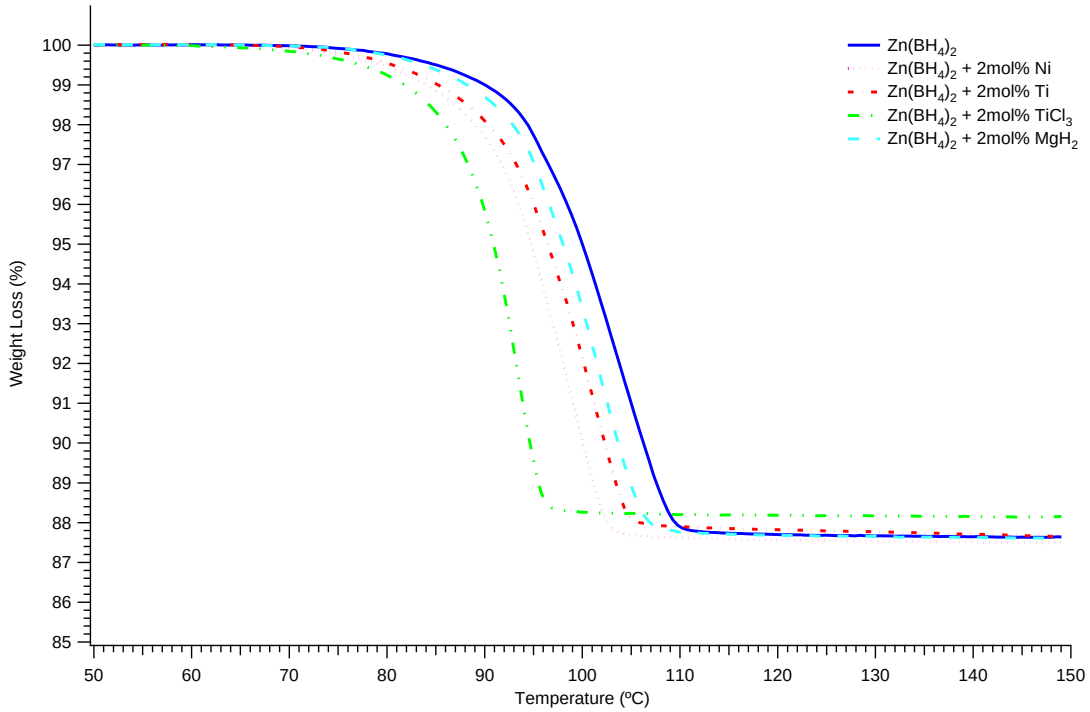

Figure 6.27 TGA decomposition of $ZnCl_2$ + $2NaBH_4$ +2mol% X (X= Ti, Ni, $TiCl_3$ and MgH_2) milled for 60 minutes, heated at 2°C/min in flowing 1 bar argon at 40 ml/min.

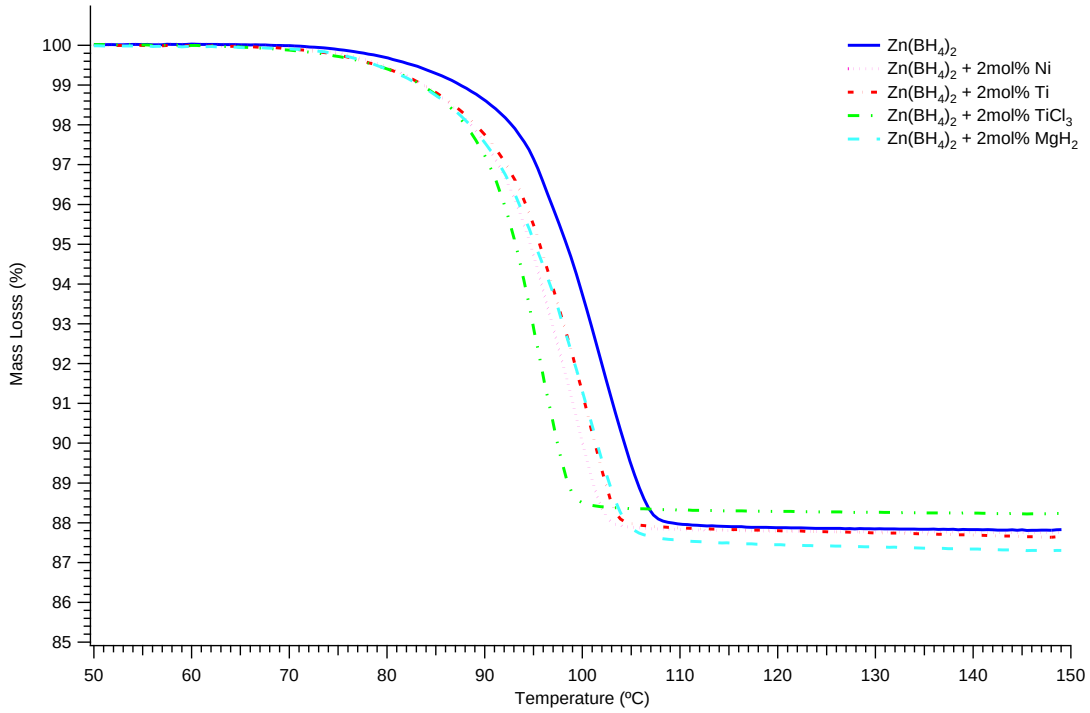

Figure 6.28 TGA decomposition of $ZnCl_2$ + $2NaBH_4$ +2mol% X (X= Ti, Ni, $TiCl_3$ and MgH_2) milled for 120 minutes, heated at 2°C/min in flowing 1 bar argon at 40 ml/min.

The results shown in Figure 6.26, Figure 6.27, Figure 6.28 and Figure 6.29 are summarised in Table 6.6. There is little difference in mass change with milling time for all the samples. There is a reduction in onset temperature with increased milling; this could be due to smaller particle size due to increased milling time, or a better distribution of additive throughout the sample. For the samples containing Ti, Ni and MgH_2, the temperature corresponding to the end of the reaction also decreases so that the overall reaction time remains the same. The exception is the sample containing $TiCl_3$, where the end temperature increases with milling time and the overall reaction time is also increased. This is probably due to the decomposition or reaction of $TiCl_3$ with sodium and sodium/zinc borohydride complexes.

Table 6.6 Summary of TGA results of $2NaBH_4 + ZnCl_2$ +2mol% X (X= Ti, Ni, $TiCl_3$ and MgH_2) samples milled for 120 minutes, heated at 2°C/min in flowing 1 bar argon.

20 mins	No addition	2% Ni	2% Ti	2% $TiCl_3$	2% MgH_2
Onset (˚C)	98.9	91.7	93.5	86.2	94.0
Mid (˚C)	107.9	98.2	100.9	90.0	101.9
End (˚C)	116.9	104.7	108.3	93.8	109.8
Reaction time (min)	9.0	6.5	7.4	3.8	7.9
Mass change (%)	-12.31	-12.37	-12.07	-11.66	-12.15
40 mins	No addition	2% Ni	2% Ti	2% $TiCl_3$	2% MgH_2
Onset (˚C)	95.2	90.3	92.2	87.0	93.5
Mid (˚C)	103.1	96.7	99.1	90.9	100.6
End (˚C)	111.0	103.1	106.1	94.9	107.6
Reaction time (min)	7.9	6.4	7.0	4.0	7.1
Mass change (%)	-12.18	-12.23	-12.05	-11.62	-12.19
60 mins	No addition	2% Ni	2% Ti	2% $TiCl_3$	2% MgH_2
Onset (˚C)	94.0	89.9	91.1	87.9	92.9
Mid (˚C)	101.5	96.2	97.9	90.9	99.5
End (˚C)	109.1	102.5	104.8	95.9	106.2
Reaction time (min)	7.6	6.3	6.9	4.0	6.7
Mass change (%)	-12.12	-12.24	-12.03	-11.62	-12.13
120 mins	No addition	2% Ni	2% Ti	2% $TiCl_3$	2% MgH_2
Onset (˚C)	92.9	89.8	90.5	89.4	89.8
Mid (˚C)	99.8	96.0	97.1	94.1	97.1
End (˚C)	106.7	102.3	103.7	98.7	104.5
Reaction time (min)	6.9	6.3	6.6	4.7	7.4
Mass change (%)	-11.91	-12.11	-11.98	-11.41	-12.32

DSC of the additive samples is shown in Figure 6.29. The samples containing Ni, Ti and MgH_2 exhibit a similar trace to that of zinc borohydride alone (i.e $2NaBH_4$+$ZnCl_2$ with no additives), with the melting not being affected but the decomposition portion of the endothermic peak becoming more compressed, which is what is observed in the TGA results. The sample containing $TiCl_3$ has a radically different shape, showing only one endothermic peak at a lower temperature than that of melting for the sodium/zinc borohydride complex.

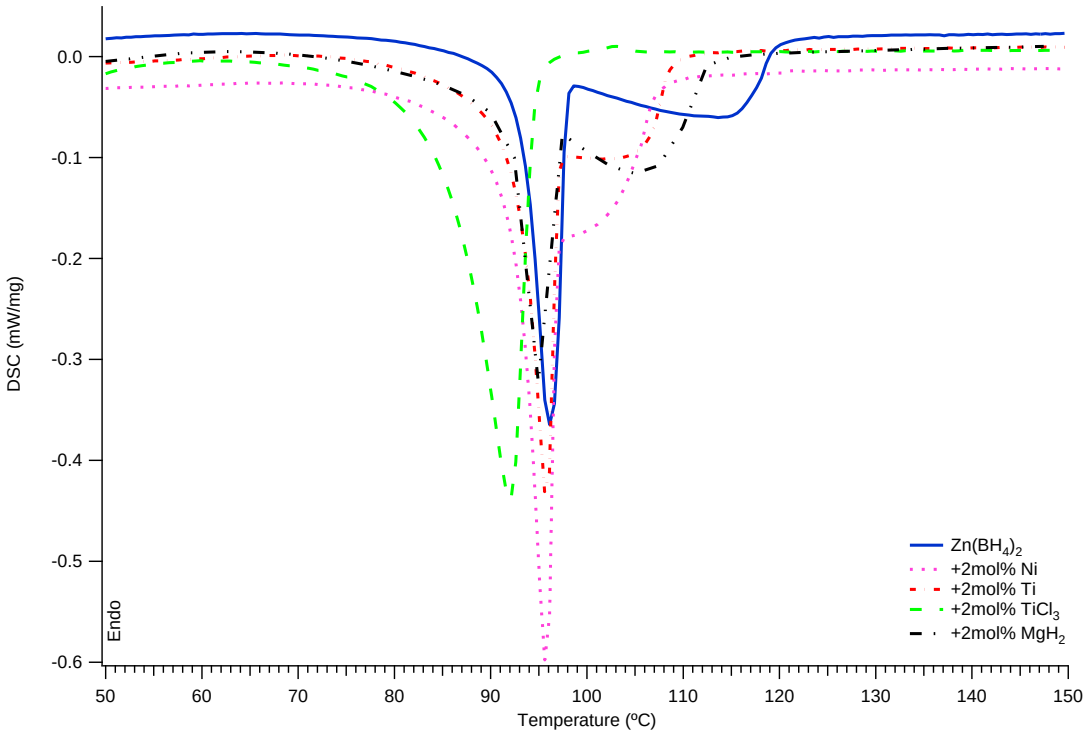

Figure 6.29 DSC of $2NaBH_4$ + $ZnCl_2$ +2mol% X (X= Ti, Ni, $TiCl_3$ and MgH_2) samples milled for 60 minutes, heated at 2°C/min in 1 bar argon at 100 ml/min.

6.7 $2ZnCl_2 + 4NaBH_4 + MgH_2$

Magnesium hydride was added to the reaction mixture before mechanical milling, in an attempt to reduce the amount of diborane released. The aim was to form zinc borohydride with discrete magnesium hydride particles. It was postulated that the magnesium hydride added to zinc borohydride would react with diborane by Nakagawa et. al. [157]. However, this work only took a brief look at the system and did not fully investigate the mechanisms involved.

Figure 6.30 shows TG/MS of $2ZnCl_2 + 4NaBH_4 + MgH_2$ milled for 60 minutes. The first decomposition reaction starts at around 80˚C and finishes at 100˚C, with a weight loss of ~7.6 wt.%. Both hydrogen and diborane are evolved. A second decomposition starts at 250˚C and finishes at 375˚C, corresponding to a weight loss of 1.5% due to the release of only hydrogen in two distinct steps.

Figure 6.30 also shows the DSC measurement, where a large exothermic peak at 90˚C overlaps with the melting and decomposition endotherms normally observed for $ZnCl_2 + 2NaBH_4$ samples [137]. There are then two endothermic peaks between 260 and 360˚C, corresponding to the evolution of hydrogen. The final endothermic peak occurs without weight loss at 360˚C and is possibly due to the melting of metallic zinc.

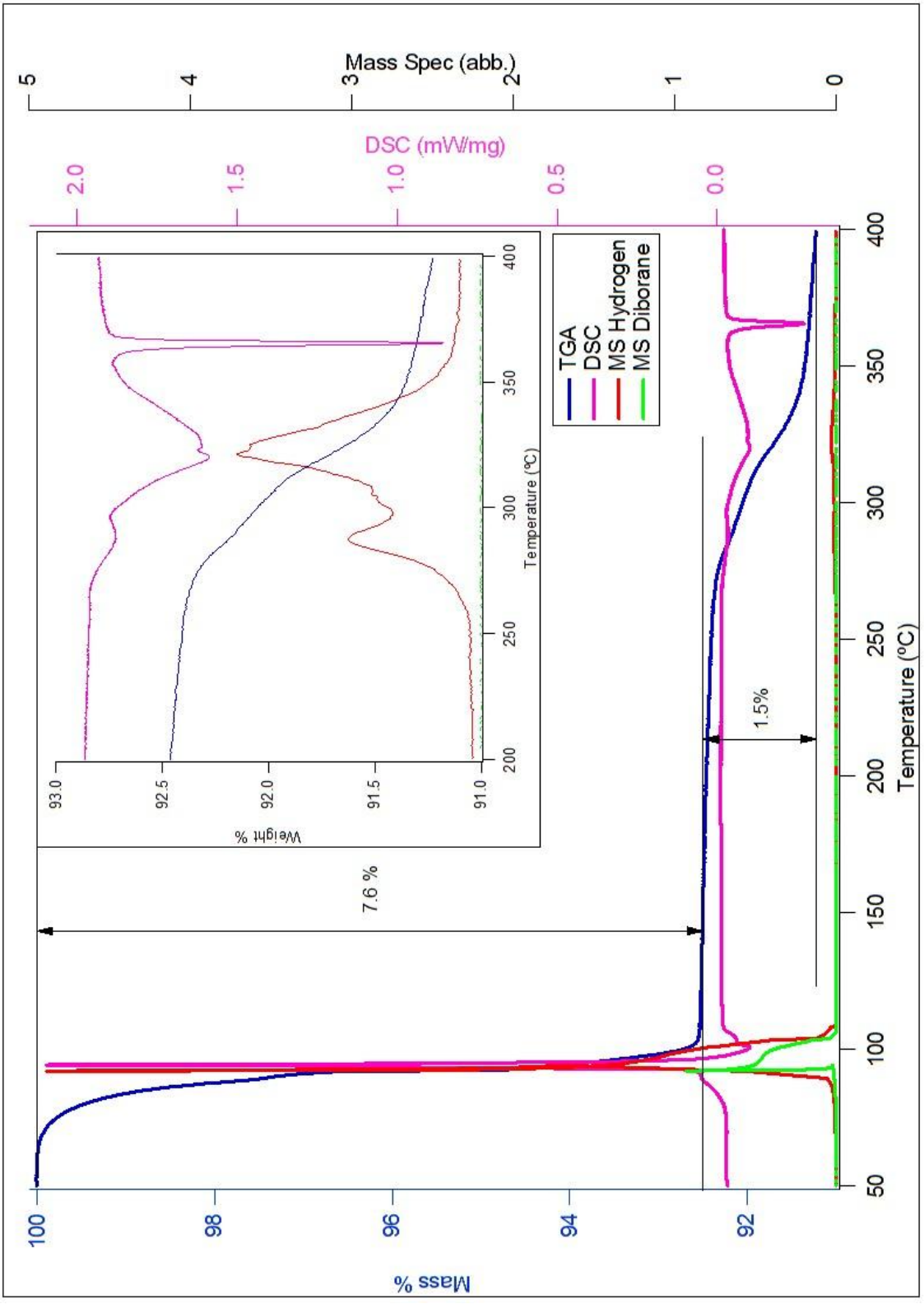

Figure 6.30 TG DSC and MS of hydrogen, diborane (B_2H_6) for a $2ZnCl_2 + 4NaBH_4 + MgH_2$ sample milled for 60 minutes, heated at 2 °C/min under 1 bar argon at 40 ml/min (for TGA/MS) and under 4 bar argon at 100 ml/min (for DSC).

The weight loss of 1.5 wt.% observed between 250 and 375˚C in Figure 6.30 is greater than the 0.45 wt.% possible from the desorption of only the MgH_2 within the sample. Figure 6.31 shows the FTIR spectra of as milled $2ZnCl_2 + 4NaBH_4 + MgH_2$ milled for 60 minutes with the characteristic stretching bands at ~2450 cm^{-1} due to B-H_t, at ~2100 cm^{-1} due to B-H_b attributed to $NaZn_2(BH_4)_5$ and a broad peak at around 625 cm^{-1} due to Mg-H.

Upon heating to 150˚C the vibrational modes due to $NaZn_2(BH_4)_5$ are no longer present, but are replaced by a spectrum with major peaks at 1100 cm^{-1} and 2300 cm^{-1} corresponding to an ionic $[BH_4]^-$ group. The lack of a peak due to MgH_2 indicates the formation of $Mg(BH_4)_2$. Upon heating to 400˚C there are no longer any large peaks.

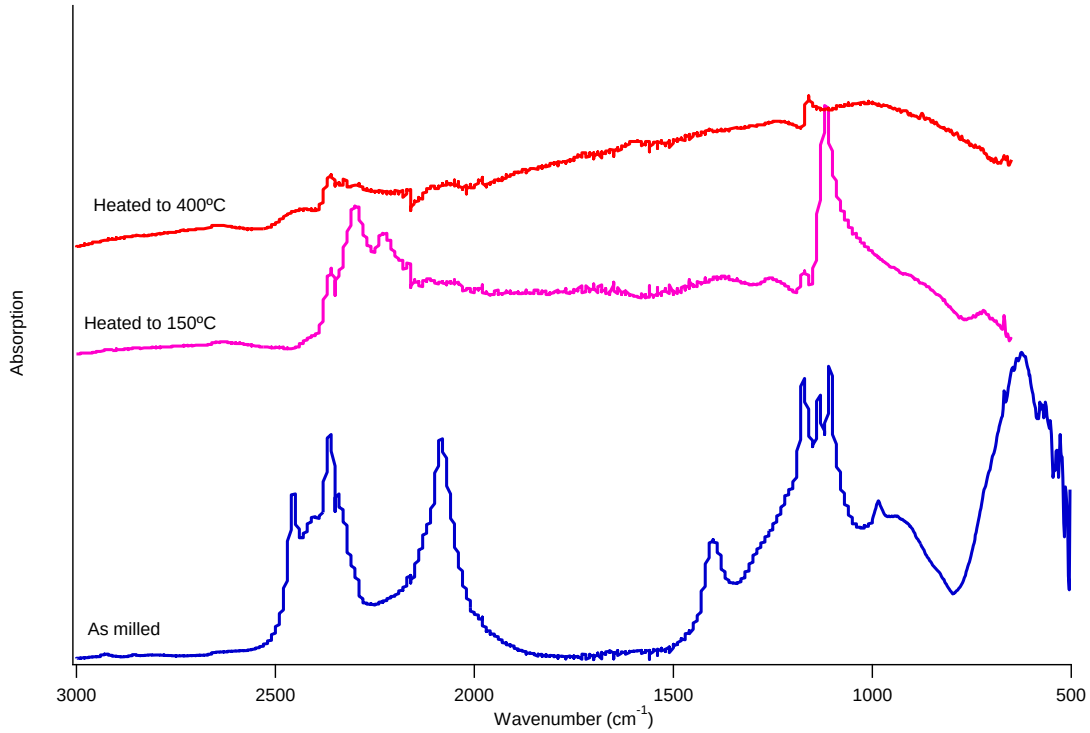

Figure 6.31 Ex-situ FTIR spectra of a $2ZnCl_2 + 4NaBH_4 + MgH_2$ sample milled for 60 minutes, and of samples then heated at 2°C/min to 150˚C or 400˚C under flowing 1 bar argon at 40 ml/min.

To further investigate the reaction path, $NaBH_4$ was substituted by $NaBD_4$. This should allow differentiation between the hydrogen of the magnesium hydride and the deuterium of the zinc borodeuteride, $NaZn_2(BD_4)_5$. Figure 6.32 shows the TG/MS of $2ZnCl_2 + 4NaBD_4 + MgH_2$. The only evolution of hydrogen (from MgH_2) occurs between 85 and 110°C. The release of deuterium (from $NaZn_2(BD_4)_5$) occurs both between 85 and 120°C, and with a 2 stage decomposition between 270 and 370°C. This indicates that decomposition above 120°C is not due to the thermal decomposition of magnesium hydride. Diborane was not looked for in detail as there were many permutations of $B_2H_xD_{6-x}$ that would require an unacceptably long scan time to produce an adequate resolution of the H_2 and D_2 peaks.

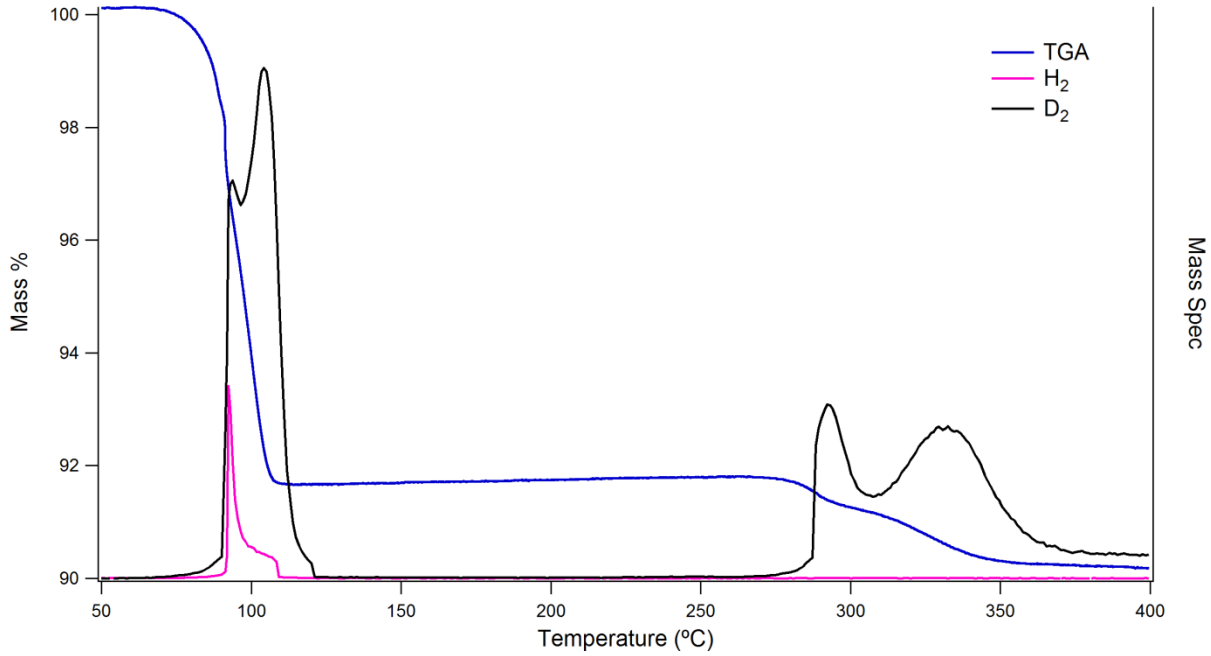

Figure 6.32 TGA of $2ZnCl_2 + 4NaBD_4 + MgH_2$ sample milled for 60 minutes, and MS of hydrogen (m/z = 2) and deuterium (m/z = 4), heated at 2 °C/min in flowing 1 bar argon at 40 ml/min.

Figure 6.33 shows the change in XRD pattern upon heating. All patterns show peaks due to the alumina crucible used and can be ignored, as it will not form part of the reaction. The presence of sodium chloride indicates that the reaction between zinc chloride and sodium borohydride has proceeded, as previously discussed in Section 6.1. The presence of diffraction peaks due to magnesium hydride at room temperature indicates that it has not become involved in any reactions during mechanical milling. Upon heating to 150°C, the presence of metallic zinc peaks indicate the thermal decomposition of zinc borohydride.

From the above results the thermal decomposition of $2ZnCl_2 + 4NaBH_4 + 0.5MgH_2$ can be described as:

90˚C : Decomposition of zinc borohydride and formation of magnesium borohydride

$$NaZn_2(BH_4)_5 + MgH_2 \rightarrow Zn + 2NaCl + xMg(BH_4)_2 + yMgB_2 + zMg + aB + bH_2 + cB_2H_6 \quad (6.7)$$

Above 250˚C : Decomposition of magnesium hydride and magnesium borohydride

$$xMg(BH_4)_2 \rightarrow dMg + eB + fMgB_2 + gH_2 \quad (6.8)$$

or as:

$$NaZn_2(BH_4)_5 + 0.5MgH_2 \rightarrow Zn + 2NaCl + xMg(BH_4)_2 + yMgB_2 + zMg + aB + bH_2 + cB_2H_6 \quad (6.9)$$

$$\rightarrow Zn + 2NaCl + (y+f)MgB_2 + (z+d)Mg + (a+e)B + (b+g)H_2 + cB_2H_6 \quad (6.10)$$

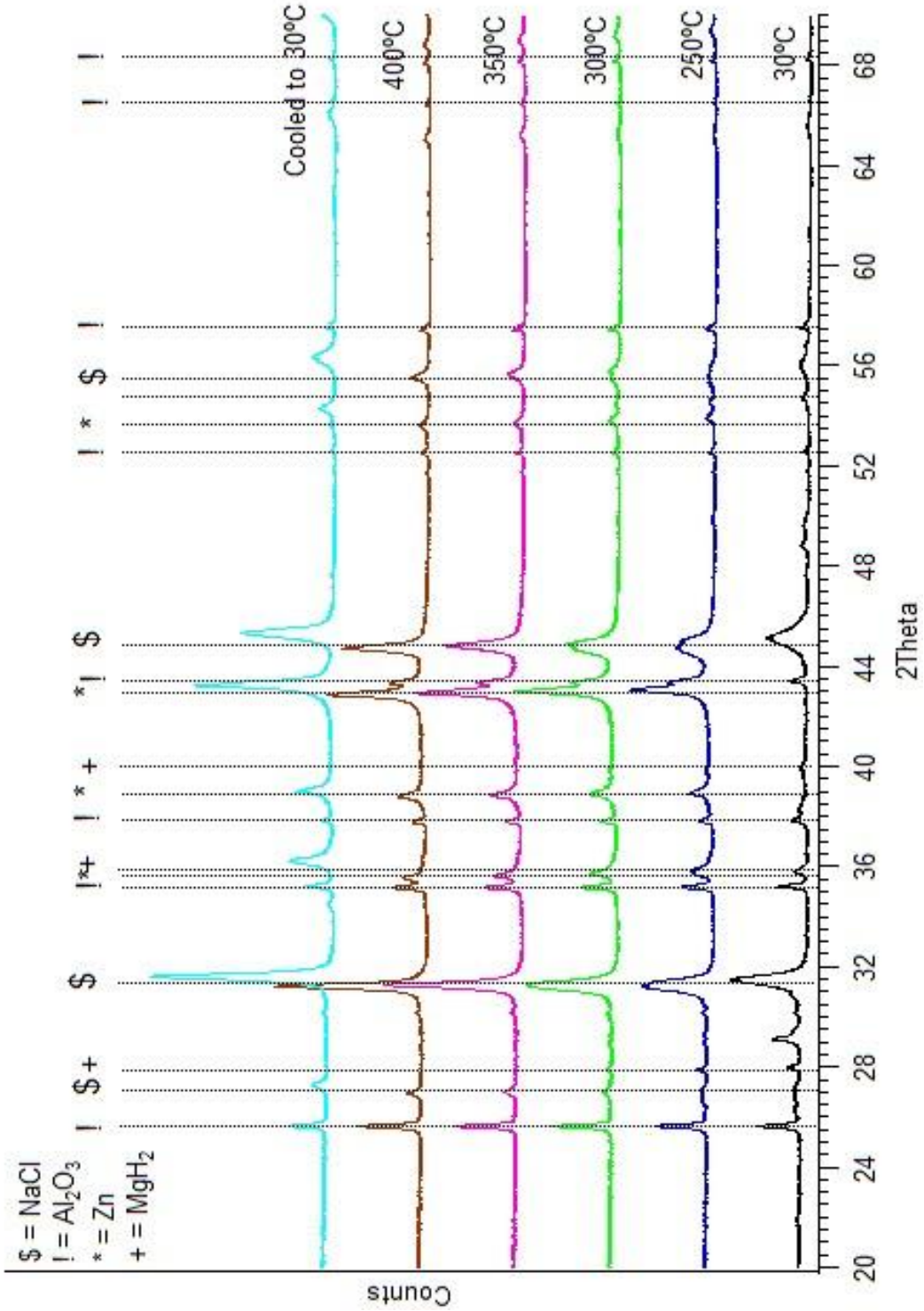

Figure 6.33 In-situ XRD patterns of a $ZnCl_2$ + $2NaBH_4$ + 0.5 MgH_2 sample milled for 60 minutes, heated at 2°C/min under flowing 2.5 bar helium at 100 ml/min.

6.8 Summary

The mechanical milling of alkali metal borohydrides and zinc chloride produced new compounds via metathesis reactions, but not the compound (Reaction 6.1) that was first expected. Instead the reaction formed a $AZn_2(BH_4)_5$ where A = Li or Na compound with sodium chloride, as shown by XRD and Raman. While the lithium and sodium borohydrides have a similar formula the bonding and crystal structure are different due to the difference in alkali metal cation.

Thermal decomposition proceeds with the evolution of both hydrogen and diborane. The decomposition temperature and rate are affected by mechanical milling. Evaluation of the decomposition products shows that crystalline sodium chloride and metallic zinc are formed along with an unknown amorphous boron-containing phase, presumed to be a boron oxide. This indicates that the decomposition mechanism is not any of the proposed mechanisms shown in reactions (6.4), (6.5) and (6.6), however, there is the possibility these decomposition mechanisms may act in competition.

It is not possible to reform the zinc borohydride complex under the conditions used, primarily due to the evolution of diborane.

Addition of 2 mol% of Ti, Ni, $TiCl_3$ and MgH_2 reduced the decomposition temperature. The addition of 2 mol% $TiCl_3$ had a significant effect on the decomposition process: reducing the mass loss and decomposition temperature, and exhibiting a single DSC endotherm that suggests a different decomposition mechanism.

The investigation into the thermal decomposition of mechanically milled $2ZnCl_2 + 4NaBH_4 + MgH_2$ was carried out using TG/MS and DSC. This has a significantly different decomposition mechanism to that of the constituent compounds (milled $ZnCl_2 + 2NaBH_4$ and MgH_2). At 90˚C the exothermic reaction between diborane and magnesium hydride results in the formation of $Mg(BH_4)_2$, with the evolution of hydrogen. Between 260 and 360˚C, decomposition of $Mg(BH_4)_2$ occurs.

7 RESULTS AND DISCUSSION: MAGNESIUM BOROHYDRIDE

Magnesium borohydride is seen as a potential hydrogen storage material due to its hydrogen content of 14.9 wt.% and decomposition temperature below 350°C with only the evolution of hydrogen. Reversibility has been demonstrated to be possible, with approximately 6.1 wt.% of hydrogen being reversibly stored, at 270°C and 400 bar. This chapter will therefore discuss the possible synthesis of magnesium borohydride through mechanical milling, the structural characterisation and the thermal decomposition mechanisms, in order to ascertain whether magnesium borohydride is a potential storage material for on-board applications.

The metathesis reaction between alkali metal borohydride and magnesium chloride mechanically milled at a stoichiometric ratio of 2:1 (shown in equation 7.1) is believed to synthesise magnesium borohydride [18, 43]. Many synthetic routes involve the use of solvent to separate the formed borohydride from the sodium chloride [88]. This work will focus on the metathesis reaction between magnesium chloride and sodium borohydride.

$$MgCl_2 + 2NaBH_4 \rightarrow Mg(BH_4)_2 + 2NaCl \quad (7.1)$$

The standard enthalpies of formation are shown in Figure 7.1. There is a change in enthalpy of $\Delta H = -75.2$ kJmol^{-1} for reaction (7.1). Here, the large heat of formation attributed to magnesium borohydride helps drive the exothermic reaction.

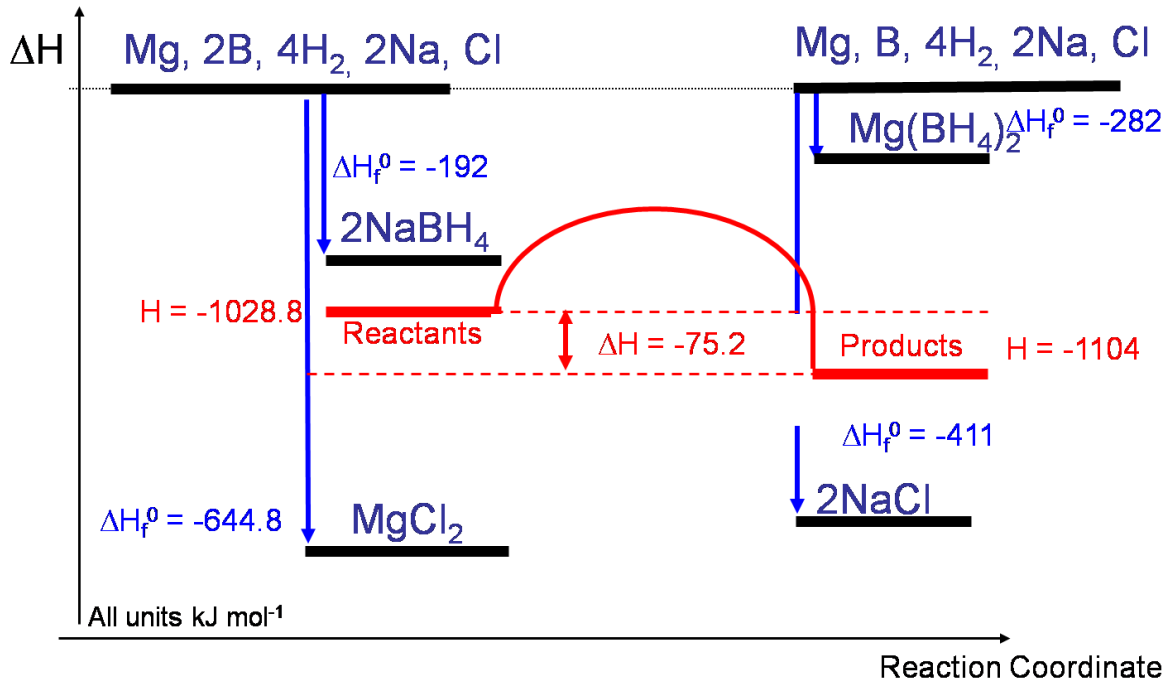

Figure 7.1 Change in enthalpy for the reaction of zinc chloride and sodium borohydride [75, 180].

The structure and thermal decomposition of magnesium borohydride, which has been studied in the past and discussed in greater detail previously (section 3.2.1), has been shown to involve four or five endotherms [81, 84, 182], the first being a solid state phase transition at around 180°C between the α-$Mg(BH_4)_2$ and the β-$Mg(BH_4)_2$ phases. Melting and a small release of hydrogen are observed between 275 and 335°C. Between 305 and 325°C, magnesium borohydride decomposes to form magnesium hydride and the intermediate magnesium dodecaborane, $MgB_{12}H_{12}$, with the evolution of hydrogen. There is then a final decomposition where the hydrogen from the magnesium hydride is released as summarised by Figure 7.2.

$$\alpha\text{-}Mg(BH_4)_2 \rightarrow \beta\text{-}Mg(BH_4)_2 \quad (7.2)$$

$$\rightarrow Mg[BH_4]_{2\,(liq)} \quad (7.3)$$

$$\rightarrow {}^{1}/_{6}Mg(B_{12}H_{12}) + {}^{5}/_{6}MgH_2 + {}^{13}/_{6}H_2 \quad (7.4)$$

$$\rightarrow Mg + 2B + 4H_2 \quad (7.5)$$

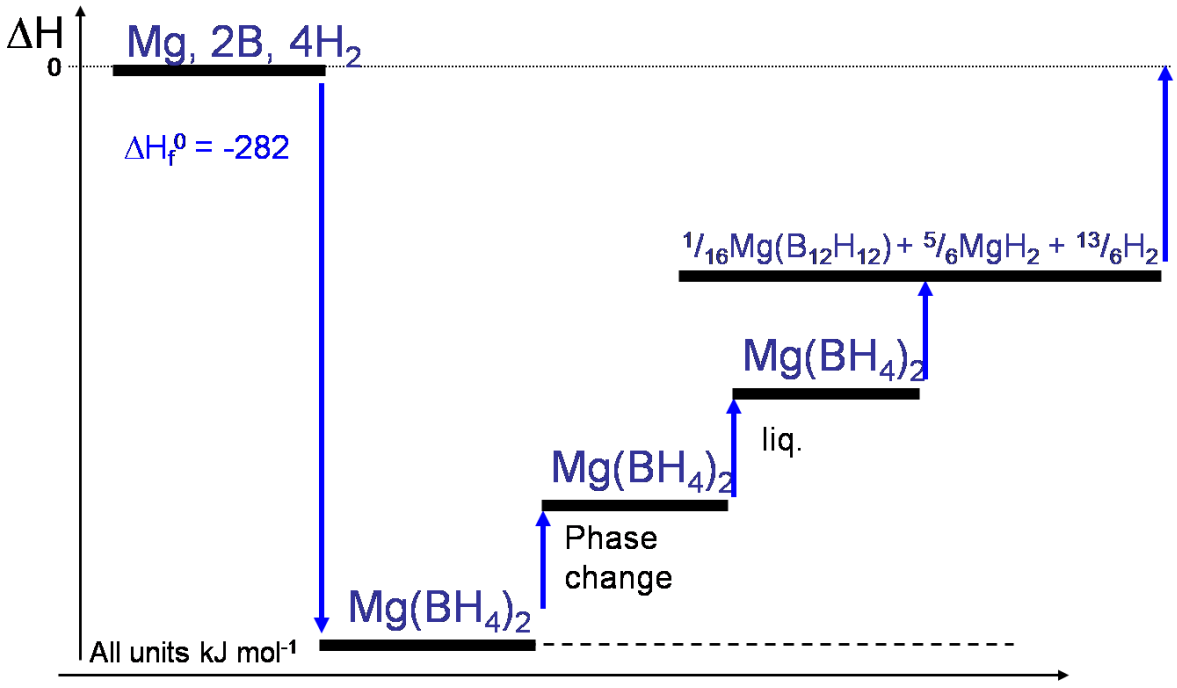

Figure 7.2 Changes in enthalpy for the decomposition of magnesium borohydride [75].

Another thermal decomposition mechanism proposed by Solovenichik et al. indicates a decomposition mechanism that has the formation of a number of amorphous intermediates, resulting in the formation of magnesium diboride [87]. Magnesium borohydride was synthesised using the metathesis reaction between sodium borohydride and magnesium chloride in a diethyl ether solution. The decomposition path suggested by Soloveichik et al. in an argon atmosphere initially follows the previously reported mechanism shown in equations (7.2) and (7.3) and then decomposes by the following method:

$$Mg(BH_4)_2 \rightarrow \text{“}MgB_2H_{5.5}\text{”}* + {}^5/_4H_2 \quad (7.6)$$

$$\rightarrow \text{“}MgBH_{2.5}\text{”}* + MgB_4* + {}^{11}/_4H_2 \quad (7.7)$$

$$\rightarrow MgH_2 + {}^1/_{12}MgB_{12}H_{12}* + MgB_4* + {}^{11}/_4H_2 \quad (7.8)$$

$$\rightarrow Mg + {}^1/_{12}MgB_{12}H_{12}* + MgB_4* + {}^7/_2\ H_2 \quad (7.9)$$

$$\rightarrow MgB_2 + 4\ H_2 \quad (7.10)$$

All five of reactions (7.6)-(7.10) evolve hydrogen; the amorphous phases are marked with an asterisk using a combination of TPD and MAS-NMR. This decomposition assumes that all the hydrogen is desorbed up to the maximum of 14.9 wt.%.

With this information, samples of $MgCl_2$ and $NaBH_4$ with a stoichiometric ratio of 1:2 were milled for 20, 40, 60, 120, 300 and 720 minutes to ascertain reaction progress and observe any changes in mechanism or kinetics associated with a change in milling time.

The investigation will be separated into three sections. Firstly, the milled material will be characterised through XRD and Raman spectroscopy to understand any difference in the structure and bonding from the starting materials. Secondly, the decomposition mechanism will be characterised through thermal analysis using TGA/MS and DSC to evaluate the milled material. Finally, the new compounds formed through decomposition will be analysed using Raman, XRD, and in-situ XRD to understand the decomposition mechanism of the milled $MgCl_2 + 2NaBH_4$ sample.

7.1 Characterisation of Milled Material

Characterisation of the milled material is necessary to determine which reaction products have been formed during mechanical milling. The focus is on ascertaining whether magnesium borohydride and sodium chloride are formed. If reaction (7.1) is followed then an understanding of which polymorph of magnesium borohydride is formed will be required. If the reaction does not proceed via equation (7.1) then an understanding of the compounds that are formed must be undertaken in order to allow subsequent analysis of the thermal decomposition.

Figure 7.3 shows the XRD patterns obtained from the milling products. The absence of reflections attributed to sodium chloride in the diffraction patterns indicates that the reaction has not proceeded via equation (7.1) and is similar to that observed by Nakamori et al. [43]. The reflections attributed to magnesium chloride become weak after 60 minutes of milling, while the reflections due to sodium borohydride become weaker and broader with increased milling time and the peaks shift to lower d-spacings. This indicates that a reaction occurs which results in the preferential breakdown of magnesium chloride and the distortion of the sodium borohydride lattice. This also suggests that the reaction has not proceeded via the predicted mechanism, reaction (7.1), but has formed an unknown amorphous phase and altered the crystal lattice of the sodium borohydride and magnesium chloride.

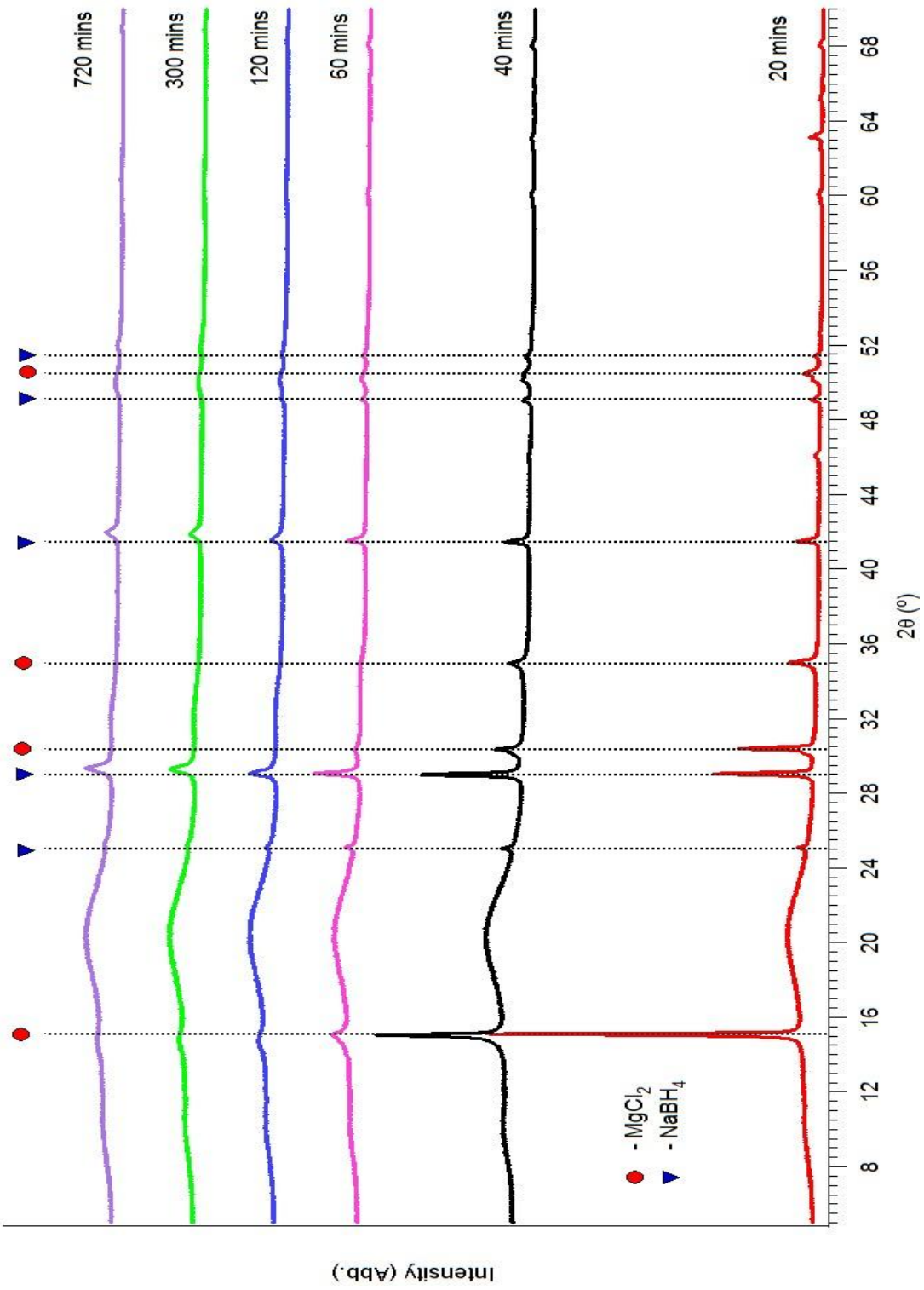

Figure 7.3 XRD patterns of milled $MgCl_2$ + $NaBH_4$ milled for 20, 40, 60, 120, 300 and 720 minutes using the domed sample holder showing $MgCl_2$ and $NaBH_4$ positions.

The lattice parameters of the magnesium chloride and sodium borohydride were determined through Pawley refinement, as shown in Table 7.1. The weight percent of the crystalline phases was also determined. Before milling, magnesium chloride accounted for 55.7 wt.% and sodium borohydride 44.3 wt.%. After milling for twenty minutes the ratio has changed to 46.0 wt.% magnesium chloride and 54.0 wt.% sodium borohydride. This trend continues with increasing milling time until 300 minutes where sodium borohydride accounts for 81.7 wt.% and magnesium chloride 18.3 wt.%. This indicates that the reaction is consuming more magnesium chloride than sodium borohydride. There is a decrease in the peak intensities with longer milling time, indicating that there is an overall reduction in the amount of crystalline material present.

The unit cells of both sodium borohydride and magnesium chloride are changed with milling. Sodium borohydride initially increases in size after 40 minutes milling and as milling duration increases the unit cell contracts. Figure 7.4 shows the change in lattice cell parameters and cell volume with milling time. The **a** parameter initially increases for up to 40 minutes milling time. There is then only a small change for 60 minutes milling time, followed by a decrease in the **a** parameter for up to 300 minutes milling. The **c** parameter increases until 120 minutes milling time before remaining constant with longer milling. The cell volume increases for the first hour of milling, before contracting to a similar volume to the sample milled for 20 minutes. The change in lattice parameters could be due to a number of factors, such as a substitution reaction or deformation caused by milling. A possible substitution reaction is where the chloride ion replaces the borohydride ion in the sodium borohydride matrix to form a solid solution [84] and the borohydride ion reacts with the magnesium to form amorphous magnesium borohydride; this is seen as the most likely mechanism.

Table 7.1 Change in lattice parameters and wt.% of the crystalline phases of $MgCl_2$ + $2NaBH_4$ milled for 20, 40, 60, 120, 300 and 720 minutes.

Milling time	$MgCl_2$				$NaBH_4$		
	lattice parameters (Å)		Cell volume ($Å^3$)	wt.%	lattice parameter (Å) a	Cell volume ($Å^3$)	wt.%
	a	c					
20	3.6425 (3)	17.6716 (10)	234.4634	46.04	6.1600 (3)	233.7449	53.96
40	3.6485(14)	17.7015(70)	235.6344	36.68	6.1639 (9)	234.1891	63.32
60	3.6486 (31)	17.8134 (106)	237.137	33.30	6.1505(13)	232.6651	66.70
120	3.6061 (42)	18.1682 (127)	236.2585	20.61	6.1281(33)	230.1323	79.39
300	3.5939 (46)	18.1148 (131)	233.9729	18.28	6.0849 (33)	225.2996	81.72
720	3.5976 (49)	18.1325 (142)	234.684	17.47	6.0748 (30)	224.1795	82.53

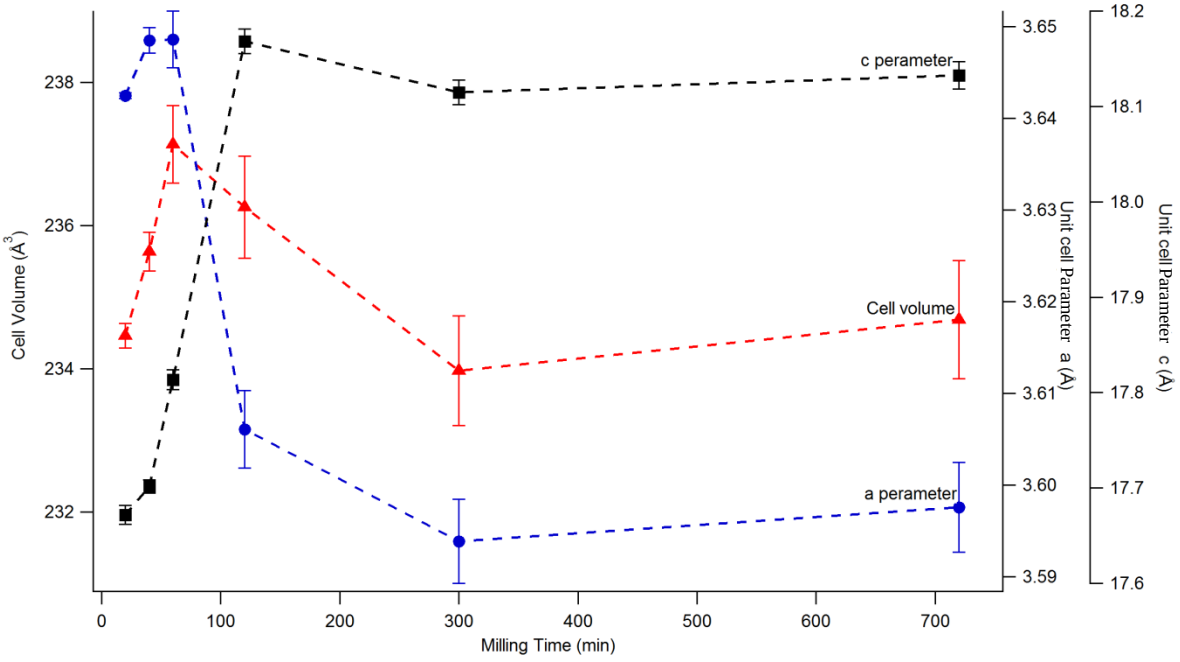

Figure 7.4 Change in unit cell parameters of $MgCl_2$ with milling time.

Figure 7.5 shows the Raman spectra of the milled samples. The characteristic ionic $[BH_4]^-$ stretch at 2250 cm^{-1} indicates that the borohydride group is in a symmetric tetrahedral arrangement, similar to that of sodium borohydride, and the spectra reported by Nakamori et al. [43]. There is also an external vibration which reduces in intensity with milling time that is not observed for pure sodium borohydride, indicating that the sodium borohydride or magnesium chloride lattice has been modified after 20 minutes of milling. With increased milling time, the external mode reduces in intensity, as do the intensities of the crystalline phases shown in Figure 7.3 and summarised in Table 7.2.

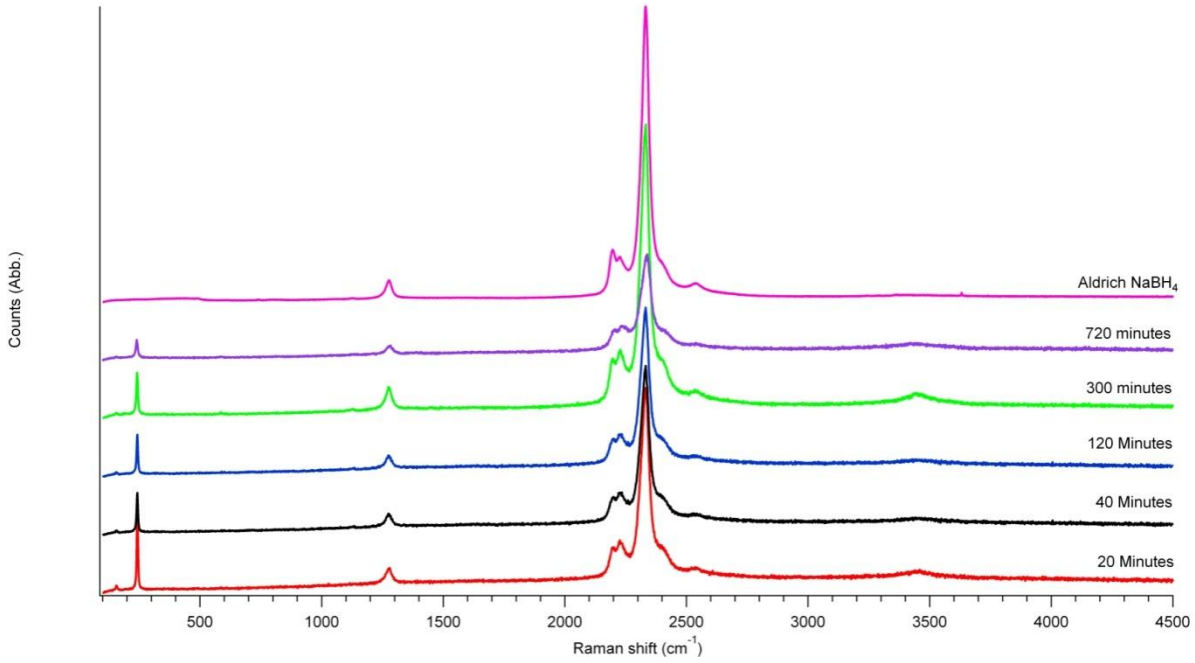

Figure 7.5 Raman spectra of $MgCl_2$ + $NaBH_4$ milled for 20, 40, 120, 300 and 720 minutes using the 488 nm excitation laser.

Table 7.2 Summary of peak positions (in cm^{-1}) from the Raman spectra.

	20 mins	40 mins	120 mins	300 mins	720 mins	$NaBH_4$
External	242.521	242.196	242.786	240.333	240.412	-
B-H bend	1277.1	1276.02	1277.87	1277.47	1279.43	1276.17
B-H stretch	2217.38	2220.09	2227.82	2226.93	2224.83	2210.66
B-H stretch	2330.81	2330.21	2332.2	2334.29	2334.36	2331.37

This all indicates that mechanical milling has not caused the expected metathesis reaction, equation (7.1), to occur and therefore magnesium borohydride, $Mg(BH_4)_2$, or sodium chloride have not been formed. This suggests that an amorphous ionic complex, such as $Na_xMg_y(BH_4)_z$ [84], is formed where the borohydride group sits in an ionic environment with little constraint and deformation of the tetrahedral symmetry.

7.2 Thermal Decomposition

TGA was performed to determine the mass loss and, when coupled with MS, which gases are evolved. Figure 7.6 compares the mass loss of samples milled for different durations from 20 to 720 minutes, with weight losses summarised in Table 7.3. The weight losses and onset temperatures agree well with literature values for the decomposition of magnesium borohydride [43, 84, 86].

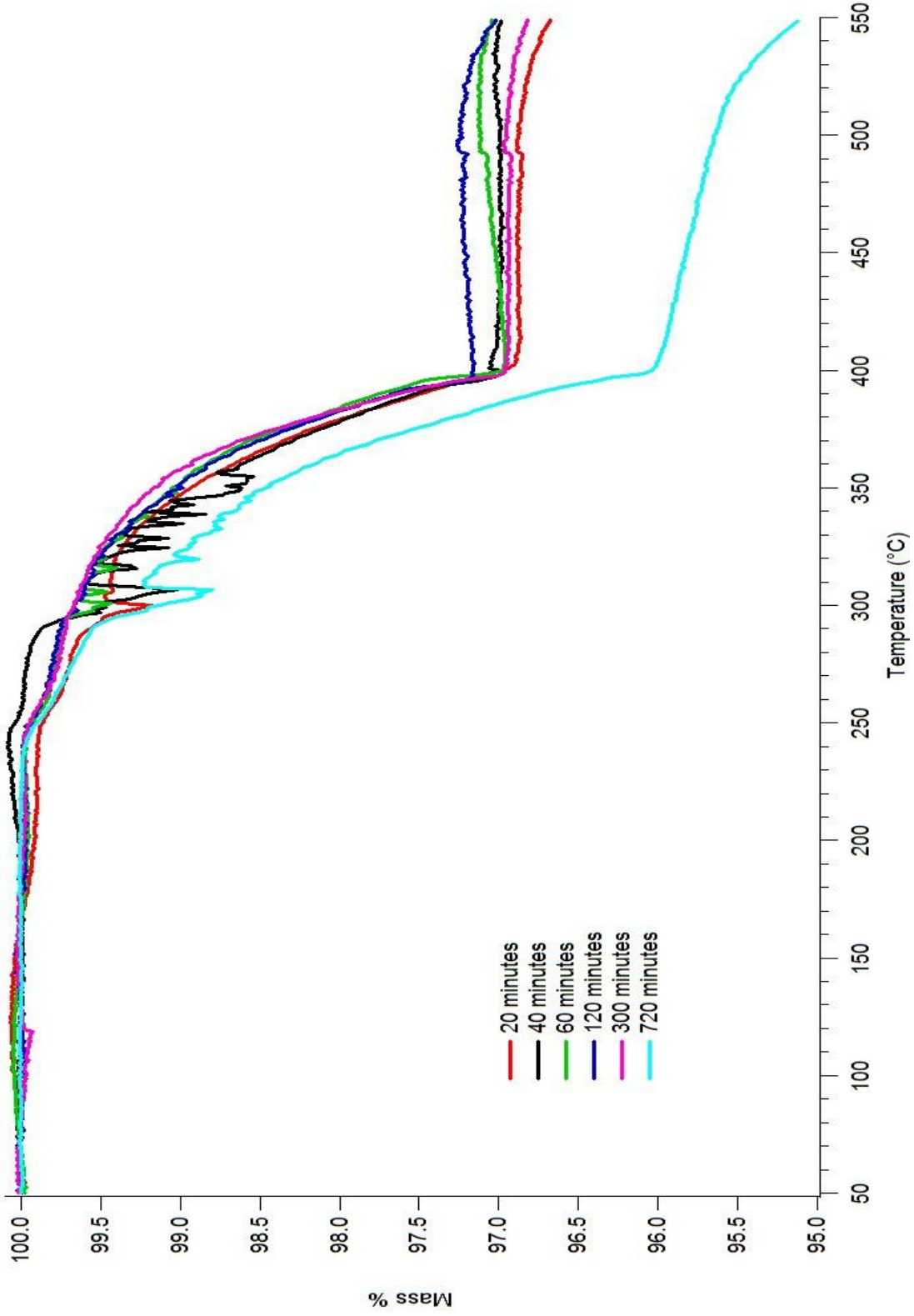

Figure 7.6 TGA of $MgCl_2$ + $NaBH_4$ milled for 20, 40, 60, 120, 300 and 720 minutes heated at 2°C/min in 1 bar argon flowing at 40 ml/min.

Table 7.3 Summary of weight loss and T_d of ball milled $MgCl_2$ + $NaBH_4$**.**

Milling duration (minutes)	**Weight Loss (%)**	**Onset temperature T_d (°C)**	**Mid temperature (°C)**	**End temperature (°C)**
20	3.12 ± 0.30	276	340	403
40	3.01 ± 0.30	283	341	400
60	2.95 ± 0.30	294	349	402
120	2.77 ± 0.50	294	346	398
300	3.06 ± 0.40	295	347	400
720	4.43 ± 0.21	290	345	400

TGA shows that desorption is ‘noisy’, indicating a vigorous reaction that shakes the balance. There is a small change in mass at 240°C, followed by the main decomposition which begins at 280°C and is complete by 410°C. There is little change in the rate of decomposition, indicating the rate of reaction is not dependent on particle size.

Figure 7.7 shows the change in mass loss with milling time. There is a decrease in mass loss from 20 to 120 minutes. The mass loss increases from 2.77 wt.% after 120 minutes, to 4.43 wt.% after 720 minutes. The observed weight loss of around 3 wt.%, which is significantly less than the 4.72 wt.% predicted by reaction (7.5), indicates that either: the reaction predicted for mechanical milling has not proceeded as would be expected; reaction (7.1) has not gone to completion; or that there is another mechanism of decomposition. The sample milled for 720 minutes has a weight loss of 4.43 wt.%, which is close to the theoretical hydrogen content of 4.72 wt.% predicted by equation (7.5).

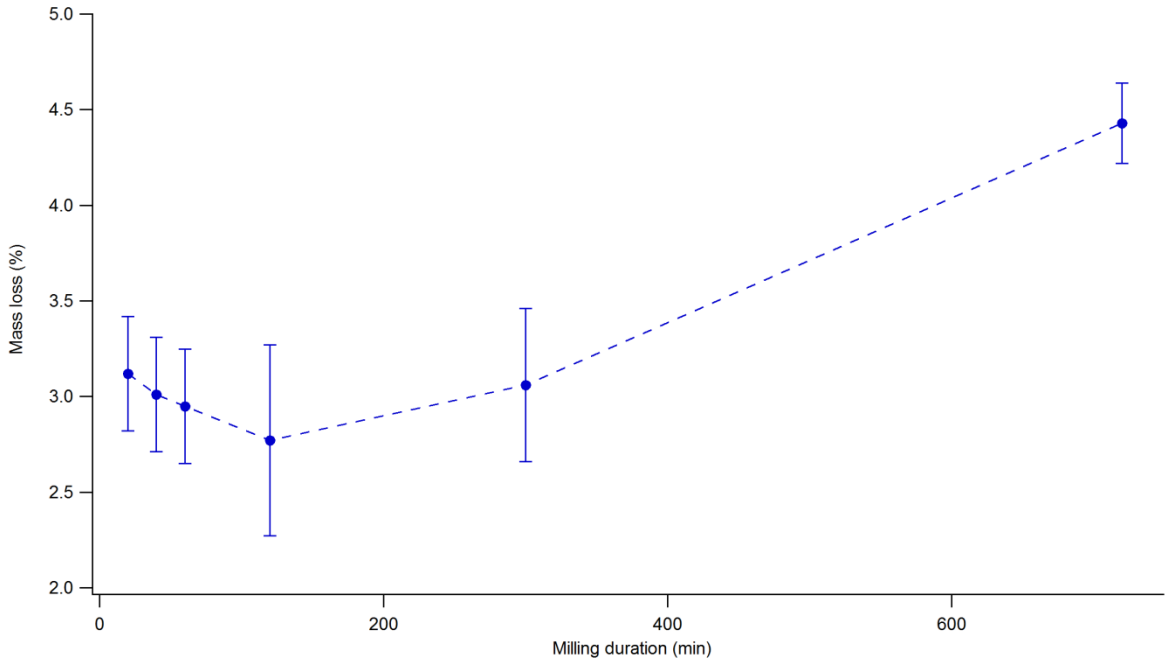

Figure 7.7 Change in mass loss with milling duration.

Figure 7.8 shows that hydrogen is the only gaseous reaction product formed by thermal decomposition of the milled material. No diborane is measured during thermal decomposition. Hydrogen desorption occurs as one large peak that has several steps, some of which are due to range changes in the MS, since the reaction appears to be violent with sudden releases of large quantities of gas. The first decomposition between 240 and 265°C is attributed to a phase change in the material. The main decomposition is observed as two overlapping peaks between 375 and 425°C which can be attributed to the decomposition of the borohydride complex and the subsequent decomposition of the reaction intermediates similar to the results observed by Nakamori et al. for mechanical milling of $2LiBH_4$ and $MgCl_2$ [43].

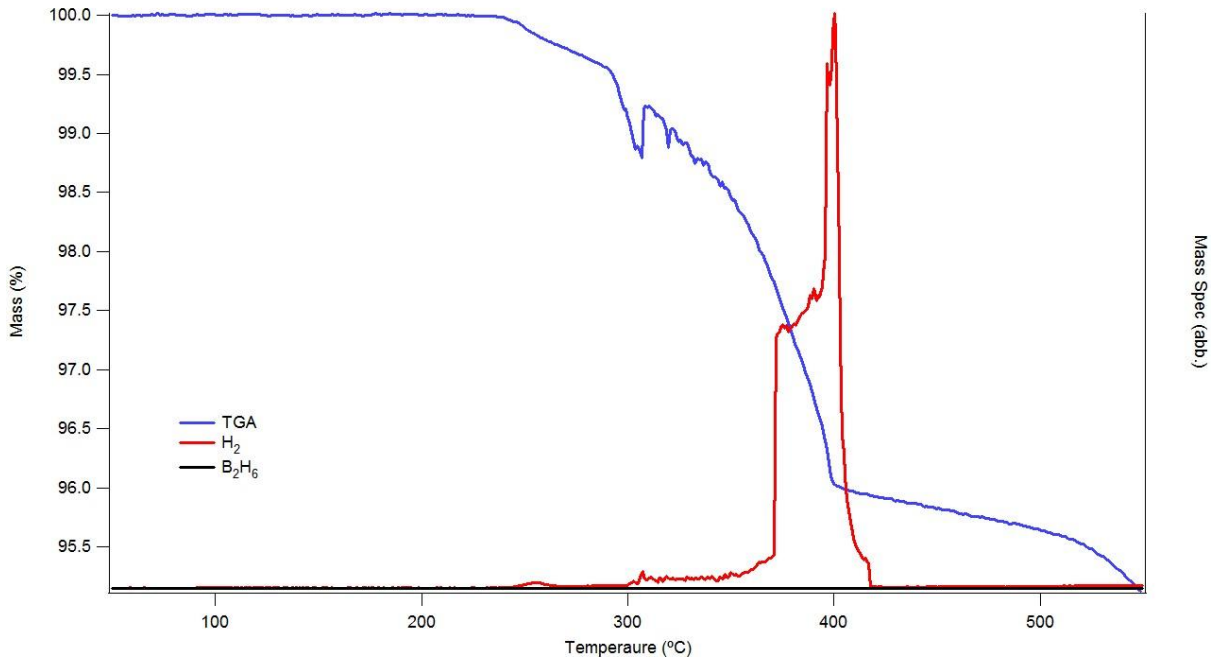

Figure 7.8 TGA and MS of $2MgCl_2 + NaBH_4$ milled for 12h, heated at 2°C/min in 1 bar argon at 40 ml/min.

Figure 7.9 shows the DSC of the sample with different milling times. The absence of a peak at 180°C due to the phase change in magnesium borohydride again indicates that mechanical milling has not formed $Mg(BH_4)_2$. The first large endotherm at approximately 250°C decreases in temperature with milling time. This could be attributed to the melting of magnesium borohydride, or that the compound that is formed by milling is accompanied by a small release of hydrogen. As shown for the sample milled for 720 minutes in Figure 7.10 , the endothermic reaction at approximately 300°C is unchanged with milling time, but is associated with some hydrogen release and mass loss. This could be due to the decomposition of the complex to form magnesium hydride.

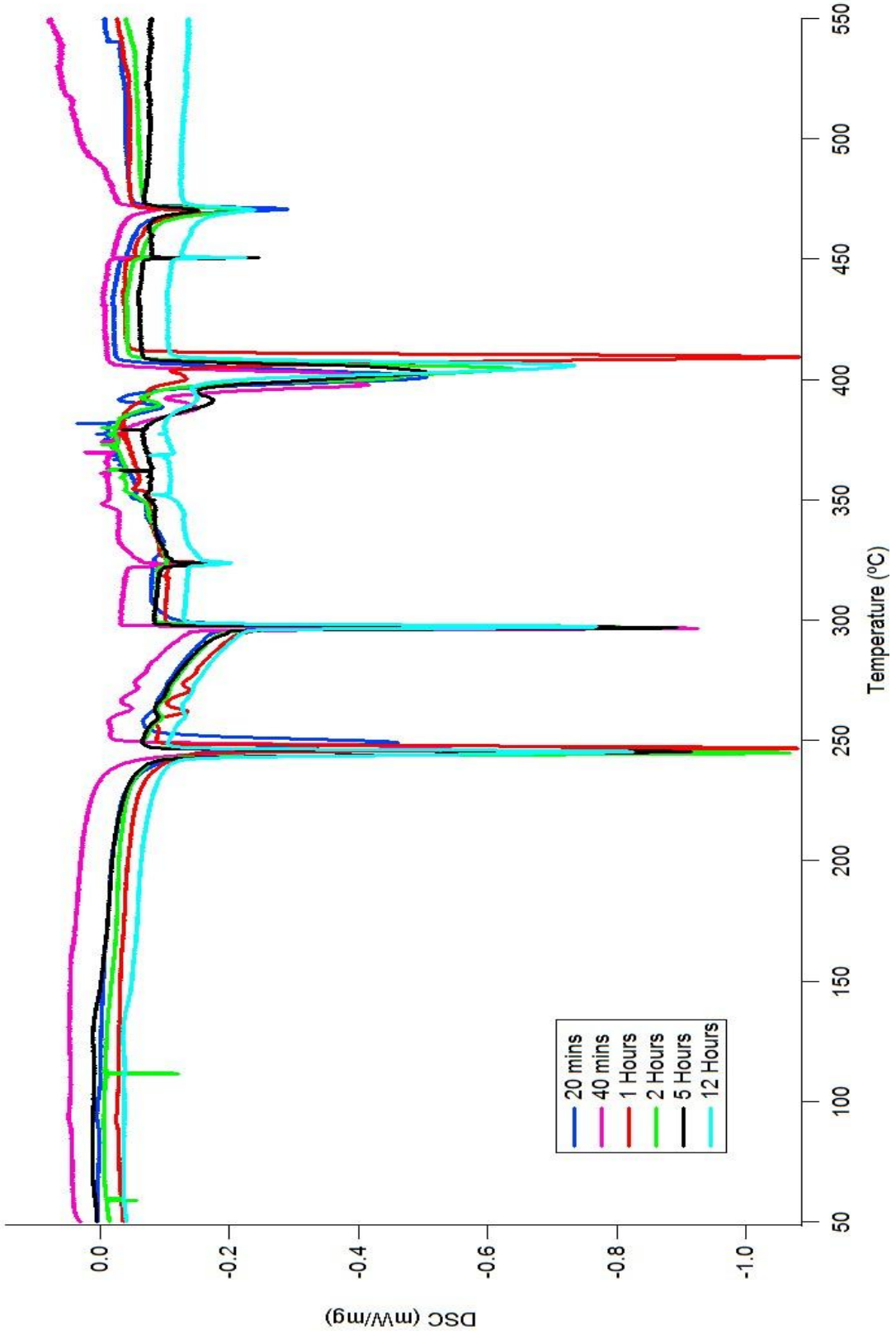

Figure 7.9 DSC of $MgCl_2$ + $NaBH_4$ milled for 720 minutes heated at 2°C/min in 4 bar argon flowing at 100 ml/min.

The final large exotherm above 400°C, that again decreases in temperature with increased milling time and is associated with a large release of hydrogen, is attributed to the decomposition of magnesium hydride. The change in decomposition temperature with milling time could be due to the reduction in particle size with increased milling time.

There are no endotherms relating to the melting of sodium borohydride at 505°C [68], indicating that there is no sodium borohydride present, which shows that there is a reaction between magnesium chloride and sodium borohydride. However, magnesium borohydride, $Mg(BH_4)_2$, is not formed by mechanical milling.

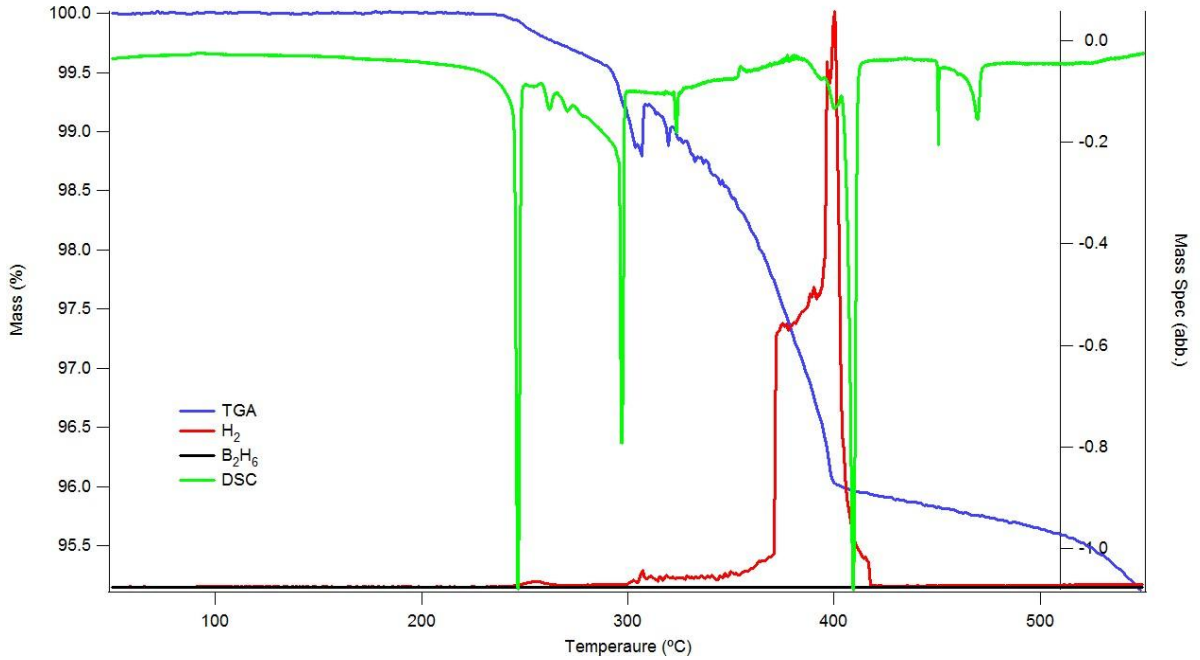

Figure 7.10 TGA/MS and DSC of $MgCl_2$ + $2NaBH_4$ milled for 720 minutes heated at 2°C/min in 1 bar argon at 40 ml/min (TGA/MS), and in 4 bar argon at 100 ml/min (DSC).

7.3 Analysis of Decomposition Products

Figure 7.11 shows the in-situ XRD of $MgCl_2$ + $NaBH_4$ milled for 300 minutes loaded in a corundum sample holder heated at 2°C/min with patterns taken isothermally at 25°C intervals in flowing 2.5 bar helium at 100 ml/min. Initially, sodium borohydride and magnesium chloride are present, as can be seen in Figure 7.12. On heating to 175°C, the reflections due to magnesium chloride become sharper and another unknown phase appears that is not sodium chloride, magnesium hydride or magnesium.

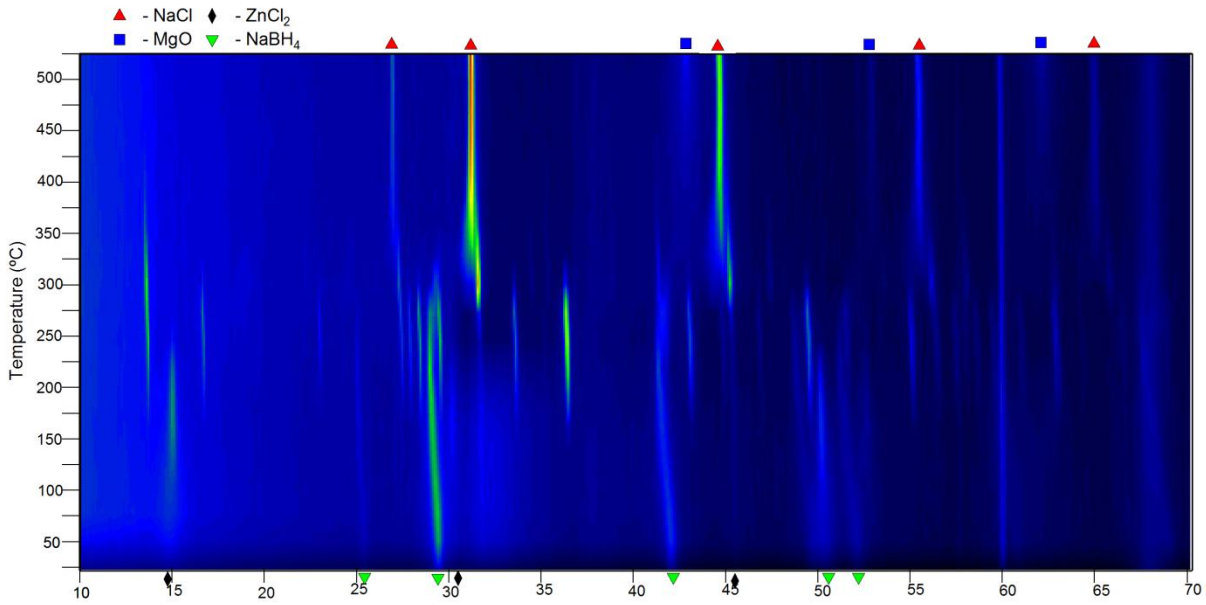

Figure 7.11 In-situ XRD of $MgCl_2$ + $2NaBH_4$ milled for 300 minutes heated at 2°C/min in 2.5 bar helium at 100 ml/min, with patterns taken at 25°C intervals.

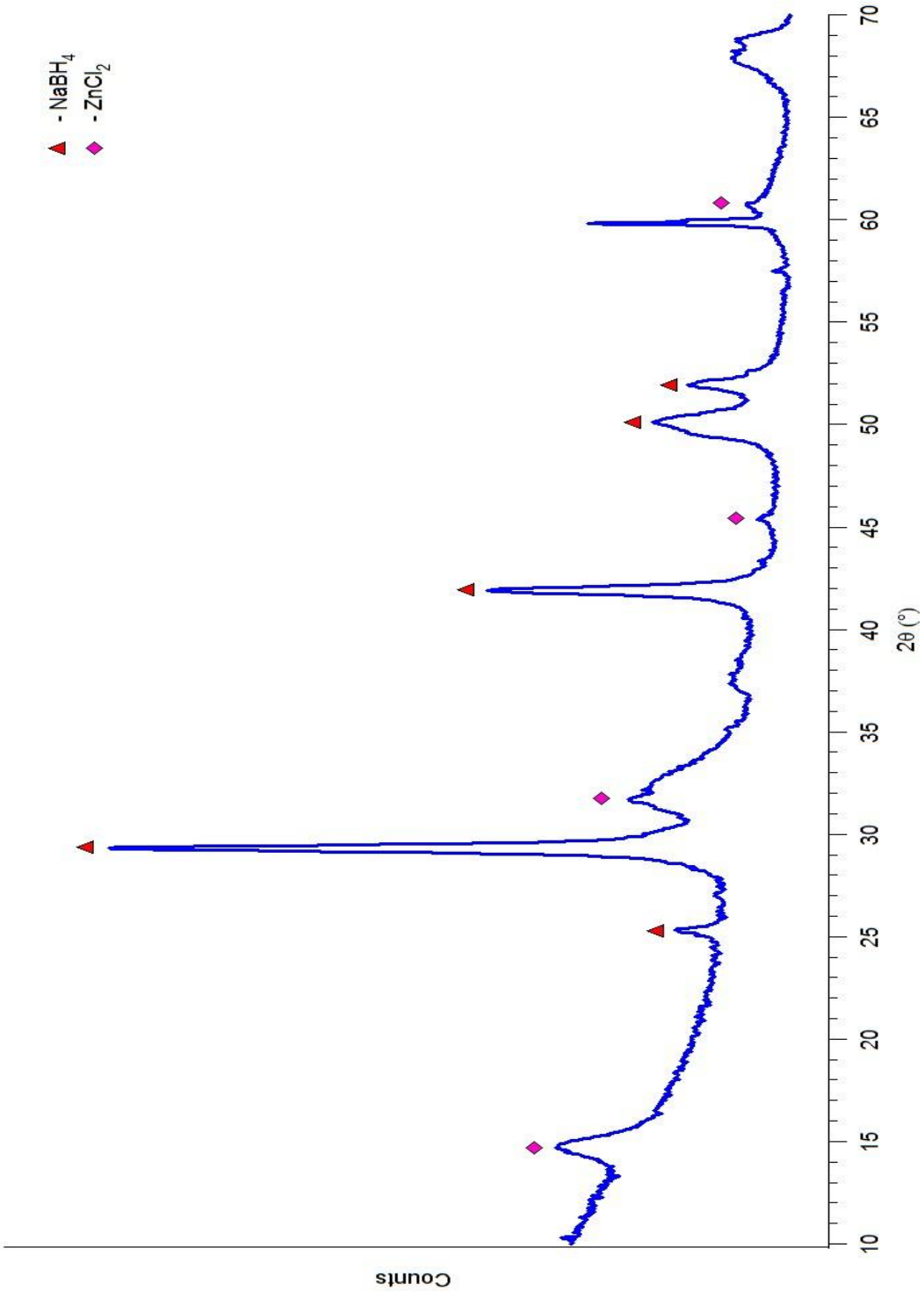

Figure 7.12 XRD pattern of $MgCl_2$ + $2NaBH_4$ milled for 300 minutes measured in-situ at 75°C in flowing 2.5 bar helium at 100 ml/min.

At room temperature, the sample contains only sodium borohydride and some magnesium chloride. On heating, the intensity of these phases, especially the magnesium chloride, increases. At 150°C a new phase (I) is observed. This phase starts to reduce in intensity at 275°C, but is present until 300°C. At 175°C two new phases are present, (II) and (III). None of the three phases matches any of the published structures of magnesium borohydride, either predicted or refined. The unknown phases are not magnesium hydride, nor Na_2MgCl_4.

Phase (II) begins to decompose at 275°C, with small quantities present until 375°C. Phase (III) also begins to decompose at 275°C and is no longer present at 300 °C. The intensity of the three unknown phases grows in intensity as the magnesium chloride and sodium borohydride peaks decrease, with magnesium chloride no longer present at 250 °C. All the sodium borohydride has been consumed by 300°C.

At 300°C an unknown phase (IV) is evident along with the formation of small amount of sodium chloride. This phase has a cubic structure with a lattice parameter a = 5.706 Å, where the peaks have been indexed in Table 7.5. This lattice parameter is slightly smaller than that of sodium chloride (a = 5.761 Å). This unknown phase (IV) is only observed until 350°C, since the sodium chloride peaks become more intense. At 375°C sodium chloride is the only crystalline material present. On further heating there is the formation of magnesium oxide.

It has not been possible to determine and refine the structures of the unknown phases (I), (II), (III), and (IV) due to the quality of the diffraction data and the lack of supporting information about the bonding. The reflection positions are summarised below in Table 7.4 and Table 7.5.

Table 7.4 Summary of the reflection positions of unknown intermediates (I), (II) and (III).

2θ	d	2θ	d
Unknown phase I		**Unknown Phase III**	
33.5139	2.673836	**16.6159**	5.335188
36.30451	2.474456	**27.35588**	3.260115
42.95109	2.105685	**27.80885**	3.208033
		28.32676	3.150546
Unknown Phase II		**29.42915**	3.034992
13.62331	6.499674	**42.95229**	2.105629
22.92547	3.879122	**46.72469**	1.944043
		49.37997	1.845546
		54.96207	1.670585
		62.74889	1.480709

Table 7.5 Indexed reflections of unknown phase (IV).

h k l	2θ	d	Intensity
0 0 1	15.51627	5.70627	0.064936
0 1 1	22.01143	4.03495	0.24771
1 1 1	27.04324	3.29452	8.848575
0 0 2	31.32653	2.85314	66.817638
0 2 1	35.13755	2.55192	0.766752
2 1 1	38.61774	2.32958	2.224685
0 2 2	44.89216	2.01747	66.43577
2 2 1	47.77909	1.90209	0.000135
0 0 3	47.77909	1.90209	0.000135
0 3 1	50.53955	1.80448	1.569711
3 1 1	53.19453	1.72051	3.5595
2 2 2	55.76042	1.64726	22.08567
0 3 2	58.25032	1.58264	1e-010
3 2 1	60.67495	1.52507	0.000129
0 0 4	65.36269	1.42657	6.529126
3 2 2	67.63985	1.38397	12.22516
0 4 1	67.63985	1.38397	12.22516
4 1 1	69.88034	1.34498	10.6361

Figure 7.13 shows the ex-situ XRD pattern of the decomposed material from the in-situ XRD measurement. There are reflections due to sodium chloride and a small fraction of magnesium oxide. There are, however, no peaks corresponding to either metallic magnesium or magnesium hydride as would be expected for decomposition via equations (7.4) and (7.5).

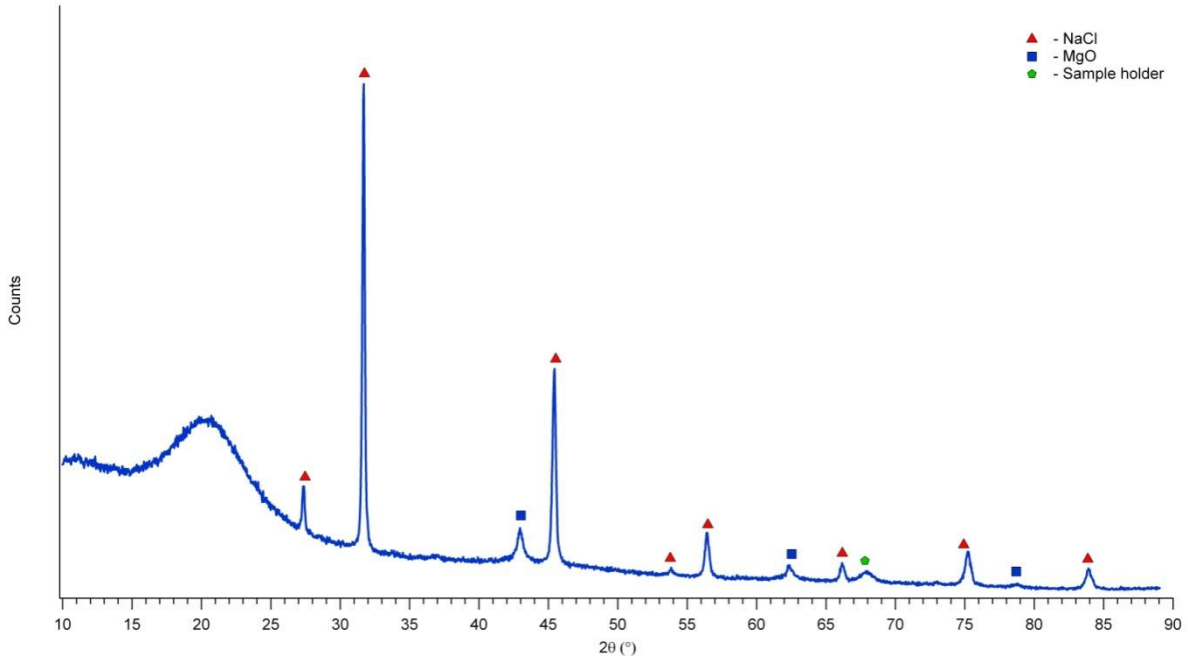

Figure 7.13 Ex-situ XRD pattern of $MgCl_2$ + $2NaBH_4$ milled for 300 minutes and heated to 500°C for the in-situ measurement in **Figure** 7.11 and cooled at 2°C/min in flowing 2.5 bar helium at 100 ml/min.

The refined spectra of Figure 7.13 are shown in Figure 7.14, showing that the decomposed sample contains a large amount of amorphous material and that there is crystalline sodium chloride accounting for around 76 wt.% of the crystalline material. The remaining crystalline material is magnesium oxide. The magnesium oxide is likely to have been formed from the oxidation of pure magnesium in the decomposition products, due to impurities in the gas stream. This indicates a molar ratio of 2.23 sodium chloride molecules to 1 magnesium atom,

suggesting that a small proportion of the magnesium has formed a compound other than metallic magnesium of thermal decomposition.

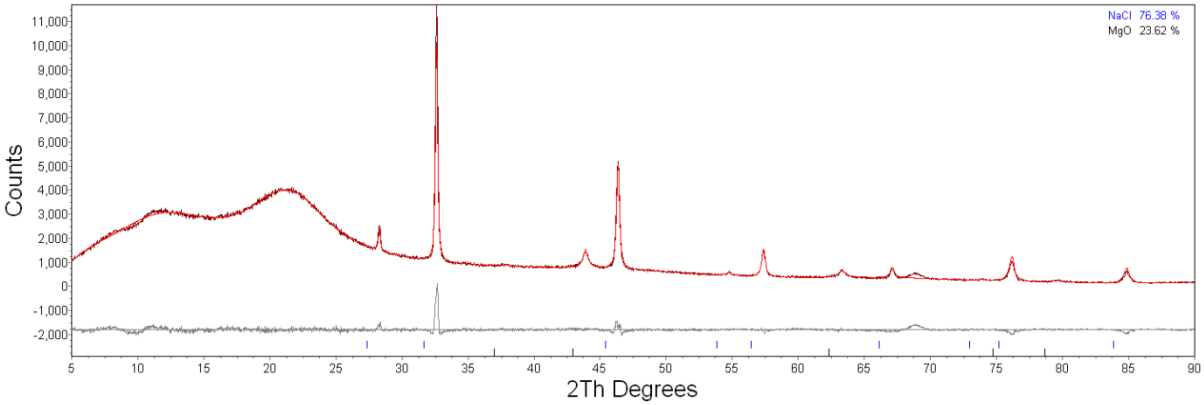

Figure 7.14 Ex-situ XRD pattern of $MgCl_2$ + $2NaBH_4$ milled for 300 minutes and heated to 500°C for the in-situ measurement in **Figure** 7.11 and cooled at 2°C/min in flowing 2.5 bar helium at 100 ml/min.

The sample from in-situ XRD was subsequently measured using Raman spectroscopy (see Figure 7.15), which shows the formation of a closo-dodecaborane $[B_{12}H_{12}]^{2-}$ compound, magnesium diboride and amorphous boron. This shows good agreement with the modes shown for free $[B_{12}H_{12}]^{2-}$ earlier in section 4.3.1. It is not possible to determine whether the $[B_{12}H_{12}]^{2-}$ is the $Na_2B_{12}H_{12}$ or the $MgB_{12}H_{12}$ compound.

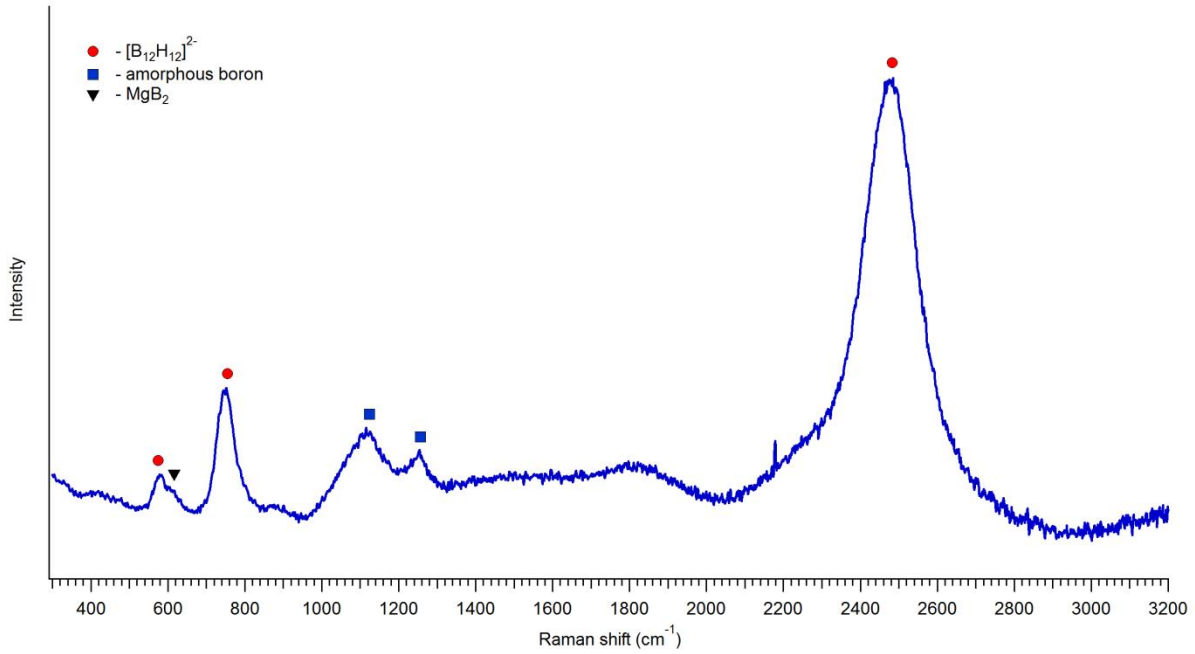

Figure 7.15 Ex-situ Raman spectra of $MgCl_2 + 2NaBH_4$ milled for 300 minutes and heated to 500°C for the in-situ measurement in **Figure** 7.11 and cooled at 2°C/min in flowing 2.5 bar helium at 100 ml/min.

7.4 Conclusion

The aim was to synthesise magnesium borohydride via the metathesis reaction between sodium borohydride and magnesium chloride. Analysis of the milled material indicates that this was unsuccessful.

There is a modification of the sodium borohydride lattice resulting in a 4.09% reduction in volume. The magnesium chloride lattice is also deformed with a reduction in lattice parameter **a** and an increase in the **c** parameter, resulting in little change in unit cell volume.

Raman spectroscopy indicates the borohydride tetrahedron is still present, and in a symmetrical environment. There is an increase in Raman shift for all the internal modes with increasing milling time. An external vibration was observed at 242 cm^{-1} in the samples, which is due to magnesium chloride.

Thermal decomposition of the milled products was performed to further understand the material behaviour, and how it compares to the reported values and published decomposition mechanism. TGA showed a 'noisy' trace, indicating a vigorous decomposition, with an onset at approximately 250°C and completion by 410°C. Samples milled for 300 minutes and less have similar weight losses of approximately 3 wt.%, which is significantly less than the theoretical maximum of 4.7 wt.%, indicating that a hydrogen-containing compound remains on decomposition. The sample milled for 720 minutes loses 4.4 wt.% which is significantly closer to the predicted 4.7 wt.%, indicating that either a different mechanism is taken for this sample compared to the other samples, or that the residual hydrogen containing compound from the other samples decomposes after 720 minutes of milling.

MS shows that only hydrogen is evolved during thermal decomposition. There is a small release of hydrogen at 250°C. The main desorption of hydrogen begins at 300°C with a sharp increase in the rate of evolution of hydrogen at 355°C, which may correspond to the decomposition of magnesium hydride. Hydrogen stops being desorbed by the sample by 425°C.

DSC showed five endotherms and no exotherms on heating to 500°C. The absence of an exotherm indicates that magnesium borohydride is not formed exothermically on heating. The first endotherm at approximately 245°C reduces in temperature with increasing milling

time, indicating that a reduction in particle size could play a part in this reaction. This endotherm corresponds to a small desorption of hydrogen and is therefore believed to be due to a phase rearrangement in the mixture. The second endotherm is sharp and unaffected by milling duration, and corresponds to the onset of hydrogen evolution. The third endotherm at 330°C is comparatively small and occurs just before the increase in desorption rate. The fourth corresponds the main evolution of hydrogen. The fifth endotherm has no associated hydrogen loss, and can be attributed to the formation of another phase or potentially to the sublimation of some of the magnesium still present.

In-situ XRD showed the room temperature magnesium chloride and sodium borohydride reflections. On heating there were four unknown phases observed. It was not possible to gather any further information about the unit cell since the diffraction data is not clear enough. It can be said, however, that the phases observed are not any of the published phases of magnesium, either low or high temperature phases, or simulated phases. None of the unknown phases correspond to the published Na_2MgCl_4 compound. The first unknown compound is observed at 150°C and is present until 300°C. The second and third unknown phases are first observed at 175°C, with the second phase present until 375°C and the third until 300°C. The fourth unknown phase appears to have cubic symmetry similar to that of sodium chloride observed between 300 and 350°C. Sodium chloride and magnesium (oxide) are the only crystalline products observed upon decomposition. No peaks due to magnesium hydride were observed during decomposition, indicating that it was not formed in a crystalline manner. It is believed that the observed magnesium oxide should have remained as metallic magnesium, but had become oxidised. The ratio of magnesium to sodium chloride does not match the stoichiometry of the starting material, therefore indicating that

either a significant proportion of the magnesium had sublimed or that it is bonded in other compounds.

Ex-situ Raman spectroscopy on the decomposed products shows the formation of $[B_{12}H_{12}]^{2-}$. This could be either $Na_2B_{12}H_{12}$ or $MgB_{12}H_{12}$. The $[B_{12}H_{12}]^{2-}$ is in a free environment where the axial and apical vibrations are not split as proposed by Li et al [177]. There are also modes due to amorphous boron and magnesium diboride.

It is therefore proposed that milled sodium borohydride and magnesium chloride in a ratio of 2:1 does not form magnesium borohydride. However, the reaction mixture produces thermal decomposition results that are comparable to those reported for magnesium borohydride [43, 84, 86], and does not behave like the reported decomposition of sodium borohydride.

XRD predicts the following reaction path for the crystalline intermediates and products for a sample milled for 720 minutes:

$$MgCl_2 + 2NaBH_4 \xrightarrow{150°C} MgCl_2 + NaBH_4 + I \quad (7.11)$$

$$\xrightarrow{175°C} MgCl_2 + NaBH_4 + I + II + III \quad (7.12)$$

$$\xrightarrow{250°C} NaBH_4 + I + II + III \quad (7.13)$$

$$\xrightarrow{300°C} II + IV \quad (7.14)$$

$$\xrightarrow{325°C} II + IV + NaCl \quad (7.15)$$

$$\xrightarrow{375°C} NaCl \quad (7.16)$$

$$\xrightarrow{400°C} NaCl + Mg \quad (7.17)$$

Equations (7.13), (7.14) and (7.15) are related to endotherms observed on the DSC. This, combined with the information from the Raman, gives an overall reaction up to 550°C of:

$$MgCl_2 + 2NaBH_4 \rightarrow 2NaCl + {}^{9}/_{10}Mg + {}^{1}/_{25}Mg[B_{12}H_{12}] + {}^{7}/_{5}B + {}^{3}/_{50}MgB_2 + {}^{94}/_{25}H_2$$

This decomposition mechanism is very similar that that proposed by Soloveichik et al. [87] in the formation of the magnesium diboride and magnesium dodecaborane. However, Soloveichik et al. indicates that all the magnesium dodecaborane decomposes to form magnesium diboride as the main phase. There is agreement with the number and temperature of the reactions observed with the work of Varin et al. [84], however, it is uncertain whether the proposed mechanism is the same. This work, however, uses solvent prepared magnesium borohydride and not mechanically milled magnesium chloride and sodium borohydride. The difference between the results could be due to the fact that the sodium chloride acts a barrier to the formation of the intermediates in large enough quantities to allow the formation of magnesium diboride. Therefore the formation of metallic magnesium and amorphous boron is the dominant mechanism.

8 RESULTS AND DISCUSSION: CALCIUM BOROHYDRIDE

Calcium borohydride is seen as a potential hydrogen storage material due to its reported reversibility and decomposition temperature at 400°C with only the evolution of hydrogen [98]. This chapter will investigate the synthesis of calcium borohydride, and its structural characterisation and thermal decomposition behaviour.

The metathesis reaction between sodium borohydride and calcium chloride mechanically milled at a stoiciometric ratio of 2:1 has been shown to result in the formation of calcium borohydride at room temperature in tetrahydrofuran, C_4H_8O (THF) [89]. This product can be purchased from Sigma-Aldrich, and the THF can be removed by heating in a vacuum:

$$CaCl_2 + 2NaBH_4 \rightarrow Ca(BH_4)_2.2THF + 2NaCl \quad (8.1)$$

$$Ca(BH_4)_2.2THF \rightarrow Ca(BH_4)_2 + 2THF \quad (8.2)$$

When the standard enthalpies of formation are compared, as shown in Figure 8.1, there is a change in enthalpy of $\Delta H = +55$ kJmol^{-1}.

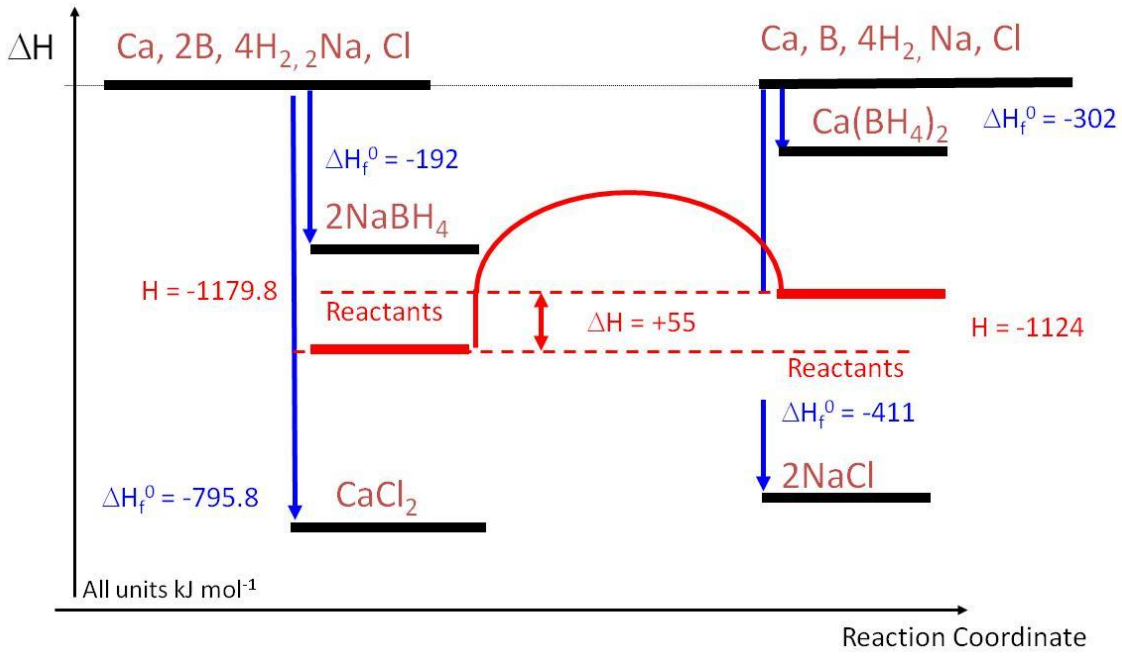

Figure 8.1 Change in enthalpy for the reaction of calcium chloride and sodium borohydride [75, 91, 180].

It has been shown that a number of phases of calcium borohydride are stable at room temperature, and that several phase changes occur during heating. The α-$Ca(BH_4)_2$ phase is thermodynamically the most stable, and is formed using a slow cooling rate. The transition of the α-$Ca(BH_4)_2$ phase into the β-$Ca(BH_4)_2$ phase takes place at around 180°C [91, 99]. Decomposition follows the phase change, with a two-step reaction: the formation of an unknown intermediate (8.4) at 320°C, which subsequently decomposes at 400°C to yield calcium hydride and boron (8.5), with a release of 8.7 wt.% hydrogen. Reactions (8.3)–(8.5) are summarised in Figure 8.2 [102, 183].

$$\alpha\text{-}Ca(BH_4)_2 \rightarrow \beta\text{-}Ca(BH_4)_2 \quad (8.3)$$

$$\rightarrow \text{‘unknown’} + xCaH_2 + yH_2 \quad (8.4)$$

$$\rightarrow CaH_2 + 2B + 3H_2 \quad (8.5)$$

An alternative to reaction (8.5) that may occur is reaction (8.6), where the boron forms CaB_6 with an associated mass change of 9.6 wt.%:

$$\rightarrow \quad {}^{2}/_{3}CaH_2 + {}^{1}/_{3}CaB_6 + {}^{10}/_{3}H_2 \qquad (8.6)$$

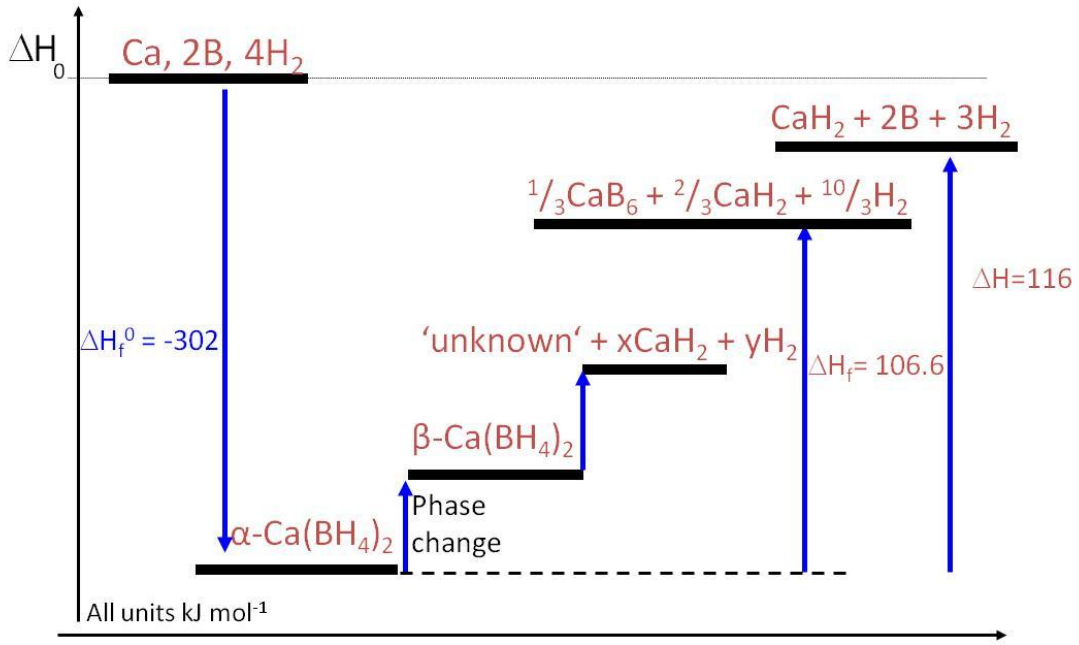

Figure 8.2 Changes in enthalpy for the decomposition of calcium borohydride [91].

In light of the above, samples were prepared by mechanically milling sodium borohydride and calcium chloride; milling times of 20, 40, 60, 120 and 300 minutes were used to ascertain reaction progress and to investigate the rate of decomposition. These samples were compared to samples of $Ca(BH_4)_2$ and $Ca(BH_4)_2.2THF$ purchased from Sigma-Aldrich.

The investigation will be presented in three sections. Firstly, the milled material will be characterised through XRD and Raman and compared with the starting materials. Secondly, the decomposition mechanism will be investigated through thermal analysis, using TGA/MS

and DSC. Thirdly, the new compounds formed after and during decomposition will be analysed using XRD / Raman and in-situ XRD, respectively.

8.1 Characterisation of the As-Received or Milled Materials

Characterisation of the as-received Sigma-Aldrich samples and the milled samples was performed by XRD, to examine the crystal structure and give information on the long range order of the sample and by Raman spectroscopy to give information on the local environment of the borohydride tetrahedron within the lattice.

8.1.1 Room Temperature Characterisation of Sigma-Aldrich $Ca(BH_4)_2$

An XRD pattern of Aldrich $Ca(BH_4)_2$, shown in Figure 8.3, is composed primarily of the β-$Ca(BH_4)_2$ phase with a small proportion of α-$Ca(BH_4)_2$ phase [167]. This is because the sample has been heated to 200°C and then cooled quickly to room temperature, 'locking' the calcium borohydride in the beta phase. Figure 8.4 shows the results of the Pawley refinement on Aldrich $Ca(BH_4)_2$ calculating that the sample consists of 3.7 wt.% α-$Ca(BH_4)_2$ and 96.3 wt.% β-$Ca(BH_4)_2$.

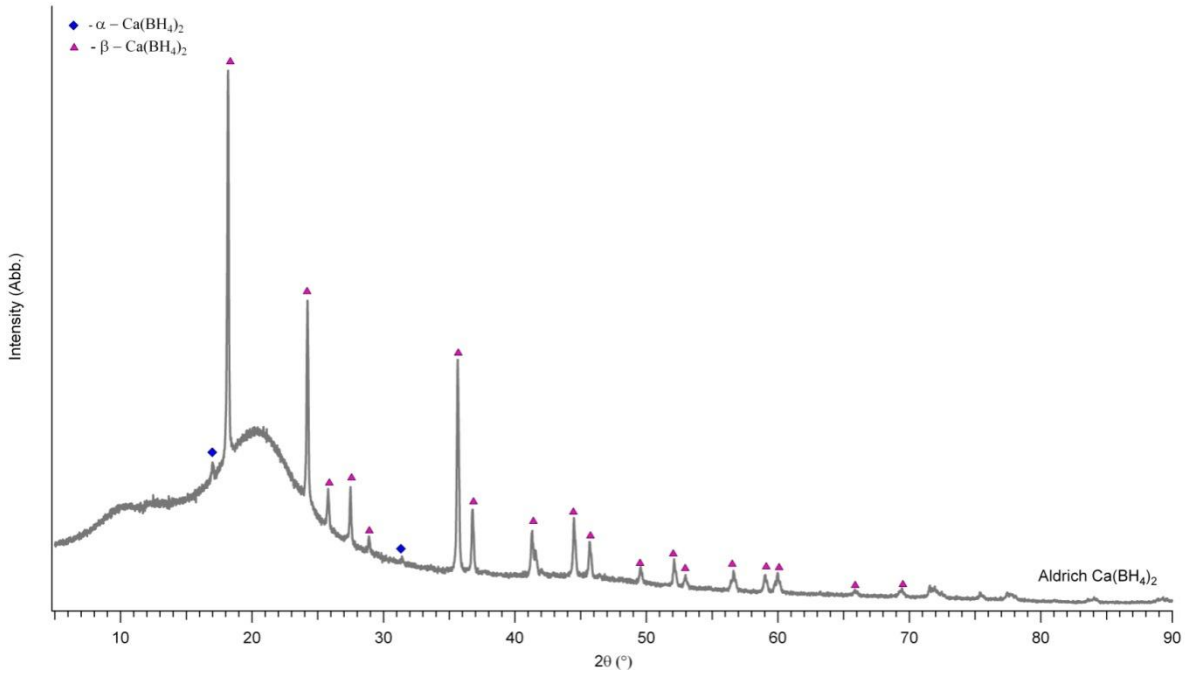

Figure 8.3 XRD pattern of Sigma-Aldrich $Ca(BH_4)_2$.

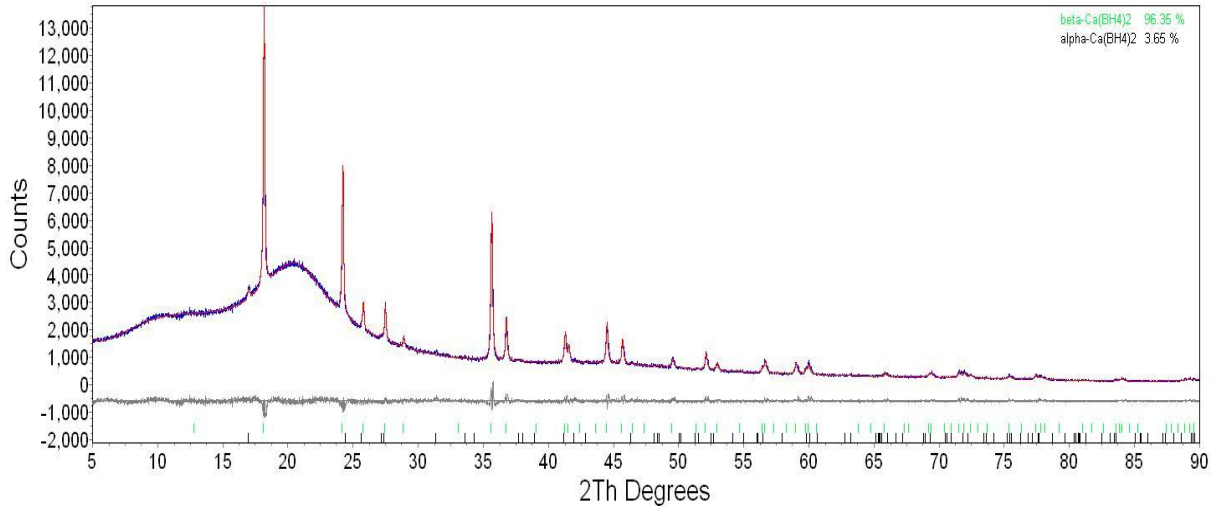

Figure 8.4 Refined XRD pattern of Aldrich $Ca(BH_4)_2$.

Buchter et al. refined the structure of both α- and β-$Ca(BH_4)_2$ [101]. The α phase is orthorhombic with lattice parameters a = 8.7461(8) Å, b = 13.0942(9) Å and c = 7.4660(7) Å. The β phase is tetragonal with lattice parameters a = 6.9468(1) Å and c = 4.3661(1) Å.

During the Reitveld refinement of the Aldrich $Ca(BH_4)_2$, the lattice parameters of α-$Ca(BH_4)_2$ were calculated to be a = 8.763(13) Å, b = 13.129(11) Å and c = 7.502(10) Å and for the β-$Ca(BH_4)_2$ to be a = 6.9175(21) Å and c = 4.3468(15) Å. The unit cells are shown below in Figure 8.5, where the greater freedom of the $[BH_4]^-$ tetrahedron can be seen.

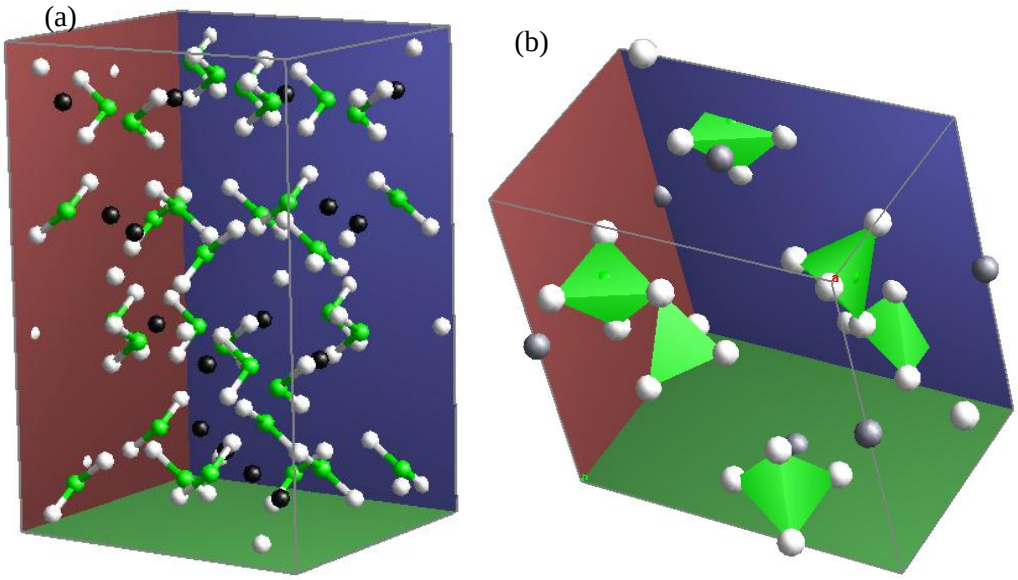

Figure 8.5 Unit cells for (a) α-$Ca(BH_4)_2$ and (b) β-$Ca(BH_4)_2$ generated using a .cif in TOPAS.

The Raman spectrum of Aldrich $Ca(BH_4)_2$ shows the presence of both α-$Ca(BH_4)_2$ and β-$Ca(BH_4)_2$ as shown in Figure 8.6 and Figure 8.7**,** respectively (and compared in Figure 8.8**)**. The vibrational modes have been assigned following the paper by Fichtner et al. [100] and are similar to that of lithium borohydride; this is discussed in greater detail later. Two external and eight internal pure vibrational modes and two overtones were observed for α-$Ca(BH_4)_2$. Six internal pure vibrational modes were observed for β-$Ca(BH_4)_2$, the peak positions of which are summarised in Table 8.1. There is good agreement with the modes observed and assigned by Fichtner et al. for both α-$Ca(BH_4)_2$ and β-$Ca(BH_4)_2$.

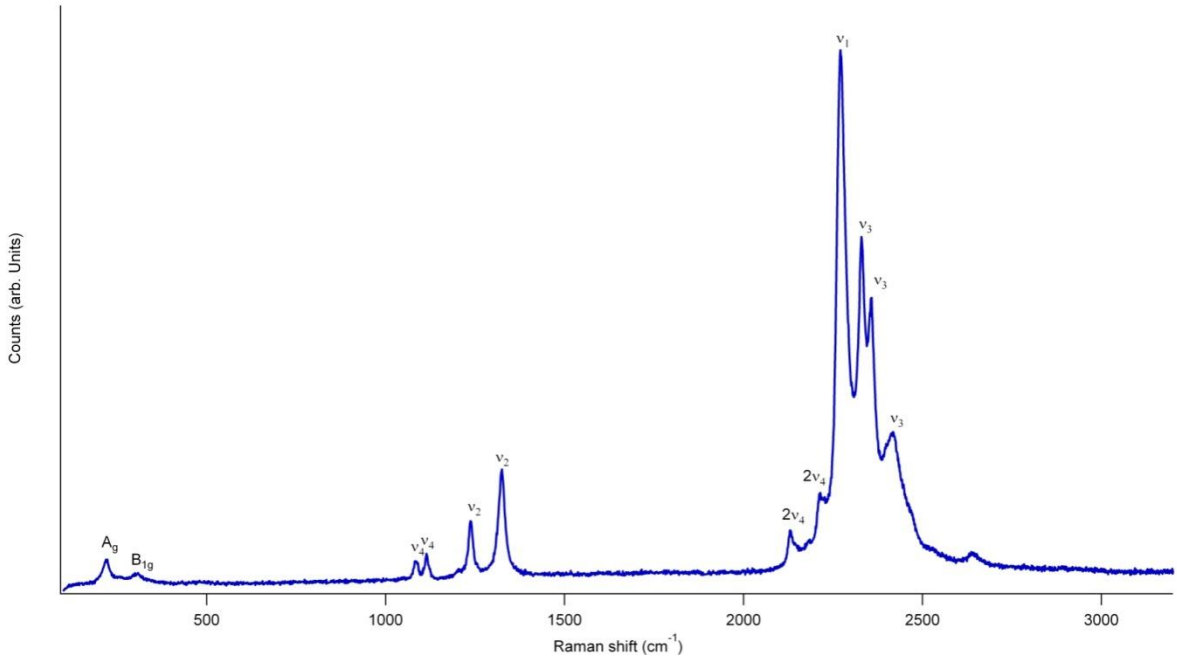

Figure 8.6 Raman spectrum of Sigma-Aldrich α-$Ca(BH_4)_2$ using a 488 nm laser.

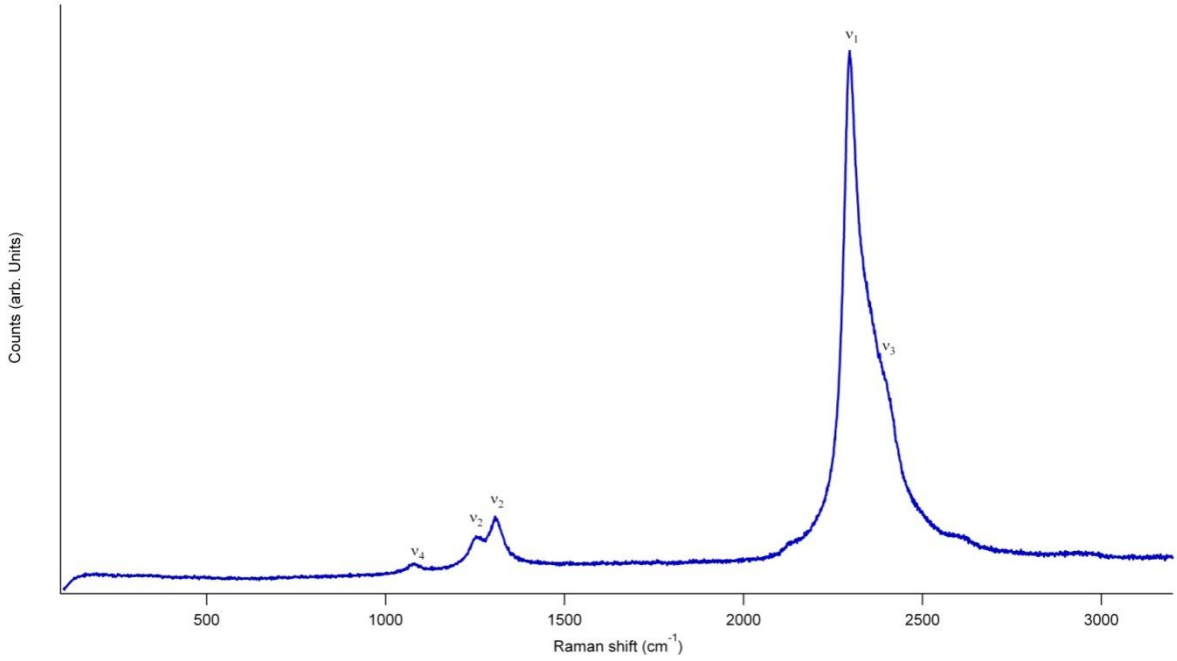

Figure 8.7 Raman spectrum of Sigma-Aldrich β-$Ca(BH_4)_2$ using a 488 nm laser.

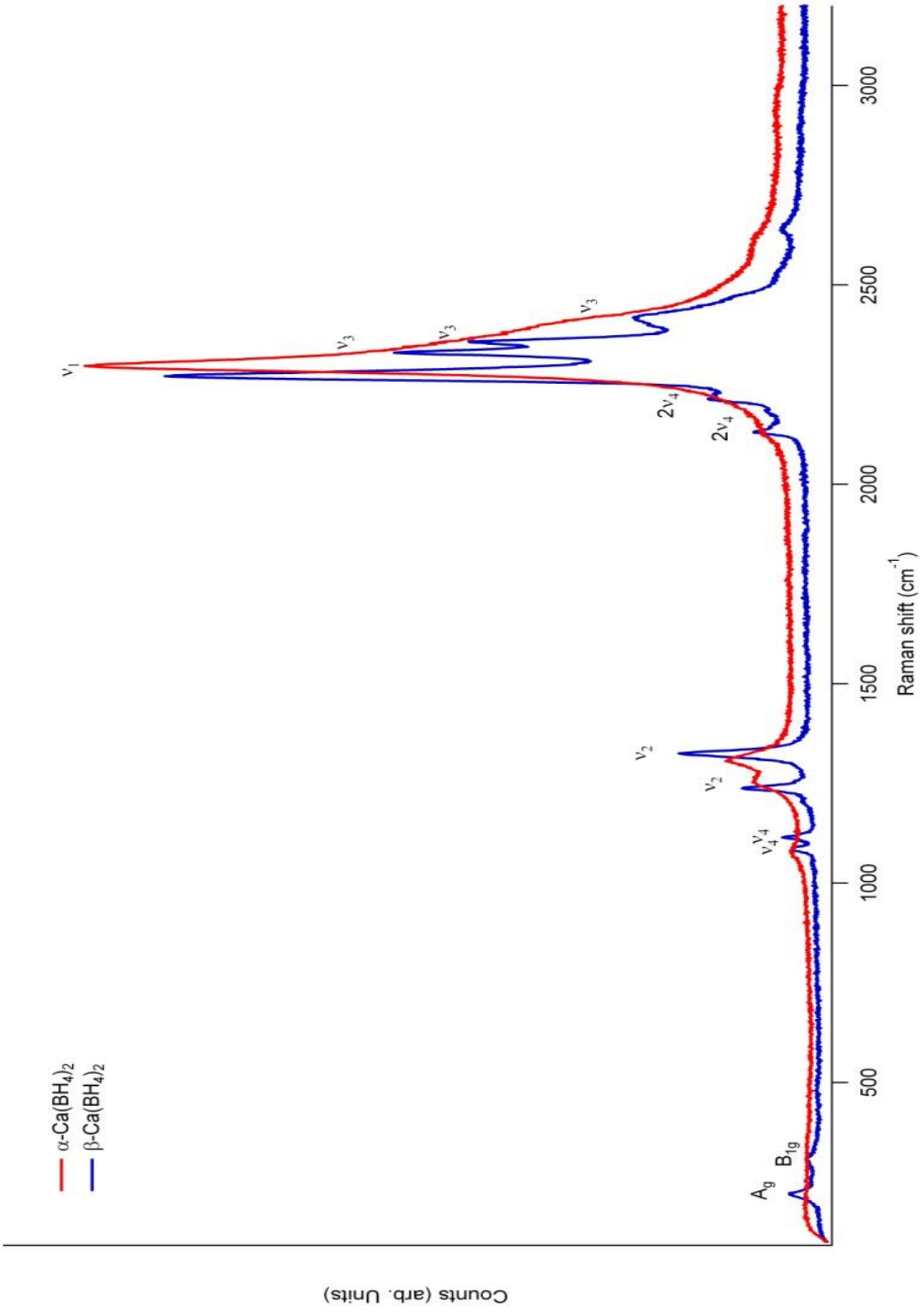

Figure 8.8 Comparison of Raman spectra of Aldrich α-$Ca(BH_4)_2$ and β-$Ca(BH_4)_2$ using a 488 nm laser, from Figures 8.6 and 8.7.

Table 8.1 Peak positions and half-width half-maximum (HWHM) values for the Raman spectra of Sigma-Aldrich $Ca(BH_4)_2$, compared with values from the literature [100].

	α-$Ca(BH_4)_2$			**β-$Ca(BH_4)_2$**		
Mode	Position cm^{-1}	HWHM cm^{-1}	Literature cm^{-1}	Position cm^{-1}	HWHM cm^{-1}	Literature cm^{-1}
			External			
$\mathbf{A_g}$	219	13.7				
$\mathbf{B_{1g}}$	298	42.16				
			Internal			
$\mathbf{\upsilon_1}$	2271	12.9	2273	2296	18.9	
$\mathbf{\upsilon_2}$	1238	7.9	1241	1250	23.6	1254
$\mathbf{\upsilon_2}$	1324	11.4	1327	1309	28.1	1310
$\mathbf{\upsilon_3}$	2330	11.8	2332	2329	17.3	
$\mathbf{\upsilon_3}$	2357	11.0	2356	2355	76.0	
$\mathbf{\upsilon_3}$	2413	45.3	2415			
$\mathbf{\upsilon_4}$	1085	7.3	1056	1078	20.8	1010
$\mathbf{\upsilon_4}$	1115	7.2	1117			
$\mathbf{\upsilon_4}$	1205	6.1	1204			

The decrease in the number of modes observed for β-$Ca(BH_4)_2$ compared to α-$Ca(BH_4)_2$ indicates an increase in symmetry of the borohydride tetrahedron. If one considers the HWHM values of the ν_2 modes, there is a significant increase from 7.9 and 11.4 cm^{-1} to 23.6 and 28.1 cm^{-1}. This spectral behaviour is consistent with that observed with lithium borohydride and other alkali metal borohydrides, and is due to increased disorder caused by the rearrangement of the borohydride tetrahedrons.

8.1.2 Characterisation of Milled Material

In order to understand the structure of the milled material, XRD was performed. Figure 8.9 shows the XRD patterns for Sigma-Aldrich $Ca(BH_4)_2$ and milled $CaCl_2$ + $NaBH_4$. The milled samples have peaks due to sodium borohydride and calcium chloride. The sodium borohydride reflections are broad and decrease in intensity with increased milling time. The pattern for calcium chloride is present for the sample milled for 20 minutes, but is very weak and broad for longer milling times. There are no peaks associated with any of the low temperature phases of $Ca(BH_4)_2$ in the milled products, indicating that $Ca(BH_4)_2$ has not been formed. However, the reduction in peak intensity of sodium chloride and calcium chloride with increased milling time indicates that an amorphous phase has been formed.

Table 8.2 and Figure 8.10 show the change in the lattice parameters of sodium borohydride for different milling times. This corresponds to a reduction in the lattice volume, indicating a possible substitution of $[BH_4]^-$ ions for chloride ions.

Table 8.2 Change in lattice parameter of $NaBH_4$ with milling time.

Milling time	a
20	6.1620 ± 0.0032
40	6.1645 ± 0.0167
60	6.1592 ± 0.0091
120	6.1298 ± 0.0219
300	6.0753 ± 0.0250

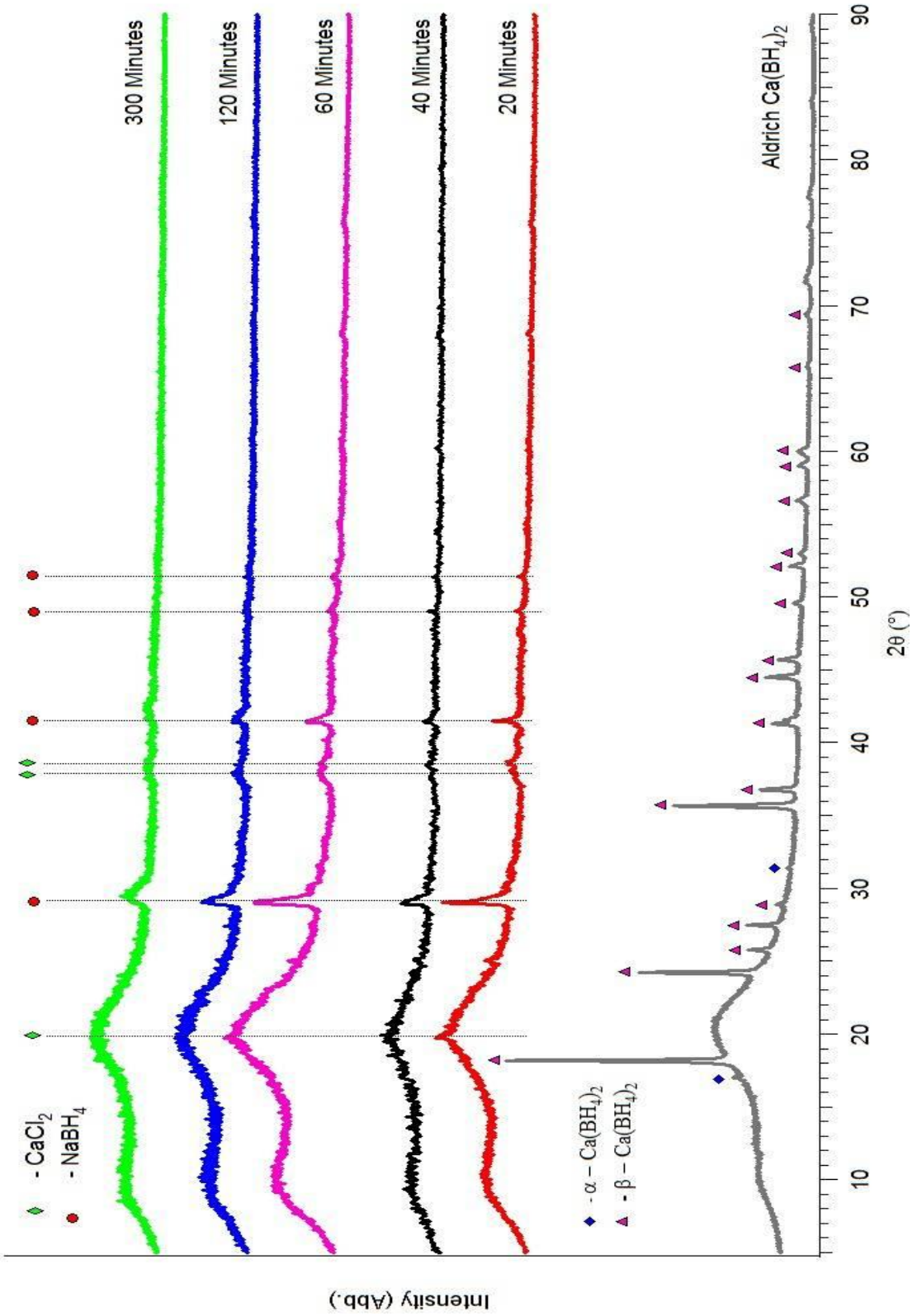

Figure 8.9 XRD patterns (obtained using the domed Kapton sample holder) for $CaCl_2$ + $2NaBH_4$ milled for various times and Sigma-Aldrich $Ca(BH_4)_2$.

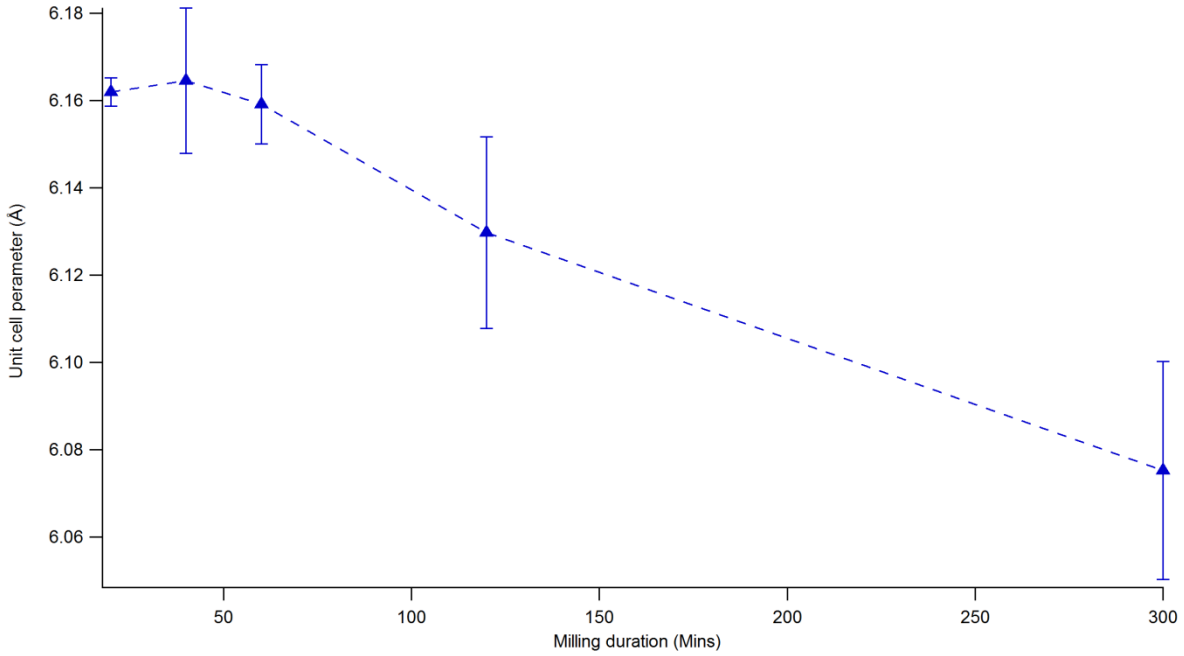

Figure 8.10 Change in the lattice parameters of sodium borohydride for different milling times.

Figure 8.11 shows the Raman spectra of the milled $CaCl_2$ + $NaBH_4$. The characteristic ionic $[BH_4]^-$ stretch at 2330 cm^{-1} and bend at 1275 cm^{-1} indicates that the borohydride group is in a symmetric tetrahedral arrangement similar to that of the sodium borohydride and different to that of the Sigma-Aldrich $Ca(BH_4)_2$. The Sigma-Aldrich $Ca(BH_4)_2$ shown is the β-$Ca(BH_4)_2$ phase, as this disordered phase is the most likely to be present in the milled material. The spectrum of the Aldrich $Ca(BH_4)_2$.2THF sample has a series of peaks between 2800 and 3100 cm^{-1} which are due to the THF, as are the majority of the peaks between 800 and 1600 cm^{-1}, masking the BH_4 bend of the $Ca(BH_4)_2$. The peaks associated with the B-H stretch are broad and are at 2280 and 2390 cm^{-1}, indicating two different B-H environments. The absence of a Ca-H-B stretch rules out a covalent structure. Therefore the two peaks are due to the mixture of phases of $Ca(BH_4)_2$ that can be present in this sample.

Upon milling for the longer durations (120 and 300 minutes) there are slight changes to the position of the vibrational modes, summarised in Table 8.3. There is an increase in the Raman shift of the ν_2 mode and a significant increase in the symmetric stretch, ν_1, from 2224 cm^{-1} in pure $NaBH_4$ to 2270 cm^{-1} after 300 minutes of milling. There is no change in the ν_3 mode at 2330 cm^{-1}, but there is an increase in the 2193cm^{-1} ν_3 mode to 2212 cm^{-1} and a decrease in the 2403 cm^{-1} ν_3 mode to 2395 cm^{-1}. This indicates a subtle change in the environment of the borohydride tetrahedron, although the change in lattice may only be in one or two directions and does not necessarily mean a uniform change in crystal structure.

Table 8.3 Peak positions of Raman modes measured in $NaBH_4$ and $Ca(BH_4)_2$.2THF milled $CaCl_2$ + 2$NaBH_4$.

		Milled $CaCl_2$ + 2$NaBH_4$					
Mode	$NaBH_4$	**20 mins**	**40 mins**	**60 mins**	**120 mins**	**300 mins**	$Ca(BH_4)_2$.2THF
υ_2	1276	1276	1276	1278	1278	1282	
υ_3	2193	2194	2212	2206	2212	2212	
υ_1	2224	2229	2270	2245	2268	2270	2261
υ_3	2331	2330	2330	2331	2332	2336	2285
υ_3	2403	2401	2378	2403	2389	2395	2390

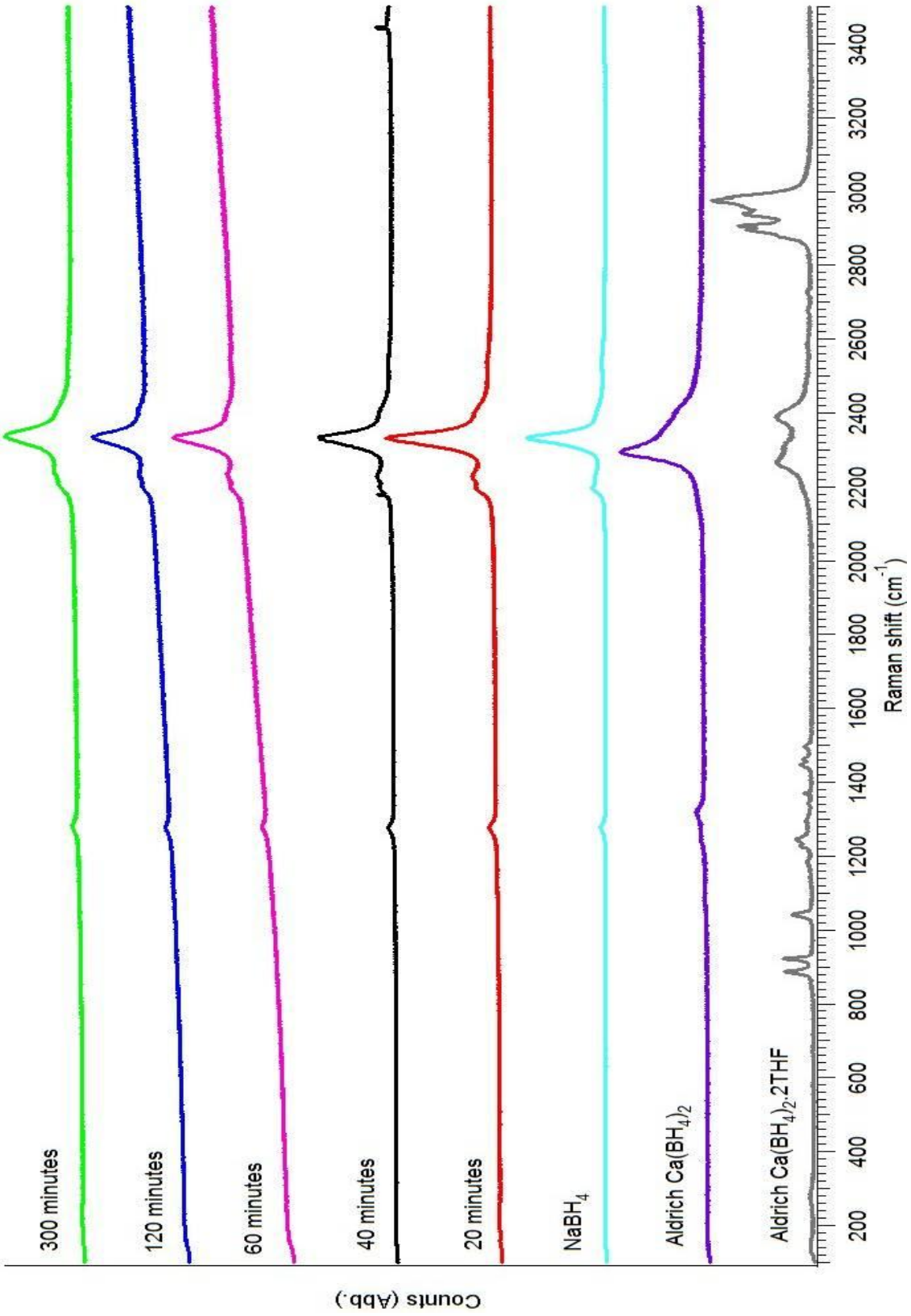

Figure 8.11 Raman spectra, obtained using the 488 nm laser, of $CaCl_2$ + $2NaBH_4$ milled for 20, 40, 60, 120 and 300 minutes, and Aldrich $NaBH_4$, $Ca(BH_4)_2$ and $Ca(BH_4)_2$.2THF.

8.1.3 Summary of the Characterisation

Characterisation of the Aldrich $Ca(BH_4)_2$ shows that it consists of both α and β phases with the β-$Ca(BH_4)_2$ being the dominant phase.

The milled materials do not form any crystalline phases, such as sodium chloride, indicating that a reaction similar to equation (8.1) has not occurred. The subtle change in lattice parameter for sodium borohydride indicates a reduction in lattice volume, which is possibly due to an exchange mechanism. The Raman results indicate that there is a slight change in the environment or constraint of the borohydride tetrahedron. This suggests that some reaction has occurred.

8.2 Thermal Decomposition

Examination of the crystal structure and the Raman spectra of milled calcium chloride and sodium borohydride showed that milling forms an unknown phase similar to sodium borohydride. Therefore the thermal decomposition of milled calcium chloride and sodium borohydride will now be investigated. First the decomposition of the Aldrich $Ca(BH_4)_2$.2THF was examined in order to understand the preparation of Aldrich $Ca(BH_4)_2$ and provide a benchmark for the milled material. The thermal decomposition of Aldrich $Ca(BH_4)_2$ was also investigated, again to provide a benchmark for the decomposition of the milled material.

The thermal decomposition of the milled material will be compared to the results obtained for the Sigma-Aldrich samples, in order to try to understand the decomposition mechanisms involved.

8.2.1 Sigma-Aldrich $Ca(BH_4)_2.2THF$

Sigma-Aldrich $Ca(BH_4)_2.2THF$ is made up of 32.6 wt.% calcium borohydride and the remaining 67.4 wt.% is due to the two THF ligands. Figure 8.12 shows TGA of Aldrich $Ca(BH_4)_2.2THF$ with two large weight losses between 70 and 200°C. The first has a loss of 33.85% and the second a loss of 30.84%, which is attributed to the loss of the THF ligands, indicating two THF sites within the lattice. The remaining weight loss of 35.32% must be related to $Ca(BH_4)_2$. This indicates that the composition of the as-received sample is closer to $Ca(BH_4)_2.1.75THF$, and that there is 3.4% weight loss at 340°C attributed to the decomposition of $Ca(BH_4)_2$. Equation (8.5) predicts a theoretical weight loss of 3.08 wt.%, while equation (8.6) predicts 3.43 wt.%. This suggests that the reaction is likely to have proceeded in a similar way to that given in equation (8.6). It also shows that heating Sigma-Aldrich $Ca(BH_4)_2.2THF$ to 200°C will remove the THF ligands without decomposing the $Ca(BH_4)_2$.

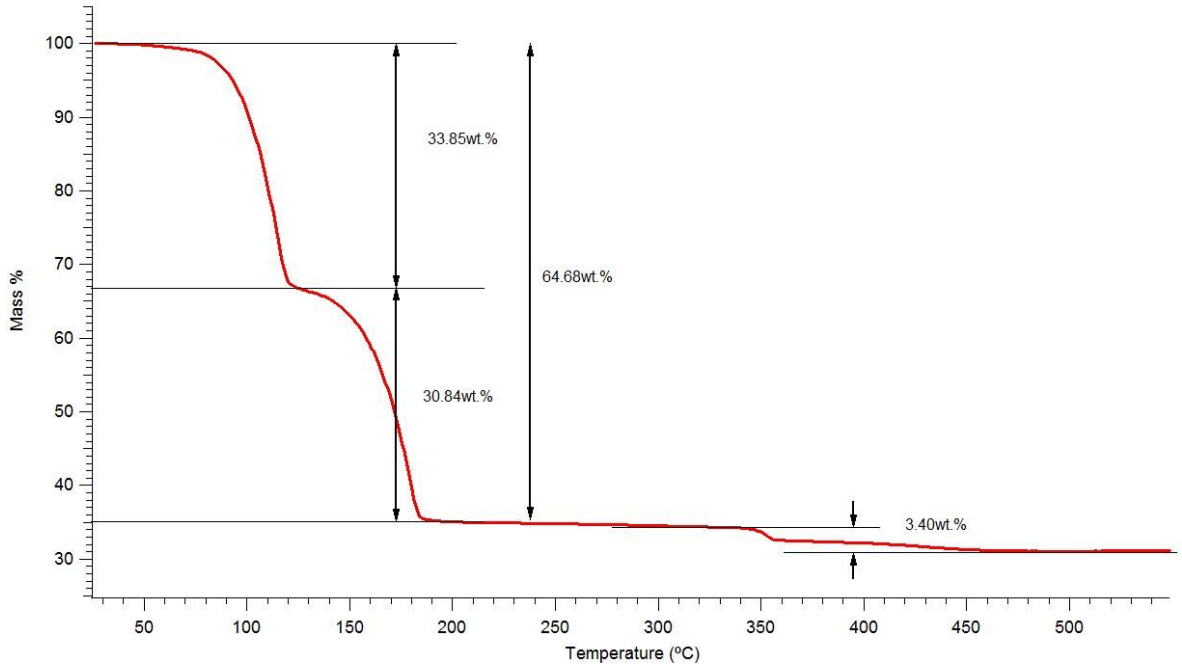

Figure 8.12 TGA of Aldrich $Ca(BH_4)_2$.2THF heated at 2°C/min in 1 bar argon at 40 ml/min.

8.2.2 Aldrich $Ca(BH_4)_2$

The TGA of Aldrich $Ca(BH_4)_2$ is shown in Figure 8.13. It shows that there is a mass loss of 9.55 wt.% which occurs in two main steps, with the onset at around 340°C. The reaction is complete by 500°C. This again indicates that the reaction proceeds in a similar way to equation (8.6), which has a theoretical weight change of 9.63 wt.%, whereas equation (8.5) has a predicted weight change of 8.67 wt.%.

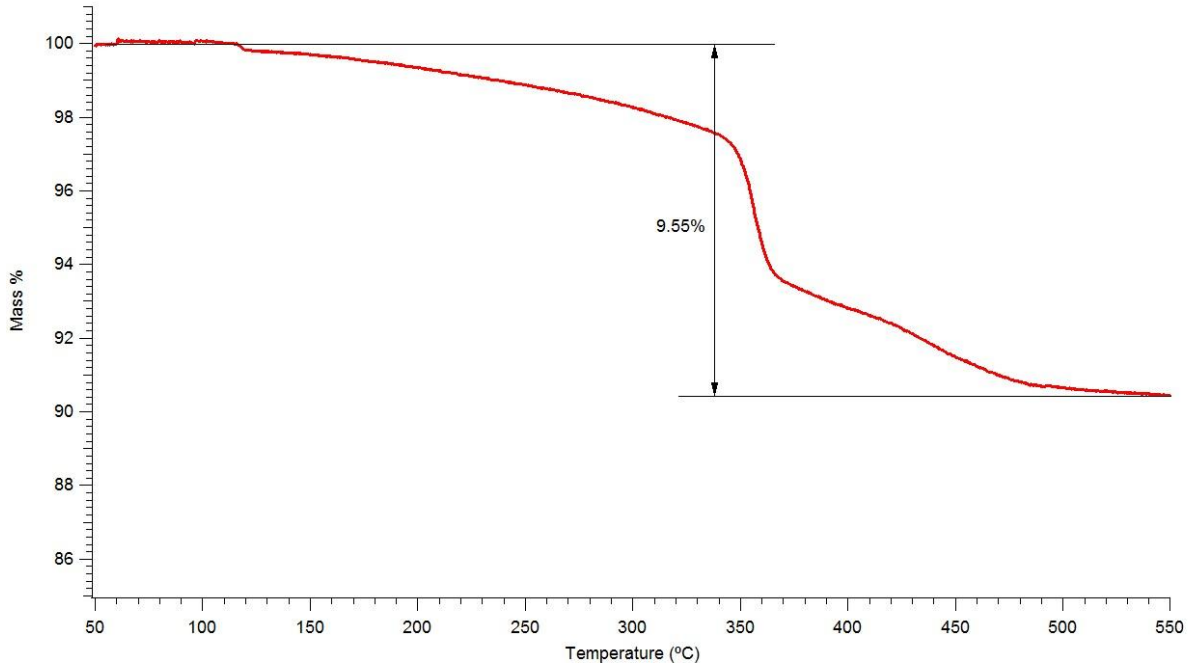

Figure 8.13 TGA of Aldrich $Ca(BH_4)_2$ heated at 2°C/min in 1.5 bar argon at 40 ml/min.

8.2.3 Milled Samples

The TGA of the mechanically milled samples is shown in Figure 8.14. The onset of decomposition occurs at around 340°C which is the same as for the commercially available Sigma-Aldrich $Ca(BH_4)_2$.2THF and Sigma-Aldrich $Ca(BH_4)_2$ samples shown in Figure 8.12 and Figure 8.13, respectively. This indicates that while the XRD of the mechanically milled products does not show that $Ca(BH_4)_2$ had been synthesised, upon heating the material behaves as if the reaction mixture contained $Ca(BH_4)_2$ with a weight loss of around 3 wt.%. This is similar to that predicted by equation (8.5) with a theoretical weight loss of 3.23 wt.%, and significantly less than both the 3.60 wt.% predicted by equation (8.6) and the theoretical maximum hydrogen content of 4.32 wt.%. This indicates that either the decomposition of the milled products proceeds via a reaction similar to equation (8.5), that the synthesis was not complete after milling, or that another mechanism is followed.

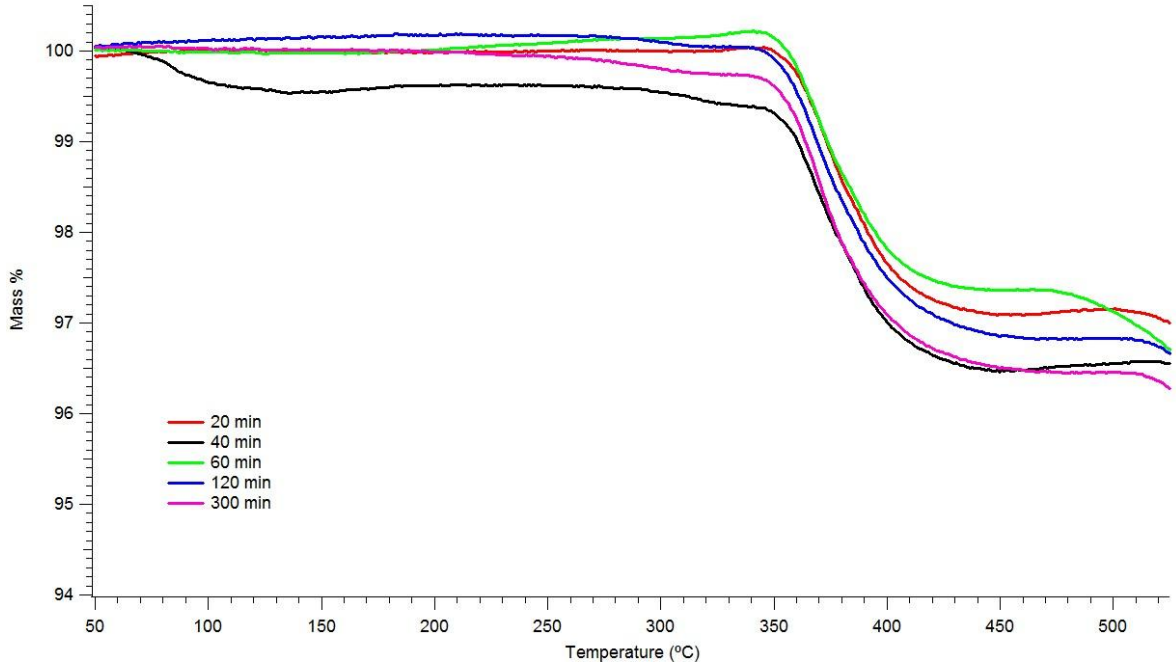

Figure 8.14 TGA of $CaCl_2$ + $NaBH_4$ samples milled for 20, 40, 60, 120 and 300 minutes, heated at 2°C/min in 1 bar argon at 40 ml/min.

Table 8.4 Summary of weight loss and decomposition temperature, T_d, of ball milled $CaCl_2$ + $2NaBH_4$, Aldrich $Ca(BH_4)_2$ and Aldrich $Ca(BH_4)_2.2THF$.

Milling duration (minutes)	**Weight Loss (%)**	**Onset temperature, T_d (°C)**
20	2.91 ± 0.16	359.2
40	3.07 ± 0.19	356.7
60	2.86 ± 0.17	353.1
120	3.23 ± 0.21	349.0
300	3.30 ± 0.19	358.8

In Figure 8.14, a weight loss was observed above 500°C for all the milled samples. This is not accompanied by a release of hydrogen as measured by MS for the sample milled for 300 minutes shown in Figure 8.15 and therefore cannot be due to the decomposition of any unreacted sodium borohydride. Therefore, this weight loss may be attributed to the sublimation of some of the reaction products.

Figure 8.15 shows that the decomposition occurs with only the evolution of hydrogen. The decomposition appears to be a single rapid decomposition with an onset at 340°C which quickly reaches a maximum at 375°C with the rate of reaction slowing until completion at 440°C.

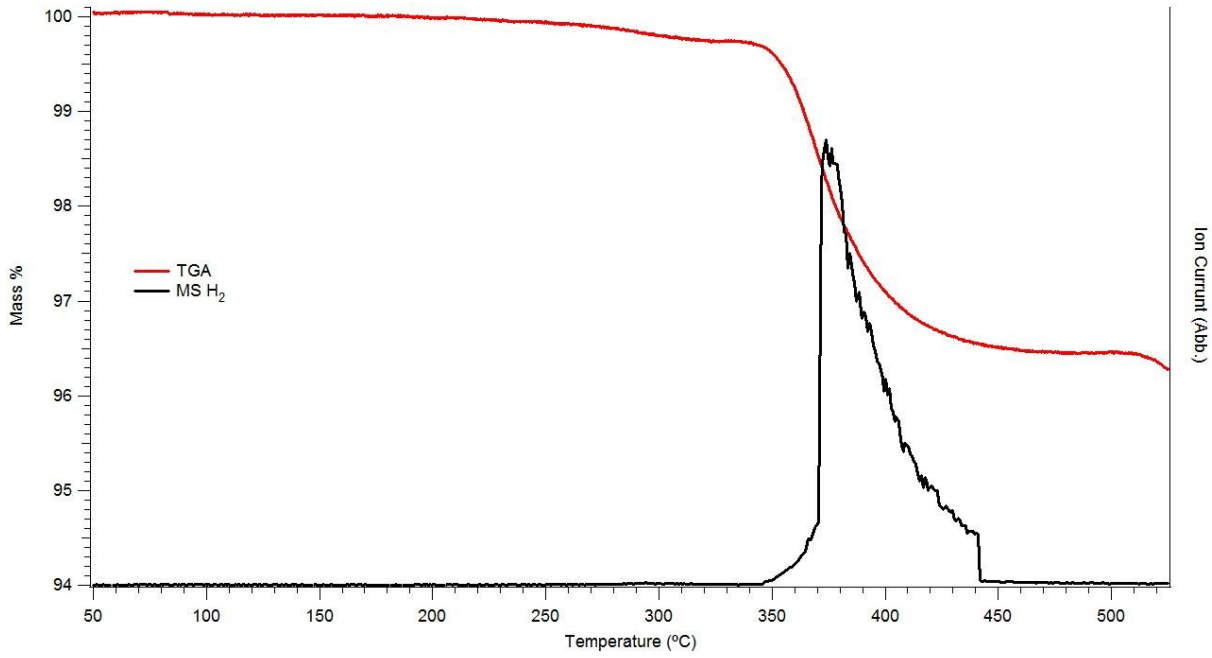

Figure 8.15 TGA MS of $CaCl_2$ + $NaBH_4$ milled for 300 minutes, heated at 2°C/min in 1 bar argon at 40 ml/min.

Figure 8.16 shows the DSC of the $CaCl_2$ + $2NaBH_4$ samples milled for different times, showing four endotherms and one exotherm. An exotherm occurs at 140°C for samples milled for between 20 and 120 minutes. This peak is then shifted to 80°C for the sample milled for 300 minutes, which is attributed to the formation and unknown phase or structural rearrangement of the amorphous phases in the milled products. There is also an endotherm at 280°C which is present for all milling times. The subsequent three overlapping endotherms occur at the same temperature as decomposition, with the two large endotherms corresponding to equations (8.2) and (8.6) forming the 'unknown' compound and subsequently CaB_6. There is no change in the temperature of the endotherms with respect to milling time, indicating that decomposition is not affected by any particle size change associated with longer milling.

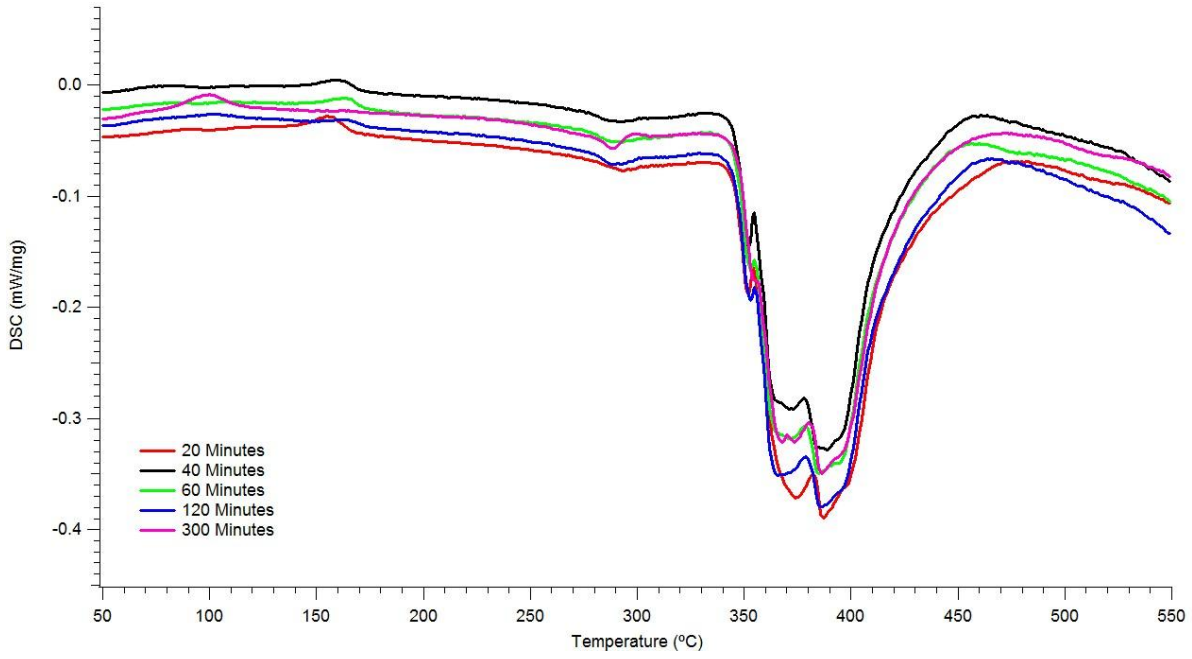

Figure 8.16 DSC of $CaCl_2$ + $NaBH_4$ samples milled for 20, 40, 60, 120 and 300 minutes, heated at 2°C/min in 4 bar argon at 100 ml/min.

Figure 8.17 shows the comparison between the TGA/MS and DSC for a sample milled for 300 minutes. It shows that the exotherm at 80°C is not associated with any mass change or hydrogen release. The phase change endotherm at 280°C is associated with a small weight change and release of hydrogen. Finally it shows that the main decomposition occurs at the same temperature as the three endotherms between 340 and 450°C, for which only hydrogen was measured.

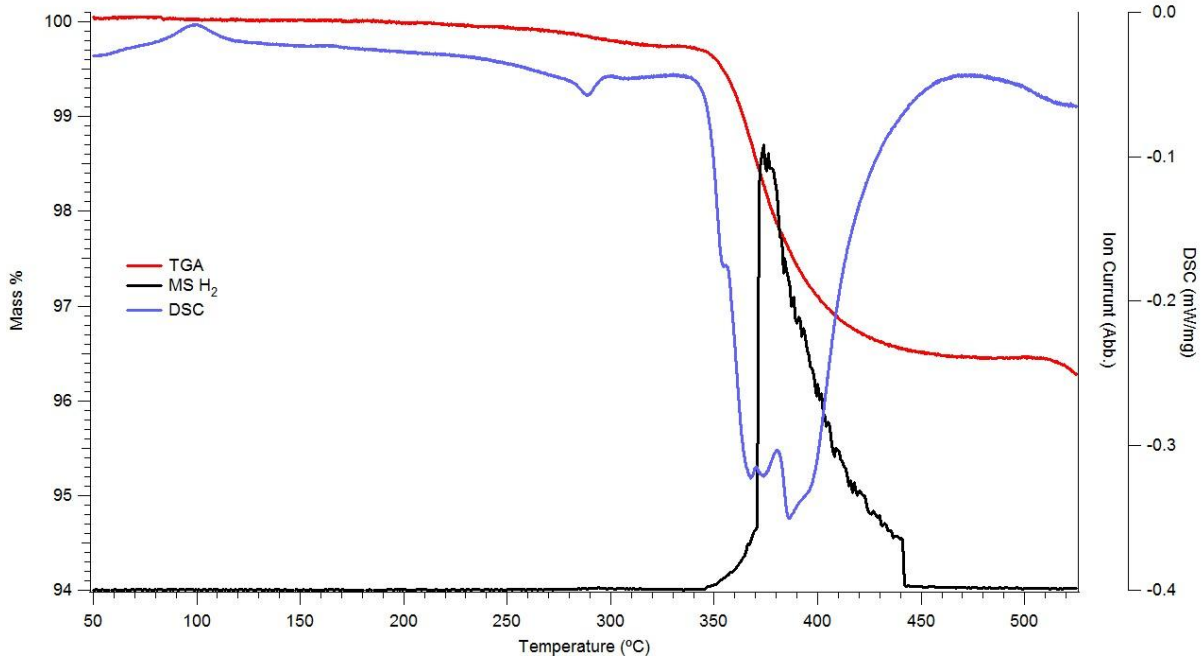

Figure 8.17 TGA/MS and DSC of $CaCl_2$ + $NaBH_4$ milled for 300 minutes, heated at 2°C/min in 1 bar argon at 40 ml/min for TGA/MS and in 4 bar argon at 100 ml/min for DSC.

8.2.4 Summary of the Thermal Decomposition

Aldrich $Ca(BH_4)_2$.2THF decomposed with the loss of the THF ligands below 200°C. Decomposition of the $Ca(BH_4)_2$ occurs at around 340°C with a weight loss of 3.4 wt.%. This

indicates a two-step reaction similar to equation (8.2) by 200°C followed by equation (8.6) at 340°C.

Aldrich $Ca(BH_4)_2$ decomposed around 340°C with the loss of 9.6 wt.%, indicating a reaction similar to equation (8.6). This provides a good reference point with which to compare the milled samples, in order to understand whether $Ca(BH_4)_2$, a similar compound or a significantly different compound is formed on milling.

The milled $CaCl_2$ + $NaBH_4$ samples decompose with only the evolution of hydrogen at 340°C, the same as for the commercial calcium borohydride samples. There is a mass change of 3 wt.%, occurring in a two-step reaction shown by DSC. This mass loss is lower than expected for the mechanism predicted for the commercial calcium borohydride samples. The DSC shows an exotherm between 80 and 150°C, which is attributed to lattice rearrangements as there is no mass change or gas evolved.

8.3 Analysis of the Decomposition Products

Decomposition of calcium borohydride was undertaken in two parts; firstly in collaboration with Dr Young-Whan Cho's group at KIST (Seoul, Korea) on $Ca(BH_4)_2$ prepared from Sigma-Aldrich $Ca(BH_4)_2$.2THF measured ex-situ on XRD and Raman [167]. Secondly the decomposition of the mechanically milled $Ca(BH_4)_2$ + 2NaCl and Sigma-Aldrich $Ca(BH_4)_2$ was measured using in-situ XRD and ex-situ Raman.

8.3.1 Sigma-Aldrich $Ca(BH_4)_2$

The $Ca(BH_4)_2$ was prepared by removing the two THF ligands, by heating Sigma-Aldrich $Ca(BH_4)_2.2THF$ up to 200°C under a dynamic vacuum. The samples were then heated to 330°C and 480°C under a static vacuum, to allow ex-situ XRD and Raman measurements. Figure 8.18 shows the XRD patterns produced at KIST [167]; these show the formation of an unknown intermediate and CaH_2 along with some residual β-$Ca(BH_4)_2$ in the sample heated to 330°C. Subsequent heating to 480°C results in the formation of only CaH_2 and some oxide, showing that all the $Ca(BH_4)_2$ has decomposed at this temperature.

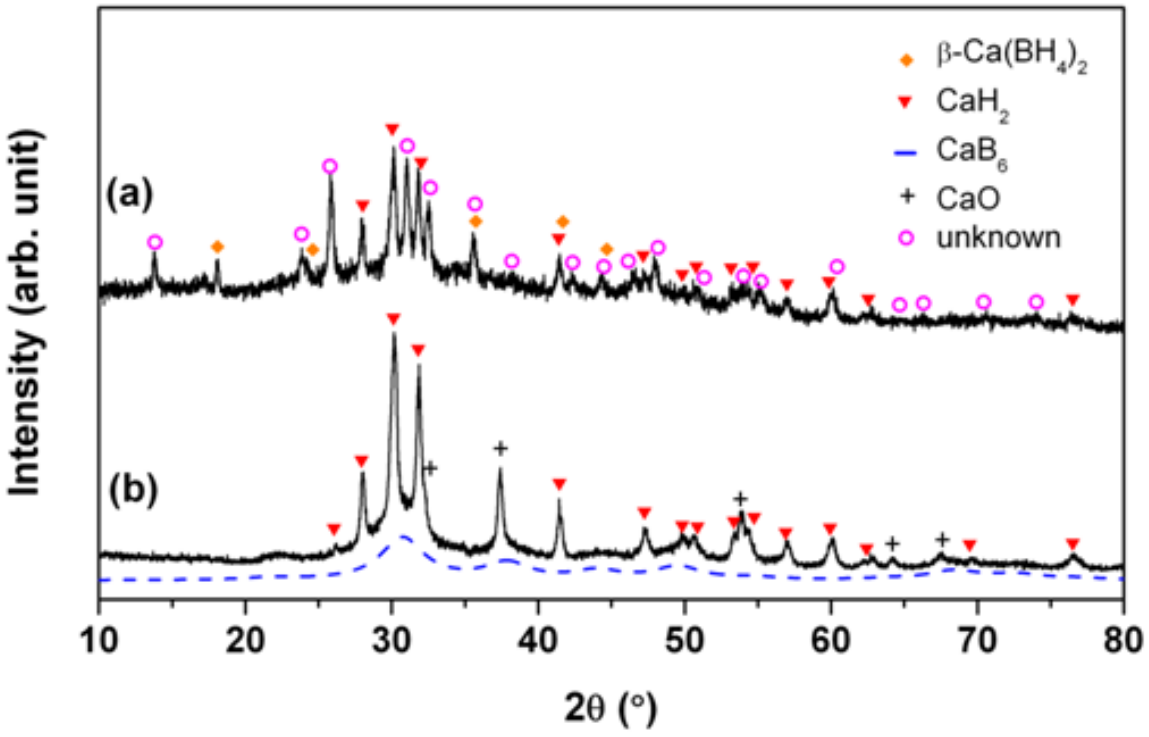

Figure 8.18 XRD patterns of $Ca(BH_4)_2$ after heating to (a) 330°C and (b) 480°C, under vacuum. Blue dashes indicate a broad background containing nanocrystalline CaB_6 [167].

Raman spectra of the samples prepared in the same way as the sample measured at KIST are shown in Figure 8.19. Sigma-Aldrich $Ca(BH_4)_2$ heated to 200°C to remove the THF ligands, has a spectrum that corresponds to α-$Ca(BH_4)_2$, as previously discussed in section 8.1.1. Upon heating to 330°C there is a large background over the whole range of the measurement, accompanied by three peaks at 760, 1135 and 1250 cm^{-1} corresponding to the T_{2g}, E_g and A_{1g} vibrations of CaB_6, respectively. This shows good correlation with as-received CaB_6 (from Sigma-Aldrich), though all peaks are shifted to lower energies. There are, however, no remaining peaks that might be attributed to the unknown phase observed by XRD in Figure 8.18, nor any peaks due to the residual β-$Ca(BH_4)_2$. The sample heated to 480°C shows the three peaks due to CaB_6 with a significantly reduced background compared to the 330°C sample. There are also no peaks due to amorphous boron or calcium dodecaborane.

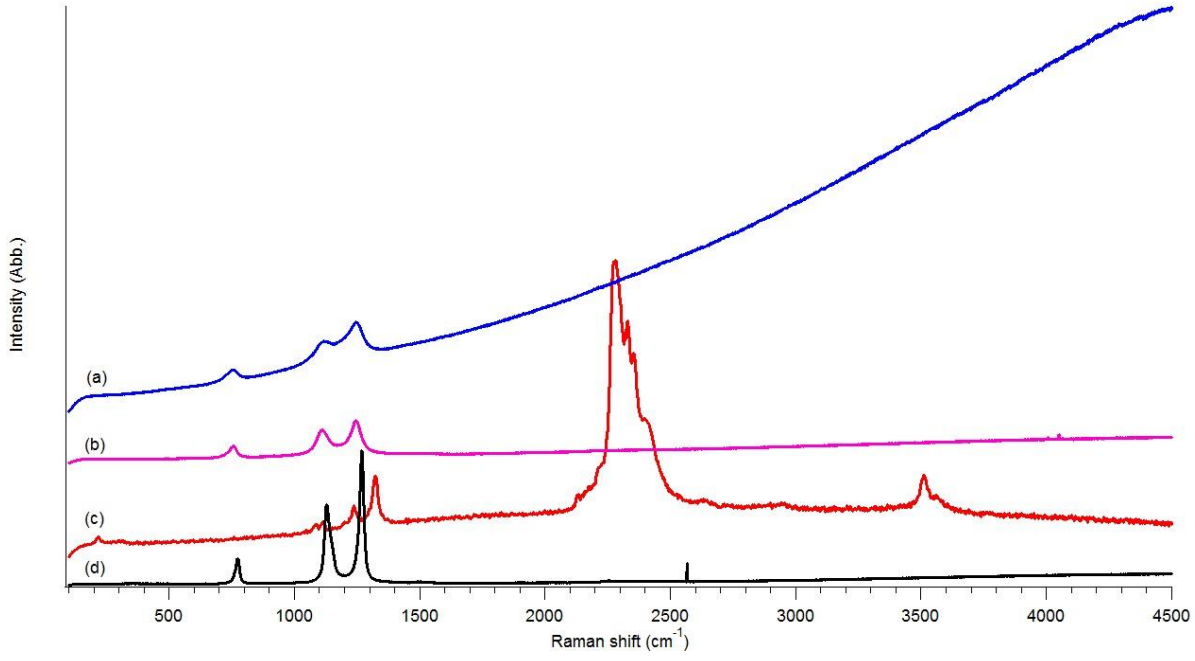

Figure 8.19 Raman spectra, measured using a 633 nm laser, of $Ca(BH_4)_2$ after heating to (a) 330°C and (b) 480°C in static vacuum compared to (c) Aldrich $Ca(BH_4)_2$.2THF heated to 200°C in dynamic vacuum and (d) Sigma-Aldrich CaB_6.

These results show that the decomposition of $Ca(BH_4)_2$ prepared from Sigma-Aldrich $Ca(BH_4)_2$.2THF ultimately yields CaH_2 and CaB_6 with the release of hydrogen. This indicates that the reaction proceeds via equation (8.6), since the absence of amorphous or crystalline boron shows that the decomposition does not proceed via reaction (8.5). The unknown intermediate shows no peaks in the Raman spectra that would indicate the formation of $CaB_{12}H_{12}$ or amorphous boron as the intermediate. However, the large background could obscure $CaB_{12}H_{12}$, as it is not possible to see the residual β-$Ca(BH_4)_2$ that is observed in the XRD pattern.

Figure 8.20 shows the in-situ XRD of Aldrich $Ca(BH_4)_2$ heated from 25 to 500°C at intervals of 25°C under flowing helium at 100 ml/min and at a pressure of 2.5 bar. The individual pattern at 25°C is shown in Figure 8.21. At this temperature the major phase present is β-$Ca(BH_4)_2$ with some α-$Ca(BH_4)_2$ also present..

From Figure 8.20 it can be seen that the α-$Ca(BH_4)_2$ phase is present until 275°C at which point only the β-$Ca(BH_4)_2$ phase is present. Decomposition occurs between 325 and 350°C. No further diffraction patterns are observed above 350°C since the sample decomposes with a large volume change and is therefore no longer in the x-ray beam. The reflections observed above 350°C are due to the corundum (Al_2O_3) sample holder used. This can be seen in Figure 8.23, which shows the diffraction pattern at 500°C.

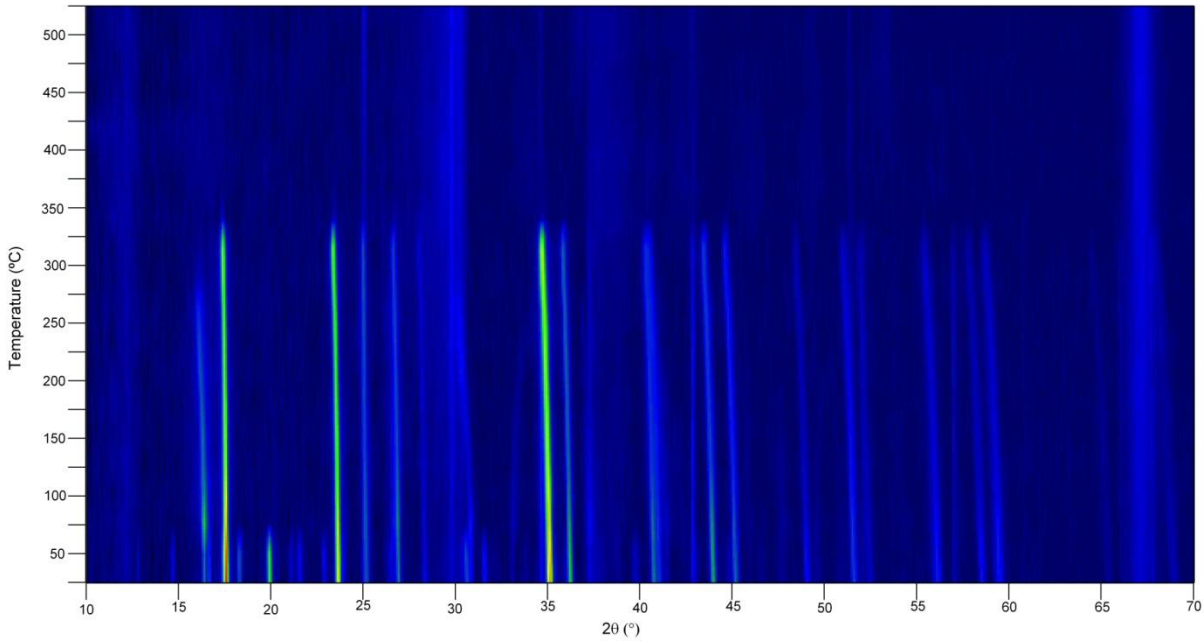

Figure 8.20 In-situ XRD of Sigma-Aldrich $Ca(BH_4)_2$, heated at 2°C/min in 2.5 bar helium at 100 ml/min. Patterns are collected isothermally every 25°C.

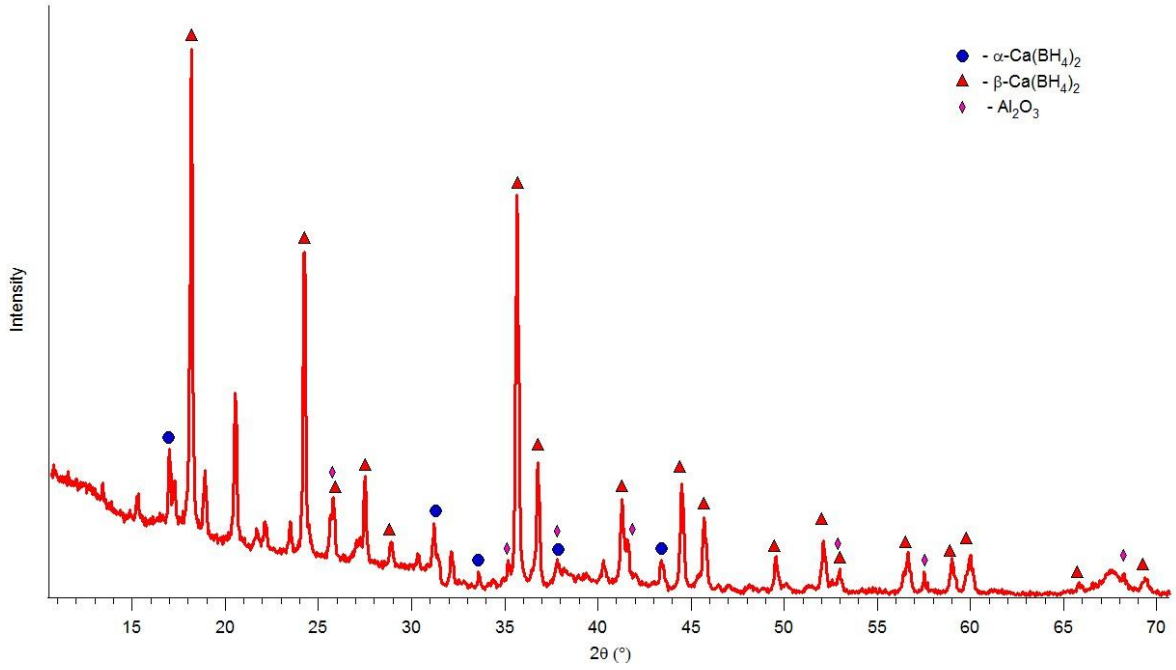

Figure 8.21 XRD pattern of Sigma-Aldrich $Ca(BH_4)_2$ measured in-situ at 25°C in 2.5 bar helium at 100 ml/min, showing $Ca(BH_4)_2$ and Al_2O_3. Unlabelled peaks are unknown.

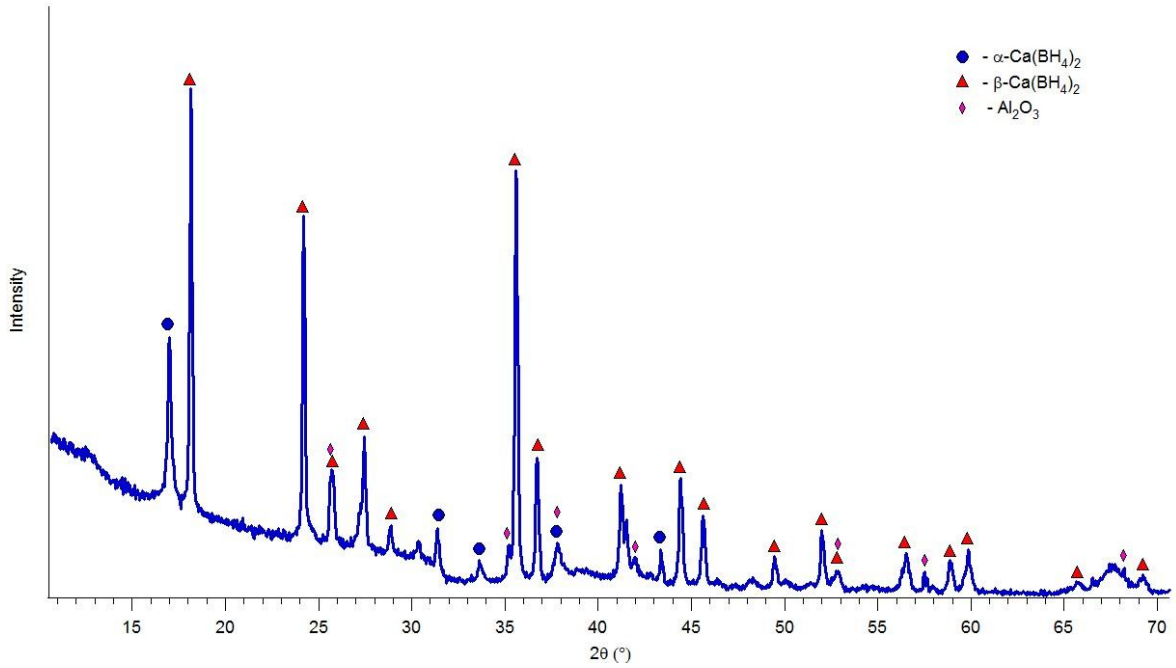

Figure 8.22 XRD pattern of Sigma-Aldrich $Ca(BH_4)_2$ measured in-situ at 75°C in 2.5 bar helium at 100 ml/min.

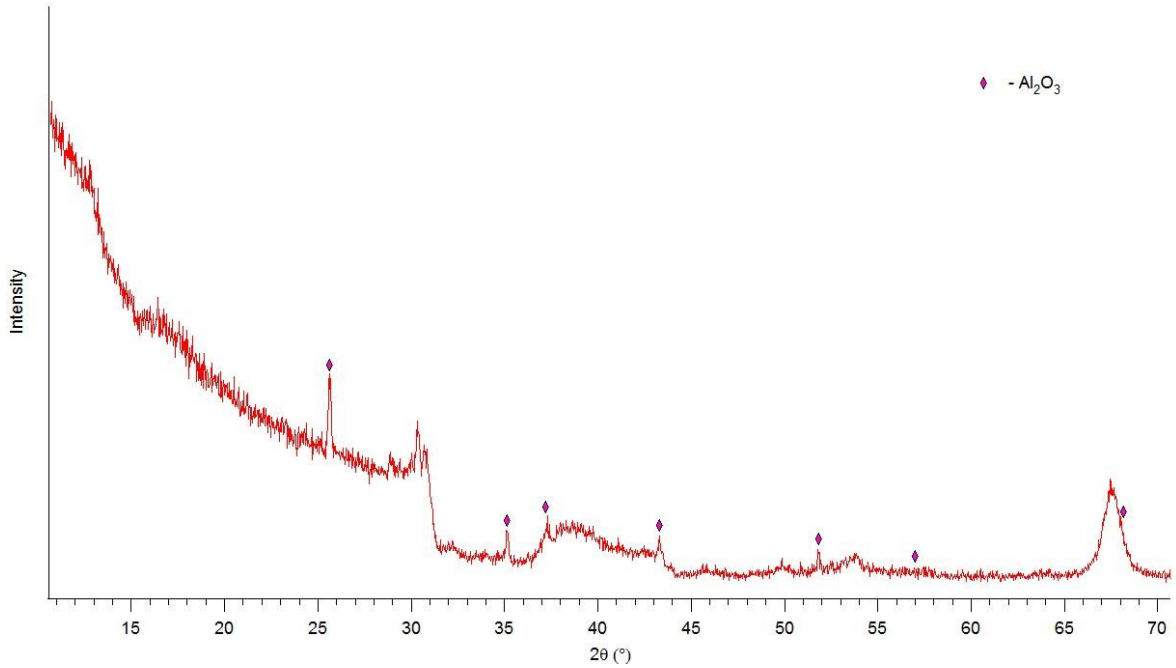

Figure 8.23 XRD pattern of Aldrich $Ca(BH_4)_2$ measured in-situ at 500°C in flowing 2.5 bar helium at 100 ml/min.

8.3.2 Milled $CaCl_2$ + 2$NaBH_4$

Figure 8.24 shows the in-situ XRD of $CaCl_2$ + $NaBH_4$ milled for 300 minutes, loaded in a corundum sample holder and heated at 2°C/min (in 2.5 bar helium flowing at 100 ml/min) with patterns taken isothermally at 25°C intervals. The sample at 25°C consists of only sodium borohydride and calcium chloride. On heating, the reflections due to $CaCl_2$ transform into reflections due to sodium borohydride, with increases in 2θ between 300 and 425°C. At 425°C, sodium chloride is formed, as seen in figure 9.18, indicating a possible substitution of the borohydride ions with chloride ions in a solid solution. The resultant products from this reaction are sodium chloride, calcium hydride with some calcium oxide.

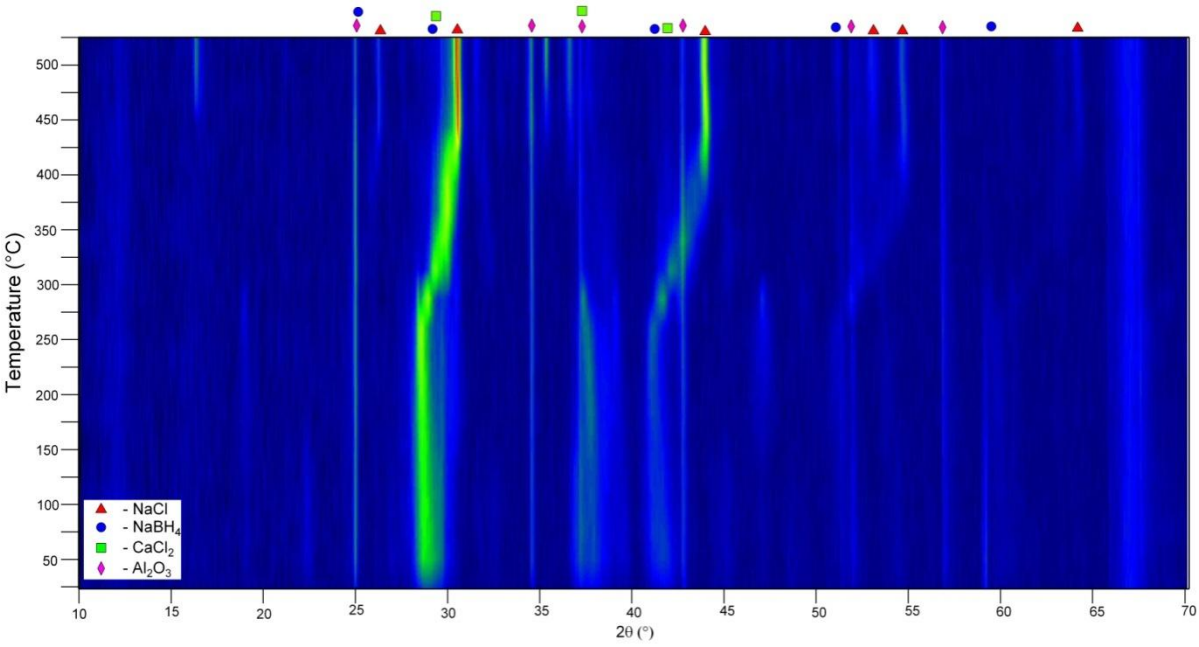

Figure 8.24 In-situ XRD of $CaCl_2$ + 2$NaBH_4$ milled for 300 minutes, heated at 2°C/min in 2.5 bar helium at 100 ml/min, with patterns taken every 25°C.

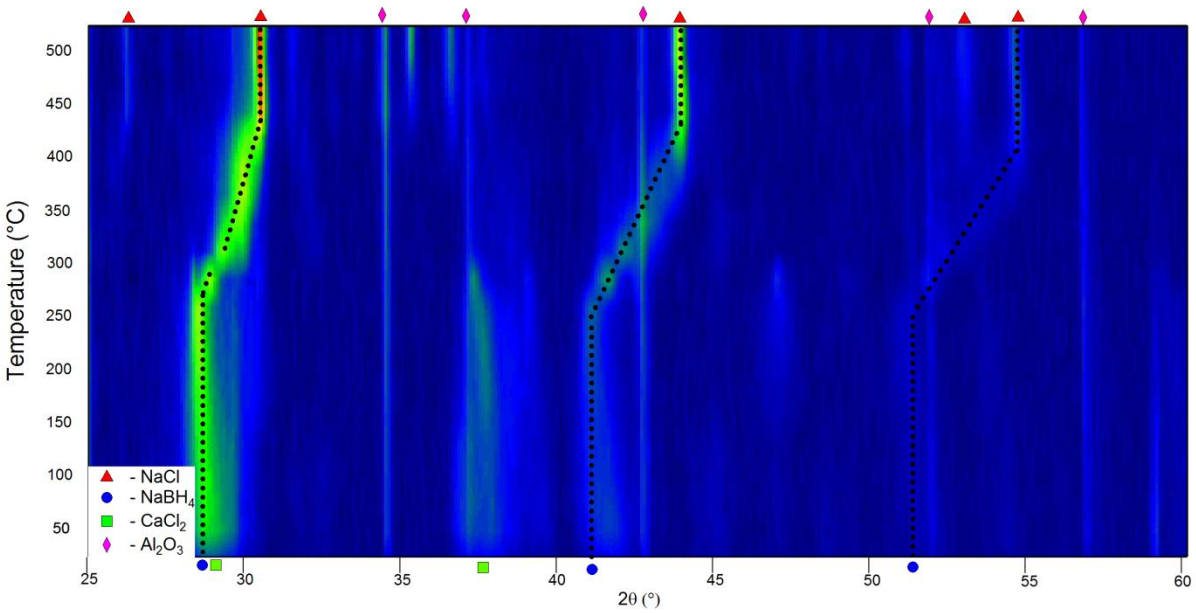

Figure 8.25 In-situ XRD of $CaCl_2$ + $2NaBH_4$ milled for 300 minutes, heated at 2°C/min in 2.5 bar helium at 100 ml/min, with patterns taken every 25°C, focusing on the region between 25 and 60° 2θ.

The reaction is shown to proceed from a modified sodium borohydride to sodium chloride. Both unit cells are cubic with a space group of P*m3m* where the sodium atoms occupy the (0, 0, 0) site and the boron or chlorine atom the (0.5, 0.5, 0.5). Figure 8.26 shows the change in lattice parameter of the cubic unit cell. There is a steady increase in the cell dimensions due to thermal expansion up to 175°C. There is then a small expansion in the lattice up to 225°C which is maintained until 300°C where the lattice reduces considerably in size, coinciding with the endotherm observed during DSC measurement. There is a continued reduction in size as decomposition takes place, with a slight change in the rate of reduction between the endotherms associated with the two-step decomposition. When decomposition is complete at 425°C there is a steady increase in lattice size with temperature due to thermal

expansion. On cooling the sample linearly reduces in size, indicating thermal contraction of the lattice.

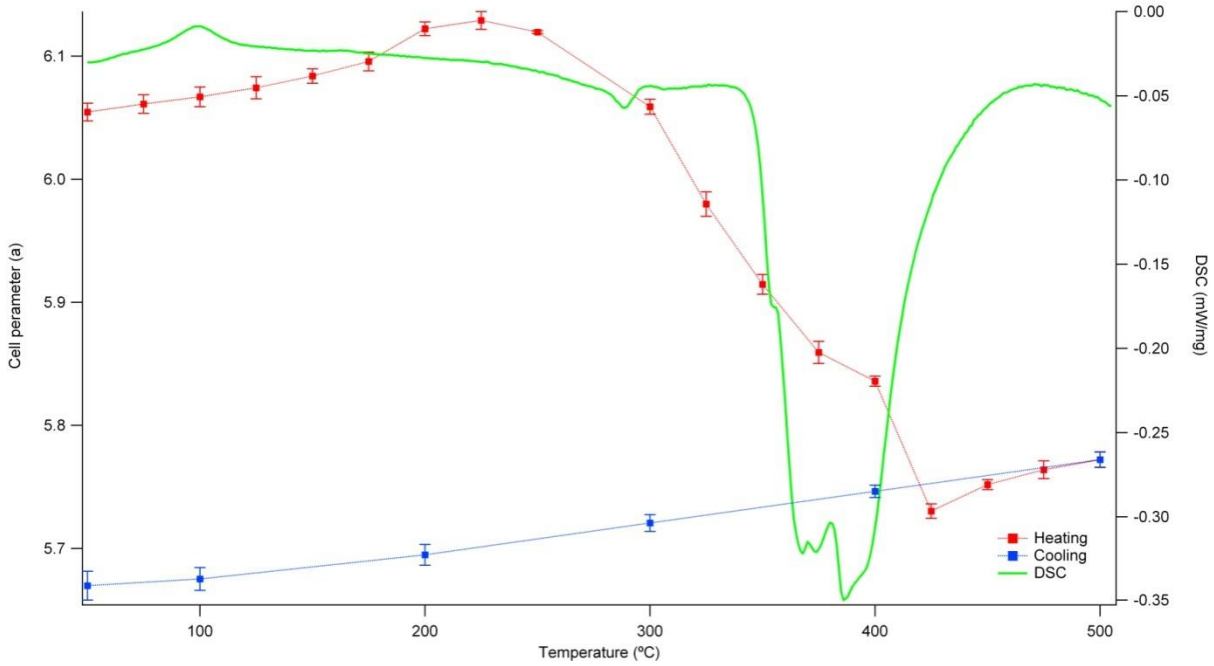

Figure 8.26 In-situ XRD of milled $CaCl_2$ + $2NaBH_4$ milled for 300 minutes, showing change in lattice parameter of the P*m3m* cubic structure with temperature, compared to DSC (from Figure 8.16).

Figure 8.27 shows the XRD pattern for the decomposed material from the in-situ measurement. There are reflections due to sodium chloride and calcium hydride and an amorphous hump at around $2\theta = 20°$, which can be attributed to either amorphous boron or calcium hexaboride. There are also reflections that can be assigned to calcium oxide, indicating that the sample has been partially oxidised.

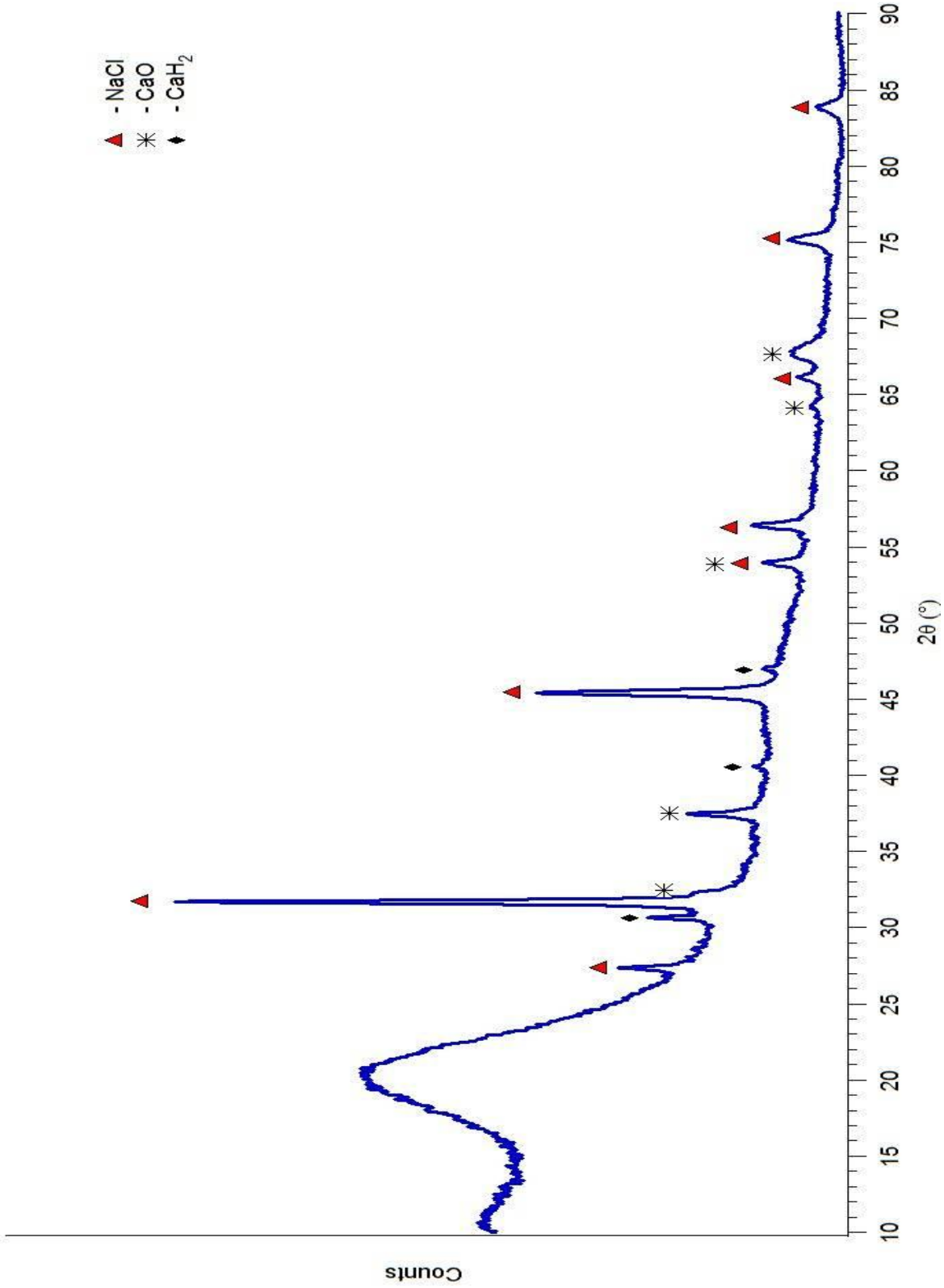

Figure 8.27 XRD pattern of $CaCl_2$ + $2NaBH_4$ milled for 300 minutes, heated to 500°C and cooled to room temperature at 2°C/min in 2.5 bar argon at 100 ml/min.

Pawley refinement of the decomposed products (see Figure 8.28) shows that 82.7 wt.% of the sample is due to sodium chloride, 3.7 wt.% is from calcium hydride, and the remaining 13.6 wt.% is due to calcium oxide. Sodium chloride would make up to 62 wt.% of the milled mixture if the reaction had proceeded via equation (8.1). If decomposition had occurred via equation (8.5) then sodium chloride would have contributed 73.5 wt.% to the crystalline products. This indicates the presence of an amorphous phase containing calcium, most probably calcium hexaboride.

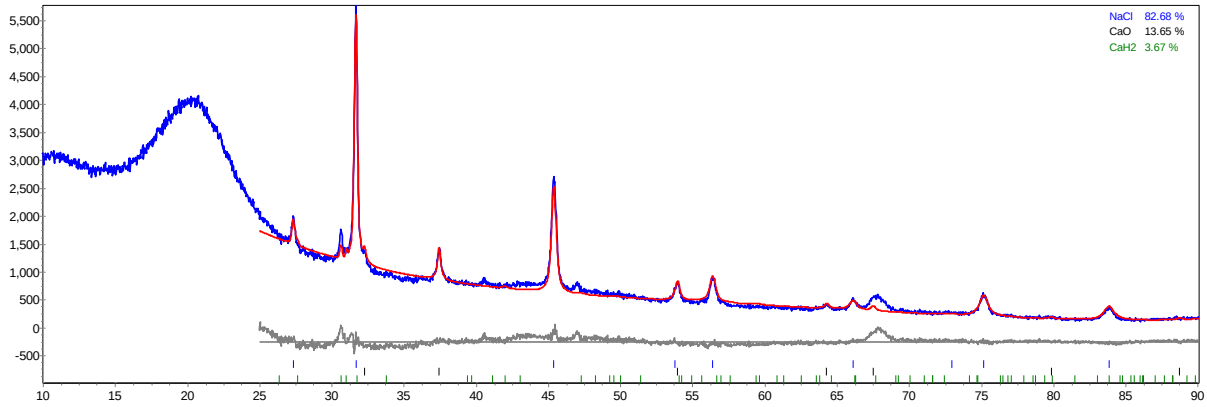

Figure 8.28 Refined XRD pattern of $CaCl_2$ + $2NaBH_4$ milled for 300 minutes, heated to 500°C and cooled to room temperature at 2°C/min in 2.5 bar helium at 100 ml/min.

The sample from the in-situ XRD measurement was also measured using Raman spectroscopy with a 488 nm laser. Figure 8.29 shows that there are three peaks at 776, 1138 and 1265 cm^{-1} that correspond to the T_{2g}, E_g and A_{1g} vibrations of calcium hexaboride, respectively. There are no peaks that can be attributed to $CaB_{12}H_{12}$ between 2200 and 2700 cm^{-1}. There are also no vibrations due to calcium oxide or hydride, which indicates that the oxide observed in the XRD patterns was on the surface and had not penetrated through the sample. There is a peak at around 4135 cm^{-1}, which it has not yet been possible to assign.

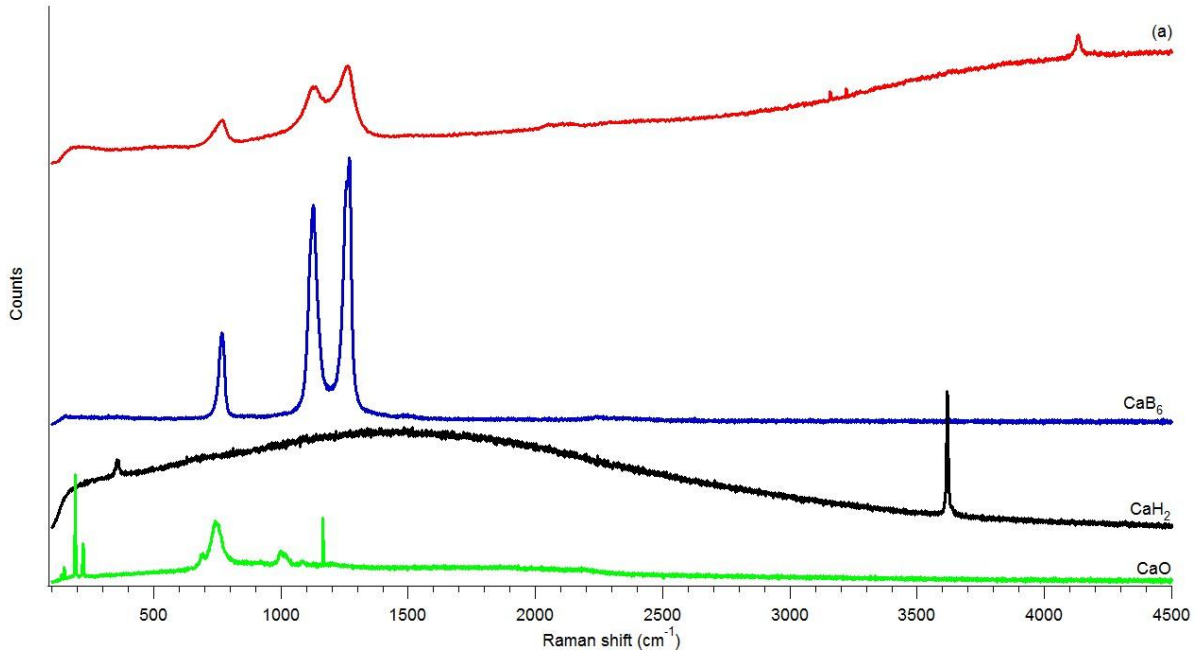

Figure 8.29 Raman spectrum measured using a 488 nm laser, of milled $CaCl_2$ + $2NaBH_4$ after in-situ XRD measurement (shown in Figure 8.27), with reference spectra for CaB_6, CaH_2 and CaO.

8.4 Summary

Samples of Sigma-Aldrich $Ca(BH_4)_2$ and $Ca(BH_4)_2$.2THF consist of ionic $[BH_4]^-$ and Ca^{2+} ions arranged predominantly in the β-$Ca(BH_4)_2$ phase for the sample without THF. Upon heating, the $Ca(BH_4)_2$.2THF sample loses both THF ligands by 200°C. Both samples then undergo two-step decomposition at around 350°C, with a weight loss of 9.6 wt.% from the $Ca(BH_4)_2$. The decomposition proceeds through an unknown intermediate at 330°C before finally decomposing to form CaH_2 and CaB_6 with the evolution of hydrogen to give an overall reaction scheme of:

$$Ca(BH_4)_2 \rightarrow aCaH_2 + bCaB_6 + cX + dH_2 \quad (8.7)$$

$$\rightarrow {}^{2}/_{3}CaH_2 + {}^{1}/_{3}CaB_6 + {}^{10}/_{3}H_2 \quad (8.8)$$

Mechanically milled $CaCl_2$ and $2NaBH_4$ did not proceed via equation (8.1) as predicted, but rather formed an ionic solid with a Raman spectrum similar to that of sodium borohydride. This suggests the formation of a compound such as $Na_xCa_y(BH_4)_{x+2y}$. Upon heating, a small exothermic peak is observed at 80°C with no mass change. This is likely to be due to a structural rearrangement of an amorphous material that is not observed by XRD. An endothermic reaction takes place at just below 300°C, at which point the reflections due to sodium borohydride during in-situ XRD showed a contraction in the lattice parameter until the formation of sodium chloride. This is likely to indicate that the chlorine atoms replace the borohydride ions in the lattice, forming a solid solution of $NaCl_x(BH_4)_{1-x}$. The substituted borohydride ions could then react with the calcium between 250 and 300°C to form calcium borohydride. Decomposition takes place at 350°C, occurring with only the evolution of hydrogen and results in the formation of calcium hydride, calcium hexaboride and sodium chloride.

It is therefore, predicted that the mechanical milling of $CaCl_2 + 2NaBH_4$ and subsequent thermal decomposition can be summarised as:

$$CaCl_2 + 2NaBH_4 \xrightarrow{Milling} \text{`}Na_xCa_y(BH_4)_{x+2y}\text{'} + CaCl_2 + NaBH_4 \quad (8.9)$$

$$\xrightarrow{250°C} NaCl_{2-x}(BH_4)_x + CaCl_2 + Na(BH_4)_{1-x}Cl_x \quad (8.10)$$

$$\xrightarrow{300°C} Ca(BH_4)_2 + CaCl_2 + Na(BH_4)_{1-x}Cl_x \quad (8.11)$$

$$\xrightarrow{325°C} 2NaCl + xCaH_2 + yCaB_6 + 4\text{-}xH_2 \quad (8.12)$$

9 RESULTS AND DISCUSSION: LITHIUM BOROHYDRIDE

Lithium borohydride is a potential hydrogen storage material due to its theoretical maximum hydrogen capacity of 18.5 wt.%. Lithium borohydride is, however, rather stable with an enthalpy of formation of ΔH = -74 kJ mol^{-1} H_2 and only desorbs hydrogen at elevated temperatures above the melting point, with the onset of decomposition at 320°C. Reversibility has been reported at elevated temperatures of 600°C and pressures of 150 bar to rehydrogenate the decomposed materials. The decomposition mechanism, intermediates and products are complex and not fully understood. This chapter will therefore describe the use of in-situ Raman microscopy to understand the decomposition mechanism, in order to ascertain the effectiveness of lithium borohydride as a potential storage material for on-board applications.

Lithium borohydride has been extensively studied as a candidate hydrogen storage material. It undergoes a number of reaction steps on thermal decomposition. Previous studies have focused on using TGA and TPD measurements [19, 58, 62, 184, 185], to give weight change and hydrogen desorption information. Züttel et al. showed that lithium borohydride mixed with silicon oxide exhibits a multi-step decomposition reaction with the formation of intermediates [58]. Also, XRD, Raman and NMR have been used to try to identify the intermediates and reaction products, finding through XRD that lithium hydride was present in the decomposed samples, and from NMR the presence of lithium dodecaborane, $Li_2B_{12}H_{12}$, and amorphous boron [53, 54, 60, 186-189].

Ohba et al. [59] calculated the theoretical phonon density of states PDOS for $Li_2B_{12}H_{12}$ which was subsequently supported by Orimo et al. with ex-situ Raman of the decomposition products of lithium borohydride showing a good correlation between the predicted and observed spectra for $Li_2B_{12}H_{12}$[60]. The spectra measured by Orimo et al. show good correlation with previous IR and Raman spectra of 'free' $B_{12}H_{12}$ previously reported in [175].

Firstly, the decomposition path for $LiBH_4$ will be summarised (as discussed more fully in Section 2.1.1.). Lithium borohydride exists at room temperature as an orthorhombic structure, o-$LiBH_4$. Upon heating to 108°C, it undergoes a phase transition to a hexagonal phase, h-$LiBH_4$. There are some reports that there is a small irreversible release of hydrogen at the phase change, however, this appears not to affect the crystal structure measured by XRD or the vibration spectra. The h-$LiBH_4$ then melts at 270°C with no detectable change in mass to form liquid lithium borohydride $Li[BH_4]$, with the onset of thermal decomposition at 320°C yielding a total weight loss of 9 wt.% up to 600°C, which is summarised below:

$$\text{o-}LiBH_4 \rightarrow \text{h-}LiBH_4 \quad (9.1)$$

$$\rightarrow Li[BH_4] \quad (9.2)$$

$$\rightarrow {}^{1}/_{12}Li_2B_{12}H_{12} + {}^{5}/_{6}LiH + {}^{13}/_{12}H_2 \quad (9.3)$$

$$\rightarrow LiH + B + {}^{3}/_{2}H_2 \quad (9.4)$$

Currently most in-situ investigations have used XRD or neutron diffraction, however, these cannot readily give information on non-crystalline or liquid phases, and also the small scattering cross-section for x-rays makes structural determination difficult. The preparation of samples measured ex-situ via XRD [186, 190], NMR [188, 191] and Raman [163] has

shown the reaction products and stable intermediates during the thermal decomposition, however, it is very difficult to detect short-lived intermediate (or by-product) species. Raman spectroscopy has the advantages that phases with short-range order can be analysed, and, by focusing the laser on regions in a sample, the reaction path can be monitored with changing temperature with a rapid scan rate, collecting a 600 cm^{-1} spectrum every 15 seconds.

The two principal studies that characterised lithium borohydride using Raman were performed by Gomes et al. in 2002 [55] and Racu et al. in 2008 [57]. The work by Gomes et al. showed the change in peak width between o–$LiBH_4$ and h-$LiBH_4$ indicating an order-disorder transition. While this work did not use any method for measuring hydrogen loss, it showed no degradation in the sample upon cooling through the phase change, indicating that the o-$LiBH_4$ to h-$LiBH_4$ transition is fully reversible. Racu et al. focused their attention on assigning the vibrations to o-$LiBH_4$; through the use of lithium borodeuteride they were able to assign 27 of the 36 Raman active modes at -268°C and 18 at 25°C.

This work aims to characterise in detail the thermal decomposition of lithium borohydride. This will be done in five sections:

- Evaluation of the low temperature orthorhombic phase,
- Investigation of the change in properties of the $[BH_4]^-$ anion through the phase change,
- Evaluation of the $Li_2B_{12}H_{12}$ species formed on decomposition,
- In-situ Raman investigation into the decomposition mechanism of lithium borohydride
- In-situ optical microscopy of the decomposition of lithium borohydride.

9.1 Assignment of the Vibrational Modes of o-$LiBH_4$ and o-$LiBD_4$

Initially the aim was to verify the work of Racu et al. [57] by measuring lithium borohydride at room and liquid nitrogen temperatures (25 and -190 °C, respectively). This was to ascertain the resolution and ability to observe and decipher the vibration modes.

There are three regions of the spectra; firstly the BX_4^- stretching between 2000 and 2500 cm^{-1} when X = H, and 1500 and 2000 cm^{-1} when X = D, secondly the BX_4^- bending between 1000 and 1350 cm^{-1} when X = H, and 800 and 1000 cm^{-1} when X = D, and thirdly between 100 and 350 cm^{-1} when X = H or D for the external modes of vibration.

The room temperature Raman spectra of $LiBH_4$ and $LiBD_4$ are shown in Figure 9.1. The $LiBD_4$ (from Sigma-Aldrich) still has some residual $LiBH_4$ present, as shown by the broad peaks around 2300 cm^{-1}. However, this should not prove a large problem for subsequent variable temperature measurement, since there is a significant difference between the vibrational frequencies for B-H and B-D bonds.

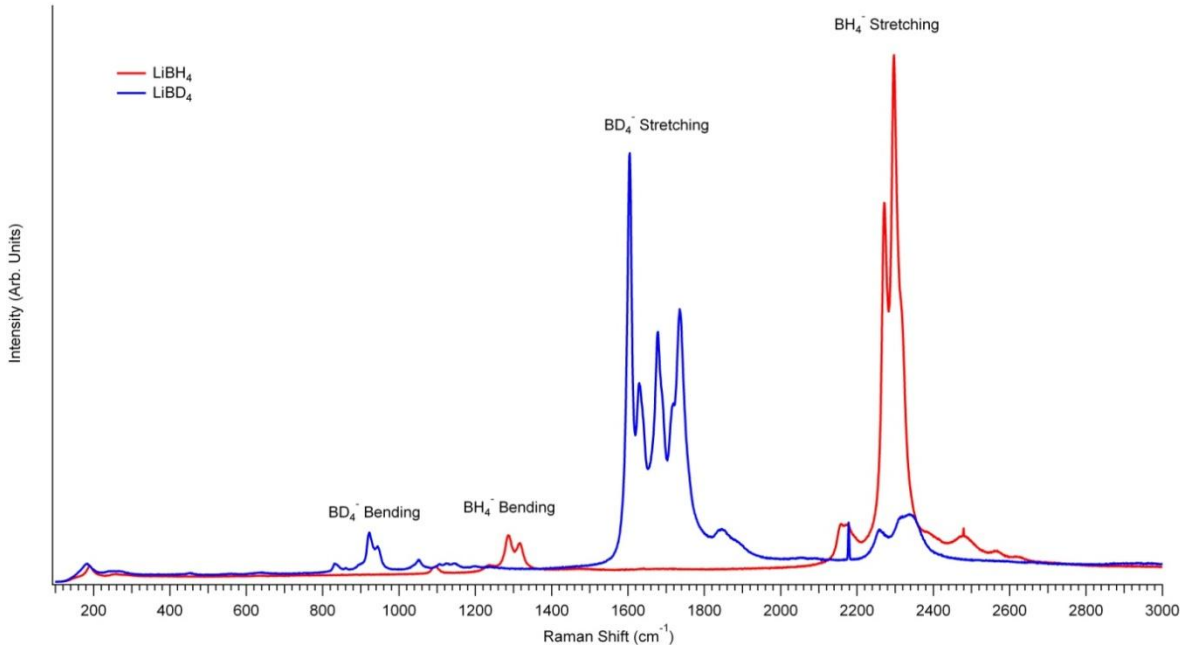

Figure 9.1 Raman spectra of $LiBH_4$ and $LiBD_4$ at room temperature measured using the 488 nm laser.

On cooling $LiBH_4$ and $LiBD_4$ to -190°C (Figure 9.2), the intensities of the peaks increase and the peak widths decrease. The largest change occurs in the region between 100 and 500 cm^{-1} where the external vibrations are more visible.

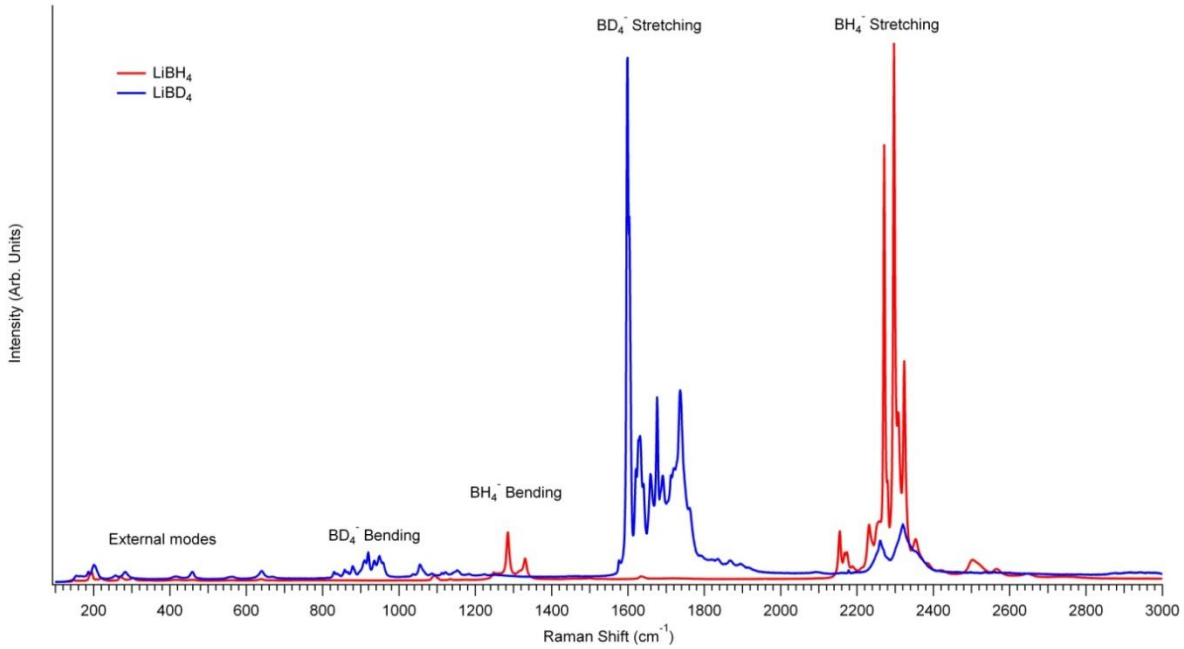

Figure 9.2 Raman spectra of $LiBH_4$ and $LiBD_4$ at -190°C measured using the 488 nm laser.

The three main regions of interest, internal stretching, bending and external modes, are shown in Figure 9.3, Figure 9.4 and Figure 9.5, respectively. The peaks are matched to the vibrational modes as shown and predicted by Racu et al. [57]; these peak positions are summarised in Table 9.1. The peak positions correlate well to those predicted by Racu et al., showing 21 of the 36 vibrations of lithium borohydride.

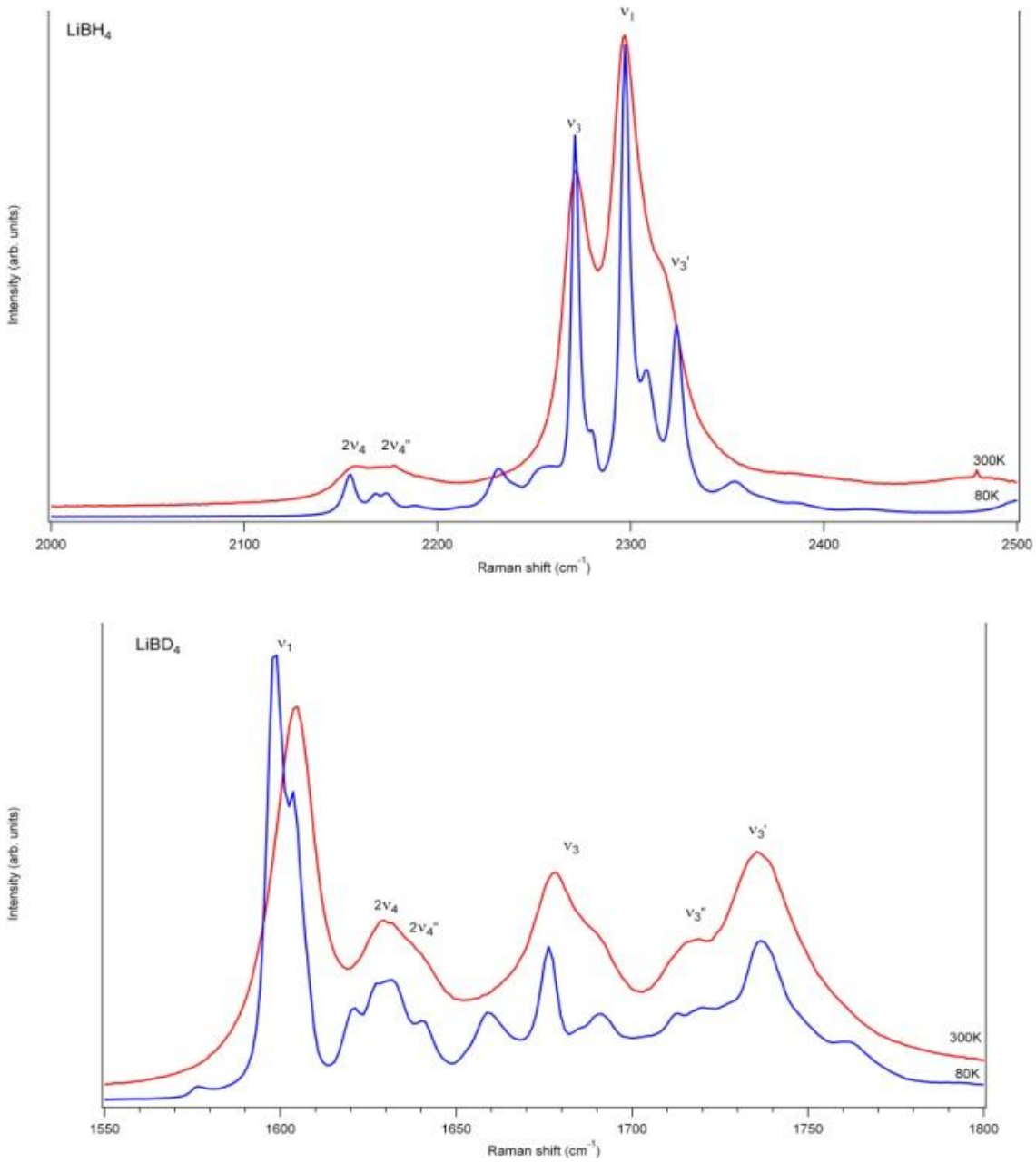

Figure 9.3 Raman spectra of internal stretching modes of $LiBH_4$ (top) and $LiBD_4$ (bottom) taken using the 488 nm laser (taken from Figure 9.1 (25 °C) and Figure 9.2 (-190 °C)).

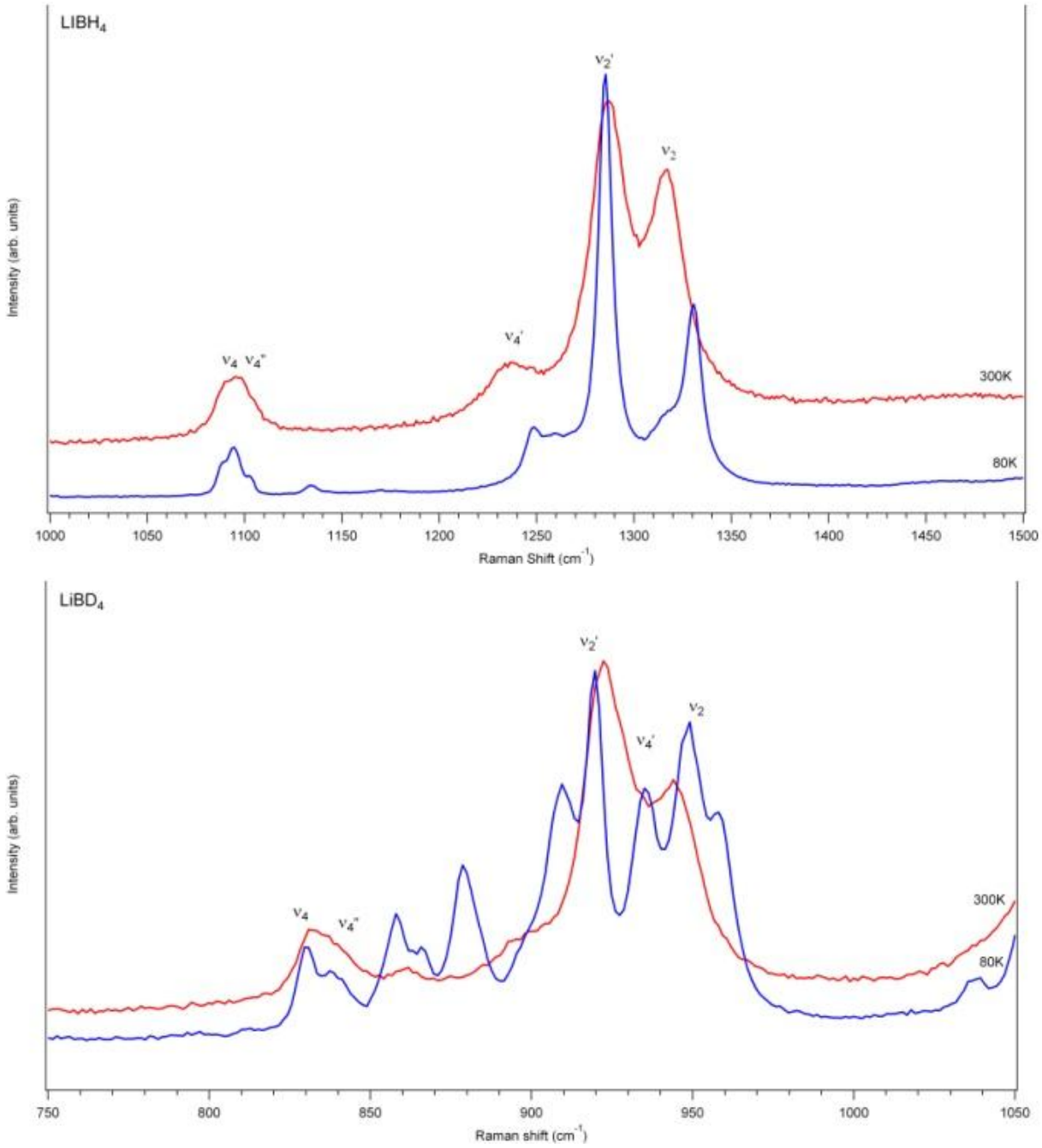

Figure 9.4 Raman spectra of the internal bending modes of $LiBH_4$ (top) and $LiBD_4$ (bottom) taken using the 488 nm laser (taken from Figure 9.1 (25 °C) and Figure 9.2 (-190 °C)).

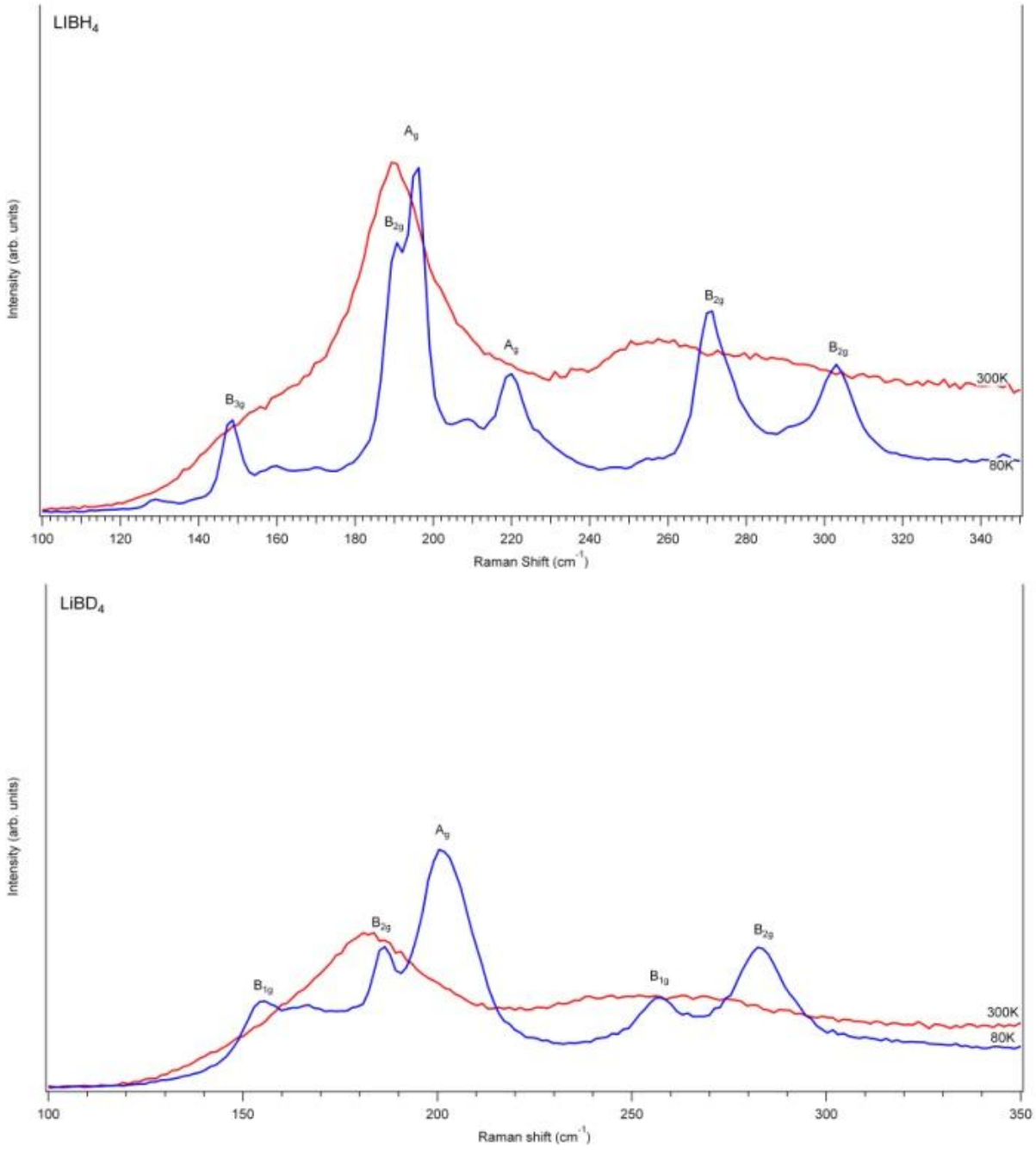

Figure 9.5 Raman spectra of the external modes of $LiBH_4$ (top) and $LiBD_4$ (bottom) taken using the 488 nm laser, (taken from Figure 9.1 (25 °C) and Figure 9.2 (-190 °C)).

Table 9.1 Measured Raman frequencies (cm^{-1}) of $LiBH_4$ and $LiBD_4$ at 25°C and at -190 °C, compared to calculated values [57].

	$LiBH_4$			$LiBD_4$		
Mode	**25 °C**	**-190 °C**	**Theoretical [57]**	**25 °C**	**-190 °C**	**Theoretical [57]**
			External Modes			
A_g			107			84.13
B_{1g}			125.6			112.13
B_{3g}			136.6			119.2
B_{3g}		149	155.3			100.43
B_{2g}		190	199.6		186	175.8
B_{1g}			212		154	157.2
A_g	191	196	213.3	181	202	194.5
A_g		221	263.3			246.3
B_{3g}			274.6			249.5
B_{2g}		172	273.3			241.9
B_{1g}			290		257	263.16
B_{2g}		302	292.3		283	269.5
A_g			350.3			331
B_{2g}			390			266.2
B_{3g}			439			318.23
B_{2g}			455.3			401.93
B_{1g}			459.6			340.7
A_g			483			380.
			Internal bending			
ν_4 (A_g)		1088	1062.6	831	830	805.5
ν_4 (B_{2g})	1094	1095	1064.66			805.7
ν''_4 (B_{1g})		1103	1070.3	839	838	807.7
ν''_4 (B_{3g})			1070.3			809.13
ν'_4 (A_g)	1248	1249	1235.3		935	919.7
ν'_4 (B_{2g})			1242.3			920.6
ν'_2 (B_{1g})	1285	1285	1260	923	920	897.43
ν'_2 (B_{3g})			1265.3			901.1
ν_2 (A_g)	1331	1331	1311.6	944	949	938.6
ν_2 (B_{2g})			1315.6			940.2
			Internal stretching			
ν_3 (A_g)	2272	2271	2327	1678	1676	1758.6
ν_3 (B_{2g})		2278	2329		1690	1768.6
ν_1 (A_g)	2296	2297	2371.6	1603	1598	1649.56
ν_1 (B_{2g})		2307	2384.6		1604	1752.16
ν''_3 (B_{1g})			2387.6	1713	1711	1772.8
ν''_3 (B_{3g})			2389.3			1774
ν'_3 (A_g)	2313	2324	2414	1736	1738	1794.7
ν'_3 (B_{2g})			2427.3		1758	1801.9

9.2 Phase Change of Lithium Borohydride

The next section of the work is to investigate the phase change from o-$LiBH_4$ to h-$LiBH_4$ as in the work started by Gomes et al. investigating how the vibrational modes changed in position and width. The phase change in lithium borohydride has also been studied by Soulié et al. using XRD [52], showing the phase change from the o-$LiBH_4$ P*nma* phase to the h-$LiBH_4$ $P6_3mc$ phase.

The phase change can be observed using DSC, as shown in Figure 9.6. The phase change has an energy of $\Delta Q = 6.00 \pm 0.03$ kJ/mol and is fully reversible over four cycles to 200°C. The onset of the phase change is at 117.5 ± 0.4 °C.

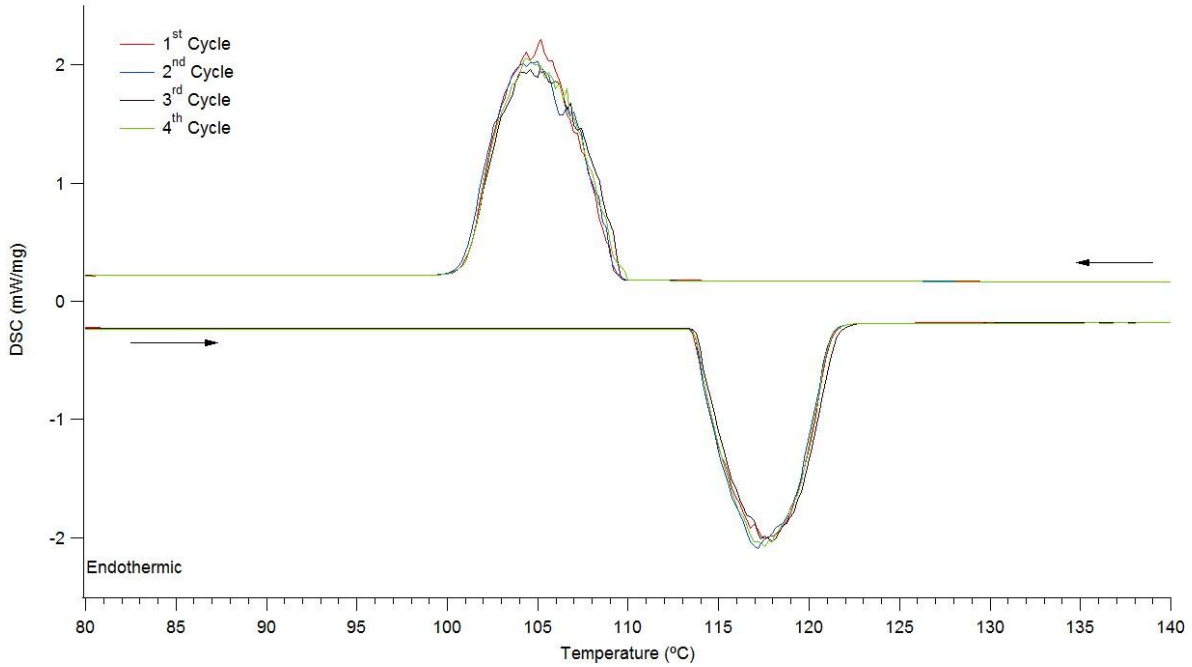

Figure 9.6 DSC of $LiBH_4$ heated to 200°C and cooled to room temperature in flowing argon at 4 bar at a constant heating and cooling rate of 2°C/min.

Figure 9.7 shows the in-situ XRD patterns for the heating of $LiBH_4$ from 20 to 200°C, showing the phase change between 110 and 120°C. The sample was then cooled to 30°C. Figure 9.8 shows the in-situ cooling with the phase change between 110 and 100°C. These results are in agreement with that seen by Soulié et al. [52] on a first-order phase transition from the P*nma* o-$LiBH_4$ to the P6_3*mc* h-$LiBH_4$ structure on heating, and the reversibility of the phase change back to the P*nma* o-$LiBH_4$ structure.

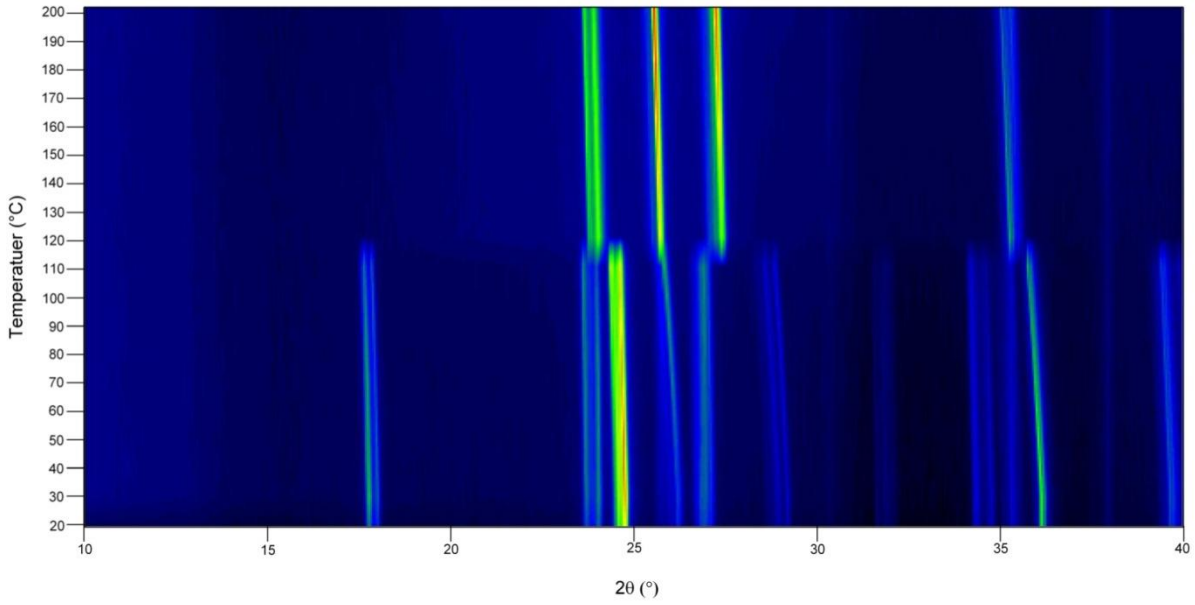

Figure 9.7 In-situ XRD of $LiBH_4$ heated at 2°C/min in flowing helium (at 100 ml/min and 2.5 bar). Diffraction patterns were taken every 10°C.

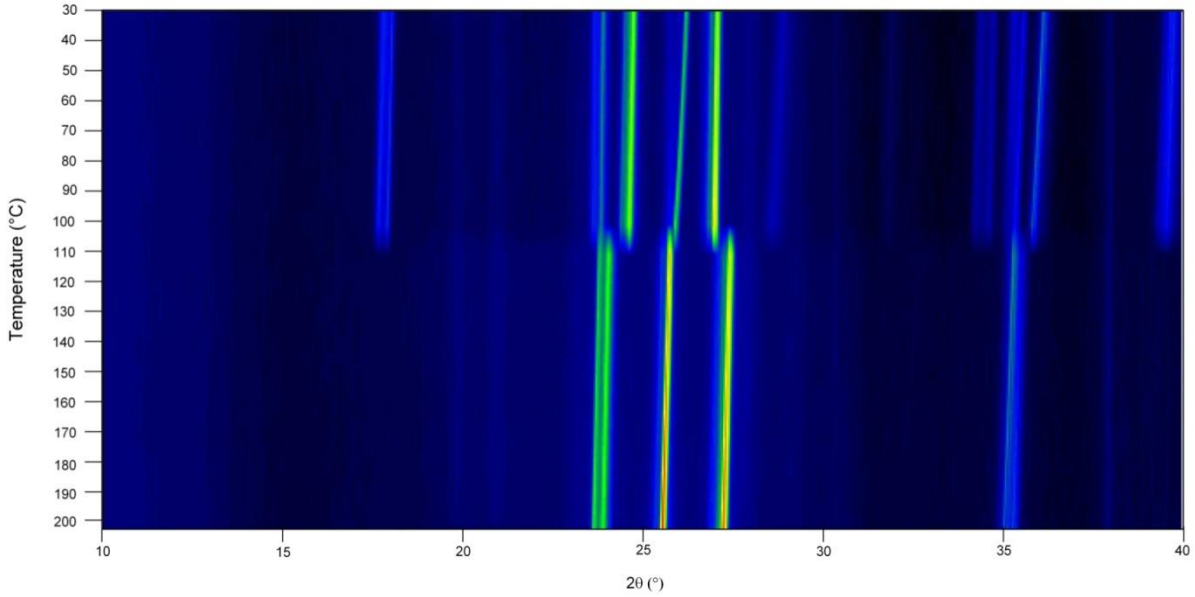

Figure 9.8 In-situ XRD of $LiBH_4$ cooled at 2°C/min in flowing helium (at 100 ml/min and 2.5 bar). Diffraction patterns were taken every 10°C.

Gomes et al. used Raman spectroscopy to evaluate the phase change and to better characterise the high temperature h-$LiBH_4$ phase. Previous work by Volkov et al. had only a partial IR spectrum around 2300 cm^{-1} [114]. Gomes et al. showed a significant shift in the ν_2 peak from around 1287 cm^{-1} to around 1302 cm^{-1}, and a significant reduction in the number of vibrations in the high temperature h-$LiBH_4$ phase, leaving only one broad B-H stretch at around 2300 cm^{-1} and one B-H bend at around 1300 cm^{-1} [55].

h-$LiBH_4$ has a simplified Raman spectrum compared to o-$LiBH_4$, as shown in Figure 9.9, since the point group symmetry of the BH_4^- anion increases in C_s to C_{3v}. Only three Raman bands, ν_2, ν_1 and ν_3, are observed; at 1303, 2294 and 2336 cm^{-1}, respectively. The ν_3 is very broad and can only be distinguished and characterised through curve fitting, with a half-width

half-maximum (HWHM) of 105 cm^{-1}. This is confirmed by the work by Gomes et al. [55]. There are no external vibrations observed for the h-$LiBH_4$.

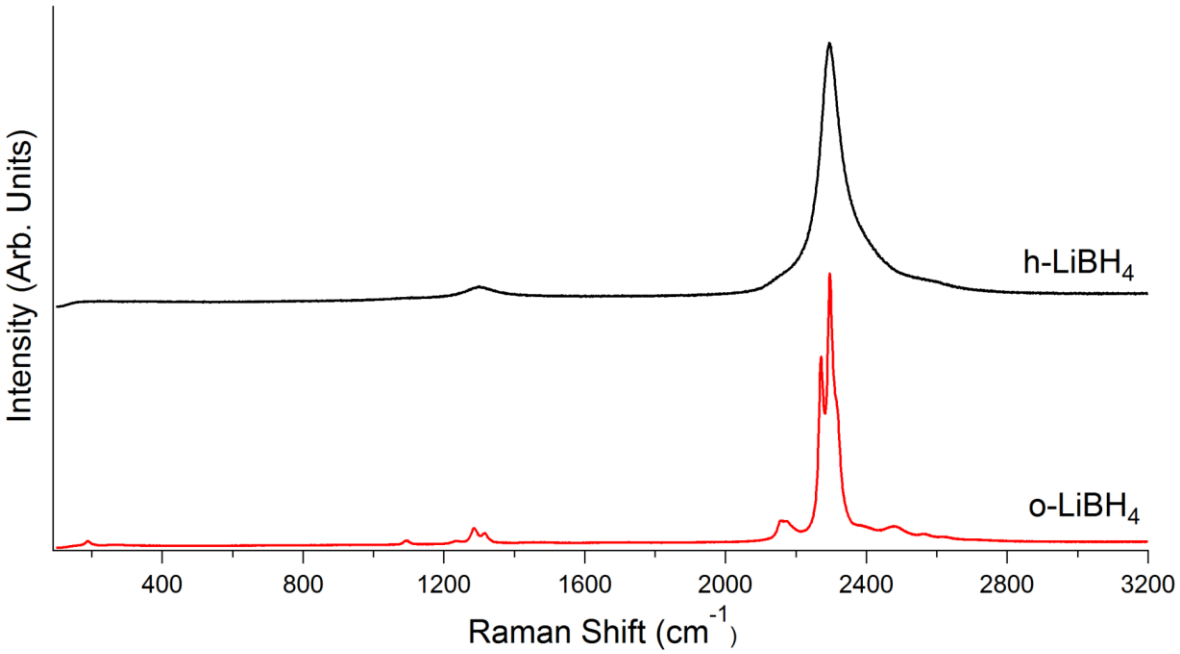

Figure 9.9 Raman spectra of o-$LiBH_4$ at room temperature and h-$LiBH_4$ at 150°C measured using the 488 nm laser.

In-situ static-mode Raman measurements were then performed with the grating held stationary, allowing a spectrum spanning ±300 cm^{-1} to be collected at 2300 cm^{-1} and 1000 cm^{-1} every 15 seconds, and with the focus position adjusted every 5th spectrum. Figure 9.10 shows the change in peak position of the ν_1, ν_3 and ν_3' modes versus temperature. There is little change in the peak positions on heating the o-$LiBH_4$ phase; once the sample goes through the phase change at 125°C to the h-$LiBH_4$ phase, the ν_3 and ν_3' modes combine to form a single ν_3, whilst the ν_1 mode remains in the same position. The phase change is at a higher temperature due to the thermocouple being located in the heating block and not near the sample.

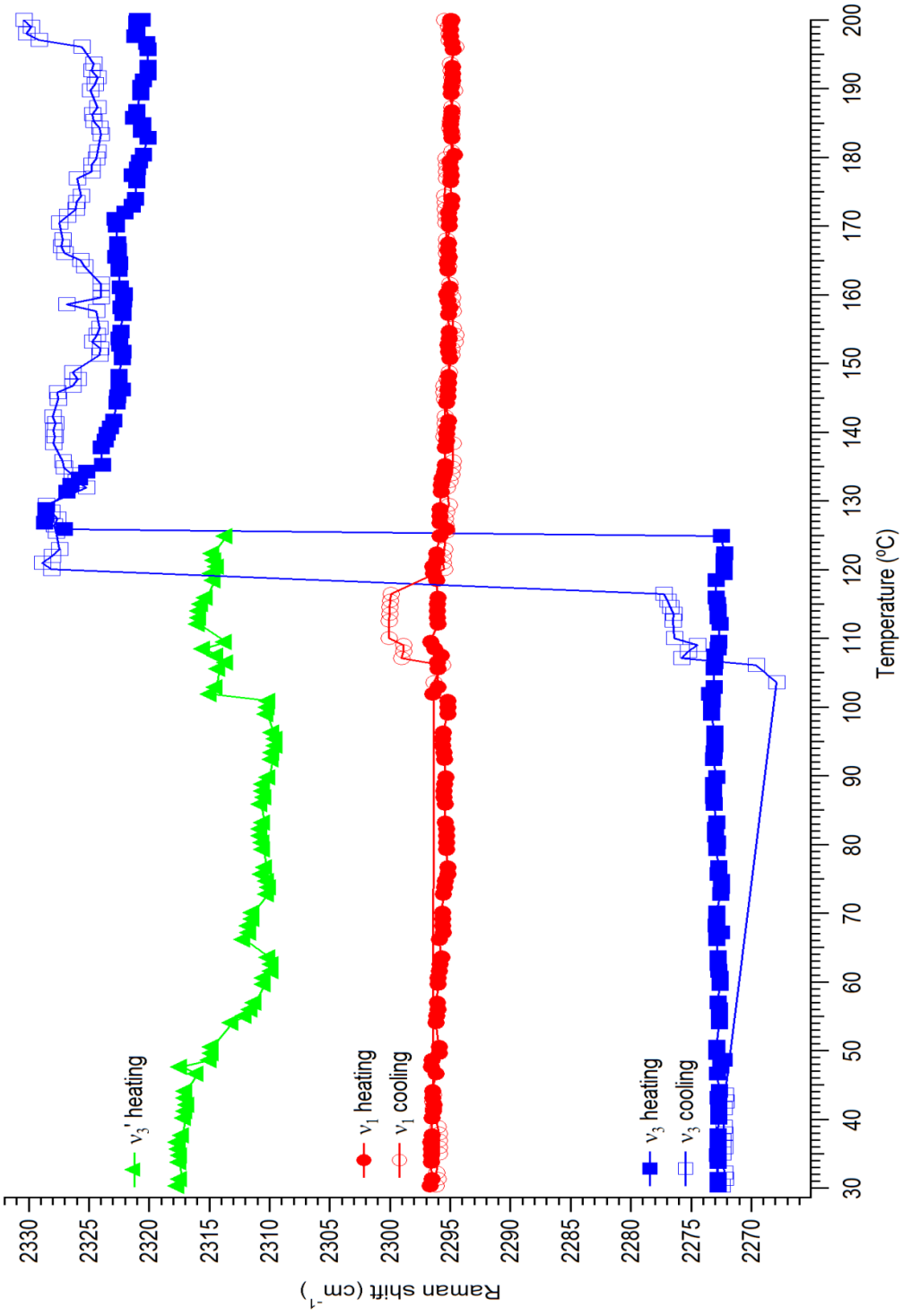

Figure 9.10 Raman shift of ν1, ν3 and ν3' modes in LiBH4 versus temperature during heating and cooling at 2°C/min in flowing argon.

On cooling, the phase change is observed at 117°C. The ν_1 and ν_3 vibrations were clearly visible, however, the ν_3' was not observed, though it could have been be masked by the ν_1 mode. Curve fitting the o-$LiBH_4$ on cooling was difficult as the peaks had become less well defined, as shown in Figure 9.11.

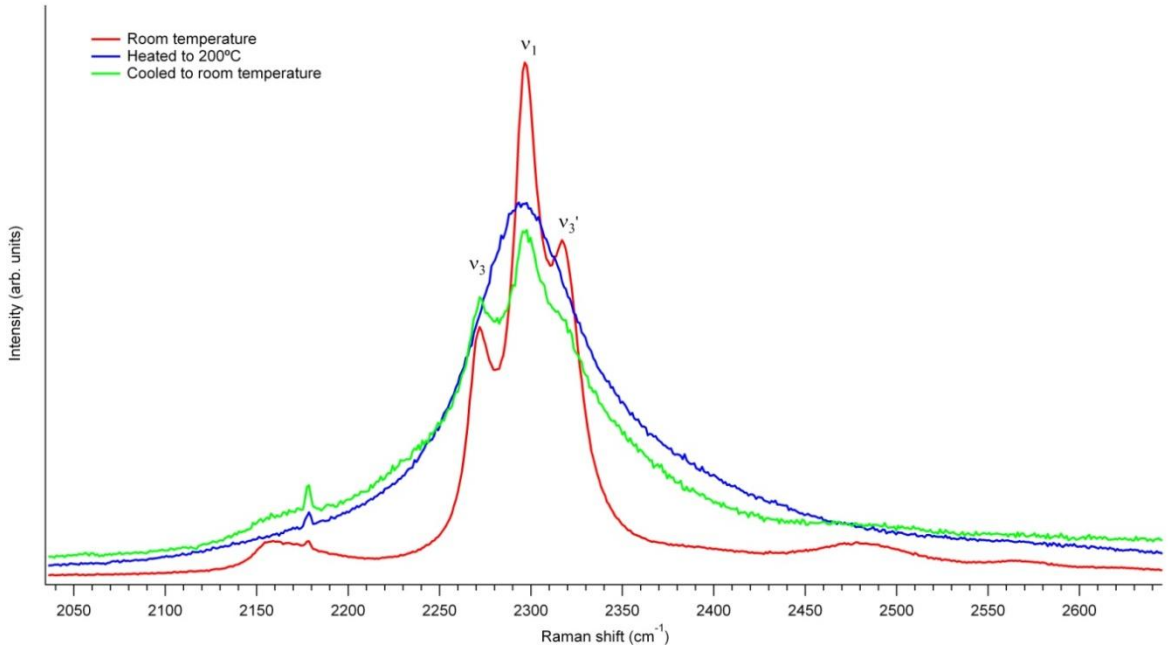

Figure 9.11 Raman spectra of $LiBH_4$ at room temperature heated to 200°C and cooled back to room temperature, with heating and cooling at a constant 2°C/min in flowing argon.

Figure 9.12 shows the change in peak position with temperature of the ν_2, ν_2' and ν_4' modes. The two components of the ν_2 mode, ν_2 and ν_2', combine at the phase change to yield a single ν_2 mode. The ν_4' disappears from the spectra after the phase change. The disappearance of the splitting ν_2 and ν_3 modes is consistent with the increased point group symmetry of the BH_4^- anion in the h-$LiBH_4$ structure.

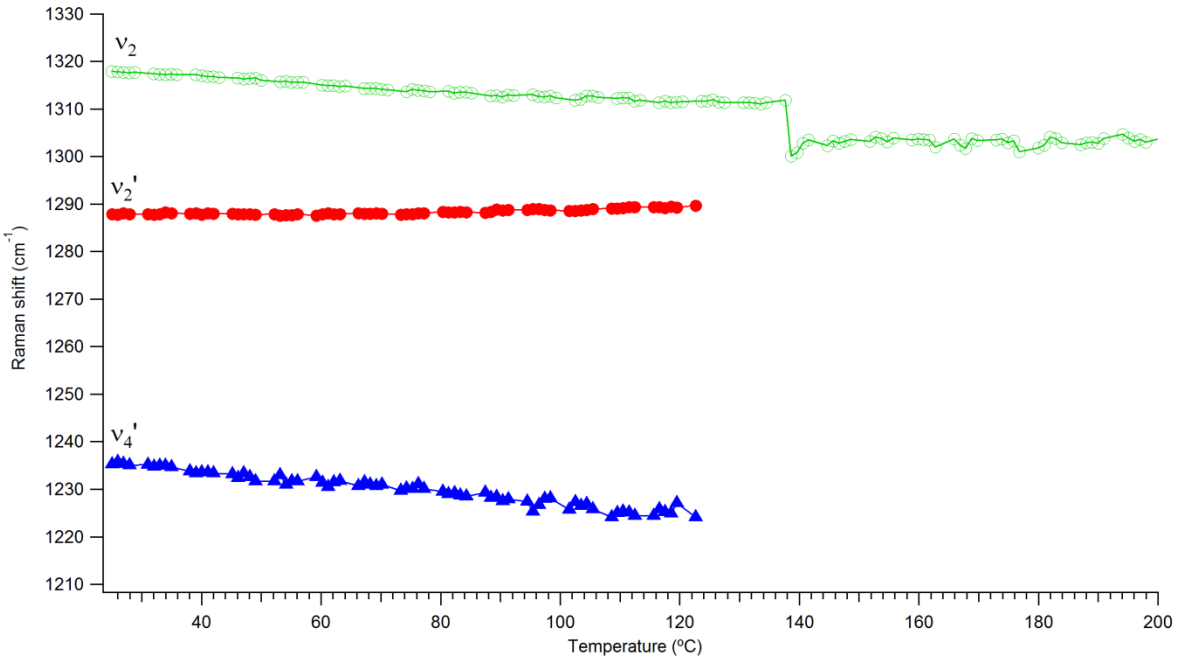

Figure 9.12 Raman shift of ν_2, ν_2' and ν_4' modes in $LiBH_4$ versus temperature during heating at 2°C/min in flowing argon.

An increase in dynamic disorder of the BH_4^- tetrahedron as the phases change from o-$LiBH_4$ to h-$LiBH_4$ can be observed by the temperature dependence of the Raman line widths on heating and cooling. Figure 9.13 shows the change in HWHM with temperature for the ν_1, ν_2 and ν_3 modes. There is an abrupt increase in peak width on heating and cooling through the phase change. Apart from the expected hysteresis in the phase transition temperature, there is no change in the peak widths on cooling back to room temperature indicating complete reversibility through the phase change. The peak widths for the ν_1 and ν_3 modes were calculated through curve fitting the measured spectra. Since the peaks are overlapping, there is a larger error, especially for the very broad ν_3 mode compared to the isolated ν_2 vibration. The HWHM at 30°C are all reasonably similar for the Raman lines: $\nu_1 \approx 8$ cm^{-1}, $\nu_2 \approx 12$ cm^{-1} and $\nu_3 \approx 9$ cm^{-1}.

After the phase change, the HWHM for the Raman lines in h-$LiBH_4$ are significantly different: $\nu_1 \approx 27$ cm^{-1}, $\nu_2 \approx 53$ cm^{-1} and $\nu_3 \approx 94$ cm^{-1}. The ν_3 mode is particularly different, becoming extremely broad and very hard to distinguish because of the ν_1 mode. This indicates an increase in dynamic disorder of the BH_4^- anions, which could be a result of either rotational freedom or large amplitude liberation motions.

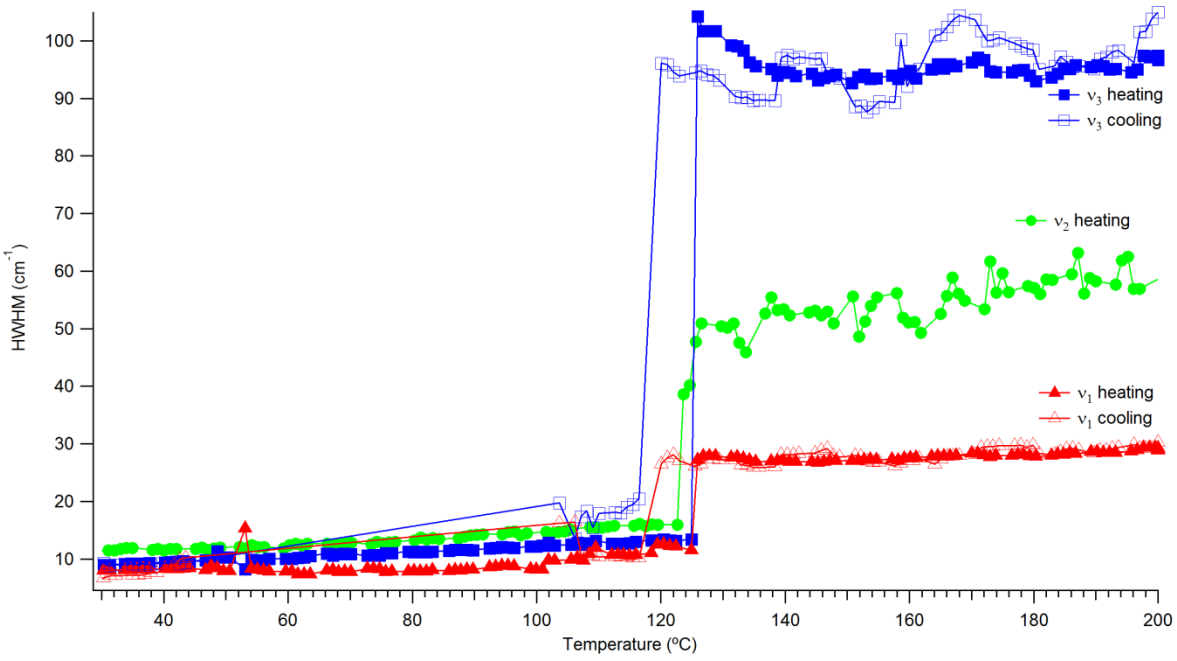

Figure 9.13 Line width HWHM as a function of temperature for the ν_1, ν_2, ν_3 modes of $LiBH_4$ at a constant heating rate of 2°C/min in flowing argon.

There are a number of physical processes that can contribute to the shape observed for Raman lines, including loss of phase coherence caused by reorientation, pure vibrational dephasing and defect introduction [192, 193].

It is possible to analyse the temperature dependence of the line widths quantitatively. The simplest reason for broadening is due to the decay of an optical photon in to two acoustic modes, phonon-phonon broadening. The line broadening, Γ_p, for this case can be described by:

$$\Gamma_p(T) = \Gamma_0 \left(1 + \frac{2}{e^y - 1}\right) \tag{9.5}$$

where Γ_0 is the temperature independent broadening due to disorder in the crystal, or harmonic line width, and $y = \hbar\omega_0/k_BT$, where ω_0 is the harmonic frequency. This type of broadening is important when the energy is lower than k_BT such as for the external modes.

The total broadening can be described as the sum of the phonon-phonon broadening, and a residual term that encompasses other types of phonon decay:

$$\Gamma(T) = \Gamma_p(T) + \Gamma_R(T) \tag{9.6}$$

where the residual broadening follows an exponential form

$$\Gamma_R(T) = Ae^{-\frac{U}{k_BT}} \tag{9.7}$$

where A is a constant and U is an activation energy.

Jenkins and Lewis [192] discuss the change in line width of the water molecules in hexa-aquo metal (II) hexafluorosilicates (IV) with temperature, and discuss broadening in terms of anharmonicity. Anharmonicity may influence the vibrational state in two ways, firstly by thermal expansion of the lattice, which results in uniform displacement of the molecules within the lattice. This yields a frequency shift but no line broadening. Secondly, by thermal fluctuations within a lattice, which cause coupling between vibrations, and lead to a change in both frequency and line width.

Racu et al and Jenkins and Lewis [57, 192] have shown that at modest temperatures the HWHM line broadening obeys an Arrhenius-type law, as shown in equation (9.8):

$$\Delta\Gamma = A + Be^{-\frac{U}{k_B T}} \tag{9.8}$$

where U is the energy of the phonon which is scattered by the vibrational state in the range k_BT. Constant A is related to the decay of the excited state and B relates to the low frequency variations.

Let us consider the υ_2 mode, since it is unhindered by other vibrational modes. Plotting ln Γ against $^1/_T$ allows the data to be fitted with a linear regression line, where the gradient is the activation energy in Kelvin (U/k_B) and the intercept is B+LnA/ Γ_0. Figure 9.14 shows the Arrhenius plot for the υ_2 mode of o-$LiBH_4$ and h-$LiBH_4$. The activation energy for o-$LiBH_4$ is 402 ± 11.4 K and 449 ± 36.3 K for h-$LiBH_4$.

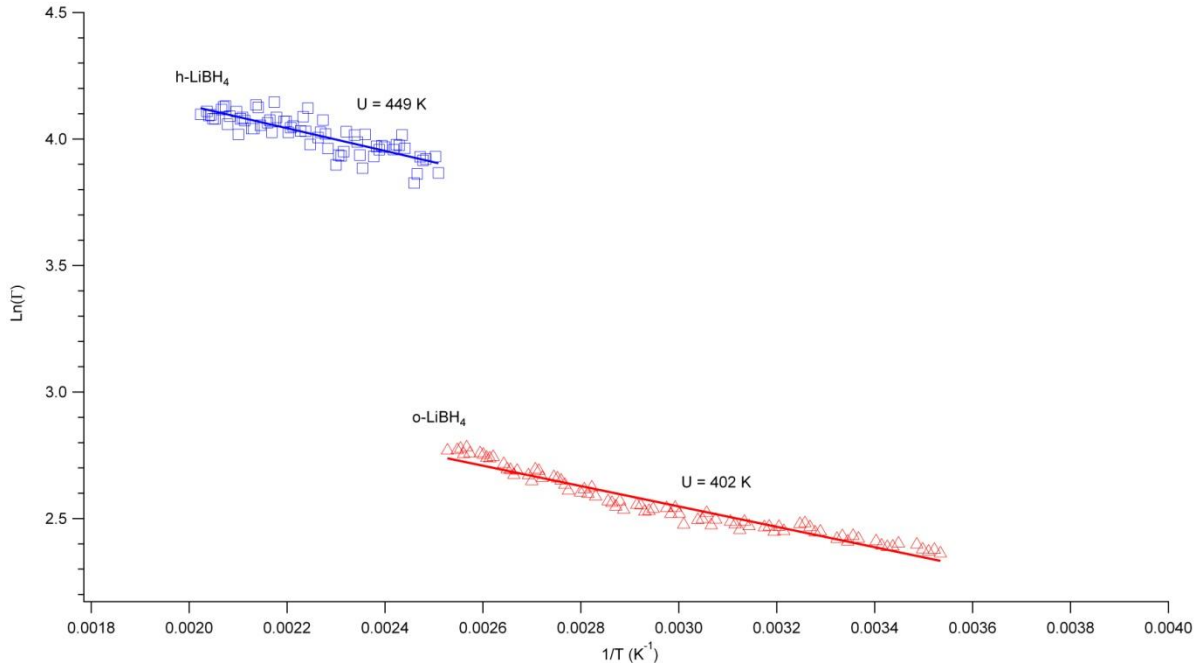

Figure 9.14 Arrhenius plot of Γ for the internal υ_2 mode of o-$LiBH_4$ and h-$LiBH_4$.

These results show that there is a change in temperature dependence of line broadening on the phase change from o-$LiBH_4$ to h-$LiBH_4$. There is insufficient temperature range to accurately determine the true nature of the broadening. It can be concluded, however, that there is a dramatic rearrangement in the BH_4^- anions allowing a greater freedom of motion whilst not allowing complete freedom of rotation.

Hagemann et al. investigated the change in HWHM of the ν_2 mode of alkali metal borohydrides with temperature. The HWHM of the ν_2 mode of $NaBH_4$, KBH_4, $RbBH_4$ and $CsBH_4$ all increase with temperature by the general expression [56]:

$$\Gamma(\omega, T) = (a + bT) + c.e^{-V/kT} \tag{9.9}$$

where V is the energy barrier to reorientation motion. If the linear contribution arising form anharmonicity is neglected, it leads to the relation

$$\Gamma(\omega, T) = a + c.e^{-VkT} \tag{9.10}$$

This expression did not fit well for the results obtained for $LiBH_4$. In 2009 Hagemann et al. showed that equation (9.11) was a poor fit, obtaining an average value of 15 ± 2 kJ/mol [194].

$$\Gamma = \Gamma_0 + A.e^{-V/RT} \tag{9.11}$$

Hagemann et al. therefore proposed the use of a more complex expression, as a non-cubic crystal was expected to exhibit several different energy barriers [194]. A precise physical meaning for V_1 and V_2 has not yet been established, as they are dependent on the symmetry of the reorientation motion.

$$\Gamma(\omega, T) = \Gamma_0 + A.e^{-V_1/RT} + B.e^{-V_2/RT} \tag{9.12}$$

When the biexponential is fitted to the data, Figure 9.15, values of 3.56 ± 0.9 and 12.75 ± 3.2 kJ/mol were obtained for V_1 and V_2. The values obtained match well with the values presented by Hagemann et al. of 2.9 ± 0.1 and 15 ± 0.5 kJ/mol [194].

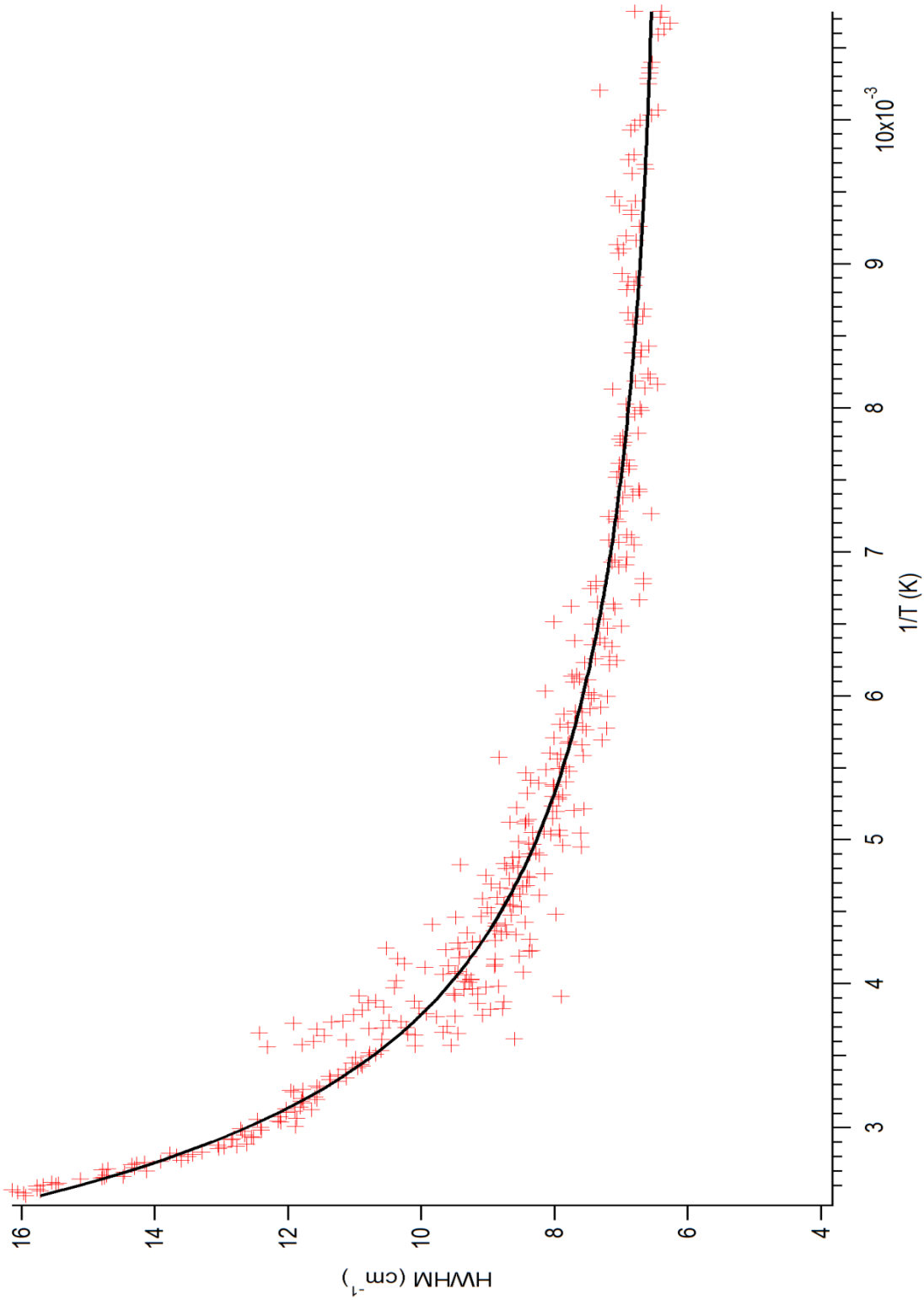

Figure 9.15 Half-width half-maximum of the ν_2 band with increasing temperature, from -190 to 110°C at 2°C/min. The solid line corresponds to the biexponential fit in equation (9.12).

9.3 Investigation into the Reaction Intermediate $Li_2B_{12}H_{12}$

As discussed above, the decomposition of lithium borohydride proceeds through the 'intermediate' lithium dodecaborane, $Li_2B_{12}H_{12}$. This compound has been observed via NMR and Raman using ex-situ techniques. This work will look at investigating this compound in-situ in order to aid the study of thermal decomposition.

Ohba et al. [59] predicted the PDOS via DFT calculations for $Li_2B_{12}H_{12}$. Figure 9.16 shows the predicted PDOS and compares it to the in-situ Raman spectra of lithium borohydride at 600°C. This shows good correlation between the peak positions in the spectra, though the intensities do not correlate so well. This therefore shows that $Li_2B_{12}H_{12}$ is formed as part of the thermal decomposition of lithium borohydride and is stable up to 600°C.

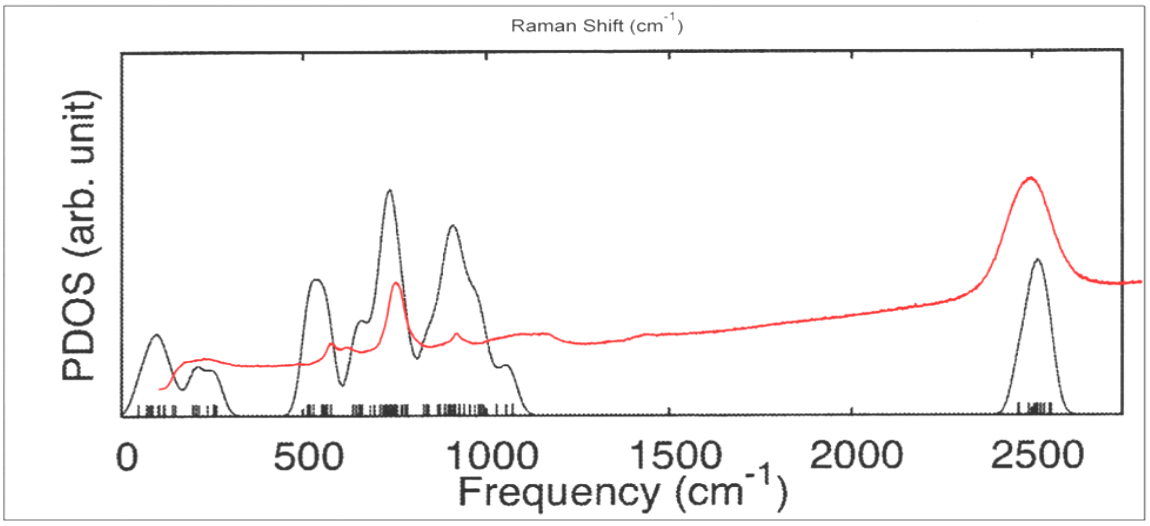

Figure 9.16 Comparison between $LiBH_4$ heated to 600°C (red line) and the Ohba et al. DFT prediction of the PDOS [59].

Investigations into closo-B_xH_y species have been conducted previously and discussed (section 4.3.1). The Raman and IR spectra of isolated $[B_{12}H_{12}]^{2-}$ have been recorded and interpreted previously [175], showing that the B-H stretches are associated with the equatorial breathing mode at 2470 cm^{-1} with a shoulder due to the apical mode. There are also cage deformation modes between 1015 and 1070 cm^{-1}. There are three IR active modes of $[B_{12}H_{12}]^{2-}$ at 4288, 1070 and 720cm^{-1} and 6 Raman modes, A_g 2518 and 743 cm^{-1} and H_g 2470, 949, 770 and 584 cm^{-1}.

Samples of $LiBH_4$ and $LiBD_4$ were heated to 600°C to form $Li_2B_{12}H_{12}$ and $Li_2B_{12}D_{12}$ as shown in Figure 9.17 and summarised in Table 9.2. The υ_1 and υ_6 modes have an isotopic ratio of around 1.7, meaning that they correspond to a vibration involving hydrogen. The υ_1 and υ_6 modes are the equatorial and apical B-H breathing modes, respectively. The υ_2 mode corresponds to the breathing mode of the boron cage, when the isotope ratio of 1.06 is compared to the mass ratio of BH and BD, 1.085. This suggests that the BH units vibrate as a single unit with no change in the BH force constant. The other modes involve cage deformations; the υ_8 mode appears to be the displacement of the BH group as a single unit, while the υ_7 and υ_9 modes involve distortion of the B-H bond during displacement.

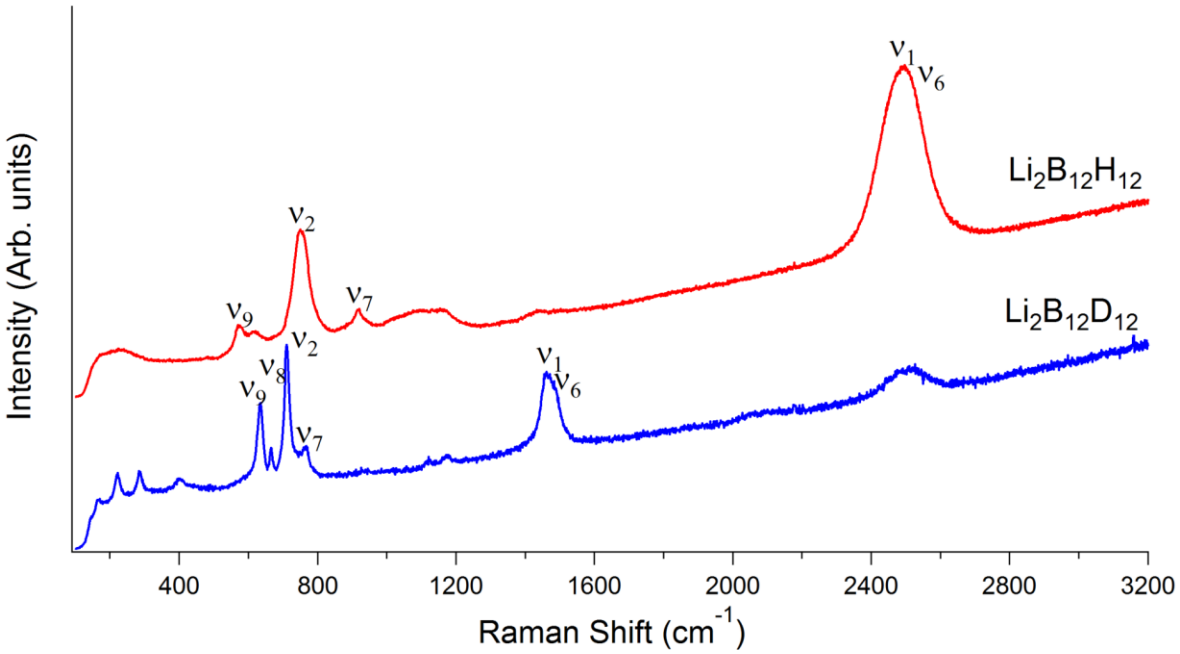

Figure 9.17 In-situ Raman spectra of $LiBH_4$ and $LIBD_4$ measured at 600°C in flowing argon at 2°C/min.

Table 9.2 Experimental frequencies (cm^{-1}) of $LiBH_4$ and $LiBD_4$ measured at 30°C and 600°C showing the isotopic dependence of the vibrations.

Mode		**$Li_2B_{12}H_{12}$**		**$Li_2B_{12}D_{12}$**		**υ_H/υ_D**	
		30°C	**600°C**	**30°C**	**600°C**	**30°C**	**600°C**
υ_1	A_g	2535	2517		1489		1.69
υ_2	A_g	746	752		660		1.06
υ_6	H_g	2479	2461		1460.2		1.69
υ_7	H_g	925	918		761		1.20
υ_8	H_g	771			711		
υ_9	H_g	585	572		634		0.90
υ_9'	H_g		611				

Figure 9.18 shows the Raman spectra of $Li_2B_{12}H_{12}$ formed through the decomposition of lithium borohydride cooled to room temperature. On cooling from 600°C to room

temperature $Li_2B_{12}H_{12}$ still remains part of the decomposition products, though background is large, indicating that $Li_2B_{12}H_{12}$ is stable on cooling to room temperature and therefore not an unstable high temperature intermediate in the decomposition.

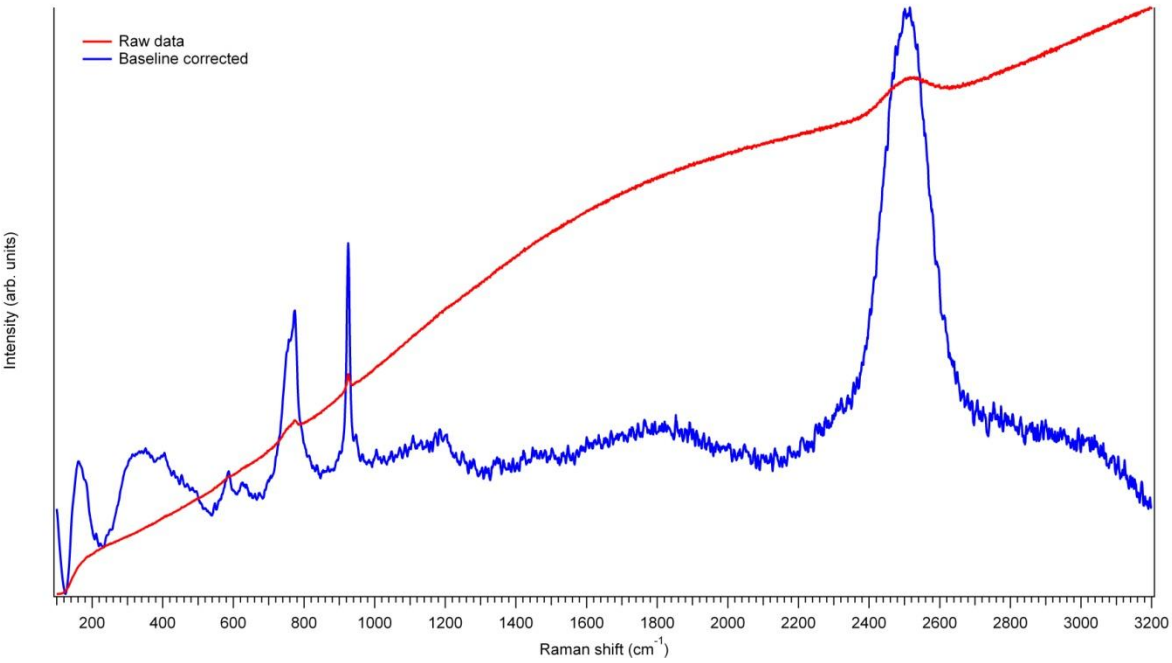

Figure 9.18 Raman spectra of $LiBH_4$ heated to 600°C and cooled to room temperature showing the as-measured spectrum and baseline corrected spectrum.

9.4 Thermal Decomposition of $LiBH_4$

As shown in section 9.1, lithium borohydride goes through a multistep decomposition process. Figure 9.19 shows the in-situ Raman measurements of $LiBH_4$ collected isothermally at 50, 150, 350, 500 and 600°C. As previously discussed in section 9.2, at 50 and 150°C $LiBH_4$ exists as o-$LiBH_4$ and h-$LiBH_4$, respectively. On further heating, lithium borohydride melts to form $Li[BH_4]$. The Raman spectrum at 350°C shows significant broadening of the Raman lines, with another large change in the peak width, as the BH_4^- anion now has complete rotational freedom. With continued heating the $Li[BH_4]$ decomposes, and at 500°C there is the formation of $Li_2B_{12}H_{12}$ and amorphous boron. On heating to 600°C the sample is almost exclusively $Li_2B_{12}H_{12}$.

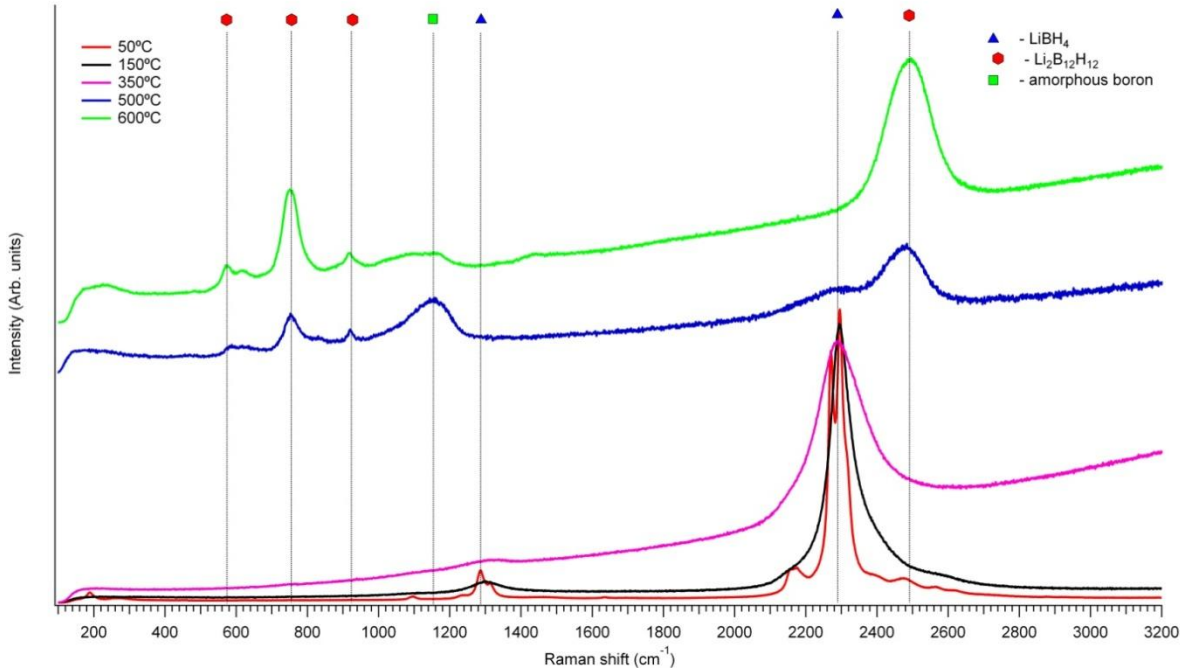

Figure 9.19 In-situ Raman of $LiBH_4$ collected isothermally at 50, 150, 350, 500 and 600°C. The sample was heated in flowing argon, at a heating rate of 2°C/min.

In-situ investigation into the thermal decomposition of lithium borohydride focused on two areas of the spectra, the B-H stretch region at 2300 ± 300 cm^{-1} and the region around 1000 ± 300 cm^{-1}, observing the B-H bend and skeletal vibrations of $Li_2B_{12}H_{12}$ and boron. Spectra covering a range of 600 cm^{-1} were collected every 15 seconds whilst the sample was heated to 600°C at 2°C/min in flowing argon.

Focusing is important for the in-situ measurements. The system is able to autofocus using the intensity of a low-power laser spot to determine focus, which means that the system will focus on the top surface of a solid or on the pan containing a liquid.

Figure 9.20 shows the normalised intensities of the B-H stretch region. Here the transition from o-$LiBH_4$ to h-$LiBH_4$ can be seen as a broadening of the 2300 cm^{-1} line around 3000 seconds (~125 °C). Melting of lithium borohydride is seen at 8000 seconds (~290 °C). After about 10250 seconds, the 2300 cm^{-1} B-H stretch of the BH_4^- ion is replaced by the hydrogen breathing mode of $Li_2B_{12}H_{12}$ at 2500 cm^{-1}. On isothermally holding at 600°C, the peak width of $Li_2B_{12}H_{12}$ appears to decrease, indicating the possible crystallisation of $Li_2B_{12}H_{12}$.

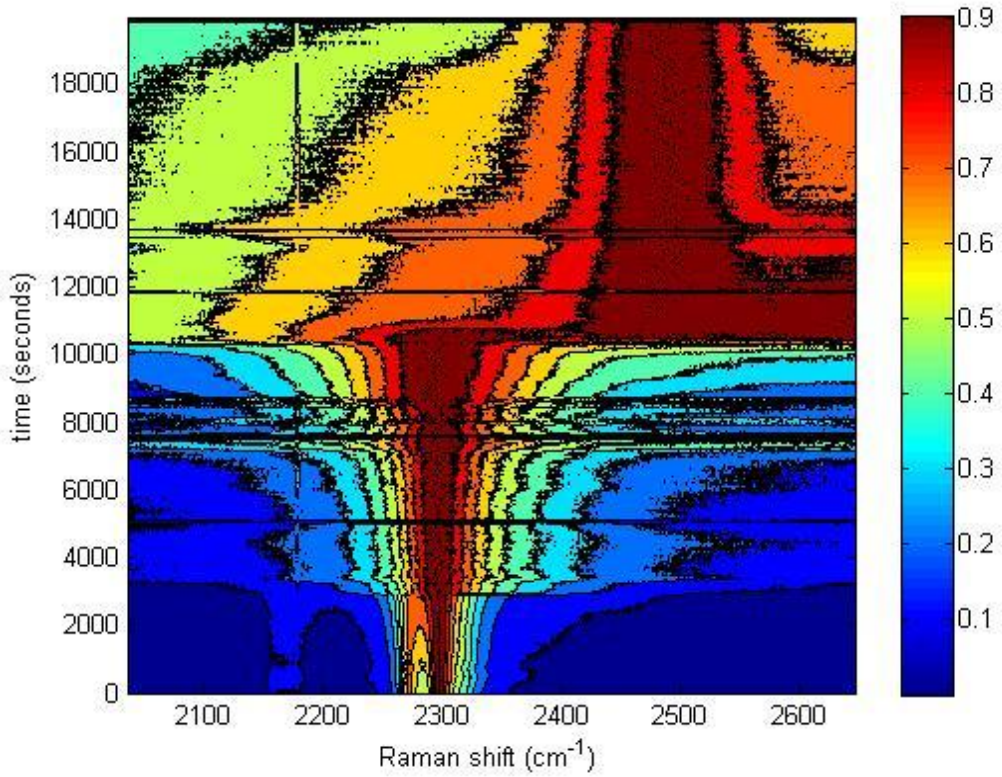

Figure 9.20 Normalised intensity of Raman spectra collected in the 2000 - 2650 cm^{-1} region during heating of $LiBH_4$ at a constant heating rate of 2°C/min (0.0333°C /s) to 600°C (17267 seconds) and then held isothermally in flowing argon.

To further understand the decomposition process, Figure 9.21 shows the change in peak position with temperature. As previously discussed in section 9.2 and shown in Figure 9.10, during the phase change from o-$LiBH_4$ to h-$LiBH_4$, the υ_3 modes combine to form a single υ_3 mode. Due to the large width of the υ_3 mode and the overlap with the ν_1 mode in h-$LiBH_4$, the curve fitting required to determine peak-width and position has larger errors compared to isolated peaks, leading to a large scatter in the data points. The υ_1 mode of h-$LiBH_4$ shows little change with temperature.

The focus position in Figure 9.21 remains fairly constant until 250°C. The focus position then increases since a different area of the sample has moved into view; this does not affect the subsequent change in height due to melting. At 290°C the sample begins to melt, and is seen as a change in focus height, where the microscope now focuses onto the pan containing the liquid lithium borohydride. The focus height above 360°C begins to increase as the reaction products precipitate out of the molten lithium borohydride.

On melting, the υ_1 and υ_3 lines of $LiBH_4$ in Figure 9.21 initially change position as the system struggles to focus on the sample as it changes height. There is then little change in peak positions of the B-H stretches in $Li[BH_4]$ until 375°C. The onset of decomposition occurs and where the $Li[BH_4]$ vibrations decrease in wavenumber. The onset of $Li_2B_{12}H_{12}$ formation is measured at 356°C, although the peak is weak and broad. At 375°C the breathing mode of $Li_2B_{12}H_{12}$ is clearly defined and has a stable position. At 420°C the vibrations due to $LiBH_4$ are barely measurable, but the two $Li_2B_{12}H_{12}$ breathing modes are fitted. The equatorial and apical breathing modes, υ_1 and υ_6, respectively, become clear enough above 420°C to fit two curves. The peak position between 350 and 420°C is fitted to a single curve and therefore gives an average position of the two vibrations. The breathing modes of $Li_2B_{12}H_{12}$ do not vary significantly with temperature. B-H stretches due to lithium borohydride are visible until around 510°C.

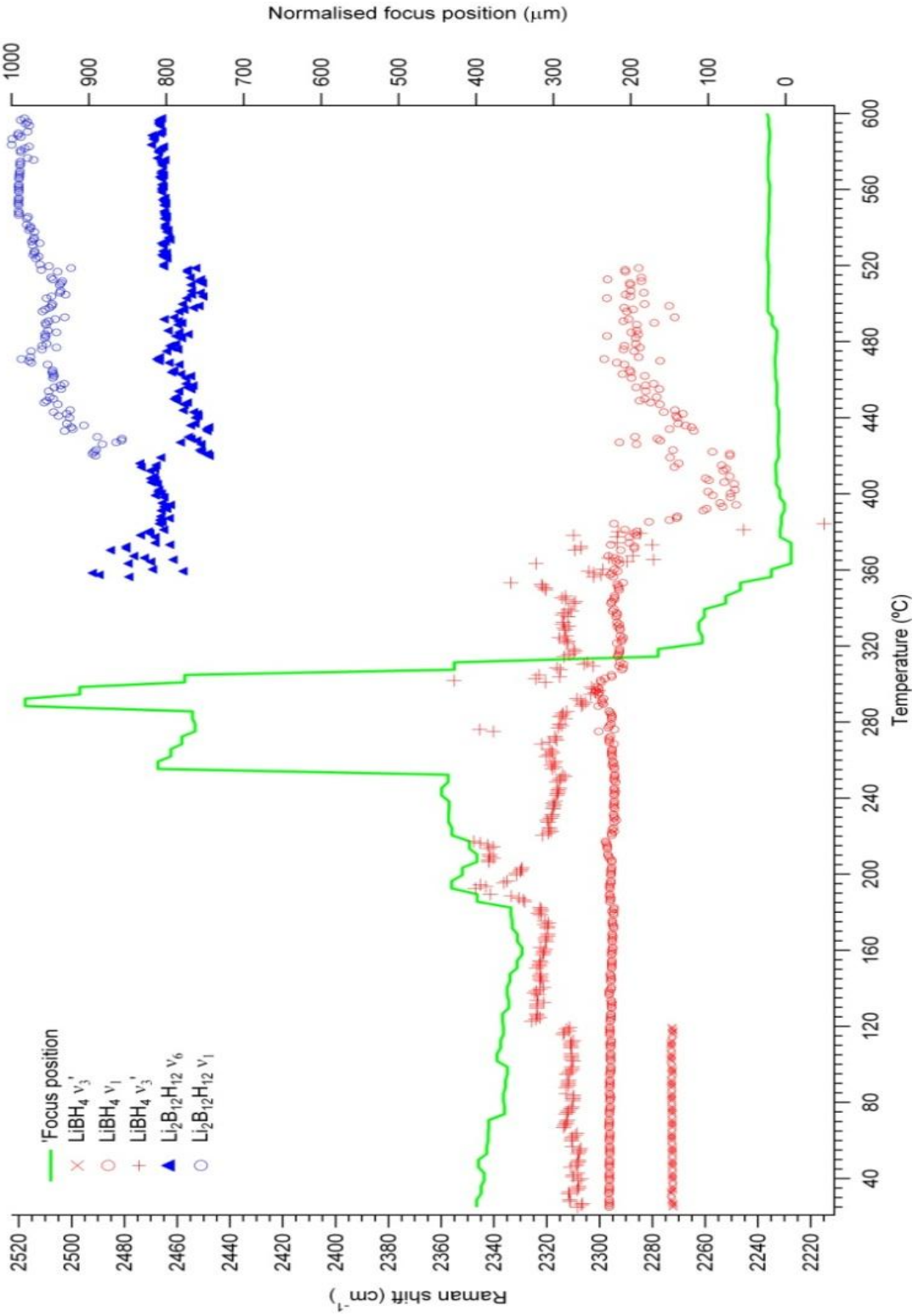

Figure 9.21 In-situ Raman peak position of the B-H stretching modes of $LiBH_4$, the hydrogen breathing modes of $Li_2B_{12}H_{12}$, and the focus height of the microscope, measured under flowing argon at a constant heating rate of 2 °C/min.

The change in peak widths with temperature and thermal decomposition is shown in Figure 9.22. The HWHM of the lithium borohydride B-H stretches go through a stepped change at the o-$LiBH_4$ to h-$LiBH_4$ phase change as previously shown in section 9.2. There is another shift in HWHM on melting; this change occurs slowly between 284 and 314°C to 65 cm^{-1} due to an increase in freedom of the BH_4^- anion. As decomposition occurs, the peak width of the B-H stretch of $LiBH_4$ again increases. The HWHM of the hydrogen breathing modes of $Li_2B_{12}H_{12}$ are around 65 and 45 cm^{-1}. For the υ_6 and υ_1 modes, they remain reasonably constant until 520°C at which point there is no BH_4^- present and the HWHM of the υ_1 decreases and there is a slight increase in the apical υ_6 mode. This is probably due to the rearrangement of the $B_{12}H_{12}^{2-}$ into a more ordered structure.

Figure 9.23 shows the normalised intensities of the B-H bend of $LiBH_4$ and the skeletal B-B bonding of amorphous boron and $Li_2B_{12}H_{12}$ around 1000 cm^{-1}. Here the transition from o-$LiBH_4$ to h-$LiBH_4$ can be seen broadening the 1300 cm^{-1} line at around 0.3 x 10^4 seconds (~125°C) and leading to the disappearance of the 1100 cm^{-1} line. Melting of lithium borohydride is seen at 0.8 x 10^4 seconds (~290 °C). After about 1.02 x 10^4 seconds (~365 °C), the 1150 cm^{-1} B-H bend of the BH_4^- ion becomes broad and the boron breathing mode of $Li_2B_{12}H_{12}$ at ~750 cm^{-1} and amorphous boron become present within the sample. On isothermally holding at 600°C, the peaks due to $Li_2B_{12}H_{12}$ appear to increase in intensity and the peaks due to amorphous boron decrease; indicating possible crystallisation of $Li_2B_{12}H_{12}$ at the expense of amorphous boron on the surface of the decomposed sample.

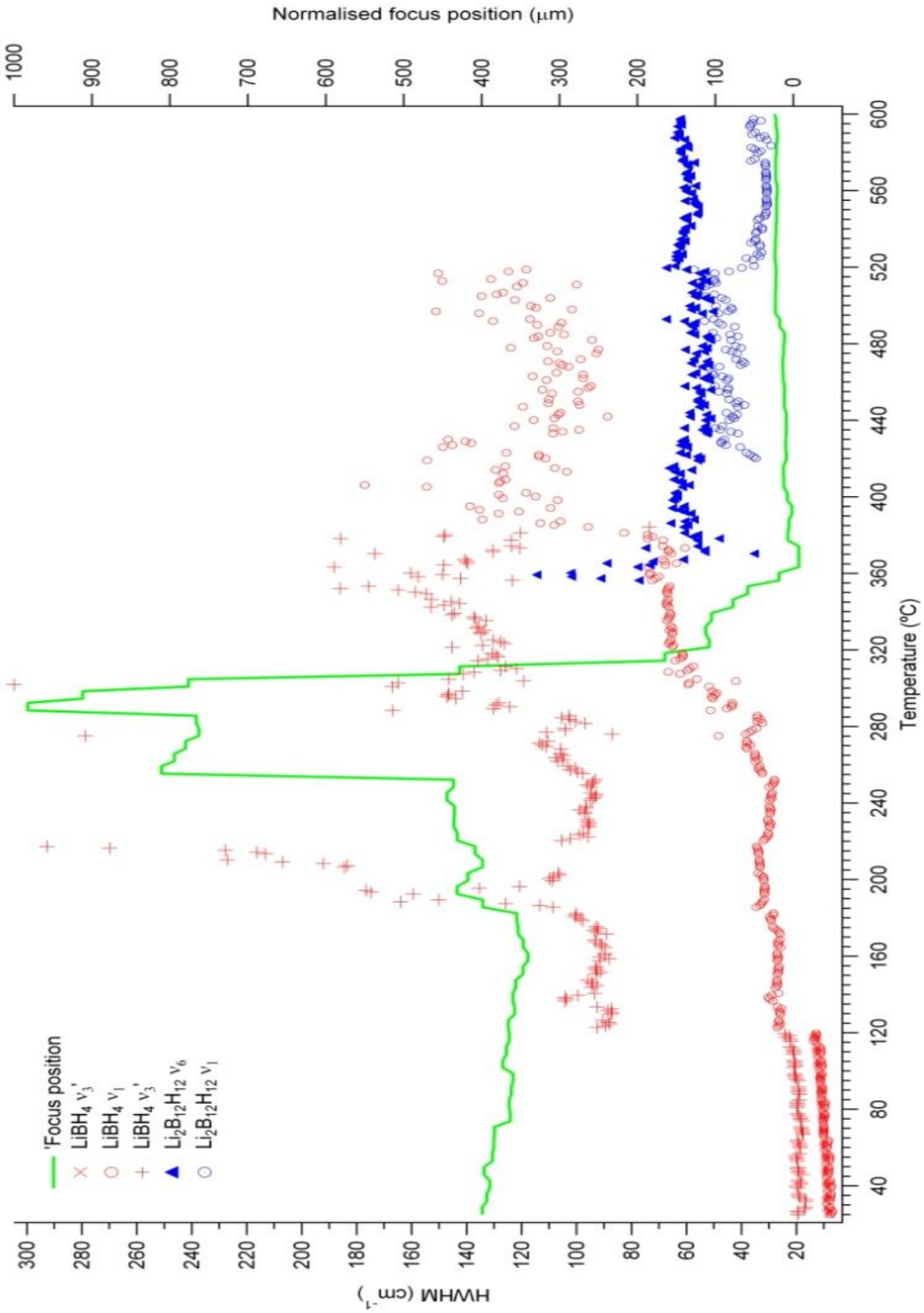

Figure 9.22 In-situ Raman HWHM of the B-H stretching modes of $LiBH_4$, the hydrogen breathing modes of $Li_2B_{12}H_{12}$, and the focus height of the microscope measured under flowing argon at a constant heating rate of 2°C/min.

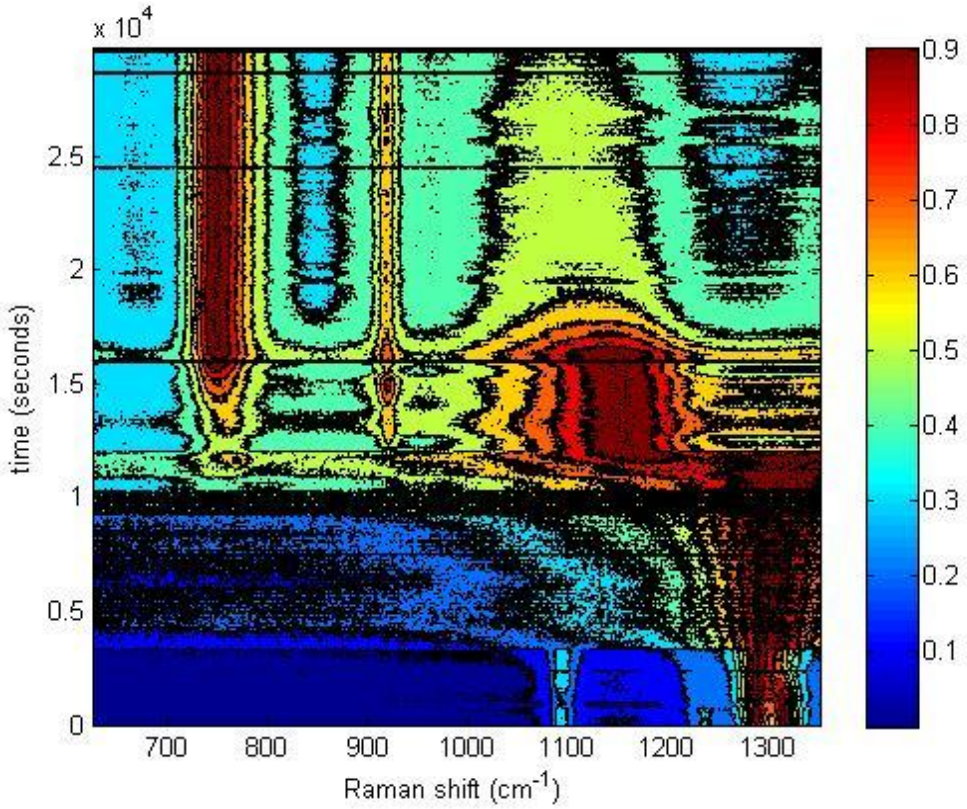

Figure 9.23 Normalised intensity of Raman spectra collected in the 650 - 1350 cm^{-1} region during heating of $LiBH_4$ at a constant heating rate of 2°C/min (0.0333K/s) to 600°C and then held isothermally in flowing argon.

The focus position is shown in Figure 9.24. The sample slowly thermally expands, increasing in height by 80 μm at 300°C. There is no obvious expansion at the phase change. On melting, the system focuses on to the sample pan, 1027 μm below the initial height. As the reaction products precipitate out of the liquid borohydride, the focusing height increases to 52 μm above the sample pan. This shows that the reaction products occupy ~5% of the original sample volume; however, liquid lithium borohydride is very mobile and can sometimes flow out of the sample container.

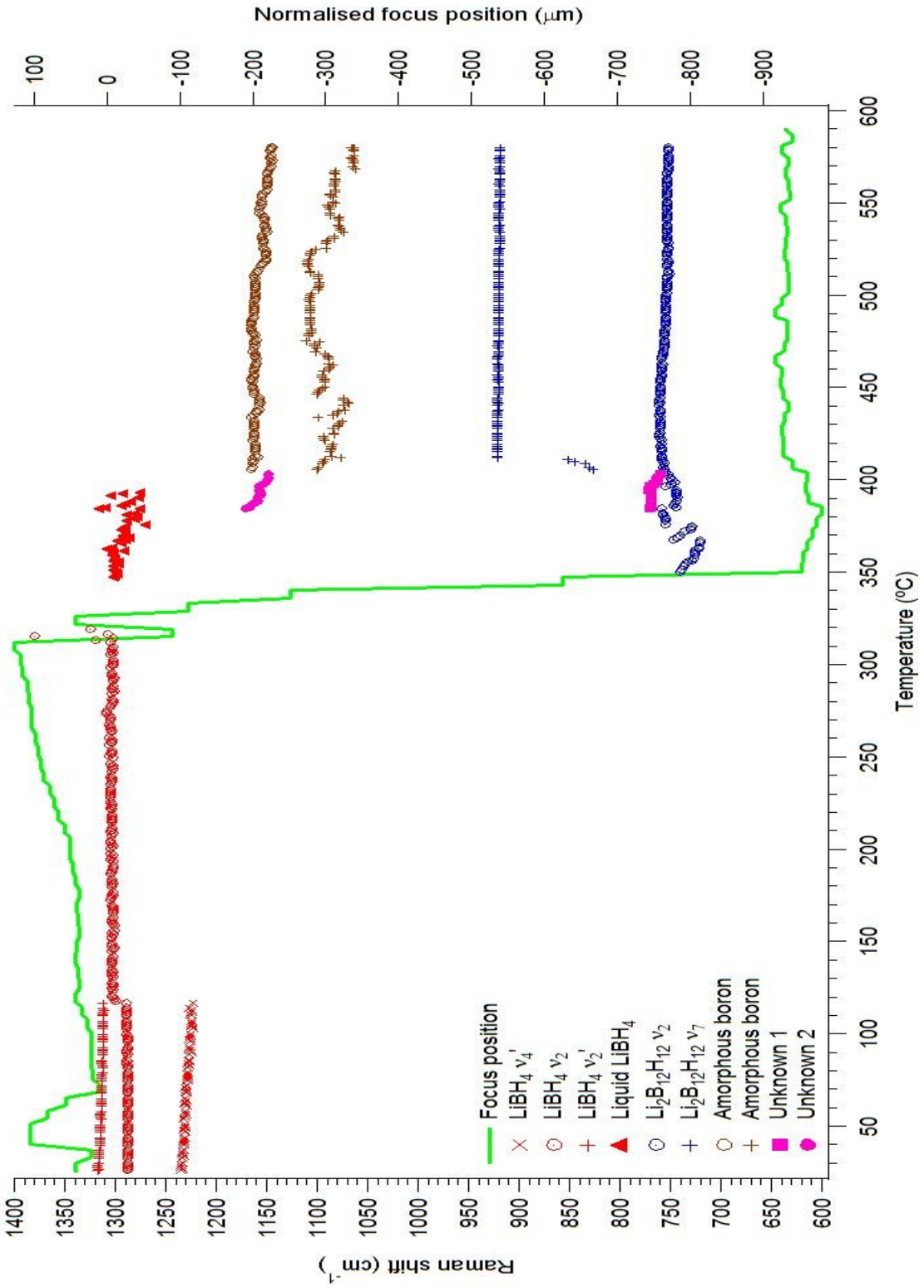

Figure 9.24 In-situ Raman peak position of the B-H bend modes of $LiBH_4$, the boron breathing modes of $Li_2B_{12}H_{12}$ and amorphous boron, and the focus height of the microscope, measured under flowing argon at a constant heating rate of 2°C/min.

The peak positions are shown in Figure 9.24. The changes in peak position below and through the phase change are the same as previously discussed in Section 9.2. The υ_2 mode moves at a rate of around 0.01 cm^{-1}/°C until 315°C at which point there is no recorded spectrum due to a lack of focus, as lithium borohydride melts. Molten lithium borohydride has a similar peak position to h-$LiBH_4$. The position slowly decreases until 390°C at which point the B-H bending mode is no longer present. $Li_2B_{12}H_{12}$ first becomes visible at 370°C with the υ_2 mode, and then the υ_7 mode appears at 430°C. There is no change in peak position above 430°C for either the υ_2 or υ_7 mode on heating up to 600°C. Amorphous boron is observed at 405°C where the peak position remains fairly constant.

There are two unassigned modes between 385 and 400°C that are not due to $Li_2B_{12}H_{12}$ or amorphous boron. It is speculated that they are likely to be due to a borane of smaller size than B_{12}. This is because the peaks are in a similar position to the B-H mode of $[B_{12}H_{12}]^{2-}$ and amorphous boron. No mode is observed in the range 2000-2600 cm^{-1} in Figure 9.21, however, it is possible that the large intensity B-H stretch and the hydrogen breathing mode may be hiding other peaks. Therefore, they are quite likely to be due to a precursor to either the $[B_{12}H_{12}]^{2-}$ or B_{12} clusters, of $Li_2B_{12}H_{12}$ or amorphous boron, respectively.

The change in peak widths with temperature and thermal decomposition are shown in Figure 9.25. The HWHM of the lithium borohydride B-H bend goes through a stepped change at the o-$LiBH_4$ to h-$LiBH_4$ phase change, since the υ_4 mode is no longer present and the two υ_2

modes combine, as previously shown in section 9.2 and Figure 9.13.

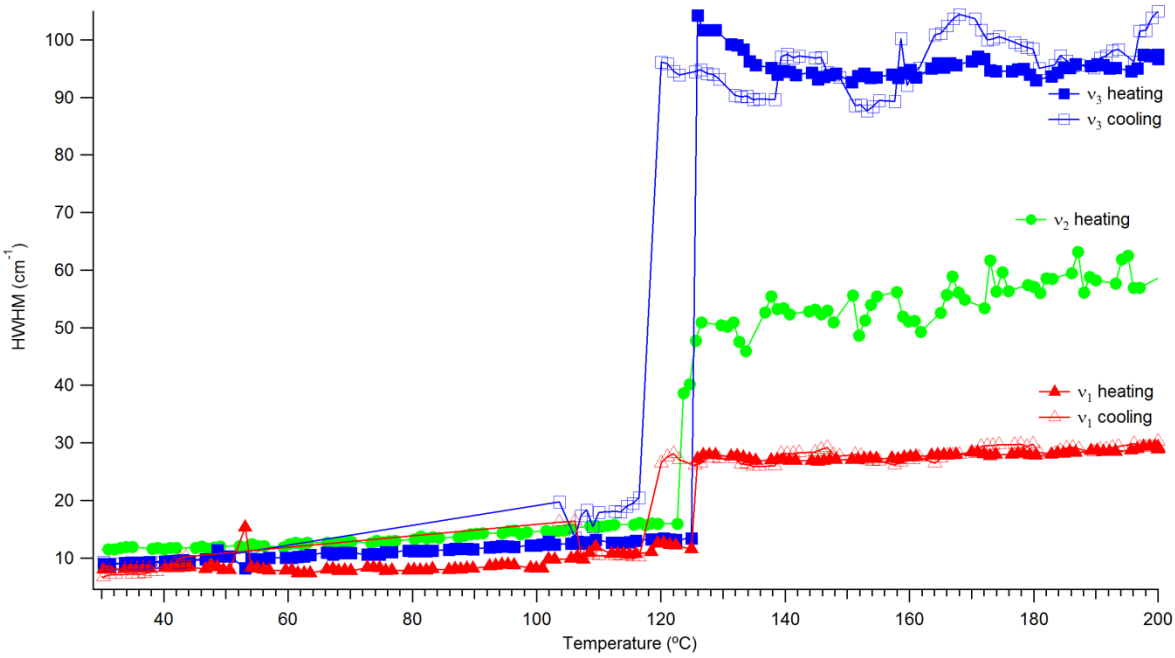

The υ_2 mode is easy to fit as it does not overlap with any other peaks; therefore this data is much less "noisy" than that shown for the overlapping υ_1 and υ_3 vibrations in Figure 9.22. There is another shift in HWHM on melting, whereby the gradient changes from 0.28 to 4.82 $cm^{-1}/°C$, due to an increase in freedom of the BH_4^- anion. The HWHM of the boron breathing modes of $Li_2B_{12}H_{12}$ are at around 8.5 and 25 cm^{-1} for the υ_7 and υ_2 modes; they remain reasonably constant with heating. The amorphous boron modes have a HWHM of around 45 and 75 cm^{-1}, which also remain fairly constant with heating, however, as the two peaks are overlapping and were resolved via curve fitting there is a certain amount of scatter. The two intermediate phases were only present for a short time.

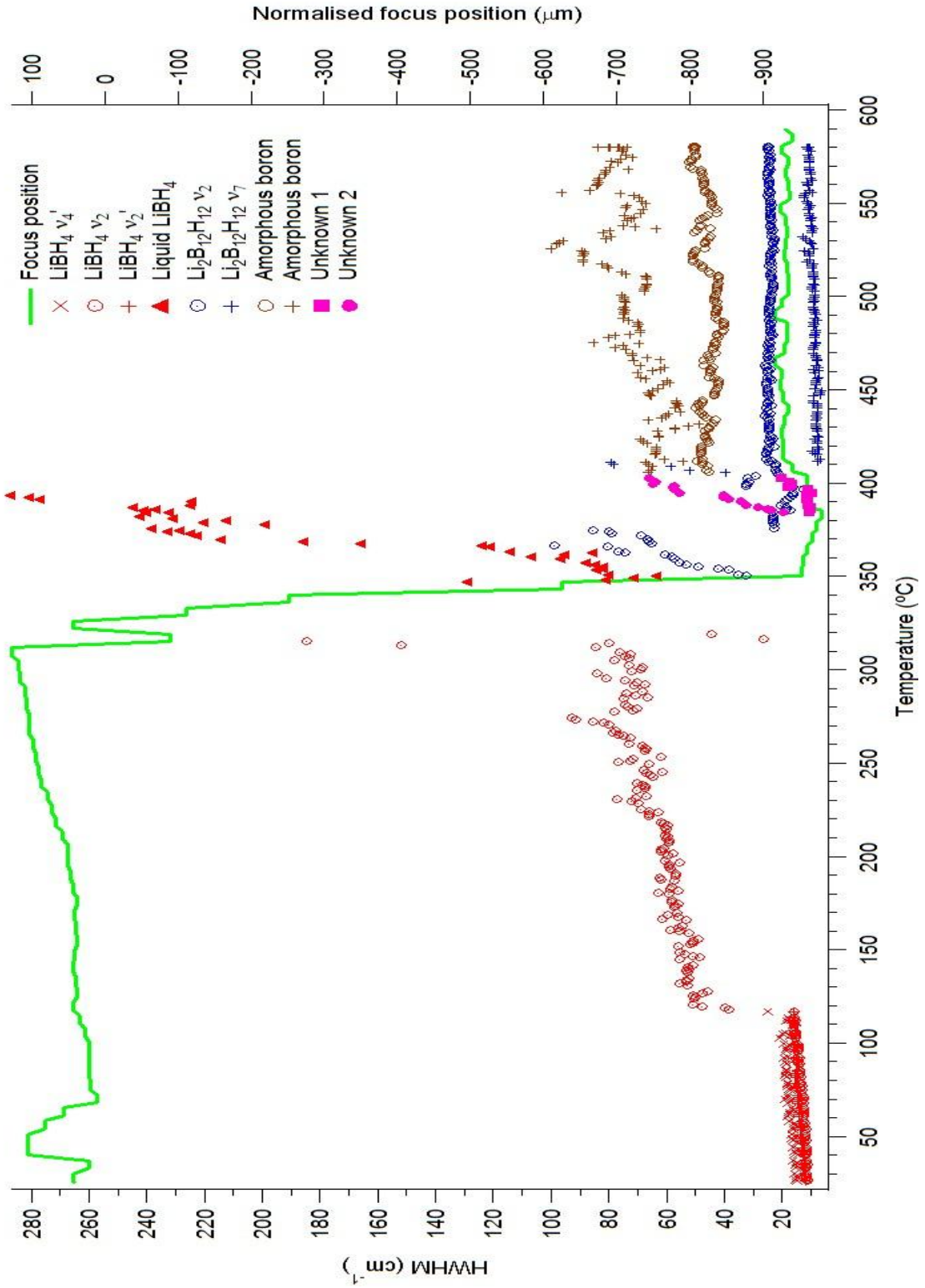

Figure 9.25 In-situ Raman HWHM of the B-H bending modes of $LiBH_4$, the boron breathing modes of $Li_2B_{12}H_{12}$ and amorphous boron, and the focus height of the microscope, measured under flowing argon at a constant heating rate of 2°C/min.

9.5 Optical Microscopy of Decomposition

A feature of the Raman spectrometer is that an optical image is taken prior to the Raman measurement. It is therefore possible to monitor the change in crystal shape and growth. The magnification used was x20 as this gives the best results for the Raman microscopy, and is able to give an indication of what happens.

Figure 9.26 shows a number of micrographs from the decomposition. Micrograph (a) shows the sample at 80°C where the large particles of lithium borohydride can be seen. Micrograph (b) shows the sample at 165°C after the phase change: there is no discernable difference between the o-$LiBH_4$ and the h-$LiBH_4$ phases. Micrograph (c) shows the sample at 330°C just as the sample can be seen to be melting. The melting process can be seen to take several minutes. After melting, Micrograph (d) is an image through the sample looking at the aluminium sample holder. When the sample temperature reaches 400°C, reaction products begin to crystallise out of the liquid lithium borohydride, as shown in Micrograph (e). At 425°C, the reaction product crystals have grown into a number of needle-like phases, as shown in Micrograph (f). On continued heating, these phases amalgamate and agglomerate, as shown in Micrograph (g).

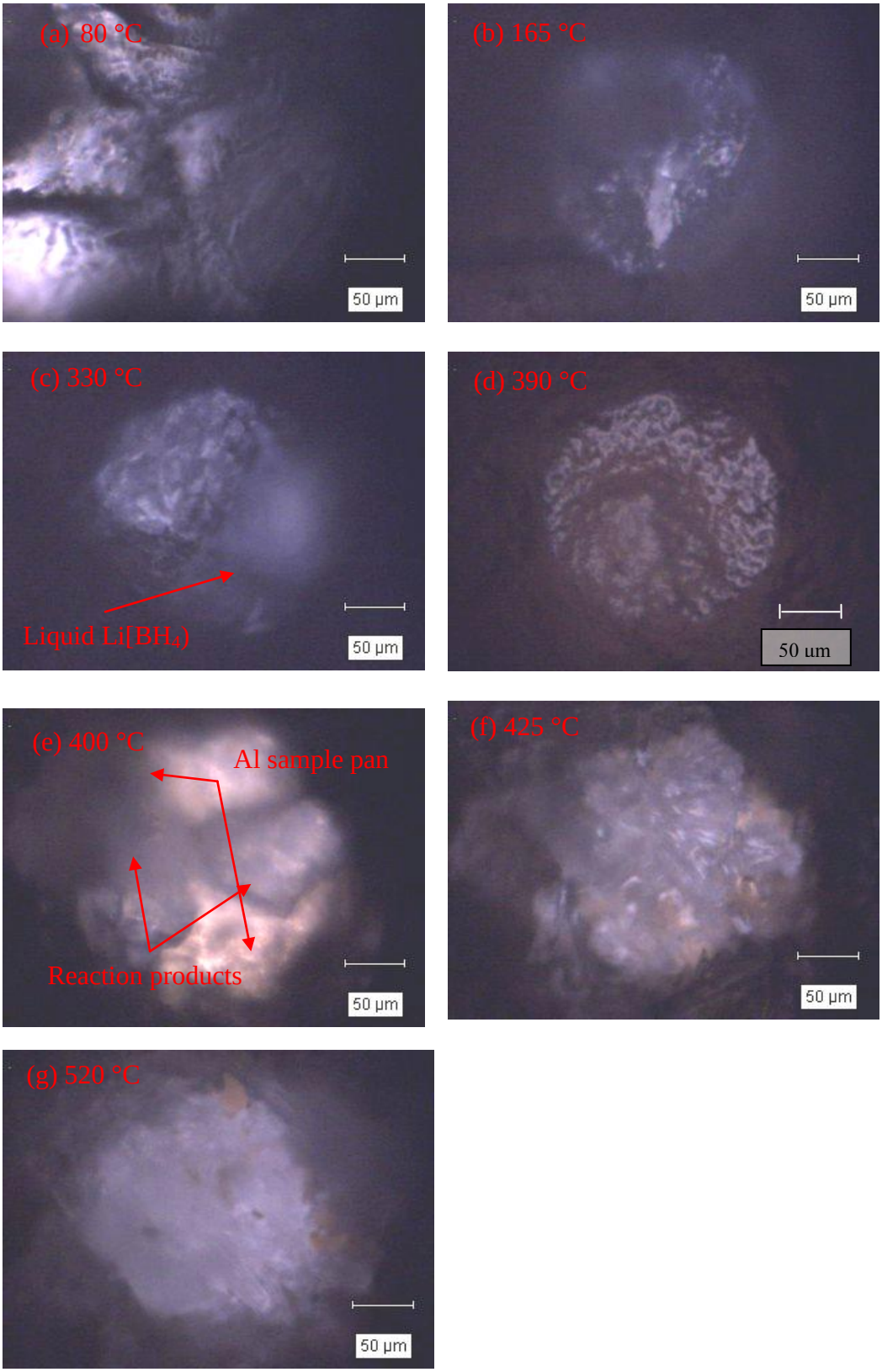

Figure 9.26 Micrographs of $LiBH_4$ heated in-situ in the Raman Microscope using an x20 long working distance objective (in flowing argon, at a constant heating rate of 2 K/min). Micrographs taken at: (a) 80°C, (b) 165°C, (c) 330°C, (d) 390°C, (e) 400°C, (f) 425°C, and (g) 520°C.

During some decomposition measurements on $LiBH_4$, it has been possible to observe bubbles of gas (assumed to be hydrogen) desorbing from the sample, as shown in Figure 9.27.

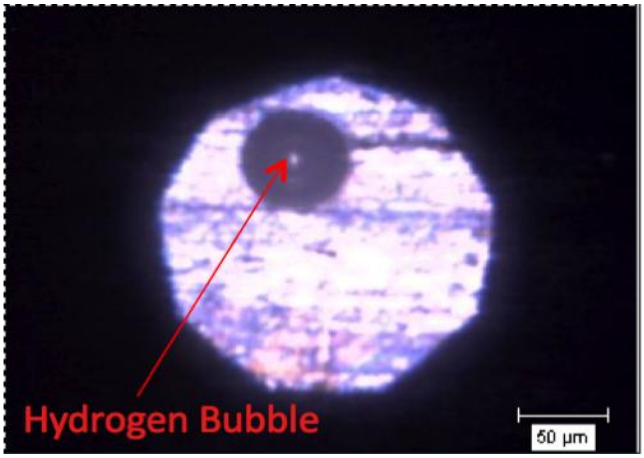

Figure 9.27 Micrograph of $LiBH_4$ heated to 400°C in a Raman microscope using an x20 long working distance objective, in flowing argon and a constant heating rate of 2°C/min.

9.6 Summary

The investigation into the orthorhombic phase of $LiBH_4$ assigned 21 of 36 vibrational modes. It was not possible to observe all 36 modes due to limitations in the spectrometer; the notch filter removes all signals between 100 and -100 cm^{-1}, and some modes can only be observed below 80 K. The modes observed correlated well with regards to position and width with those reported by Gomes et al. Racu et al. [55, 57].

$LiBH_4$ was heated to 200°C to investigate the change in properties of the $[BH_4]^-$ anion, and this agreed well with the work by Gomes et al.. There is a marked increase in the peak width and reduction in the number of modes observed showing the increase in symmetry of the $[BH_4]^-$ anion and increased dynamic disorder within the lattice. On cooling through the phase

change there is no hysteresis in the number of vibrations, however, there is a loss of intensity and definition making distinguishing the modes more difficult. As part of this work, we were able to collect more data points in the o-$LiBH_4$ and h-$LiBH_4$ and therefore were able to show the change in activation energy of the υ_2 mode, as discussed by Gomes et al. [55].

Characterisation of the lithium dodecaborane $Li_2B_{12}H_{12}$ was performed. $Li_2B_{12}H_{12}$ was formed through the decomposition of $LiBH_4$ heated to 600°C in accordance with previous studies into the decomposition of $LiBH_4$. The vibrational modes were assigned in accordance with the literature [175], and the peak positions correspond well to Raman measurements and PDOS calculations in the literature [59]. This section also showed that $Li_2B_{12}H_{12}$ is stable on cooling from 600°C, indicating that it is not a reaction intermediate but rather a reaction product formed during the thermal decomposition of lithium borohydride.

The main focus of the work was the investigation into the mechanism of decomposition of lithium borohydride using in-situ Raman microscopy. This work shows for the first time the onset of the formation of $Li_2B_{12}H_{12}$ occurs at ~370°C, followed by the formation of amorphous boron at ~400°C. On isothermally heating the reaction products, it appears that $Li_2B_{12}H_{12}$ is the dominant species left in the reaction mixture upon decomposition.

The observation of the two intermediate modes between 385 and 400°C, not assigned to $Li_2B_{12}H_{12}$, was of great interest. The position of these peaks indicate that they are due to B-B bonding, which suggests a precursor phase to either the formation of $Li_2B_{12}H_{12}$ or amorphous boron. It is hard to ascertain the full nature of the intermediate as any B-H bonding will be difficult to observe with the B-H stretch of $Li[BH_4]$ and the hydrogen breathing mode of $Li_2B_{12}H_{12}$ having very strong signals.

While lithium hydride was not observed in this work as it is Raman inactive, it is assumed to be present as many other investigations have found it to be [19, 58]. This gives us a reaction scheme of:

$$o\text{-}LiBH_4 \rightarrow h\text{-}LiBH_4 \quad (9.6)$$

$$\rightarrow Li[BH_4] \quad (9.7)$$

$$\rightarrow wLi_2B_{12}H_{12} + x \text{ unknown} + yLiH + zH_2 \quad (9.8)$$

$$\rightarrow aLi_2B_{12}H_{12} + b\ B + c\ LiH + d\ H_2 \quad (9.9)$$

The final section looked at the microscopy taken during the Raman measurement. Here melting was observed, followed by the evolution of gas and the precipitation of needle shaped phases. On continued heating, the phases grew and agglomerated. Using the focus height it was also possible to observe the change in height on melting and also the formation of the reaction products.

The main limitations of in-situ Raman microscopy are that it measures spectra in a very specific location, typically on the top surface of a solid. Therefore, several measurements are required in order to obtain compositional information that is reasonably representative of a bulk sample. The advantages of this technique over ex-situ techniques such as IR, Raman and MAS-NMR, are the ability to measure the changes in the sample with very small temperature steps and the ability to observe short-lived intermediate species. In addition, when compared to in-situ XRD, in-situ Raman has the advantage of being able to detect amorphous and liquid phases present during the thermal decomposition of borohydrides.

10 CONCLUSIONS

The main aim of this thesis was to investigate the metathesis reaction between alkali metal borohydrides and metal chlorides to form homoleptic metal borohydrides using mechanical milling. It was found that, under the conditions used in this study, mechanically milling zinc, calcium and magnesium chlorides with sodium or lithium borohydrides did not result in the formation of the corresponding homoleptic borohydride. However, novel compounds were produced that had different thermal decomposition properties compared to the starting material (i.e. alkali metal borohydride).

10.1 Zinc Borohydride

The reaction between zinc chloride and sodium or lithium borohydride resulted in the formation of a compound whose x-ray diffraction pattern corresponded to the $AZn_2(BH_4)_5$ (where A = Li or Na), compounds, recently reported by Ravnsbaek et al. [138]. While they have similar crystal structures, the sodium and lithium complexes have different bonding as shown by different Raman spectra and decomposition temperatures, with the sodium complex decomposing at lower temperatures. The thermal decomposition of the $AZn_2(BH_4)_5$ occurs at between 75 and 85°C with the evolution of both hydrogen and diborane.

Jeon and Cho [137] and Ravnsbaek [138] both postulated that the decomposition mechanism involved the decomposition of equal amounts of diborane and hydrogen to yield metallic zinc and alkali metal chloride as the only solid decomposition products. However, this work has

shown that the weight losses are not consistent with these proposed mechanisms: there is evidence of a boron compound present after decomposition up to 150°C. This suggests that a competing mechanism occurs, perhaps similar to that put forward by Wiberg and Henle [134], indicating that the ratio of hydrogen to diborane is greater than 1.

Thermal decomposition of the zinc borohydride complex occurs with two endothermic reactions. One endotherm is attributed to the melting of the complex, and this is unaffected by milling duration. The second broader endotherm is due the decomposition of the complex, and its onset temperature is reduced with increased milling time, while the width of the endotherm is reduced with milling time. It is believed that this might be due to a reduction in particle size of the formed complex; however, further measurements are required to confirm this. The thermal decomposition of the zinc borohydride complex is summarised below, where XCl is an unknown chlorine-containing compound:

$$AZn_2(BH_4)_5 + XCl \rightarrow Zn + 2ACl + aB + bH_2 + cB_2H_6 \quad (10.1)$$

XCl could potentially be the Na_2ZnCl_4 compound recently reported by Ravnsbaek et al [138]. If so, this would give:

$$AZn_2(BH_4)_5 + A_2ZnCl_4 \rightarrow Zn + 2ACl + aB + bH_2 + cB_2H_6 \quad (10.2)$$

The addition of 2 mol% of Ti, Ni, $TiCl_3$ and MgH_2 reduced the decomposition temperature by around 7°C. The addition of 2 mol% $TiCl_3$ had a significant effect on the decomposition process, reducing the mass loss and decomposition temperature by 0.7 wt.% and 12°C, respectively, and exhibiting a single DSC endotherm that suggests a different decomposition mechanism, possibly a metathesis reaction.

The investigation into the thermal decomposition of mechanically milled $2ZnCl_2 + 4NaBH_4 + MgH_2$ was carried out using TG/MS and DSC. This had a significantly different decomposition mechanism to that of the constituent compounds (milled $ZnCl_2 + 2NaBH_4$ and magnesium hydride). At 90˚C the exothermic reaction between diborane and magnesium hydride results in the formation of $Mg(BH_4)_2$, with the evolution of hydrogen. Between 260 and 360˚C, decomposition of this $Mg(BH_4)_2$ then occurs.

Decomposition of the $2ZnCl_2 + 4NaBH_4 + MgH_2$ can be summarised by the following reactions:

$$2NaZn_2(BH_4)_5 + MgH_2 \rightarrow 4Zn + 2NaCl + xMg(BH_4)_2 + yMgB_2 + zMg + aB + bH_2 + cB_2H_6 \quad (10.3)$$

$$\rightarrow Zn + 2NaCl + (y+f)MgB_2 + (z+d)Mg + (a+e)B + (b+g)H_2 + cB_2H \quad (10.4)$$

The first occurs at 90°C with a weight loss of 7.6 wt.% corresponding to the decomposition of the zinc borohydride complex and the reaction between diborane and magnesium hydride. The resultant magnesium borohydride then decomposes between 260 and 360°C with a weight loss of 1.5 wt.%. Reversibility of this system has not been investigated, however, the release of small amounts of diborane at 90°C make total reversibility unlikely.

10.2 Magnesium Borohydride

The aim was to synthesise magnesium borohydride via the metathesis reaction between sodium borohydride and magnesium chloride, however, analysis of the ball-milled material

shows that this did not occur. There is a modification of the sodium borohydride lattice resulting in a 4.1% reduction in volume. The magnesium chloride lattice is also deformed with changed lattice parameters: a reduction in **a** and an increase in **c**. However, Raman spectroscopy indicates that the borohydride tetrahedron is still present, and in a symmetrical environment.

Thermal decomposition of the milled products gave a 'noisy' trace, indicating a vigorous decomposition on the TGA, with an onset at approximately 250°C and completion by 410°C. Samples milled for 300 minutes and less have similar weight losses of approximately 3 wt.%. The sample milled for 720 minutes loses 4.4 wt.%, close to the maximum 4.7 wt.%. Mass spectrometry shows that only hydrogen is evolved during thermal decomposition (to the limit of the MS system used to detect trace gases).

DSC showed five endotherms and no exotherms on heating to 500°C. The first endotherm at around 250°C corresponds to a small desorption of hydrogen, and is therefore believed to be due to a phase rearrangement in the mixture. The second endotherm is sharp and unaffected by milling duration, and corresponds to the onset of hydrogen evolution. The third endotherm at 330°C is comparatively small and occurs just before the increase in desorption rate. The fourth corresponds to the main evolution of hydrogen. The fifth endotherm has no associated hydrogen loss, and can be attributed to the formation of another phase or potentially to the sublimation of some of the magnesium still present.

On heating there were four unknown phases observed using in-situ XRD. It was not possible to gather any further information about the unit cell, since the diffraction data is not clear enough. It can be said, however, that the phases observed are not any of the published phases

of magnesium borohydride, or Na_2MgCl_4. Sodium chloride and magnesium (oxide) are the only crystalline products observed upon decomposition. No peaks due to magnesium hydride were observed during decomposition, indicating that it was not formed in a crystalline manner. It is thought that the observed magnesium oxide should have remained as metallic magnesium, but had become oxidised. Ex-situ Raman spectroscopy on the decomposed products shows the formation of $[B_{12}H_{12}]^{2-}$, which could be either $Na_2B_{12}H_{12}$ or $MgB_{12}H_{12}$. There are also Raman modes due to amorphous boron and magnesium diboride.

It is therefore proposed that milled sodium borohydride and magnesium chloride in a ratio of 2:1 does not form magnesium borohydride. However, the reaction mixture produces thermal decomposition and results in terms of weight loss and temperature are comparable to those reported for magnesium borohydride [43, 84, 86].

XRD predicts the following reaction path for the crystalline intermediates and products for a sample milled for 720 minutes:

$$MgCl_2 + 2NaBH_4 \xrightarrow{150°C} MgCl_2 + NaBH_4 + I \quad (10.5)$$

$$\xrightarrow{175°C} MgCl_2 + NaBH_4 + I + II + III \quad (10.6)$$

$$\xrightarrow{250°C} NaBH_4 + I + II + III \quad (10.7)$$

$$\xrightarrow{300°C} II + IV \quad (10.8)$$

$$\xrightarrow{325°C} II + IV + NaCl \quad (10.9)$$

$$\xrightarrow{375°C} NaCl \quad (10.10)$$

$$\xrightarrow{400°C} NaCl + Mg \quad (10.11)$$

This, combined with the information from the Raman, gives an overall reaction up to 550°C of:

$$MgCl_2 + 2NaBH_4 \rightarrow 2NaCl + {}^{9}/_{10}Mg + {}^{1}/_{25}Mg[B_{12}H_{12}] + {}^{7}/_{5}B + {}^{3}/_{50}MgB_2 + {}^{94}/_{25}H_2 \quad (10.12)$$

The onset of the reaction is at 290°C and is complete by 400°C with a weight loss of 4.4 wt.%. It is assumed that $MgB_{12}H_{12}$ is formed in preference to $Na_2B_{12}H_{12}$ as the XRD does not account for all the magnesium.

10.3 Calcium Borohydride

Samples of Sigma-Aldrich $Ca(BH_4)_2$ and $Ca(BH_4)_2$.2THF consist of ionic $[BH_4]^-$ and Ca^{2+} ions arranged predominantly in the β-$Ca(BH_4)_2$ phase for the sample without THF. Upon heating, the $Ca(BH_4)_2$.2THF sample loses both THF ligands by 200°C. Both samples then undergo a two-step decomposition process at around 350°C, with a weight loss of 9.6 wt.% from the $Ca(BH_4)_2$. The decomposition proceeds through an unknown intermediate phase at 330°C before finally decomposing to form CaH_2 and CaB_6 with the evolution of hydrogen to give an overall reaction scheme of:

$$Ca(BH_4)_2 \xrightarrow{330°C} aCaH_2 + bCaB_6 + cX + dH_2 \quad (10.13)$$

$$\xrightarrow{400°C} {}^{2}/_{3}CaH_2 + {}^{1}/_{3}CaB_6 + {}^{10}/_{3}H_2 \quad (10.14)$$

Mechanically milled $CaCl_2$ and $2NaBH_4$ did not proceed via the predicted route. This suggests the formation of a compound such as $Na_xCa_y(BH_4)_{x+2y}$. The reflections due to sodium borohydride during in-situ XRD showed a contraction in the lattice parameter until the formation of sodium chloride. This is likely to indicate that the chlorine atoms replace the borohydride ions in the lattice, forming a solid solution of $NaCl_x(BH_4)_{1-x}$. It is believed substituted borohydride ions then instantly react with the remaining calcium chloride to form an intermediate $CaCl_{2-x}(BH_4)_x$ with subsequent reactions forming calcium borohydride, $Ca(BH_4)_2$. Subsequent decomposition of the formed calcium borohydride takes place at 350°C, occurring with only the evolution of around 3 wt.% hydrogen and results in the formation of calcium hydride, calcium hexaboride and sodium chloride.

$$CaCl_2 + 2NaBH_4 \xrightarrow{Milling} \text{`}Na_xCa_y(BH_4)_{x+2y}\text{'} + CaCl_2 + NaBH_4 \quad (10.15)$$

$$\xrightarrow{250°C} NaCa_{2-x}(BH_4)_x + CaCl_2 + Na(BH_4)_{1-x}Cl_x \quad (10.16)$$

$$\xrightarrow{300°C} Ca(BH_4)_2 + CaCl_2 + Na(BH_4)_{1-x}Cl_x \quad (10.17)$$

$$\xrightarrow{325°C} 2NaCl + xCaH_2 + yCaB_6 + 4\text{-}xH_2 \quad (10.18)$$

10.4 Lithium Borohydride

An investigation into the orthorhombic phase of $LiBH_4$, using Raman Spectroscopy, assigned 21 vibrational modes. It was not possible to observe all 36 modes due to limitations in the spectrometer, notch filter and the fact that some modes can only be observed at temperatures below 80 K. The position and width of observed modes correlated well with those reported by Gomes et al. and Racu et al. [55, 57].

$LiBH_4$ was heated to 200°C to investigate the change in properties of the $[BH_4]^-$ anion during transformations to and from the o-$LiBH_4$ and h-$LiBH_4$ phases; this agreed well with the work by Gomes et al.. There is a marked increase in the peak width and reduction in the number of modes observed, showing the increase in symmetry of the $[BH_4]^-$ anion and increased dynamic disorder within the lattice. On cooling through the phase change, there is no hysteresis in the number of vibrations, however, there is a loss of intensity and definition making distinguishing the modes more difficult. As part of this work, it was possible to collect more Raman spectra as a function of temperature for o-$LiBH_4$ and h-$LiBH_4$, thus making it possible to more accurately determine the change in activation energy of the υ_2 mode, as discussed by Gomes et al. [55].

Characterisation of the lithium dodecaborane ($Li_2B_{12}H_{12}$) was performed. $Li_2B_{12}H_{12}$ was formed through the decomposition of $LiBH_4$ heated to 600°C (under Ar), in accordance with previous studies in to the decomposition of $LiBH_4$ [60]. $Li_2B_{12}H_{12}$ is stable on cooling from 600°C, indicating that it is not a reaction intermediate but rather a reaction product formed during the thermal decomposition of lithium borohydride.

Investigation of the mechanism of decomposition of lithium borohydride (under 1 bar flowing argon), was performed using in-situ Raman microscopy. This work shows for the first time that the onset of the formation of $Li_2B_{12}H_{12}$ occurs at ~370°C, followed by the formation of amorphous boron at ~400°C. On isothermally heating the reaction products, it appears that $Li_2B_{12}H_{12}$ is the dominant species left in the reaction mixture upon decomposition.

Of particular interest, two intermediate modes were observed between 385 and 400°C, which could not be assigned to $Li_2B_{12}H_{12}$. The position of these peaks indicates that they are due to B-B bonding, which suggests a precursor phase to either the formation of $Li_2B_{12}H_{12}$ and/or amorphous boron. It is difficult to ascertain the full nature of the intermediate by Raman spectroscopy, as any B-H bonding may well be partially masked by the very strong signals of the B-H stretch of $Li[BH_4]$ and the hydrogen breathing mode of $Li_2B_{12}H_{12}$.

While lithium hydride was not observed in this work since it is Raman inactive, its presence has been reported in many other investigations [19, 58]. This gives a reaction scheme of:

$$o\text{-}LiBH_4 \rightarrow h\text{-}LiBH_4 \quad (10.19)$$

$$\rightarrow Li[BH_4] \quad (10.20)$$

$$\rightarrow wLi_2B_{12}H_{12} + x\ \text{unknown} + yLiH + zH_2 \quad (10.21)$$

$$\rightarrow aLi_2B_{12}H_{12} + bB + cLiH + dH_2 \quad (10.22)$$

In-situ microscopy was performed during the thermal decomposition of lithium borohydride: melting was observed around 280°C, followed by the evolution of gas and the precipitation of needle-shaped phases at 360°C. On continued heating, the phases grew and agglomerated above 400°C. Using the focus height (i.e. the Raman microscope automatically focuses onto the surface of non-transparent materials), it was also possible to observe the change in height of the sample on melting (into a transparent liquid) and the formation of the reaction products.

The main limitations of in-situ Raman microscopy are that it measures spectra in a very specific location, typically on the top surface of a solid. Therefore, several measurements are required in order to obtain compositional information that is reasonably representative of a bulk sample. The advantages of this technique over ex-situ techniques such as IR, Raman and MAS-NMR, are the ability to measure the compositional changes in the sample with very small temperature steps and the ability to observed short-lived intermediate species. In addition, when compared to in-situ XRD, in-situ Raman has the advantage of being able to detect amorphous and liquid phases present during the thermal decomposition of borohydrides.

10.5 General Considerations

This project carried out measurements on four different borohydride complexes in order to understand firstly their possible application as a hydrogen storage material, and secondly to characterise the thermal decomposition processes. While mechanical milling of zinc, magnesium and calcium chlorides with sodium borohydride has not yielded the respective homoleptic borohydrides, the results show that a change in decomposition mechanism is observed from sodium borohydride. The group II metals, magnesium and calcium, retain the ionic character of sodium borohydride, exhibiting a substitution mechanism whereby chlorine ions replace the borohydride ions in the cubic sodium borohydride lattice forming sodium chloride. Zinc chloride reacts with sodium borohydride to form a complex covalent structure significantly different from that of the alkali metal borohydride starting material.

Results from calcium indicate that the weight change and onset temperature of commercially available calcium borohydride made using a THF solvent and mechanically milled $CaCl_2$ + $2NaBH_4$ are the same. This would indicate while the homoleptic borohydrides are not formed on milling, they may be formed in-situ during heating.

Reversibility was not investigated during this work; there are reports suggesting that calcium borohydride is reversible when in conjunction with magnesium hydride [97]. Reversibility studies will be essential if the investigated borohydrides are to become hydrogen storage media.

11 FUTURE WORK

Borohydrides have the potential to be used as onboard storage media for hydrogen in mobile applications. There is, however, the need for further research and development before use in commercial applications.

- Investigations into the possible formation of homoleptic zinc borohydride through different synthetic methods should be undertaken, to understand firstly if it is possible to form and secondly what the thermal decomposition temperatures are.
- This study has focused on the mechanical milling of zinc, magnesium and calcium chlorides with sodium and lithium borohydrides. There are many other possible borohydrides that have the potential to be used as hydrogen storage materials and warrant further investigation such as manganese and hafnium borohydride.
- Full characterisation of the crystal structure (including hydrogen position) for the $NaZn_2(BH_4)_5$ complex, through Raman spectroscopy, neutron diffraction and inelastic neutron scattering.
- In-situ studies of the $NaZn_2(BH_4)_5$ complex should be carried out using XRD, neutron diffraction and Raman spectroscopy to further the understanding of the decomposition mechanism.
- In-situ studies of the $NaZn_2(BH_4)_5 + MgH_2$ reactive mixture should be performed to better understand thermal decomposition mechanisms and intermediates using XRD, neutron diffraction and Raman.

- The decomposition mechanism of milled $MgCl_2 + 2NaBH_4$ has a number of unknown compounds. Synthesis of the $MgCl_2 + 2LiBH_4$ could provide information about a possible solid solution that may form. An investigation into the stability and bonding of the intermediates would provide valuable information.
- Further investigations using Raman microscopy into the unknown phase observed on the decomposition of Sigma-Aldrich $Ca(BH_4)_2$ should be carried out to determine the decomposition mechanism.
- The substitution of chlorine from calcium chloride into the sodium borohydride lattice to form sodium chloride, whilst the decomposition temperature and weight percent were similar to that of commercial calcium borohydride is interesting. Therefore, an investigation into use of orthorhombic lithium borohydride as a reagent instead of cubic sodium borohydride may allow the formation of calcium borohydride.
- A detailed study of lithium borohydride using Raman spectroscopy was performed, highlighting an unknown phase present on decomposition. Investigations into the nature, composition and stability are needed. This unknown could be an oxide or hydroxide.
- Further investigations into the reversibility are needed to ascertain whether recombination is possible.
- The use of NMR to analyse the starting material, intermediates and decomposition products would provide valuable information.
- Further investigations into the reactive composite $Ca(BH_4)_2 + MgH_2$ should be performed.

12 LIST OF REFERENCES

1. Orimo, S., Y. Nakamori, G. Kitahara, K. Miwa, N. Ohba, S. Towata, and A. Zuttel. *Dehydriding and rehydriding reactions of $LiBH_4$*. Journal of Alloys and Compounds, 2005. **404**: p. 427-430.
2. Energy_Information_Administration. *Greenhouse gasses, climate change and energy*. 2008 May 2008 [cited DOE/EIA-X012 01/09/09]; Available from: http://www.eia.doe.gov/bookshelf/brochures/greenhouse/greenhouse.pdf.
3. Economist.com. *Hands to the Pump*. 2007 [cited 2009 01/09/09]; Available from: http://www.economist.com/PrinterFriendly.cfm?story_id=9430924.
4. IEA. *Monthly oil market report*. 2003 3-3-05; Available from: http://omrpublic.iea.org/omrarchive/10dec03dem.pdf.
5. Energy_Information_Administration. *International Energy Outlook 2009* [web site] 2009 27/05/09 [cited 2009 01/09/09]; Available from: http://www.eia.doe.gov/oiaf/ieo/world.html.
6. Ricci, M., P. Bellaby, and R. Flynn. *What do we know about public perceptions and acceptance of hydrogen? A critical review and new case study evidence*. International Journal Of Hydrogen Energy, 2008. **33**: p. 5868-5880.
7. U.S.Department_of_Energy. *Types of Fuel Cells*. 23/06/2009 [cited 2009 01/09/09]; Available from: http://www1.eere.energy.gov/hydrogenandfuelcells/fuelcells/fc_types.html.
8. Schlapbach, L. and A. Zuttel. *Hydrogen-storage materials for mobile applications*. Nature, 2001. **414**: p. 353-358.
9. Zuttel, A. *Materials for hydrogen Storage*. Materials Today, 2003: p. 24-33.
10. Dillich, S. *Hydrogen Storage*. annual review 09 storage 2009 [cited 2009 15/09/09]; Available from: http://www.hydrogen.energy.gov/pdfs/review09/st_0_dillich.pdf.
11. Wolf, J. *Liquid-Hydrogen Technology for Vehicles*. MRS Bulletin, 2002: p. 684-687.
12. Zuttel, A. *Hydrogen storage methods*. Naturwissenschaften, 2004. **91** (4): p. 157-172.
13. Zuttel, A. and S.-i. Orimo. *Hydrogen in Nanostructured, Carbon-Related, and Metallic Materials*. MRS Bulletin, 2002: p. 705-711.
14. Langmi, H.W., A. Walton, M.M. Al-Mamouri, S.R. Johnson, D. Book, J.D. Speight, P.P. Edwards, I. Gameson, P.A. Anderson, and I.R. Harris. *Hydrogen adsorption in zeolites A, X, Y and RHO*. Journal of Alloys and Compounds, 2003. **356**: p. 710-715.
15. Rosi, N.L., J. Eckert, M. Eddaoudi, D.T. Vodak, J. Kim, M. O'Keeffe, and O.M. Yaghi. *Hydrogen Storage in Microporous Metal-Organic Frameworks*. Science, 2003. **300** (5622): p. 1127-1129.
16. Grochala, W. and P.P. Edwards. *Thermal decomposition of the non-interstitial hydrides for the storage and production of hydrogen*. Chemical Reviews, 2004. **104** (3): p. 1283-1315.
17. Nakamori, Y., H.W. Li, M. Matsuo, K. Miwa, S. Towata, and S. Orimo. *Development of metal borohydrides for hydrogen storage*. Journal of Physics and Chemistry of Solids, 2008. **69** (9): p. 2292-2296.
18. Orimo, S.I., Y. Nakamori, J.R. Eliseo, A. Zuttel, and C.M. Jensen. *Complex hydrides for hydrogen storage*. Chemical Reviews, 2007. **107**: p. 4111-4132.

19. Zuttel, A., S. Rentsch, P. Fischer, P. Wenger, P. Sudan, P. Mauron, and C. Emmenegger. *Hydrogen storage properties of LiBH4*. Journal of Alloys and Compounds, 2003. **356**: p. 515-520.
20. Graham, T. *On the Absorption and Dialytic Separation of Gases by Colloid Septa*. Phil. Trans. R. Soc. Lond., 1866. **156**: p. 399-439.
21. Reilly, J.J. and R.H. Wiswall. *Reaction of hydrogen with alloys of magnesium and nickel and the formation of Mg_2NiH_4.* Inorganic Chemistry, 1968. **7** (11): p. 2254-2256.
22. Manchester, F.D. and D. Khatamian. *Mechanisms for Activation of Intermetallic Hydrogen Absorbers*. Materials Science Forum, 1988. **31** p. 261-296.
23. Bowman_Jr., R.C. and B. Fultz. *Metallic Hydrides I: Hydrogen Storage and Other Gas-Phase Applications*. MRS Bulletin, 2002: p. 688-693.
24. Bowman, R.C. and B. Fultz. *Metallic Hydrides I: Hydrogen Storage and Other Gas-Phase Applications*. MRS Bulletin, 2002: p. 688-693.
25. Gutfleisch, O., N. Schlorke-de Boer, N. Ismail, M. Herrich, A. Walton, J. Speight, I.R. Harris, A.S. Pratt, and A. Zuttel. *Hydrogenation properties of nanocrystalline Mg- and Mg_2Ni-based compounds modified with platinum group metals (PGMs)*. Journal of Alloys and Compounds, 2003. **356**: p. 598-602.
26. Zuttel, A., A. Borgschulte, and S.I. Orimo. *Tetrahydroborates as new hydrogen storage materials*. Scripta Materialia, 2007. **56** (10): p. 823-828.
27. Schlesinger, H.I., R.T. Sanderson, and A.B. Burg. *Metallo borohydrides. I. Aluminum borohydride*. Journal Of The American Chemical Society, 1940. **62**: p. 3421-3425.
28. Burg, A.B. and H.I. Schlesinger. *Metallo borohydrides. II. Beryllium borohydride*. Journal Of The American Chemical Society, 1940. **62**: p. 3425-3429.
29. Schlesinger, H.I. and H.C. Brown. *Metallo borohydrides. III. Lithium borohydride*. Journal Of The American Chemical Society, 1940. **62**: p. 3429-3435.
30. Beach, J.Y. and S.H. Bauer. *The structure of the hydrides of boron. VI. $A1B_3H_{12}$*. Journal Of The American Chemical Society, 1940. **62**: p. 3440-3442.
31. Marks, T.J. and J.R. Kolb. *Covalent Transition-Metal, Lanthanide, And Actinide Tetrahydroborate Complexes*. Chemical Reviews, 1977. **77** (2): p. 263-293.
32. Orimo, S., Y. Nakamori, and A. Zuttel. *Material properties of MBH_4 (M= Li, Na, and K)*. Materials Science And Engineering B-Solid State Materials For Advanced Technology, 2004. **108** (1-2): p. 51-53.
33. Renaudin, G., S. Gomes, H. Hagemann, L. Keller, and K. Yvon. *Structural and spectroscopic studies on the alkali borohydrides MBH_4 (M = Na, K, Rb, Cs)*. Journal of Alloys and Compounds, 2004. **375** (1-2): p. 98-106.
34. Wiberg, E. and H. Noth. *UBER WASSERSTOFF-VERBINDUNGEN DES THALLIUMS .6. ZUR KENNTNIS EINES THALLIUM(III)-BORANATS TLCL(BH4)2*. Zeitschrift Fur Naturforschung Part B-Chemie Biochemie Biophysik Biologie Und Verwandten Gebiete, 1957. **12** (1): p. 63-65.
35. Riktor, M.D., M.H. Sorby, K. Chlopek, M. Fichtner, F. Buchter, A. Zuettel, and B.C. Hauback. *In situ synchrotron diffraction studies of phase transitions and thermal decomposition of $Mg(BH_4)_2$ and $Ca(BH_4)_2$*. Journal of Materials Chemistry, 2007. **17**: p. 4939-4942.
36. Bauer, S.H. *REANALYSIS OF THE ELECTRON DIFFRACTION DATA ON BE(BH4)2 AND AL(BH4)3*. Journal Of The American Chemical Society, 1950. **72** (1): p. 622-623.

37. Shang, S.L., T. Wang, and Z.K. Liu. *Thermodynamic modelling of the B-Ca, B-Sr and B-Ba systems*. Calphad-Computer Coupling of Phase Diagrams and Thermochemistry, 2007. **31** (2): p. 286-291.
38. Adams, D.M. and Churchil.Rg. *Programme for normal co-ordinate calculations; vibrational analysis of diborane and halides M_2X_6(M = Al, Ga, or ln)*. Journal of the Chemical Society a -Inorganic Physical Theoretical, 1970 (5): p. 697-703.
39. Schlesinger, H.I., H.C. Brown, and G.W. Schaeffer. *The borohydrides of gallium*. Journal Of The American Chemical Society, 1943. **65**: p. 1786-1787.
40. Sato, T., K. Miwa, Y. Nakamori, K. Ohoyama, H.W. Li, T. Noritake, M. Aoki, S.I. Towata, and S.I. Orimo. *Experimental and computational studies on solvent-free rare-earth metal borohydrides $R(BH_4)_3$ (R = Y, Dy, and Gd)*. Physical Review B, 2008. **77** (10): p. 104114.
41. James, B.D. and M.G.H. Wallbrige. *Metal Tetrahydroborates*. Progress in Inorganic Chemistry, 1970. **11**: p. 99-231.
42. Nakamori, Y., K. Miwa, A. Ninomiya, H.W. Li, N. Ohba, S.I. Towata, A. Zuttel, and S.I. Orimo. *Correlation between thermodynamical stabilities of metal borohydrides and cation electronegativites: First-principles calculations and experiments*. Physical Review B, 2006. **74**: p. 045126.
43. Nakamori, Y., H.W. Li, K. Miwa, S. Towata, and S. Orimo. *Syntheses and hydrogen Desorption properties of metal-borohydrides $M(BH_4)_n$ (M = Mg, Sc, Zr, Ti, and Zn; n=2-4) as advanced hydrogen storage materials*. Materials Transactions, 2006. **47** (8): p. 1898-1901.
44. Schlesinger, H.I., H.C. Brown, B. Abraham, A.C. Bond, N. Davidson, A.E. Finholt, J.R. Gilbreath, H. Hoekstra, L. Horvitz, E.K. Hyde, J.J. Katz, J. Knight, R.A. Lad, D.L. Mayfield, L. Rapp, D.M. Ritter, A.M. Schwartz, I. Sheft, L.D. Tuck, and A.O. Walker. *New Developments in the Chemistry of Diborane and the Borohydrides .1. General Summary*. Journal Of The American Chemical Society, 1953. **75** (1): p. 186-190.
45. Fedneva, E.M., V.I. Alpatova, and V.I. Mikheeva. Russian Journal of Inorganic Chemistry, 1964. **9** (6): p. 826-827.
46. Noth, H. and G. Mikulaschek. *Anorganische Reaktionen der Alkaliboranate*. Angewandte Chemie, 1961. **73** (11): p. 371-383.
47. Goerrig, D., Synthesis of $LiBH_4$ from the elements, 1985, Germany, Patent Number 1077644
48. Orima, S., Y. Nakamori, G. Kitahara, K. Miwa, N. Ohba, S. Towata, and A. Zuttel. *Dehydriding and rehydriding reactions of LiBH4*. Journal of Alloys and Compounds, 2005. **404**: p. 427-430.
49. Cakanyildirim, C. and M. Guru. *Processing of $LiBH_4$ from its elements by ball milling method*. Renewable Energy, 2008. **33** (11): p. 2388-2392.
50. Agresti, F. and A. Khandelwal. *Evidence of formation of $LiBH_4$ by high-energy ball milling of LiH and B in a hydrogen atmosphere*. Scripta Materialia, 2009. **60** (9): p. 753-755.
51. Friedrichs, O., A. Borgschulte, S. Kato, F. Buchter, R. Gremaud, A. Remhof, and A. Zuttel. *Low-Temperature Synthesis of $LiBH_4$ by Gas-Solid Reaction*. Chemistry-a European Journal, 2009. **15** (22): p. 5531-5534.
52. Soulie, J.P., G. Renaudin, R. Cerny, and K. Yvon. *Lithium boro-hydride $LiBH_4$*. Journal of Alloys and Compounds, 2002. **346** (1-2): p. 200-205.
53. Mosegaard, L., B. Moller, J.E. Jorgensen, Y. Filinchuk, Y. Cerenius, J.C. Hanson, E. Dimasi, F. Besenbacher, and T.R. Jensen. *Reactivity of $LiBH_4$: In situ synchrotron*

radiation powder X-ray diffraction study. Journal of Physical Chemistry C, 2008. **112**: p. 1299-1303.

54. Corey, R.L., D.T. Shane, R.C. Bowman, and M.S. Conradi. *Atomic Motions in $LiBH_4$ by NMR*. Journal of Physical Chemistry C, 2008. **112** (47): p. 18706-18710.
55. Gomes, S., H. Hagemann, and K. Yvon. *Lithium boro-hydride $LiBH_4$ II. Raman spectroscopy*. Journal of Alloys and Compounds, 2002. **346** (1-2): p. 206-210.
56. Hagemann, H., S. Gomes, G. Renaudin, and K. Yvon. *Raman studies of reorientation motions of $[BH_4]^-$ anionsin alkali borohydrides*. Journal of Alloys and Compounds, 2004. **363** (1-2): p. 126-129.
57. Racu, A.M., J. Schoenes, Z. Lodziana, A. Borgschulte, and A. Zuttel. *High-resolution Raman spectroscopy study of phonon modes in $LiBH_4$ and $LiBD_4$*. Journal of Physical Chemistry A, 2008. **112** (40): p. 9716-9722.
58. Zuttel, A., P. Wenger, S. Rentsch, P. Sudan, P. Mauron, and C. Emmenegger. *$LiBH_4$ a new hydrogen storage material*. Journal Of Power Sources, 2003. **118** (1-2): p. 1-7.
59. Ohba, N., K. Miwa, M. Aoki, T. Noritake, S. Towata, Y. Nakamori, S. Orimo, and A. Zuttel. *First-principles study on the stability of intermediate compounds of $LiBH_4$*. Physical Review B, 2006. **74** (7): p. 075110.
60. Orimo, S.I., Y. Nakamori, N. Ohba, K. Miwa, M. Aoki, S. Towata, and A. Zuttel. *Experimental studies on intermediate compound of $LiBH_4$*. Applied Physics Letters, 2006. **89** (2): p. 021920.
61. Hwang, S.J., R.C. Bowman, J.W. Reiter, J. Rijssenbeek, G.L. Soloveichik, J.C. Zhao, H. Kabbour, and C.C. Ahn. *NMR confirmation for formation of $[B_{12}H_{12}]^{2-}$ complexes during hydrogen desorption from metal borohydrides*. Journal of Physical Chemistry C, 2008. **112** (9): p. 3164-3169.
62. Au, M., A. Jurgensen, and K. Zeigler. *Modified lithium borohydrides for reversible hydrogen storage (2)*. Journal of Physical Chemistry B, 2006. **110** (51): p. 26482-26487.
63. Au, M., A.R. Jurgensen, W.A. Spencer, D.L. Anton, F.E. Pinkerton, S.J. Hwang, C. Kim, and R.C. Bowman. *Stability and Reversibility of Lithium Borohydrides Doped by Metal Halides and Hydrides*. Journal of Physical Chemistry C, 2008. **112** (47): p. 18661-18671.
64. Schlesinger, H.I., H.C. Brown, H.R. Hoekstra, and L.R. Rapp. *New Developments in the Chemistry of Diborane and the Borohybrides .5. Reactions of Diborane with Alkali Metal Hydrides and Their Addition Compounds - New Syntheses of Borohydrides - Sodium and Potassium Borohydrides*. Journal Of The American Chemical Society, 1953. **75** (1): p. 199-204.
65. Schlesinger, H.I. and H.C. Brown. *New Developments in the Chemistry of Diborane and the Borohydrides .10. Uranium(Iv) Borohydride*. Journal Of The American Chemical Society, 1953. **75** (1): p. 219-221.
66. Li, Z.P., N. Morigazaki, B.H. Liu, and S. Suda. *Preparation of sodium borohydride by reaction of MgH_2 with dehydrated borax through ball milling reaction of MgH_2 with at room temperature*. Journal of Alloys and Compounds, 2003. **349** (1-2): p. 232-236.
67. Schlesinger, H.I., H.C. Brown, A.E. Finholt, J.R. Gilbreath, H.R. Hoekstra, and E.K. Hyde. *New Developments in the Chemistry of Diborane and of the Borohydrides .9. Sodium Borohydride, Its Hydrolysis and Its Use as a Reducing Agent and in the Generation of Hydrogen*. Journal Of The American Chemical Society, 1953. **75** (1): p. 215-219.

68. Steryladkina, Z.K., O.N. Kryukova, and V.I. Mikheeva. Russian Journal of Inorganic Chemistry, 1965. **10** (3): p. 316-318.
69. Li, Z.P., B.H. Liu, N. Morigasaki, and S. Suda. *Preparation of potassium borohydride by a mechano-chemical reaction of saline hydrides with dehydrated borate through ball milling*. Journal of Alloys and Compounds, 2003. **354** (1-2): p. 243-247.
70. Mikheeva, V.I., M.S. Selivokhina, and O.N. Kryukova. *Fusion diagram in the potassium hydroborate-potassium hydroxide system*. Russian Journal of Inorganic Chemistry, 1962. **7** (7): p. 838-841.
71. Mikheeva, V.I. and S.M. Arkhipev. *Rubidium and Caesium Tetrahydroborates*. Russian Journal of Inorganic Chemistry, 1966. **11** (7): p. 805-810.
72. Wiberg, E. and R. Bauer. *Zur Kenntnis Eines Magnesium-Bor-Wasserstoffs $Mg(BH_4)_2$*. Zeitschrift Fur Naturforschung Section B-a Journal of Chemical Sciences, 1950. **5** (7): p. 397-397.
73. Wiberg, E. and R. Bauer. *Neues zur kenntnis des Magnesium-bor-wasserstoffs $Mg(BH_4)_2$*. zeitschrift Fur Naturforschung, 1952. **7b**: p. 58-59.
74. Chlopek, K., C. Frommen, A. Leon, O. Zabara, and M. Fichtner. *Synthesis and properties of magnesium tetrahydroborate, $Mg(BH_4)_2$*. Journal of Materials Chemistry, 2007: p. 3496 - 3503.
75. Vajeeston, P., P. Ravindran, A. Kjekshus, and H. Fjellvag. *High hydrogen content complex hydrides: A density-functional study*. Applied Physics Letters, 2006. **89** (7): p. 071906.
76. Dai, B., D.S. Sholl, and J.K. Johnson. *First-principles study of experimental and hypothetical $Mg(BH_4)_2$ crystal structures*. Journal of Physical Chemistry C, 2008. **112** (11): p. 4391-4395.
77. Filinchuk, Y., R. Cerny, and H. Hagemann. *Insight into $Mg(BH_4)_2$ with Synchrotron X-ray Diffraction: Structure Revision, Crystal Chemistry, and Anomalous Thermal Expansion*. Chemistry of Materials, 2009. **21** (5): p. 925-933.
78. Zhou, X.F., Q.R. Qian, J. Zhou, B. Xu, Y.J. Tian, and H.T. Wang. *Crystal structure and stability of magnesium borohydride from first principles*. Physical Review B, 2009. **79** (21): p. 212102.
79. Ozolins, V., E.H. Majzoub, and C. Wolverton. *First-principles prediction of a ground state crystal structure of magnesium borohydride*. Physical Review Letters, 2008. **100** (13): p. 135501.
80. Her, J.H., P.W. Stephens, Y. Gao, G.L. Soloveichik, J. Rijssenbeek, M. Andrus, and J.C. Zhao. *Structure of unsolvated magnesium borohydride $Mg(BH_4)_2$*. Acta Crystallographica Section B-Structural Science, 2007. **63**: p. 561-568.
81. Konoplev, V.N. and V.M. Bakulina. *Some Properties of Magnesium Hydridoborate*. Izvestiya Akademii Nauk Sssr-Seriya Khimicheskaya, 1971 (1): p. 159.
82. Li, H.W., K. Kikuchi, Y. Nakamori, K. Miwa, S. Towata, and S. Orimo. *Effects of ball milling and additives on dehydriding behaviors of well-crystallized $Mg(BH_4)_2$*. Scripta Materialia, 2007. **57**: p. 679-682.
83. Cerny, R., Y. Filinchuk, H. Hagemann, and K. Yvon. *Magnesium borohydride: Synthesis and crystal structure*. Angewandte Chemie-International Edition, 2007. **46** (30): p. 5765-5767.
84. Varin, R.A., C. Chiu, and Z.S. Wronski. *Mechano-chemical activation synthesis (MCAS) of disordered $Mg(BH_4)_2$ using $NaBH_4$*. Journal of Alloys and Compounds, 2008. **462** (1-2): p. 201-208.
85. Zanella, P., L. Crociani, N. Masciocchi, and G. Giunchi. *Facile high-yield synthesis of pure, crystalline $Mg(BH_4)_2$*. Inorganic Chemistry, 2007. **46** (22): p. 9039-9041.

86. Li, H.W., K. Kikuchi, Y. Nakamori, N. Ohba, K. Miwa, S. Towata, and S. Orimo. *Dehydriding and rehydriding processes of well-crystallized $Mg(BH_4)_2$ accompanying with formation of intermediate compounds*. Acta Materialia, 2008. **56** (6): p. 1342-1347.
87. Soloveichik, G., J.H. Her, P.W. Stephens, Y. Gao, J. Rijssenbeek, M. Andrus, and J.C. Zhao. *Ammine magnesium borohydride complex as a new material for hydrogen storage: Structure and properties of $Mg(BH_4)_2$center dot $2NH_3$*. Inorganic Chemistry, 2008. **47** (10): p. 4290-4298.
88. Soloveichik, G.L., Y. Gao, J. Rijssenbeek, M. Andrus, S. Kniajanski, R.C. Bowman, S.J. Hwan, and J.C. Zhao. *Magnesium borohydride as a hydrogen storage material: Properties and dehydrogenation pathway of unsolvated $Mg(BH_4)_2$*. International Journal Of Hydrogen Energy, 2009. **34** (2): p. 916-928.
89. Titov, L.V. *Synthesis of Calcium Borohydride*. Doklady Akademii Nauk Sssr, 1964. **154** (3): p. 654.
90. Tomkinson, J. and T.C. Waddington. *Inelastic Neutron-Scattering from Alkali-Metal Borohydrides and Calcium Borohydride*. Journal of the Chemical Society-Faraday Transactions Ii, 1976. **72**: p. 528-538.
91. Miwa, K., M. Aoki, T. Noritake, N. Ohba, Y. Nakamori, S. Towata, A. Zuttel, and S. Orimo. *Thermodynamical stability of calcium borohydride $Ca(BH_4)_2$*. Physical Review B, 2006. **74** (15): p. 155122.
92. Barkhordarian, G., T.R. Jensen, S. Doppiu, U. Bosenberg, A. Borgschulte, R. Gremaud, Y. Cerenius, M. Dornheim, T. Klassen, and R. Bormann. *Formation of $Ca(BH_4)_2$ from hydrogenation of CaH_2+MgB_2 composite*. Journal of Physical Chemistry C, 2008. **112** (7): p. 2743-2749.
93. Ronnebro, E., E.H. Majzoub, and T. McDaniel, *Discovery and Development of Metal Hydrides for Reversible On-board Storage*, in *DOE Hydrogen Energy Program Review Report*. 2007, Sandia National Laboratories.
94. Barkhordarian, G., T. Klassen, M. Dornheim, and R. Bormann. *Unexpected kinetic effect of MgB_2 in reactive hydride composites containing complex borohydrides*. Journal of Alloys and Compounds, 2007. **440** (1-2): p. L18-L21.
95. Kim, J.H., S.A. Jin, J.H. Shim, and Y.W. Cho. *Thermal decomposition behavior of calcium borohydride $Ca(BH_4)_2$*. Journal of Alloys and Compounds, 2008. **461** (1-2): p. L20-L22.
96. Kim, J.H., S.A. Jin, J.H. Shim, and Y.W. Cho. *Reversible hydrogen storage in calcium borohydride Ca(BH4)(2)*. Scripta Materialia, 2008. **58** (6): p. 481-483.
97. Kim, J.H., J.H. Shim, and Y.W. Cho. *On the reversibility of hydrogen storage in Ti- and Nb-catalyzed Ca(BH4)(2)*. Journal Of Power Sources, 2008. **181** (1): p. 140-143.
98. Ronnebro, E. and E.H. Majzoub. *Calcium borohydride for hydrogen storage: Catalysis and reversibility*. Journal of Physical Chemistry B, 2007. **111** (42): p. 12045-12047.
99. Aoki, M., K. Miwa, T. Noritake, N. Ohba, M. Matsumoto, H.W. Li, Y. Nakamori, S. Towata, and S. Orimo. *Structural and dehydriding properties of $Ca(BH_4)_2$*. Applied Physics a-Materials Science & Processing, 2008. **92** (3): p. 601-605.
100. Fichtner, M., K. Chlopek, M. Longhini, and H. Hagemann. *Vibrational spectra of $Ca(BH_4)_2$*. Journal of Physical Chemistry C, 2008. **112** (30): p. 11575-11579.
101. Buchter, F., Z. Lodziana, A. Rernhof, O. Friedrichs, A. Borgschulte, P. Mauron, A. Zuttel, D. Sheptyakov, G. Barkhordarian, R. Bormann, K. Chlopek, M. Fichtner, M. Sorby, M. Riktor, B. Hauback, and S. Orimo. *Structure of $Ca(BD_4)_2$ beta-phase from combined neutron and synchrotron X-ray powder diffraction data and density*

functional calculations. Journal of Physical Chemistry B, 2008. **112** (27): p. 8042-8048.
102. Filinchuk, Y., E. Ronnebro, and D. Chandra. *Crystal structures and phase transformations in $Ca(BH_4)_2$*. Acta Materialia, 2009. **57** (3): p. 732-738.
103. Majzoub, E.H. and E. Ronnebro. *Crystal Structures of Calcium Borohydride: Theory and Experiment*. Journal of Physical Chemistry C, 2009. **113** (8): p. 3352-3358.
104. Makhaev, V.D., A.P. Borisov, and E.B. Lobkovskii. Russian Journal of Inorganic Chemistry, 1984. **29** (5): p. 666-669.
105. Hoekstra, H.R. and J.J. Katz. *The Preparation And Properties Of The Group Iv-B Metal Borohydrides*. Journal Of The American Chemical Society, 1949. **71** (7): p. 2488-2492.
106. Volkov, V.V. and K.G. Myakishev. *Synthesis Of Titanium(Iii) Tetrahydroborate From Ticl3 And Libh4*. Bulletin Of The Academy Of Sciences Of The Ussr Division Of Chemical Science, 1987. **36** (6): p. 1321-1321.
107. Volkov, V.V. and K.G. Myakishev. *On Mechanochemical Reaction Of Synthesis Of Titanium(III) Tetrahydroborate*. Sibirskii Khimicheskii Zhurnal, 1992 (5): p. 105-108.
108. Reid, W.E., J.M. Bish, and A. Brenner. *Electrodeposition Of Metals From Organic Solutions .3. Preparation And Electrolysis Of Titanium And Zirconium Compounds In Nonaqueous Media*. Journal Of The Electrochemical Society, 1957. **104** (1): p. 21-29.
109. James, B.D., R.K. Nanda, and Wallbrid.Mg. *Spectroscopic Studies Of Borohydride Derivatives Of Zirconium And Hafnium*. Journal of the Chemical Society a -Inorganic Physical Theoretical, 1966 (2): p. 182.
110. James, B.D., R.K. Nanda, and Wallbrid.Mg. *Reactions Of Lewis Bases With Tetrahydroborate Derivatives Of Group 4a Elements . Preparation Of New Zirconium Hydride Species*. Inorganic Chemistry, 1967. **6** (11): p. 1979.
111. Jensen, J.A., J.E. Gozum, D.M. Pollina, and G.S. Girolami. *Titanium, Zirconium, And Hafnium Tetrahydroborates As Tailored Cvd Precursors For Metal Diboride Thin-Films*. Journal Of The American Chemical Society, 1988. **110** (5): p. 1643-1644.
112. Tomkinson, J. and T.C. Waddington. *Inelastic Neutron-Scattering From Zirconium Borohydride*. Journal of the Chemical Society-Faraday Transactions Ii, 1976. **72**: p. 1245-1250.
113. Jensen, J.O. *Calculation of the vibrational frequencies and structure of zirconium tetrahydroborate*. Vibrational Spectroscopy, 2003. **31** (2): p. 227-250.
114. Volkov, V.V., E.V. Sobolev, Z.A. Grankina, and I.S. Kalinina. *Infrared spectra of Zirconium, Hafnium and alkali metals Tetrahydroborates*. Russian Journal of Inorganic Chemistry, 1968. **13** (3): p. 343-347.
115. Jensen, J.O. *Vibrational frequencies and structural determination of hafnium tetrahydroborate*. Spectrochimica Acta Part A-Molecular And Biomolecular Spectroscopy, 2003. **59** (2): p. 379-392.
116. Jensen, J.A. and G.S. Girolami. *Transition-metal tetrahydroborates as models of methane activation - Synthesis and reactivity of $TI(BH_4)_3(PMe_3)_2$ AND $V(BH_4)_3(PMe_3)_2$*. Abstracts of Papers of the American Chemical Society, 1986. **192**: p. 57.
117. Jensen, J.A. and G.S. Girolami. *Vanadium tetrahydroborates - Preparation adn characterization of $V(ETA\text{-}2\text{-}BH_4)_3(PMe_3)_2$ and the unusual unidentate BH_4^- complex $V(ETA\text{-}1\text{-}BH_4)_2(DMPE)_2$*. Journal Of The American Chemical Society, 1988. **110** (13): p. 4450-4451.

118. Jensen, J.A. and G.S. Girolami. *Vanadium(III) thtrahydroborates - Preperation, reaction chemistry, and crystal-structures of $V(BH_4)_3(PMe_3)_2$ and the oxo dimer $[V(BH_4)_2(PMe_3)_2]2O$*. Inorganic Chemistry, 1989. **28** (11): p. 2114-2119.
119. Parry, R.W., D.R. Schultz, and P.R. Girardot. *The preperation and properties of hexamminecolbolt(II) borohydride, hexaamminechromium(III) borohydride and ammonium borohydride*. Journal Of The American Chemical Society, 1958. **80** (1): p. 1-3.
120. Hein, F. and Schmiede.K. *On preparation of sodium and lithium tetraphenylochromates*. Journal of Organometallic Chemistry, 1967. **8** (3): p. 503.
121. Noth, H. and M. Seitz. *Preperation and characterization of chromium(II) tetrahydroborate - tetrahydrofuran (1/2)*. Journal Of The Chemical Society-Chemical Communications, 1976 (24): p. 1004-1004.
122. Mirviss, S.B. *Mechanism of oxidation of trialkylboranes*. Journal of Organic Chemistry, 1967. **32** (6): p. 1713.
123. Monnier, G. Ann. Chim. (Cachan, Fr.), 1957. **13**: p. 14-57.
124. Choudhury, P., V.R. Bhethanabotla, and E. Stefanakos. *Manganese Borohydride As a Hydrogen-Storage Candidate: First-Principles Crystal Structure and Thermodynamic Properties*. Journal of Physical Chemistry C, 2009. **113** (30): p. 13416-13424.
125. Cerny, R., N. Penin, H. Hagernann, and Y. Filinchuk. *The First Crystallographic and Spectroscopic Characterization of a 3d-Metal Borohydride: $Mn(BH_4)_2$*. Journal of Physical Chemistry C, 2009. **113** (20): p. 9003-9007.
126. Schaeffer, G.W., J.S. Roscoe, and A.C. Stewart. *The reduction of iron(III) chloride with lithium aluminohydride and lithium borohydride - iron (II) borohydride*. Journal Of The American Chemical Society, 1956. **78** (4): p. 729-733.
127. Stewart, A.C. and G.W. Schaeffer. *The reaction of cobalt (II) bromide with lithium borohydride and lithium aluminohydride*. Journal of Inorganic & Nuclear Chemistry, 1956. **3** (3-4): p. 194-197.
128. Schenk, P.W. and W. Muller. *Komplexe schwermetall-boranate*. Angewandte Chemie-International Edition, 1959. **71** (14): p. 457-457.
129. Maltseva, N.N., Sterlyad.Zk, and V.I. Mikheeva. *Reaction between aqueous solutions of sodium borohydride and nickel chloride*. Doklady Akademii Nauk Sssr, 1965. **160** (2): p. 352.
130. Wiberg, E. and W. Henle. *Zur kenntnis eines kupfer-bor-wasserstoffs $CuBH_4$*. Zeitschrift Fur Naturforschung Section B-a Journal of Chemical Sciences, 1952. **7** (9-10): p. 582-582.
131. Klingen, T.J. *Reaction of copper (II) chloride with lithium borohydride*. Inorganic Chemistry, 1964. **3** (7): p. 1058.
132. Wiberg, E. and W. Henle. *Zur Kenntnis Eines Silber-Bor-Wasserstoffs $AgBH_4$*. Zeitschrift Fur Naturforschung Section B-a Journal of Chemical Sciences, 1952. **7** (9-10): p. 575-576.
133. Noth, H. Angew Chemistry, 1961. **73**: p. 371-383.
134. Wiberg, E. and W. Henle. *Zur Kenntnis Eines Atherloslichen Zink-Bor-Wasserstoffs Zn(Bh4)2*. Zeitschrift Fur Naturforschung Section B-a Journal of Chemical Sciences, 1952. **7** (9-10): p. 579-580.
135. Maltseva, N.N., N.S. Kedrova, L.V. Gorobinskii, L.A. Petrova, and V.D. Makhaev. *Syntheses of $Zn(BH_4)_2$ and $RbBH_4$ center dot 18C6 using mechanochemical activation*. Russian Journal Of Coordination Chemistry, 1999. **25** (4): p. 246-248.
136. Matthews, J., Zinc Borohydride for hydrogen storage applications, Department of Metallurgy and Materials. University of Birmingham. 2005

137. Jeon, E. and Y. Cho. *Mechanochemical synthesis and thermal decomposition of zinc borohydride*. Journal of Alloys and Compounds, 2006. **422** (1-2): p. 273-275.
138. Ravnsbaek, D., Y. Filinchuk, Y. Cerenius, H.J. Jakobsen, F. Besenbacher, J. Skibsted, and T.R. Jensen. *A Series of Mixed-Metal Borohydrides*. Angewandte Chemie-International Edition, 2009. **48**: p. 6659-6663.
139. Maltseva, N.N., K.G. Myakishev, B.I. Saidov, N.S. Kedrova, Gorbacheva, II, O.G. Potapova, and V.V. Volkov. *Synthesis Of Zinc Borohydride And Its Derivatives By Mechanoactivation Of Mixtures Of Alkali-Metal Borohydrides With Zinc-Chloride*. Zhurnal Neorganicheskoi Khimii, 1989. **34** (6): p. 1430-1434.
140. Wiberg, E. and W. Henle. *Zur Kenntnis Eines Cadmium-Bor-Wasserstoffs $Cd(BH_4)_2$*. Zeitschrift Fur Naturforschung Section B-a Journal of Chemical Sciences, 1952. **7** (9-10): p. 582-582.
141. Wiberg, E., O. Dittmann, H. Noth, and M. Schmidt. *Uber wasserstoff-verbindungen des thalliums .5. Zur kinntnis eines thallium(I)-boranats $TlBH_4$ und thallium(I)-alanats $TlAlH_4$*. Zeitschrift Fur Naturforschung Part B-Chemie Biochemie Biophysik Biologie Und Verwandten Gebiete, 1957. **12** (1): p. 62-63.
142. Waddington, T.C. *Thallous borohydride, $TlBH_4$*. Journal of the Chemical Society, 1958 (DEC): p. 4783-4784.
143. Jensen, J.O. *Vibrational frequencies and structural determination of aluminum tetrahydroborate*. Spectrochimica Acta Part A-Molecular And Biomolecular Spectroscopy, 2003. **59** (7): p. 1565-1578.
144. Emery, A.R. and R.C. Taylor. *Raman Spectra And Vibrational Assignments Of Aluminum Borohydride And Some Isotopic Derivaties*. Spectrochimica Acta, 1960. **16** (11-1): p. 1455-1463.
145. Brokaw, R.S. and R.N. Pease. *The kinetics of the thermal decomposition of aluminum borohydride*. Journal Of The American Chemical Society, 1952. **74** (6): p. 1590-1591.
146. Wiberg, E., O. Dittmann, H. Noth, and M. Schmidt. *Uber wasserstoff-verbindungen des indiums .3. Zur kenntnis von lithium-trihalogenoindanaten $LiInX_3H$*. Zeitschrift Fur Naturforschung Part B-Chemie Biochemie Biophysik Biologie Und Verwandten Gebiete, 1957. **12** (1): p. 56-57.
147. Amberger, E. and M.R. Kula. *Darstellung und eigenschaften con zinn(II)-methodxyd und zinn(II)-boranat*. Angewandte Chemie-International Edition, 1963. **75** (11): p. 476.
148. Siddiqi, K.S., F. Aqra, S.A. Shah, and S.A.A. Zaidi. *The tridentate bonding mode of tetrahydroborate towards germanium and tin*. Polyhedron, 1994. **13** (2): p. 247-249.
149. Zange, E. *Entwicklung eines mikroverfahrens zur darstellung von boranaten der schweren lanthaniden*. Chemische Berichte-Recueil, 1960. **93** (3): p. 652-657.
150. Mirsaidov, U., A. Badalov, M. Khikmatov, K. Nazarov, and V.K. Marufi. *Thermodynamic Characteristics Of Lanthanum And Neodymium Borohydrides*. Zhurnal Fizicheskoi Khimii, 1991. **65** (11): p. 2914-2919.
151. Ehemann, M. and H. Noth. *Metal boranates and boranato metallates .4. Boranato complexes $M(BH_4)_4$+N(N-) of zirconium, hafnium and thorium*. Zeitschrift Fur Anorganische Und Allgemeine Chemie, 1971. **386** (1): p. 87.
152. Banks, R.H., N.M. Edelstein, R.R. Rietz, D.H. Templeton, and A. Zalkin. *Preparation And Properties Of Actinide Borohydrides - $Pa(BH_4)4$, $Np(BH_4)_4$, And $Pu(BH_4)_4$*. Journal Of The American Chemical Society, 1978. **100** (6): p. 1957-1958.
153. Reilly, J.J. and R.H. Wiswall. *Reaction of hydrogen with alloys of magnesium and copper*. Inorganic Chemistry, 1967. **6** (12): p. 2220.

154. Vajo, J.J., S.L. Skeith, F. Mertens, and S.W. Jorgensen. *Hydrogen-generating solid-state hydride/hydroxide reactions*. Journal of Alloys and Compounds, 2005. **390** (1-2): p. 55-61.
155. Vajo, J.J. and G.L. Olson. *Hydrogen storage in destabilized chemical systems*. Scripta Materialia, 2007. **56** (10): p. 829-834.
156. Vajo, J.J., T.T. Salguero, A.E. Gross, S.L. Skeith, and G.L. Olson. *Thermodynamic destabilization and reaction kinetics in light metal hydride systems*. Journal of Alloys and Compounds, 2007. **446**: p. 409-414.
157. Nakagawa, T., T. Ichikawa, Y. Kojima, and H. Fujii. *Gas emission properties of the MgH_x-$Zn(BH_4)_2$ systems*. Materials Transactions, 2007. **48** (3): p. 556-559.
158. Housecroft, C.E., *Boranes and metallaboranes: Structure, bonding and reactivity*. 2 ed. Ellis Horwood series in inorganic chemistry, ed. J. Burgess. 1989: Ellis Horwood.
159. Muetterties, E.L., *Boron hydride chemistry*. 1 ed. 1975: Academic Press.
160. Price, W.C. *The Absorption Spectrum of Diborane*. Journal of Chemical Physics, 1948. **16** (9): p. 894-902.
161. Bell, R.P. and H.C. Longuethiggins. *The Normal Vibrations Of Bridged X_2Y_6 Molecules*. Proceedings Of The Royal Society Of London Series A-Mathematical And Physical Sciences, 1945. **183** (995): p. 357-374.
162. Harvey, K.B. and N.R. McQuaker. *Low temperature infrared and Raman spectra of lithium borohydride*. Canadian Journal of Chemistry, 1971. **49** (20): p. 3282.
163. Miwa, K., N. Ohba, S. Towata, Y. Nakamori, and S. Orimo. *First-principles study on lithium borohydride $LiBH_4$*. Physical Review B, 2004. **69** (24): p. 245120.
164. Maekawa, H., M. Matsuo, H. Takamura, M. Ando, Y. Noda, T. Karahashi, and S.I. Orimo. *Halide-Stabilized $LiBH_4$, a Room-Temperature Lithium Fast-Ion Conductor*. Journal Of The American Chemical Society, 2009. **131** (3): p. 894–895.
165. Shane, D.T., R.C. Bowman, and M.S. Conradi. *Exchange of Hydrogen Atoms Between BH4 in LiBH4*. Journal of Physical Chemistry C, 2009. **113** (13): p. 5039-5042.
166. Ravnsbark, D., Y. Filinchuk, Y. Cerenius, H.J. Jakobsen, F. Besenbacher, J. Skibsted, and T.R. Jensen. *A Series of Mixed-Metal Borohydrides*. Angewandte Chemie-International Edition, 2009. **48**: p. 6659-6663.
167. Kim, Y., D. Reed, Y.S. Lee, J.Y. Lee, J.H. Shim, D. Book, and Y.W. Cho. *Identification of the Dehydrogenated Product of $Ca(BH_4)_2$*. Journal of Physical Chemistry C, 2009. **113** (14): p. 5865-5871.
168. Schmitt, K., C. Stuckl, H. Ripplinger, and B. Albert. *Crystal and electronic structure of BaB_6 in comparison with CaB_6 and molecular $[B_6H_6]^{2-}$*. Solid State Sciences, 2001. **3** (3): p. 321-327.
169. Ogita, N., S. Nagai, N. Okamoto, M. Udagawa, F. Iga, M. Sera, J. Akimitsu, and S. Kunii. *Raman scattering investigation of RB6 (R = Ca, La, Ce, Pr, Sm, Gd, Dy, and Yb)*. Physical Review B, 2003. **68** (22): p. 224305.
170. Ogita, N., S. Nagai, N. Okamoto, F. Iga, S. Kunii, J. Akimitsu, and M. Udagawa. *Raman scattering study of hexaboride crystals*. in *2nd Hiroshima Workshop on Transport and Thermal Properties of Advanced Materials*. 2002. Higadhi Hiroshima, Japan.131-134
171. Shang, S.L., Y. Wang, and Z.K. Liu. *First-principles calculations of phonon and thermodynamic properties in the boron-alkaline earth metal binary systems: B-Ca, B-Sr, and B-Ba*. Physical Review B, 2007. **75** (2): p. 11.
172. Ogita, N., S. Nagai, N. Okamoto, F. Iga, S. Kunii, T. Akamtsu, J. Akimitsu, and M. Udagawa. *Raman scattering study of CaB_6 and YbB_6*. in *14th International*

Symposium on Boron, Boride and Related Compounds. 2002. St Petersburg, RUSSIA.461-465
173. Lonzarich, G. [cited 2009 24 September 2009]; Available from: http://www-qm.phy.cam.ac.uk/research/MgB2.jpg.
174. Bohnen, K.P., R. Heid, and B. Renker. *Phonon dispersion and electron-phonon coupling in MgB_2 and AlB_2*. Physical Review Letters, 2001. **86** (25): p. 5771-5774.
175. Muetterties, E.L., R.E. Merrifield, W.H. Knoth, J.R. Downing, and H.C. Miller. *Chemistry of boranes .3. Infrared and Raman spectra of $B_{12}H_{12}^{2-}$ and related anions*. Journal Of The American Chemical Society, 1962. **84** (13): p. 2506-2511.
176. Молекула. [cited 2009 15th Febuary 2009]; Available from: http://www.nanometer.ru/2007/05/02/nanotechnology.html.
177. Li, H.W., K. Miwa, N. Ohba, T. Fujita, T. Sato, Y. Yan, S. Towata, M.W. Chen, and S. Orimo. *Formation of an intermediate compound with a $B_{12}H_{12}$ cluster: experimental and theoretical studies on magnesium borohydride $Mg(BH_4)_2$*. Nanotechnology, 2009. **20** (20): p. 204013.
178. Li, H.W., K. Kikuchi, T. Sato, Y. Nakamori, N. Ohba, M. Aoki, K. Miwa, S. Towata, and S. Orimo. *Synthesis and Hydrogen Storage Properties of a Single-Phase Magnesium Borohydride $Mg(BH_4)_2$*. Materials Transactions, 2008. **49** (10): p. 2224-2228.
179. Evans, J.S.O. *TOPAS accademic*. 07-Aug-2009 [cited 20-Aug-2009; Available from: http://www.dur.ac.uk/john.evans/topas_academic/topas_main.htm.
180. Lide, D.R., ed. *CRC Handbook of Chemistry and Physics*. 89th ed. 2009, CRC.
181. Borgschulte, A., A. Zuttel, P. Hug, A.M. Racu, and J. Schoenes. *Hydrogen-deuterium exchange in bulk $LiBH_4$*. Journal of Physical Chemistry A, 2008. **112** (21): p. 4749-4753.
182. Wiberg, E. and R. Bauer. *Neues Zur Kenntnis Des Magnesium-Aluminium-Wasserstoffs $Mg(AlH_4)_2$*. Zeitschrift Fur Naturforschung Section B-a Journal of Chemical Sciences, 1952. **7** (2): p. 131-132.
183. Kim, J.H., S.A. Jin, J.H. Shim, and Y.W. Cho. *Reversible hydrogen storage in calcium borohydride $Ca(BH_4)_2$*. Scripta Materialia, 2008. **58** (6): p. 481-483.
184. Dilts, J.A. and E.C. Ashby. *Study Of Thermal-Decomposition Of Complex Metal Hydrides*. Inorganic Chemistry, 1972. **11** (6): p. 1230-1236.
185. Nakamori, Y. and S. Orimo. *Destabilization of Li-based complex hydrides*. Journal of Alloys and Compounds, 2004. **370** (1-2): p. 271-275.
186. Mosegaard, L., B. Moller, J.E. Jorgensen, U. Bosenberg, M. Dornheim, J.C. Hanson, Y. Cerenius, G. Walker, H.J. Jakobsen, F. Besenbacher, and T.R. Jensen. *Intermediate phases observed during decomposition of $LiBH_4$*. Journal of Alloys and Compounds, 2007. **446**: p. 301-305.
187. Filinchuk, Y., D. Chernyshov, and R. Cerny. *Lightest borohydride probed by synchrotron X-ray diffraction: Experiment calls for a new theoretical revision*. Journal of Physical Chemistry C, 2008. **112** (28): p. 10579-10584.
188. Her, J.H., M. Yousufuddin, W. Zhou, S.S. Jalisatgi, J.G. Kulleck, J.A. Zan, S.J. Hwang, R.C. Bowman, and T.J. Uclovict. *Crystal Structure of $Li_2B_{12}H_{12}$: a Possible Intermediate Species in the Decomposition of $LiBH_4$*. Inorganic Chemistry, 2008. **47** (21): p. 9757-9759.
189. Skripov, A.V., A.V. Soloninin, Y. Filinchuk, and D. Chernyshov. *Nuclear Magnetic Resonance Study of the Rotational Motion and the Phase Transition in $LiBH_4$*. Journal of Physical Chemistry C, 2008. **112** (47): p. 18701-18705.

190. Kang, J.K., S.Y. Kim, Y.S. Han, R.P. Muller, and W.A. Goddard. *A candidate $LiBH_4$ for hydrogen storage: Crystal structures and reaction mechanisms of intermediate phases*. Applied Physics Letters, 2005. **87** (11): p. 3.
191. Hwang, S.J., R.C. Bowman, J.W. Reiter, J. Rijssenbeek, G.L. Soloveichik, J.C. Zhao, H. Kabbour, and C.C. Ahn. *NMR confirmation for formation of [B12H12](2-) complexes during hydrogen desorption from metal borohydrides*. Journal of Physical Chemistry C, 2008. **112** (9): p. 3164-3169.
192. Jenkins, T.E. and J. Lewis. *The anomalous termperature-viriation of the symmetric stretching vibration NU-S(H_2O) in hexa-aquo metal (II) hexafluorosilicate (IV)*. Journal of Raman Spectroscopy, 1981. **11** (1): p. 1-3.
193. Laubereau, A. and W. Kaiser. *Vibrational dynamics of liquids and solids investigated by picosecond light-pulses*. Reviews of Modern Physics, 1978. **50** (3): p. 607-665.
194. Hagemann, H., Y. Filinchuk, D. Chernyshov, and W. van Beek. *Lattice anharmonicity and structural evolution of $LiBH_4$: an insight from Raman and X-ray diffraction experiments*. Phase Transitions, 2009. **82** (4): p. 344-355.